

به نام خدا



مرکز دانلود رایگان
مهندسی متالورژی و مواد

www.Iran-mavad.com



Materials Forming, Machining and Tribology

J. Paulo Davim *Editor*

Modern Manufacturing Engineering

 Springer

www.iran-mavad.com

مرجع علمی مهندسی مواد

Materials Forming, Machining and Tribology

Series editor

J. Paulo Davim, Aveiro, Portugal

More information about this series at <http://www.springer.com/series/11181>

J. Paulo Davim
Editor

Modern Manufacturing Engineering

 Springer

Editor

J. Paulo Davim

Department of Mechanical Engineering

University of Aveiro

Aveiro

Portugal

ISSN 2195-0911

ISSN 2195-092X (electronic)

Materials Forming, Machining and Tribology

ISBN 978-3-319-20151-1

ISBN 978-3-319-20152-8 (eBook)

DOI 10.1007/978-3-319-20152-8

Library of Congress Control Number: 2015941349

Springer Cham Heidelberg New York Dordrecht London

© Springer International Publishing Switzerland 2015

This work is subject to copyright. All rights are reserved by the Publisher, whether the whole or part of the material is concerned, specifically the rights of translation, reprinting, reuse of illustrations, recitation, broadcasting, reproduction on microfilms or in any other physical way, and transmission or information storage and retrieval, electronic adaptation, computer software, or by similar or dissimilar methodology now known or hereafter developed.

The use of general descriptive names, registered names, trademarks, service marks, etc. in this publication does not imply, even in the absence of a specific statement, that such names are exempt from the relevant protective laws and regulations and therefore free for general use.

The publisher, the authors and the editors are safe to assume that the advice and information in this book are believed to be true and accurate at the date of publication. Neither the publisher nor the authors or the editors give a warranty, express or implied, with respect to the material contained herein or for any errors or omissions that may have been made.

Printed on acid-free paper

Springer International Publishing AG Switzerland is part of Springer Science+Business Media
(www.springer.com)

Preface

Nowadays, Manufacturing Engineering is defined as a discipline “which involves the ability to plan the processes and practices of manufacturing and to research and develop systems, processes, machines, tools and equipment for producing quality products”. Manufacturing is the “art” of transformation of materials into products. Fundamental subjects of manufacturing engineering include: materials technology, forming and sheet metal working, traditional and non-traditional machining, joining and assembly processes, automation and manufacturing systems, green and lean manufacturing, etc.

The purpose of this book is to present a collection of examples illustrating research in “Modern Manufacturing Engineering”. Chapter 1 of the book provides submicro- and nanostructuring of materials by severe plastic deformation. Chapter 2 is dedicated to cross rolling (a metal forming process). Chapter 3 describes a finite element method in machining processes. Chapter 4 contains information about machining and machining modelling of metal matrix composites. Chapter 5 contains information about intelligent CNC tool path optimization for sculptured surface machining through virus-evolutionary genetic algorithm. Chapter 6 is dedicated to friction stir welding: (scope and recent developments). Chapter 7 describes innovative joining technologies based on tube. Chapter 8 contains information about lean manufacturing. Chapter 9 provides object-based final-year project (designing and manufacturing a quick stop device). Finally, Chap. 10 is dedicated to quantifying quality of learning during teaching an undergraduate unit (manufacturing processes).

This book can be used as a research book for final undergraduate engineering course or as a topic on manufacturing engineering at the postgraduate level. Also, this book can serve as a useful reference for academics, researchers, mechanical, manufacturing, industrial and materials engineers, professionals in manufacturing and related industries. The scientific interest in this book is evident for many important centres of research, laboratories and universities as well as industry. Therefore, it is hoped this book will inspire and enthuse others to undertake research in manufacturing engineering.

The Editor acknowledges Springer for this opportunity and for their enthusiastic and professional support. Finally, I would like to thank all the chapter authors for their availability for this work.

Aveiro, Portugal
May 2015

J. Paulo Davim

Contents

1	Submicro and Nanostructuring of Materials by Severe Plastic Deformation	1
	Viktor P. Astakhov	
2	Cross Rolling: A Metal Forming Process	41
	Matruprasad Rout, Surjya K. Pal and Shiv B. Singh	
3	Finite Element Method in Machining Processes: A Review	65
	Carlos H. Lauro, Lincoln C. Brandão, Sergio L.M. Ribeiro Filho, Robertt A.F. Valente and J. Paulo Davim	
4	Machining and Machining Modeling of Metal Matrix Composites—A Review	99
	Angelos P. Markopoulos, Ioannis S. Pressas, Ioannis G. Papantoniou, Nikolaos E. Karkalos and J. Paulo Davim	
5	Intelligent CNC Tool Path Optimization for Sculptured Surface Machining Through a Virus-Evolutionary Genetic Algorithm.	143
	Nikolaos A. Fountas, Nikolaos M. Vaxevanidis, Constantinos I. Stergiou and Redha Benhadj-Djilali	
6	Friction Stir Welding: Scope and Recent Development	179
	Rahul Jain, Kanchan Kumari, Ram Kumar Kesharwani, Sachin Kumar, Surjya K. Pal, Shiv B. Singh, Sushanta K. Panda and Arun K. Samantaray	
7	Innovative Joining Technologies Based on Tube Forming.	231
	L.M. Alves, C.M.A. Silva and P.A.F. Martins	

8	Lean Manufacturing	249
	Ali Hosseini, Hossam A. Kishawy and Hussein M. Hussein	
9	Object-Based Final-Year Project: Designing and Manufacturing a Quick Stop Device	271
	A. Pramanik, Hem Sanghvi and A.K. Basak	
10	Quantifying Quality of Learning During Teaching an Undergraduate Unit: Manufacturing Processes	301
	A. Pramanik and M.N. Islam	
	Index	319

Chapter 1

Submicro and Nanostructuring of Materials by Severe Plastic Deformation

Viktor P. Astakhov

Abstract This chapter discusses the development of the metallurgical structure of submicro and nanostructured metallic materials in Severe Plastic Deformation (SPD). Particular attention is paid to Equal-Channel Angular Pressing (ECAP) as the most feasible way to achieve the major objectives of grain refinement, distinguished as strength enhancement, superplasticity, and improvement in creep resistance. The need and essence of the multi-pass process is explained in detail. Particular attention is paid to the deformation mode in SPD. It is shown that the discussed objectives can be achieved if this deformation mode is simple shear. The chapter also presents the development and modeling of large strain extrusion machining (LSEM), comparing the results obtained in this process with those in ECAP.

1.1 Introduction

There is considerable current interest in fabricating metals with ultrafine grain sizes. Several methods are now available for attaining metals with extremely small grain sizes, usually within the nanometer range, including inert gas condensation, high energy ball milling, and sliding wear. However, these procedures have not been developed sufficiently to date though they are capable of producing large bulk samples which are free of any residual porosity. As a result of these limitations, attention has been devoted to the alternative processes of Equal-Channel Angular Pressing (ECAP) and High-Pressure Torsion (HPT) in which ultrafine grains are introduced into a material through intense plastic straining [1]. In practice, ECAP appears to have greater utility than HPT because there is a potential for scaling-up the process for industrial applications through procedures such as the development

V.P. Astakhov (✉)

General Motors Business Unit of PSMi, 1792 Elk Ln, Okemos, MI 48864, USA
e-mail: astakhov@scientist.com

© Springer International Publishing Switzerland 2015
J.P. Davim (ed.), *Modern Manufacturing Engineering*, Materials Forming,
Machining and Tribology, DOI 10.1007/978-3-319-20152-8_1

1

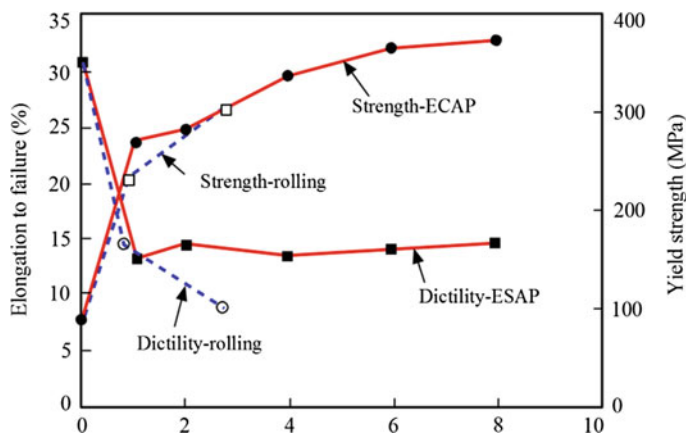


Fig. 1.1 A comparison of yield strength and ductility for an Al-3004 alloy processed by cold-rolling or ECAP

of multi-pass facilities where high strains are attained in a single passage through the ECAP die.

The major objective of ECAP is grain refinement, i.e., to obtain materials with ultrafine (submicro) and nanosized grains. Although many benefits of useful physical properties of such materials can be used in the design and technology [2], the following improvements are well studied/documentated.

Strength enhancement, i.e., obtaining strength of more than two times greater than that for the same materials of conventional grain size. Strength and ductility are the key mechanical properties of any material but these properties typically have opposing characteristics. Thus, materials may be strong or ductile but they are rarely both. The reason for this dichotomy is of a fundamental nature as the plastic deformation mechanisms of metallic materials associate with the generation and movement of dislocations.

It is well known that application of severe plastic deformation (SPD) in conventional deformation processing techniques such as rolling, drawing, and extrusion leads to a significantly higher strength and a relatively low ductility. SPD processing using ECAP leads to reduction in the ductility which is generally less than in more conventional deformation processing techniques. For example, experiments conducted to compare the strength and ductility of the 3004 aluminum alloy processed by ECAP and cold-rolling [3] showed that the yield strength increased monotonically with the increasing equivalent strain imparted into the alloy by either cold rolling or ECAP (Fig. 1.1). It is apparent also that the overall ductility exhibits different trends for these two processing methods. After one ECAP pass, equivalent to a strain of ~ 1 , the elongation to failure or the ductility of the alloy decreases from ~ 32 to ~ 14 %. However, there is no additional reduction in the ductility with additional ECAP passes and therefore with the imposition of even larger strains. By contrast, cold-rolling decreases ductility by a similar magnitude initially but thereafter the ductility continues to decrease with increasing rolling strain, although at a

slower rate. Consequently, processing by ECAP leads ultimately to greater retention of ductility than conventional cold-rolling.

Recent findings of extraordinary high strength and good ductility in several bulk ultrafine-grained metals produced by severe plastic deformation are well analyzed by Valiev and Langdon [4].

Superplasticity, i.e., obtaining a significant increase in the strain at fracture in certain work materials. For example, as reported by Figueiredo and Langdon [5], mechanical testing of extruded ZK60 alloy at temperature of 473 K showed that the elongation at fracture was 830 % for a received material, whereas this became 3050 % after two passes through equal channel extrusion die. As reported by Kawasaki et al. [6], testing of a Pb-62 % Sn eutectic alloy after four passes through an equal channel extrusion die showed superplastic elongations at intermediate strain rates with a maximum elongation to failure of 2,665 %. Musin et al. [7] reported superplastic behavior of an Al-4.1 %Mg-2.0 %Li-0.16 %Sc-0.07 %Zr alloy (1421 Al) subjected to intense plastic straining by equal channel angular extrusion in the temperature interval 250–450 °C at strain rates ranging from 1.4×10^{-5} to 1.4 s^{-1} . The grain size after ECAE was about 0.8 μm and the fraction of high angle boundaries was about 80 pct. The highest elongation of 1850 % without failure appeared at a temperature of 400 °C and strain rate of $1.4 \times 10^{-2} \text{ s}^{-1}$.

Improvement in creep resistance. Creep strength and ductility are the key creep properties of creep-resistant materials but these properties typically have opposing characteristics. Thus, materials with conventional grain sizes may be strong or ductile but they are rarely both. Recent findings of high strength and good ductility in several nanocrystalline (grain size <100 nm) and ultrafine-grained (grain size <1 μm) metals and alloys [8] produced using severe plastic deformation processes and creep testing showed much superior behavior of these materials.

The traditional picture of plastic deformation behavior of many polycrystalline metallic materials includes strain hardening defined as an increase in the flow stress with strain [9]. It is believed that strain hardening is caused by the interaction of dislocations and other microstructural mechanisms associated with defects [10]. Such a mechanical response to the applied load, however, seems to be no longer valid when the grain size of the material is reduced far into submicron scale. For example, in nanocrystalline Cu, deformation behavior falls into two patterns. It was revealed [11] that, if the grain size is small enough (in Cu it is for the grain size from 5 to 50 nm), grain boundary sliding starts to dominate in the deformation behavior. This finding was later confirmed for other metallic materials, for example, for nanocrystalline Ni [12]. It was found that electrodeposited nanocrystalline Ni, subjected to plastic strain, did not build up a residual dislocation network.

Analyzing the literature on deformation behavior, Olejnik and Rosochowski [13] classified deformational behavior of polycrystalline metals according to their grain size as shown in Fig. 1.2. For sizes greater than 1000 nm (coarse-grained polycrystalline metals), traditional deformation mechanisms govern deformation behavior. In the range from 1000 nm down to 30 nm, disordered grain boundaries begin to dominate in the mechanical behavior (ultrafine-grained polycrystalline metals). This transition becomes much more profound below 100 nm. At smaller grain sizes

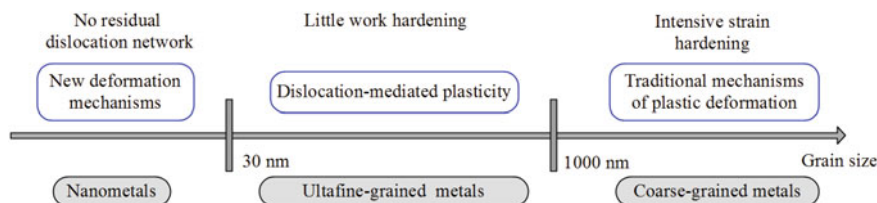


Fig. 1.2 Classification of polycrystalline metals according to grain size

(<30 nm), the atomic sliding at grain boundaries increases, leading to virtually no further work hardening of the plastically deformed metal.

The objective of this chapter is to familiarize readers with particularities of the ECAP, including machining-extrusion processes, pointing out some issues existing in SPD processes and to present the research advances to address common concerns.

1.2 Severe Plastic Deformation as a Feasible Way to Achieve Grain Refinement

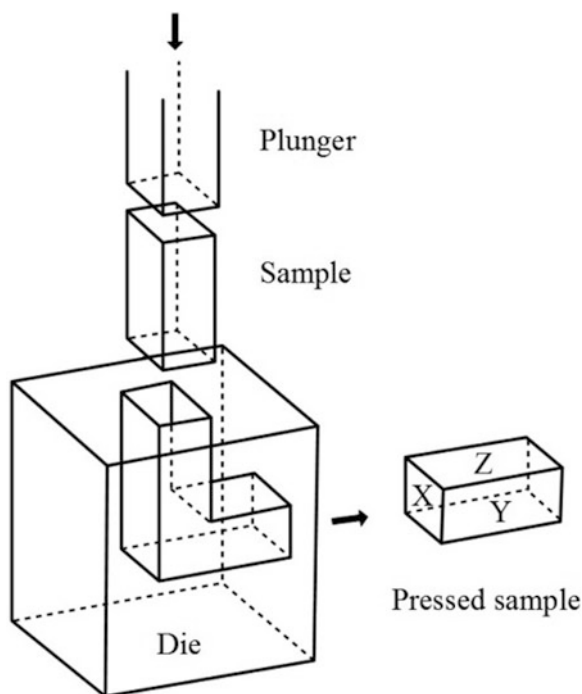
It is well known that one important and feasible way for grain refinement in metals is application of severe plastic deformation [10]. Plastic working remains efficient in terms of producing small grain sizes only in the range down to 30 nm for most metals and their alloys. For now, the nanometals territory has been restricted to new synthesis-based methods of materials fabrication.

The amount of plastic strain produced by classical metal forming operations is often limited because of the work material or tool failure. Compressive forming conditions are preferable to hamper void nucleation, growth, and coalescence which lead to ductile fracture. In some sequential processes such as rolling or drawing, large reductions of the material thickness can be achieved. However, the shapes produced by these processes are not bulk enough to be used for further conversion into products. Thus, new metal forming processes capable of generating very large or severe plastic deformation (SPD) without major change in the billet geometry have been developed.

Originally, the term SPD was defined as “intense plastic straining under high imposed pressure” [8]. Nowadays, its ‘covering area’ extends to all metal forming processes that are based on simple shear and/or repetitive reversed straining and tend to preserve the initial shape of the billet [14]. Common SPD processes, originally developed for grain refinement, are: (1) High-pressure torsion, (2) Equal channel angular extrusion, (3) Cyclic extrusion-compression, (4) Multiaxial forging, (5) Accumulative roll-bonding, (6) Repetitive corrugation and straightening [13].

Historically, ECAP was first developed in the Soviet Union in the 1970s as a metal forming process where high strain rates could be introduced into metal billets

Fig. 1.3 Schematic illustration of ECAP showing the three orthogonal planes X , Y , and Z



by simple shear, but its early development received only limited attention in the scientific community. This situation changed in the 1990s when the potential for using ECAP to produce ultrafine-grained (UFG) metals (classified today as nanomaterials) with new unique properties (i.e., superplasticity) was revealed in the reports and overviews by the Ufa (Russia) team [8]. Since then, vigorous studies of this process in many countries led to multiple industrial applications of ECAP.

The principle of ECAP is depicted schematically in the three-dimensional illustration in Fig. 1.3 [15]. The ECAP die contains two channels, equal in cross-section, intersecting at an angle near the center of the die. The test sample is machined to fit within these channels and it is pressed through the die using a plunger. The straining imposed on the sample as it goes through the die is illustrated schematically in Fig. 1.4, where for simplicity, it is assumed that the angle of intersection between the two channels is 90° . Thus, simple shear is imposed at the shearing plane between the two adjacent segments labeled 1 and 2 in Fig. 1.4. Three planes may be defined within the sample at the point of exit from the die, as indicated in Fig. 1.3 where plane X is perpendicular to the longitudinal axis of the sample and planes Y and Z are parallel to the side and top faces, respectively.

Figure 1.5 illustrates a section through the die and defines two internal angles, namely an angle Φ_{die} between the channels and an angle Ψ_{dz} at the outer arc of curvature where the two channels intersect. When the sample passes through the die, the value of the von Mises equivalent strain is dependent on the values of these

Fig. 1.4 The principle of shearing between elements 1 and 2 in ECAP

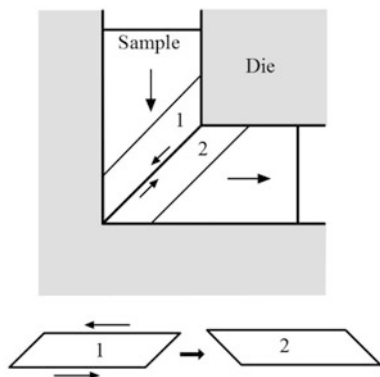
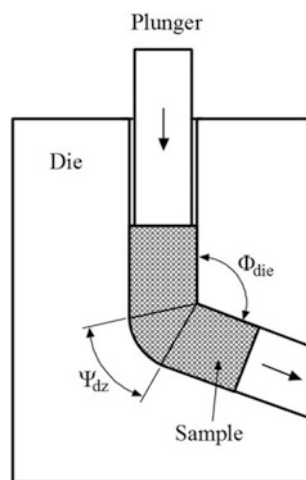


Fig. 1.5 A section through an ECAP die showing the two internal angles Φ_{die} and Ψ_{dz}



two angles. Because the cross-sectional dimensions of the sample remain unchanged with a single passage through the die, the sample may be pressed repetitively through the die in order to achieve very high total strain. The total shear strain accumulated through a series of repetitive pressings is calculated as

$$\gamma_{\text{sh}} = N \left[2 \cot \left(\frac{\Phi_{\text{die}} + \Psi_{\text{dz}}}{2} \right) + \Psi_{\text{dz}} \right] \quad (1.1)$$

where N is the total number of passes through the die.

It follows from—Eq. (1.1) when $\Psi_{\text{dz}} = 0^\circ$, the total shear strain is calculated as

$$\gamma_{\text{sh}} = 2N \cot \frac{\Phi_{\text{die}}}{2} \quad (1.2)$$

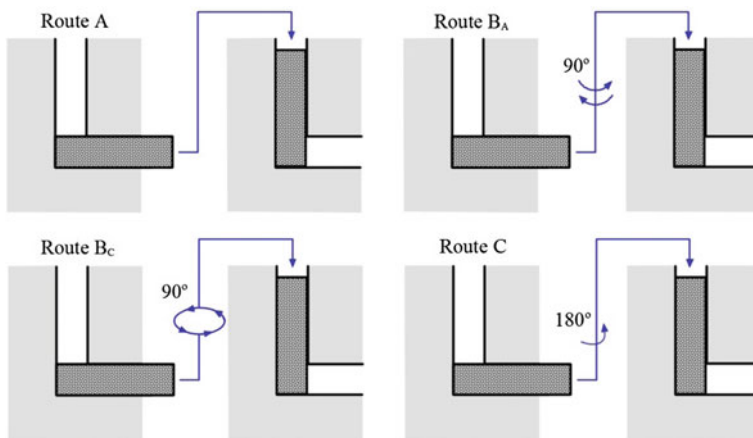


Fig. 1.6 The four fundamental processing routes in ECAP pressing

Finally, the total equivalent strain accumulated through a series of repetitive pressings, ε_N , is given by the relationship [15]

$$\varepsilon_N = \frac{N}{\sqrt{3}} \left[2 \cot \left(\frac{\Phi_{\text{die}} + \Psi_{dz}}{2} \right) + \Psi_{dz} \right] \quad (1.3)$$

Various approaches have been developed also to estimate the strain in situations where the two channels of the die have different cross-sectional dimensions and FEM has been used to examine the significance of any gap that may form between the sample and the die wall at the outer arc of curvature between the two channels [8].

Detailed experiments on pure aluminum, using dies having values of Φ_{die} ranging from 90° to 157.5° , showed that an ultrafine microstructure of essentially equiaxed grains, separated by grain boundaries having high angles of misorientation, was attained most easily when imparting a very intense plastic strain with a value of Φ_{die} very close to 90° [16]. For a value of $\Phi_{\text{die}} = 90^\circ$, it follows from Eq. (1.3) that the equivalent strain imposed on a single passage through the die is very close to 1 for any value of Ψ_{dz} . Therefore, the strain is close to $\sim N$ for a total of N passes through the die.

When a sample is pressed repetitively through an ECAP die, it has been recognized that the overall shearing characteristics within the crystalline sample may be changed by a rotation of the sample between the individual pressings. Commonly, three distinct processing routes are considered [8]: route A in which the sample is not rotated between repetitive pressings, route B in which the sample is rotated by 90° between each pressing, and route C in which the sample is rotated by 180° between each pressing. A further possibility appeared when it was noted that route B may be undertaken either by rotating the sample by 90° in alternate directions between each individual pressing, termed route B_A, or by rotating the sample by 90° in the same direction between each individual pressing, termed route B_C. The principles of these four different routes are illustrated schematically in Fig. 1.6.

1.3 Addressing Common Concerns: Multi-pass, Materials Used, and Strain Achieved

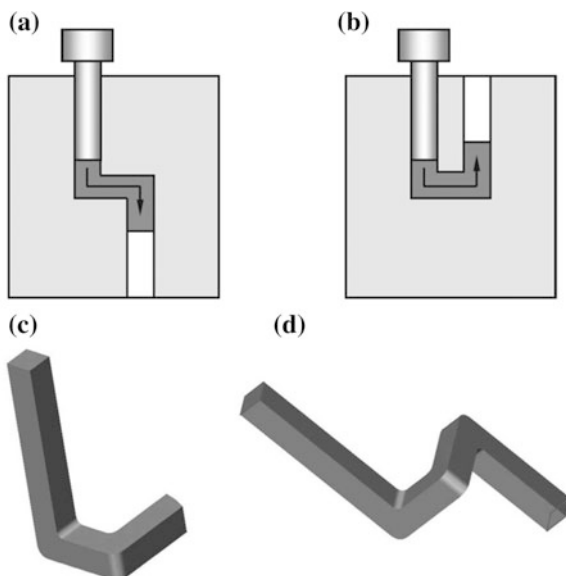
In analyzing ECAP, particularly in the developing new methods of ECAP as for example, metal cutting assisted, it is important to understand why multi-pass processes in ECAP are used. Two common misconceptions are sometimes used to justify the development of new ‘unusual’ processes. The first one is the plastic strain imposed by ECAP is insufficient for needed grain refinements because, as mentioned above, the strain imposed on a single passage through the die in ECAP is normally close to 1. The second one is that only ‘soft’ materials can be used, i.e., a “significant limitation of ECAP is the inability to induce large strains in high-strength materials, such as nickel-based high-temperature alloys and tool steels, as well as materials that are traditionally difficult to deform. Particularly notable examples of the latter include metals having hexagonal close-packed (hcp) structures, including magnesium, titanium and their alloys” [17].

Addressing the first concern about insufficient strain in ECAP, one should consider that in ECAP, more complicated die designs than that shown in Fig. 1.3 can be utilized to achieve any (material-allowed) strain in one pass. A simple solution as an S-shaped channel die [18] is shown in Fig. 1.7a. This scheme is equivalent to route C in Fig. 1.6. It is understood that dies having a sequence of S-shaped channels can be used to achieve the desirable strain in one pass. Figure 1.7b shows a die design with a U-shape channel [8] where route A in Fig. 1.6 is realized. Using two-turn channels doubles the strain produced in one pass and increases the the productivity of ECAP. In order to obtain even greater strains and homogeneous microstructures of equiaxed grains separated by high-angle boundaries, route B_C should be used [15]. A square channel, with two-turns and all angles equal to $\pm 90^\circ$, configured to realize route B_C in die, is drawn in Fig. 1.7c. Figure 1.7d shows a three-turn channel for a similar configuration used for processing commercial purity aluminum [13].

Addressing the above-mentioned concern with work material, the author should say the following: as early as 1998, Shadat, M. A. defended at Texas A&M University a PhD thesis “The effect of equal channel angular extrusion on the microstructure and mechanical properties of AISI 1552, AISI 4340, and A2 tool steels,” where ‘ECAPbility’ of low, medium, and high-carbon (tool) steels were investigated and extrusion regimes for these materials are suggested (<http://repository.tamu.edu/handle/1969.1/ETD-TAMU-1998-THESIS-S53>). Since then, a great body of research on ECAP of various steel and hcp materials, such as pure zinc and titanium, as well as their alloys were published as summarized in [1, 8]. Among these are the papers on ECAP of stainless steel [19], magnesium alloy [20], low [21], and medium-carbon alloyed steels and pure titanium [22].

Luo et al. [23] and McDonald et al. [24] took a more innovative approach to selection of a cost-effective feedstock for ECAP forming of commercially pure titanium (ASTM Grade 2) and Ti-6Al-4V (ASTM Grade 5, mill annealed condition) rods. Machining of components made of titanium and its alloys generates

Fig. 1.7 Channel designs for multi-turn ECAP: **a** two-turn (route C in Fig. 1.6), **b** two-turn (route A in Fig. 1.6), **c** two-turn (route B_C in Fig. 1.6), **d** three-turn (route B_C in Fig. 1.6)



significant quantities of machining chips. To recycle these chips conventionally is very costly and energy-intensive, so the potential for their direct consolidation to a viable semi-product would carry clear benefits.

In case of Ti-6Al-4V, machining chips were produced by dry milling and were cleaned in ethanol. These chips were then charged and compacted into an ECAP die (Fig. 1.8) in a wrapping of stainless steel and graphite for lubrication and ECAP was conducted for 4 passes at 590 °C at a speed of 5 mm/min with the aid of a back pressure (PB) of 50 MPa. The as-consolidated material possessed a refined microstructure and contained a series of oxide layers associated with the boundary of each machining chip. Higher magnification examination indicated that certain chip boundaries had been broken down by the severe shear experience during ECAP. The authors concluded that increased numbers of passes might induce the breakdown and dispersion of further chip boundaries and the achievement of oxide dispersion strengthening.

The above analysis suggests that ECAP places no limitation on the type and grade of the work material.

A need for multiple passes is explained by the requirement to achieve homogeneous microstructures of equiaxed grains separated by high-angle boundaries. There are two fundamental characteristics associated with the development of a homogeneous microstructure through ECAP. These characteristics are related to the ultimate stable grain size which is achieved by the pressing process and the number of passes needed to attain a homogeneous microstructure. In general terms, it appears that metals exhibiting low rates of recovery are especially attractive for production of extremely fine grain sizes but the number of passes needed to achieve homogeneous arrays of grains in these materials is then increased. For example,

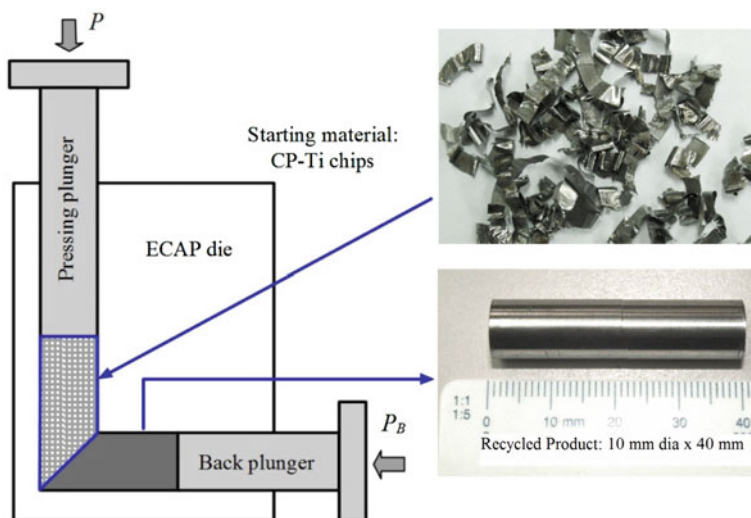


Fig. 1.8 Recycling of Ti machining chips by ECAP

experiments have shown that, for materials subjected to ECAP at room temperature using route B_C, the ultimate stable grain sizes are ~ 1.3 , ~ 0.45 and ~ 0.27 μm for samples of pure aluminum, an Al-1 % Mg alloy and an Al-3 % Mg alloy, but homogeneity of the microstructure requires pressing through, respectively, 4, 6, and 8 passes for these three materials [15].

Figure 1.9 helps to understand the essence of grain formation in ECAP. As can be seen, a generally spherical grain accrues an ellipsoid shape after the first pass. The higher the strain, the greater elongation of axis 21 compared to axis 11. In other words, no matter how high strain is, it is impossible to achieve equiaxed grains. Figure 1.9 also shows that if route A is used, the ellipsoid formed at the first pass is further elongated. As such, the direction of shear slips is set by angle, Φ_{die} about the axis perpendicular to that of the extrusion channel. When the number of passes, N , is increased much smaller grain size can be achieved. However, the problem to obtain equiaxed grains remains if route A is used.

Figure 1.10 illustrates the formation of the microstructure in ECAP when the routes shown in Fig. 1.6 are used. In this figure, the planes labeled 1 through 4 denote the shearing that occurs on the first four pressings through the die and the planes X, Y, and Z are indicated. Processing through route A therefore leads to shearing on two planes intersecting at 90° , processing through route C leads to repetitive shearings on the same plane, and processing through routes B_A and B_C leads to shearing on a set of planes intersecting at 120° .

Figure 1.11 indicates the significance using of multiple passes in ECAP. High purity (99.996 %) Cu was processed at room temperature using ECAP route B_C. The strength and ductility were measured by uniaxial tensile tests and the resulting engineering stress–strain curves are shown in Fig. 1.11 for the Cu samples tested at

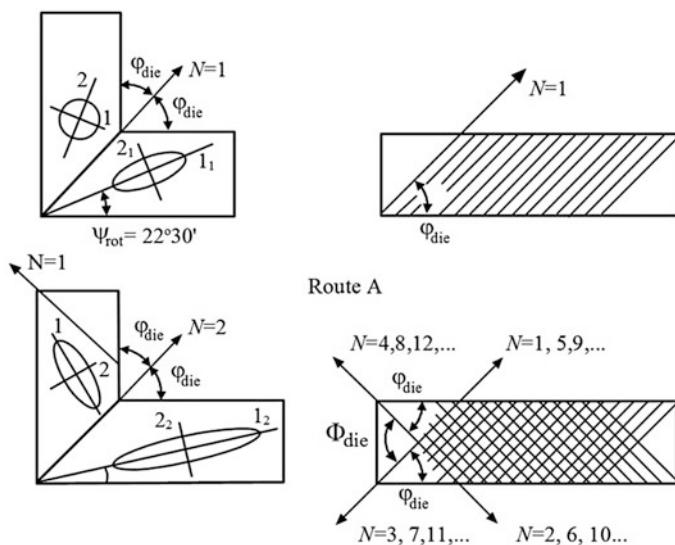


Fig. 1.9 Formation of microstructure

room temperature in the initial coarse-grained condition and in three processed states [25]. It is apparent that the initial coarse-grained Cu, with grain size of about 30 μm , has a typical low yield stress with significant strain hardening and a large elongation to failure. At the same time, cold-rolling of the copper to a thickness reduction of 60 % significantly increases the strength, as shown by curve 2, but dramatically decreases the elongation to failure. This result is consistent with the classical mechanical behavior of metals that are deformed plastically. The same tendency is true also for Cu subjected to two passes of ECAP. However, further straining of Cu to 16 passes of ECAP, as shown by curve 4, simultaneously increases both the strength and the ductility. This is a very remarkable result that, at the time of the investigation in 2002, had never been observed in metals processed by plastic deformation. Accordingly, the effect was termed the “paradox of strength and ductility in SPD-processed metals” [25].

Another two issues concerned some proponents of the development of new methods of ECAP: the efficiency of ECAP, as multi-pass processes are involved, and the ability to produce ‘long products’ as the dimensions of the billet might be restricted by the die’s size and press capacity. It can be shown that these two are resolved in the practice of ECAP.

A great number of various ECAP procedures have been developed to address efficiency of operation [8]. As an example, a simple procedure that effectively eliminates the need for removing specimens from the die between each pass is to make use of rotary-die ECAP. This approach is illustrated schematically in Fig. 1.12 [26]. The facility consists of a die containing two channels, having the same cross-section, intersecting at the center of the die at an angle of 90°. Three

Fig. 1.10 The shearing planes associated with the four different processing routes

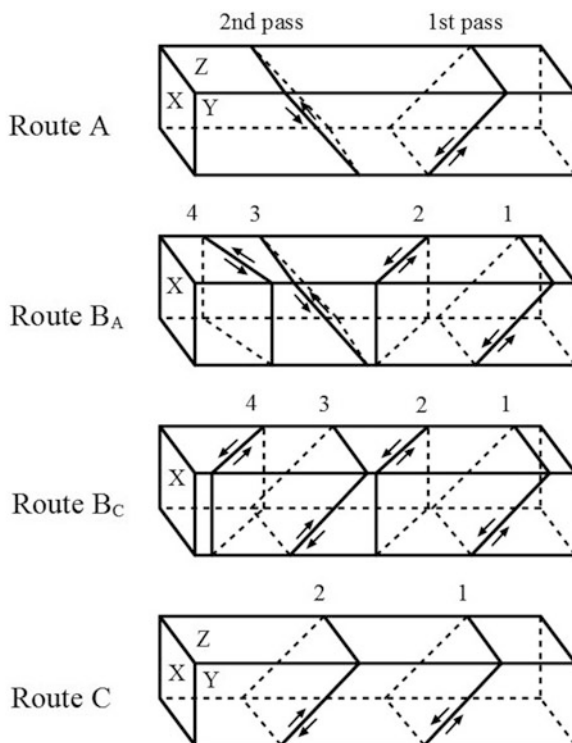
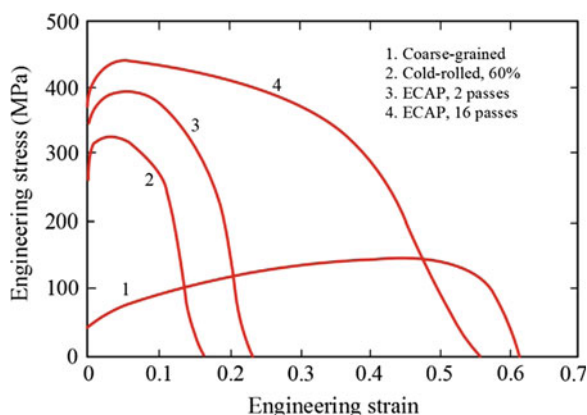


Fig. 1.11 Tensile engineering stress–strain curves for Cu tested at 22 °C with a strain rate of 10^{-3} s^{-1} ; the processing conditions for each curve are indicated



punches of equal length are inserted in the lower section of the vertical channel and in the horizontal channel as shown in Fig. 1.12a. The sample is inserted in the vertical channel so that it rests on the lower punch and an upper punch is inserted to press the sample with a plunger. The configuration after a single pressing is shown in Fig. 1.12b and the die is then rotated by 90° so that the sample may be pressed

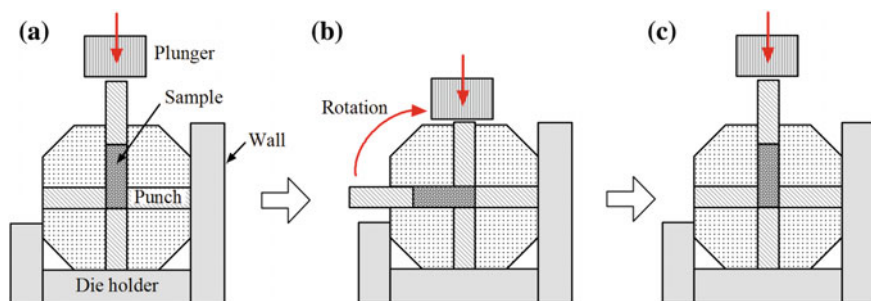


Fig. 1.12 The ECAP process using a rotary-die: **a** initial state, **b** after one pass and **c** after 90° rotation

again as shown in Fig. 1.12c. Significant advantages of this type of pressing are the simplicity and efficiency of operation. Rotary-die ECAP has been used effectively for consecutive pressings up to 32 passes [4].

Addressing the concern on ability to produce ‘long products,’ the author can say the following: it has been recognized for some time that any extensive industrial application of ECAP requires the development of some form of continuous processing technique that can be used efficiently in the production of relatively large volumes of material. Significant progress has been made in developing continuous ECAP procedures for the processing of long metal strips [4]. A few examples from such a development are discussed next.

A process was developed using a rolling facility combined with the principles of ECAP. This process is known as dissimilar-channel angular pressing (DCAP). The principle of the process is illustrated schematically in Fig. 1.13. As can be seen, the material in the form of a thin strip is fed into the facility between two rolls, extruded slightly to reduce the thickness from 1.55 to 1.45 mm, and then it flows into the outlet channel with the original thickness of 1.55 mm. The terminology DCAP arises therefore because of the small difference in the thickness associated with the passage into the outlet channel. A detailed experimental study of this process confirms not only its feasibility but also the ability to produce essentially equiaxed grains separated by reasonably straight grain boundaries [27].

Figure 1.14 shows the principle of two more continuous ECAP processes. The conshearing method (Fig. 1.14a) employs a continuous rolling mill. The material is fed into the mill between satellite rollers and a large central roller and all of these rollers rotate at the same peripheral speed in order to generate a large extrusion force. The strip passes between the rollers and ultimately passes from the mill through an abutment where it is displaced through an angle Φ_{die} . Detailed experiments using commercial purity aluminum strips showed that optimum conditions were achieved for ECAP when the angle $\Phi_{\text{die}} = 65^\circ$.

The principle of the ECAP–Conform process is illustrated schematically in Fig. 1.14b. As shown in the diagram, a rotating shaft in the center contains a groove and the workpiece is fed into this groove. The workpiece is driven forward by

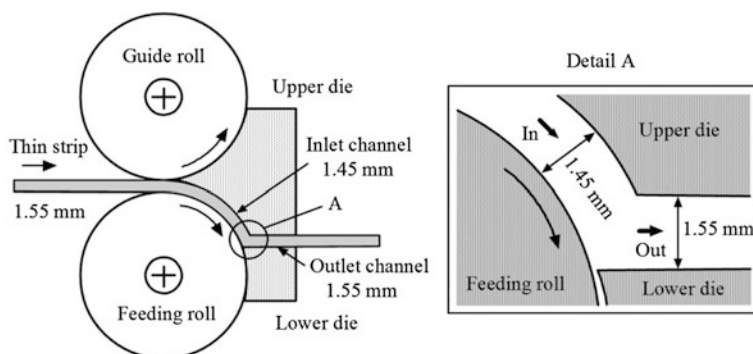


Fig. 1.13 The principle of the DCAP process for use in continuous production

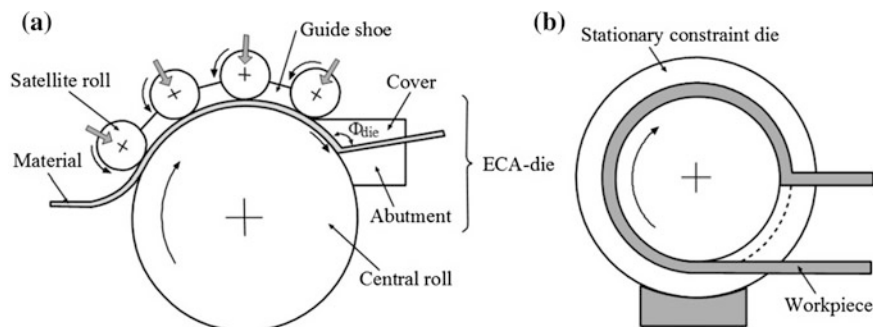


Fig. 1.14 Schematic illustration of continuous ECAPs: **a** conshearing process and **b** conform process

frictional forces on the three contact interfaces with the groove so that the workpiece rotates with the shaft. However, the workpiece is constrained within the groove by a stationary constraint die and this die also stops the workpiece and forces it to turn at an angle by shear as in a regular ECAP. The setup shown in Fig. 1.14b has this angle close to 90° , which is the most commonly used channel intersection angle in ECAP. This setup effectively makes the ECAP process continuous. Other ECAP parameters, such as the die angle and the strain rate, can also be incorporated into the facility.

Detailed experiments have confirmed that ECAP may be used to attain high superplastic elongations at very rapid strain rates provided particles are present, as in many commercial alloys, to restrict the growth of these ultrafine grains at the high temperatures required for superplastic flow. The first example of this effect was achieved using commercial Al–Mg–Li–Zr and Al–Cu–Zr alloys where the elongations to failure were as high as $>1000\%$ at the rapid strain rate of $\sim 10^{-2} \text{ s}^{-1}$.

There have been numerous reports of the occurrence of high strain rate superplasticity in various materials processed by ECAP [15].

1.4 Theoretical Foundations of ECAP

As discussed above, intensive plastic deformation has become a recognized approach in materials processing. Several deformation methods have been reported: ECAP, cyclic extrusion/compression, torsion/compression, multi-axis forging, and accumulated roll bonding. These processes were designed for particular applications and have different technical characteristics. Although similar in total strain, they are diverse in deformation modes, which may range from pure shear to simple shear as well as from monotonic loading to cyclic and cross loading. Because of different imposed stress/strain histories, the results attained by these methods are difficult to compare and the effect of the deformation mode on structure should be clarified.

1.4.1 Deformation Mode

Evolution of structures under mechanical working is strongly related to the stress/strain history imposed upon the material by deformation. Therefore, processing optimization is an important scientific and industrial problem. In the case of structure formation, it is difficult to formulate some simple and unique optimization principle because the final results may be defined by different operation mechanisms.

A simple but effective approach from the practical point of view was developed, nevertheless, by Segal [28] using a typical example of a plane plastic flow through a convergent die with friction as shown in Fig. 1.15a. It was found instructive to discuss this approach in great detail.

The straining history of material elements at any location is determined by the continuum stress/strain state during their movement along streamlines. For simplicity of considerations, i.e., to avoid complications induced by finite strains and elasticity, it is convenient to use the theory of rigid/plastic flow [29]. In directions of slip lines α, β , the mechanical state of rigid plastic material may be described by a symmetric stress tensor $\mathbf{T}_\sigma = \{\sigma, k\}$ and an antisymmetric strain rate tensor $\mathbf{T}_\varepsilon = \{\eta_\alpha, \eta_\beta\}$ where σ is the mean stress component, k is the material yield shear stress, η_α and η_β are shear strain rates along α and β slip lines. In the deviator space, all possible stress states are identical, whereas strain rate states may range from pure shear when $\eta_\alpha = \eta_\beta$ to simple shear when $\eta_\alpha \neq 0$ and $\eta_\beta = 0$ [30]. For the maximum plastic friction $\tau = k$, these limits are at the axis of symmetry (streamline a-a, Fig. 1.15a) and at die walls (streamline c-c, Fig. 1.15a). The intermediate streamlines have states confined between pure shear and simple shear. It should be

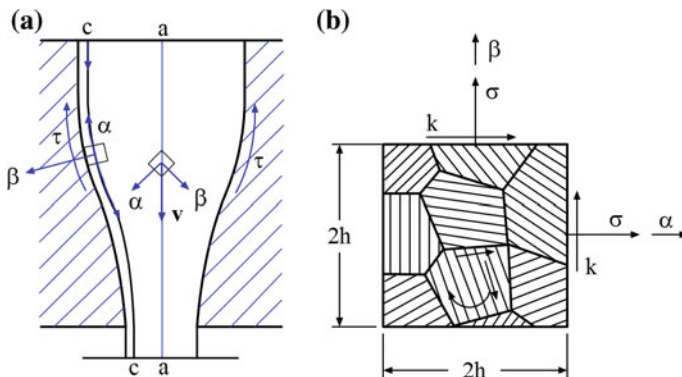


Fig. 1.15 Models of: **a** plane plastic flow through a convergent die and **b** a material element along slip lines

noted that the present description is different from the common strain rate tensor of Cauchy $\mathbf{T}_{\dot{\epsilon}} = \{\eta, \eta\}$ where

$$\eta = (\eta_{\alpha} + \eta_{\beta})/2 \quad (1.4)$$

Although Eq. (1.4) provides the equivalent dissipation of plastic work, it supposes a symmetrical distortion of elements $\eta_{\alpha} = \eta_{\beta}$ that is only a characteristic of pure shear. To compare different deformation modes, they should be normalized to Eq. (1.4). Then all possible situations may be described by a single parameter c using equations

$$\eta_{\alpha} = (2 - c)\eta, \quad \eta_{\beta} = c\eta \quad (1.5)$$

The parameter c is a characteristic of the deformation mode. In such a representation $c = 0$ corresponds to pure shear, $c = 1$ corresponds to simple shear, and $0 < c < 1$ corresponds to intermediate deformation modes. Typical distortions of material elements in these cases are shown in Fig. 1.16.

1.4.2 Pure and Simple Shear

In analytical modeling of manufacturing operations including metal cutting, the concept of pure and/or simple shear is often used interchangeably [31–36]. Moreover, many books on engineering plasticity (e.g. [37, 38]) state that in general case of deformation, the simple shear can be represented as the sum of pure shear and rigid body rotation. As the latter does not contribute to the formation of the deformed structure, an impression is formed that these two deformation modes are

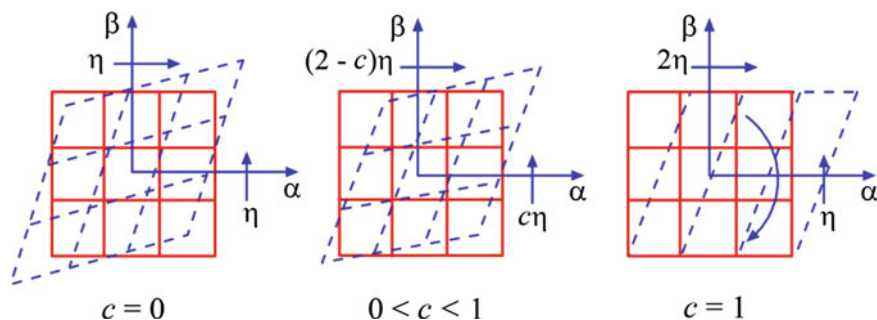


Fig. 1.16 Deformation modes along slip lines

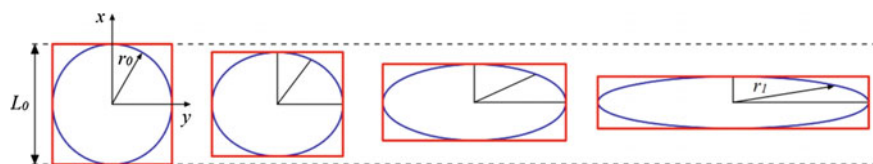


Fig. 1.17 Graphical representation of pure shear

the same. Therefore, it was found instructive to explain these concepts in some details in order to reveal their differences.

Pure shear is perfect coaxial deformation. Coaxial deformation implies that lines along the principal strain axes (axes x and y in Fig. 1.17) have the same orientation as they had in the unreformed state. Pure shear results in no change of area. During pure shear the axes of the strain ellipsoid do not rotate and the incremental and finite strain ellipsoids are coaxial as shown in Fig. 1.17. Pure shear can be found in compression test of a shot cylindrical specimen with no friction generated at the specimen/platens interfaces. Note that a critical point is that the initial dimension L_0 changes in deformation. The shear strain in pure shear is commonly denoted as α and calculated as

$$\alpha = \frac{r_1}{r_0} \quad (1.6)$$

where the senses of r_1 and r_0 are shown in Fig. 1.17.

Simple shear occurs when an applied shear force F acts tangentially to the top area A , as shown in Fig. 1.18a. The shear stress τ measures the intensity of a reaction to externally applied loading sustained by the material as it maintains equilibrium with this force. This stress is calculated as

$$\tau = \frac{F}{A} \quad (1.7)$$

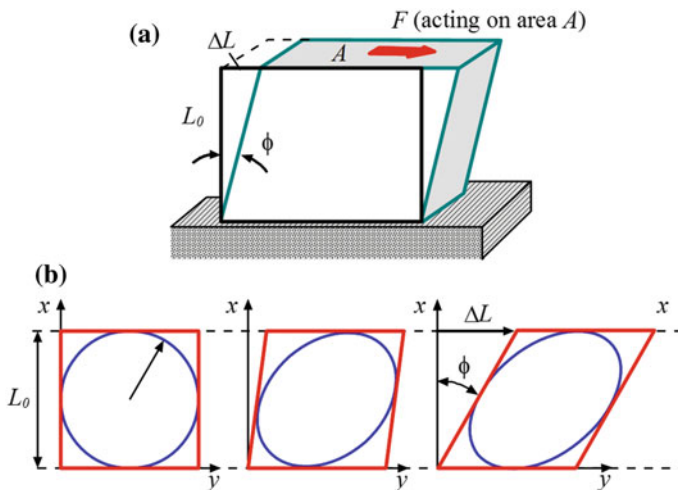


Fig. 1.18 Simple shear: **a** the concept, and **b** graphical representation of deformation evolution

As a result, a body is subjected to a uniform shear, parallel to some direction, involving no change in area. The shear strain is a dimensionless measure of distortion and is defined in Fig. 1.18a as

$$\gamma = \tan \phi = \frac{\Delta L}{L_0} \quad (1.8)$$

In Eq. (1.8), ϕ is the angular change in the right angle measured in radians. Within the elastic region the shear displacement ΔL is small so ϕ is also small. For small enough angles, the tangent of an angle is equal to the angle itself (when measured in radians) so that the engineering shear strain can be approximated as $\gamma \approx \phi$ (rad). Such a simplification is often used in engineering plasticity derivations. Note that this is not nearly the case in metal cutting when large deformations take place.

Figure 1.18b shows the graphical representation of the deformation by simple shear. Note that contrary to pure shear, dimension L_0 does not change in deformation.

1.4.3 Structure Development

The particular effects of deformation mode can be identified for two limiting cases of pure shear and simple shear. Similar to Fig. 1.16a, pure shear is realized in mid-thickness during rolling. Because of low friction and slowly convergent flow, for cold rolling pure shear is the dominant deformation mode in the central area.

This process was extensively investigated, and many experimental results on structure evolution can be found in [39, 40] and others. In the case of simple shear, the situation is more complicated. The standard torsion test of cylindrical or thin walled samples provides uniform straining only before a plateau at the loading diagram for most metals that fit to strains less than 2. At larger strains torsion is localized near some cross-section and is not more controllable. Alternative methods of simple shear such as ECAP, compression of shaped rings, and tensile of shaped sheets were developed by constrained shear inside a narrow area. In these cases, deformation history retains into the same volume that provides reliable data during severe shear straining.

When a small volume of material is uniformly loaded, micro-flow inside structural elements such as grains is inhomogeneous. Based on numerical experimental results on deformation microstructures during intensive straining, two distinctive areas of structure evolution can be identified: (1) continuous homologous evolution of dislocation structures originated by crystallographic glide in grain subdivided areas and (2) highly localized flow originated by shear band formation. Deformation mode and loading history play important roles in specific realization and sequence of these stages.

At the plastic state, material elements along slip lines are subjected to the normal stress σ and the tangential stress k (Fig. 1.15b). For small elements of typical size $2h$, the uniformity of macro-strain rates into α and β directions defines boundary conditions for velocity components v_α , v_β along slip lines

$$\begin{aligned} v_\alpha &= \pm(2-c)v_{nr}, & v_\beta &= \pm cv_{nr}/h \text{ at } \beta = \pm h \\ v_\alpha &= \pm(2-c)v_{nr}\beta/h, & v_\beta &= \pm cv_{nr} \text{ at } \alpha = \pm h \end{aligned} \quad (1.9)$$

where $v_{nr} = h\dot{\eta}$ is a normalized velocity.

The conditions set by Eq. (1.9) may correspond to a multitude of states from pure shear to simple shear and should be accommodated by local crystallographic slides and rotations in aggregates of grains inside the elements. Thus, this equation demonstrates the statistical effect of the parameter c and deformation mode on realizations of micro-flow in polycrystalline materials. Their particular distributions are defined by physical conditions for evolution of dislocation structures. According to the general framework [41, 42], dislocation structures organize incidental dislocation boundaries (IDBs) and geometrically necessary boundaries (GNBs). GNBs play an especially important role. When strain increases, GNBs evolve in a few steps: reorganization in deformation bands (DBs), decrease of spacing to a cell size, rotation to a total flow direction, and an increase in misorientation angles [4]. Simultaneous changes in microstructure and texture during such evolution lead to material hardening or softening. Depending on the material and deformation mode, hardening may extend continuous evolution to large strains, while softening may interrupt that by localized flow at moderate strains.

If, however, softening becomes predominant, continuous evolution is substituted by flow localization in SBs. SBs analyzed in many papers (see, for example, [40, 43])

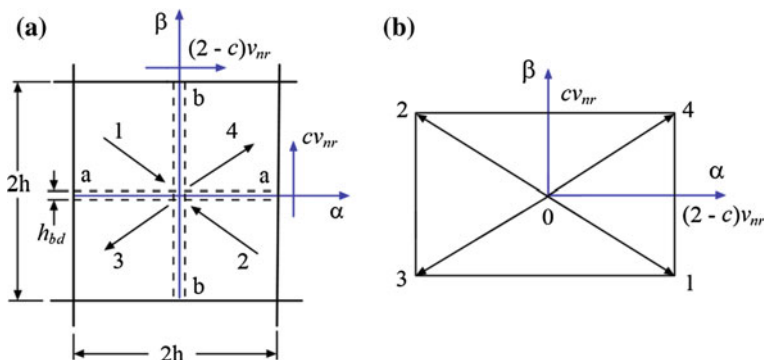


Fig. 1.19 **a** Micro-localized flow and **b** velocity hodograph along slip lines

manifest a few typical features. They are very thin planar materials, layers inside of which strains are significantly larger than outside. An average distance between bands approximates to a cell size. Crystallographic multi-slip activity in SBs results in gradually increased angles of misorientation along their boundaries. SBs have non-crystallographic orientations that always follow to continual principal shears and they penetrate a few grains without a noticeable deviation. Upon origination, SBs substitute a preexisting structure and define the final structure of heavily deformed metals.

Consider localized flow of statistically representative material element shown in Fig. 1.19a. A simple discontinuous flow pattern can be accepted for SBs a–a and b–b at the element boundaries oriented along α and β slip lines. It is assumed that a thickness of SBs $h_{bf} \ll h$. A velocity hodograph for four adjacent elements 1, 2, 3, and 4 (Fig. 1.19) that satisfies boundary conditions Eq. (1.9) is shown in Fig. 1.19b. Arrows in Fig. 1.19a depict trajectories inside of elements. Normal velocity component v_n and discontinuity of tangential velocity component $[v]$ at SBs are

$$\begin{aligned} v_n &= 2cv_{nr}, & [v] &= 2(2-c)v_{nr} & \text{along } \alpha - \text{slip lines} \\ v_n &= 2(2-c)v_{nr}, & [v] &= 2cv_{nr} & \text{along } \beta - \text{slip lines} \end{aligned} \quad (1.10)$$

After crossing these lines, the material undergoes shear strains

$$\gamma_\alpha = [v]/v_n = (2-c)/c, \quad \gamma_\beta = c/(2-c) \quad (1.11)$$

Diagrams ABD and AEF for γ_α and γ_β in function of the parameter c (Fig. 1.20a) show the difference between γ_α and γ_β is essential for $c < 0.5$ and dramatic when $c \rightarrow 0$. This effect is not revealed by the Cauchy strain rate tensor that reduces all deformation modes to pure shear. As velocity v_n remains constant through SBs, the time necessary to cross a shear band is $t_{csb} = h_{sb}/2ch\eta$. Inside the SBs, strain increases in proportion with time

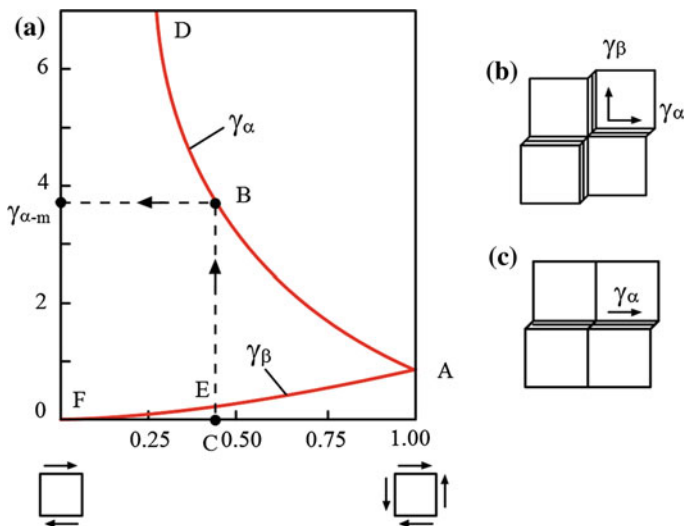


Fig. 1.20 Micro-localized flow: **a** shear distribution along slip lines; **b** material distortion for pure shear; **c** material distortion for simple shear

$$\gamma_{\alpha} = 2(2 - c)ht\eta/b_{sb}, \quad 0 < t < t_{csb} \quad (1.12)$$

In the case of simple shear $c = 0$, $t \rightarrow \infty$, the material cannot cross SBs and strains may increase unrestrictedly. The maximum strains from Eq. (1.12) conform to Eq. (1.11). At the fixed deformation mode $c = \text{const}$, this complies with point B of diagram ABD on Fig. 1.20a. For $t < t_{csb}$, Eq. (1.12) describes straight line CEB along which strain increases with time from $\gamma_{\alpha} = 0$ at $t = 0$ (point C) to $\gamma_{\alpha-m}$ defined by Eq. (1.11) (point B). In two limit cases, the maximum strains are

$$\begin{aligned} \gamma_{\alpha} &= \gamma_{\beta} = 1 && \text{for pure shear} \\ \gamma_{\alpha} &= 4ht\eta/h_{sb} && \text{for simple shear} \end{aligned} \quad (1.13)$$

These cases correspond to the specific distortions of microstructure shown in Fig. 1.20b, c for a small deformation step. In both cases, flow localization results in planar structures. However, for pure shear, the standardized strain $\gamma_{sh} = 1$ is gradually spread over the material with time that detects characteristic ‘herring bone’ structures observed during rolling with large reductions [40]. For simple shear, the strain is accumulated into the same shear band and may attain a very high level that predisposes to long thin bands usually associated with localization [44, 45].

The present simplified analysis silently assumes that localized flow is entirely concentrated in SBs and corresponds to multi-slip activity. Crystallographic rotations inside SBs and relative to surrounding matrix are proportional to the strains defined by Eq. (1.13), irrespective of acting slip systems. These rotations define the

corresponding angles of misorientations. Therefore, strains (Eq. 1.13) correlate directly to nucleation of new boundaries and structure refinement during localized flow. As one can see, simple shear can provide very large strains inside SBs with time, in contrast to moderate strain $\gamma_{sh} = 1$ in the case of pure shear. Although time t in Eq. (1.13) is usually unknown, the estimation for γ_{sh} in the case of simple shear may be found from formula $\gamma \sim \gamma_{mc} h / b_{sb}$, where γ_{mc} is uniform macro shear; for $h \gg b_{sb}$, $\gamma_{sh} \gg \gamma_{mc}$. Consequently, high angle boundaries may be developed soon along SBs originated by simple shear of some normalized intensity, whereas pure shear will require repeated processing. Hirsh et al. [46] described SBs with shear strain up to 10 consisting of very fine ($<0.1 \mu m$) highly misoriented crystallites. In another example, Korbøl and Richert [47] observed two symmetrical families of SBs with shear strains of about 0.6 that is close to $\gamma_{sh} = 1$ for pure shear. In this case the SBs developed elongated subgrains and a large number of cyclic extrusion/compression was needed for structure refinement.

Among the different paths of non-monotonic deformation, the practical interest presents cross loading when the stress-strain state is changed abruptly. This is a case of multi-pass processing with variation of billet orientation or deformation mode. For pure shear cross-loading cannot contribute significantly to structure refinement because of moderate straining along two equivalent shear directions (SDs) and stable continuous evolution. However, during simple shear of prestrained metals, cross-loading results in immediate material softening and flow localization [48, 49]. If an angle of cross-loading is sufficiently large, a new family of SBs is formed so that intersections of SBs may subdivide microstructure for fine fragments even at relative low strains at each processing step.

The presented analysis provides the theoretical foundation for ECAP explaining practically all its phenomena observed experimentally, including that shown in Fig. 1.1, “paradox of strength and ductility in SPD-processed metals” [25], superplasticity, and so on. It signifies the importance of simple shear achieved in SPD processing only in ECAP. In other words, it clearly proves that the channels must be equal to achieve this deformation mode, i.e., to achieve significant grain refinement, and thus to gain advantages of submicro and nanostructure materials. More detailed physical background of these phenomena can be found in the fundamental work by Baygüzimer [50].

The conclusions of the present analysis are supported by a great number of experimental results obtained using sophisticated measuring techniques including:

- Optical microscopy to study the shearing of the original grains as they pass through the shearing plane within the die. An initial examination of shearing at the macroscopic level provides an opportunity to make direct comparisons with the theoretical predictions, both for the three-dimensional shearing behavior of large solid bodies and for the slip systems visible on orthogonal sections after ECAP.
- Selected area electron diffraction (SAED) for comparison of the resultant microstructures. It proved that an array of ultrafine equiaxed grains is achieved

most easily in ECAP with a die having a channel angle of 90° as its results in grain boundaries having high angles of misorientation.

- Transmission electron microscopy for determination of grain sizes produced by ECAP and the nature of any dislocation interactions occurring within the grains.
- Electron backscatter diffraction (EBSD) to measure orientation of grain boundaries. The EBSD data indicates that the number of high angle-boundaries ($>15^\circ$) measured in the specimens after ECAP [51] as predicted by the above-described model.
- Differential scanning calorimetry (DSC) for study of thermal phenomena of ECAP.

The most important experimental results are well summarized by Valiev and Langdon [4].

1.5 Extrusion-Cutting

1.5.1 General Idea of the Process

The idea of extrusion machining was first introduced by De Chiffre [52] as a process that can be used to: (a) determine the flow stress of metals being deformed under conditions of high strain rate and high temperature, conditions prevailing in the machining of metals, and (b) produce strips and wires by a method that is expected to be more economical than the present methods.

According to De Chiffre, the analogy existing between geometrically restrained orthogonal cutting and plane side-extrusion with inclined bottom wall can be illustrated as shown in Fig. 1.21. Figure 1.21a shows a schematic of a typical side-extrusion with inclined bottom wall. A qualitative slip-line field was added by De Chiffre without pointing out how this field was constructed. As a result, no velocity hodograph was included into consideration. According to De Chiffre, 'the same' slip-line field is valid when the lower wall is replaced by a rigid zone, where no deformation occurs Fig. 1.21b, c shows the slip-line field (no explanation how it was figured out) when the upper wall, named as the shoe, is moved away from the bottom wall termed as the cutting tool (which is actually the rake face of the cutting tool) in this case. Figure 1.21d shows the limiting position of the shoe relative to the tool. After this position, the shoe is no longer active and conventional orthogonal cutting takes place. De Chiffre noted that, in practice, this sharp limit cannot exist and a more gradual shift from restrained to unrestrained cutting is expected. This occurrence implies nevertheless no restriction for the analysis and use of the process.

Using the slip-line field and upper-bound theories, De Chiffre derived equations for average shear strain, shear strain rate, and temperature in the deformation zone. To do that, he made the following assumptions:

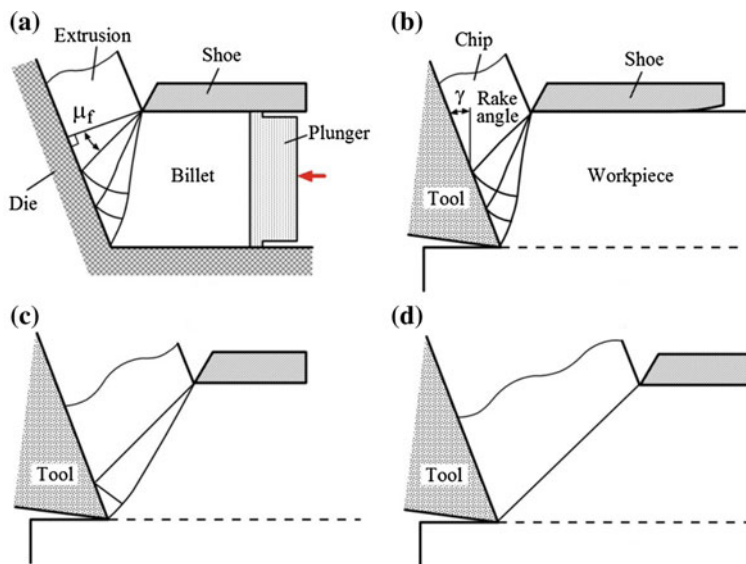


Fig. 1.21 Analogy between extrusion-cutting and side-extrusion: **a** plane side-extrusion with inclined bottom wall, **b** extrusion-cutting with a large deformation zone, **c** extrusion-cutting with narrow deformation zone, **d** theoretical limit of extrusion-cutting

1. The tool is sharp and no deformation takes place in the material lying underneath the horizontal line passing through the tool edge.
2. Plane strain conditions.
3. The friction condition on the rake face is unaffected by the position of the shoe. The friction condition is expressed by the friction factor $m_{DC} = \tau/k$, where τ is the shear stress on the tool rake face and k is the shear flow stress. According to De Chiffre, this assumption means that the friction angle μ_f , related to m_{DC} through $\cos 2\mu_f = m$, is constant for different positions of the shoe.
4. The work material is rigid-plastic, which means that its shear flow stress k is constant through the deformation zone.
5. The shear flow stress k is unaffected by the position of the shoe.

Analyzing these assumptions from the point of modern knowledge on material deformation including facts gained in studies of extrusion, one may conclude that these assumptions, besides 2, are unrealistic. This is because of the existence of a significant machining residual stress [both the superficial and in-depth are the case in any machining (e.g. [53]) (assumption 1)]; the friction factor m_{DC} should include the normal stress over the contact interface as according to De Chiffre, it is related to the angle of friction (assumption 3); real work material cannot be representation of the work as rigid-plastic as significant strain-hardening takes place (assumption 4); the flow shear stress k is affected by the state of stress altered by the position of the shoe

(assumption 5). It is needed to mention, however, there were no better methods than the slip-line field and upper-bound theories used by De Chiffre that at the time of the study, so he had no options but to make the discussed assumptions to develop at least the first approximation of the model.

The introduction of extrusion-cutting was not noticed until De Chiffre published the results of his experimental study [54] emphasizing the quality of the brass chip obtained. The objective of the study was to produce brass strips for *subsequent blanking of electrical details*. Brass disks of diameter 220 mm, max. 6 mm thick, made of 63 % Cu-brass, and sharp high speed steel tools were used in the tests.

The experimental results reveal that cutting can be carried out as a stable process only under certain conditions, including the following:

- The machine and the setup must be rigid to prevent vibrations;
- The cutting tool and the shoe must be sharp and the shoe must be mounted at an entrance angle of about 2° ;
- The ratio of the chip and uncut chip thicknesses equal to 1.5 should be used;
- At the beginning of the cut, the feed should be no more than half the shoe offset with respect to the tool.
- The quality of the strip produced depends strongly on the tool-shoe gap. When the gap is large, there is no restriction to the chip back surface. Thus, the conditions are similar to the conventional cutting case, so that the chip is produced as a hard strip with a rough-free surface. As the gap is decreased, partial chip extrusion takes place and a fully extruded chip is obtained for gaps less than twice the feed. The best strip quality is achieved when the chip width is about 1.5-fold greater than the uncut chip thickness. If the gap is decreased further, the material resistance to being extruded becomes significantly higher and vibrations and considerable wrinkling and side cracks of the strip take place. When the tool shoe gap is less than the uncut chip thickness, side cracks start occurring in the strip,
- The total force acting on the tool is almost twice greater in cutting-extrusion than that in orthogonal cutting under the same cutting conditions (i.e., the same work material, tool, setup, uncut chip thickness, etc.).

1.5.2 Shear Strain

Using an intuitively constricted velocity (Fig. 1.21) and then applying the upper-bound theory, De Chiffre obtained the following formula for the final shear strain

Table 1.1 Shear strain in ECAP and in orthogonal cutting

Half-die angle, Φ_{die} (°)	Corresponding rake angle, γ , (°)	Shear strain in ECAE calculated using Eq. (1.2)	Shear strain in extrusion-cutting/orthogonal cutting calculated using Eqs. (1.14)/(1.16)
25	-40	4.29	4.29
37.5	-15	2.61	2.61
45	0	2.00	2.00
52.5	15	1.53	1.53
65	40	0.93	0.93

$$\gamma_{\text{sh}} = \frac{\zeta}{\cos \gamma} + \frac{1}{\zeta \cos \gamma} - 2 \tan \gamma \quad (1.14)$$

where ζ is the chip compression factor, defined as

$$\zeta = h_{\text{c-e}}/h_{\text{D}} \quad (1.15)$$

i.e., the ratio of the extruded chip thickness, $h_{\text{c-e}}$ (referred by De Chiffre as the gap between shoe and tool) and the uncut chip thickness, h_{D} (referred by De Chiffre as the depth of cut). In metal cutting, this ratio is known as the chip compression ratio.

The equation for shear strain derived by De Chiffre for extrusion-cutting (Eq. 1.14) is the same as that for orthogonal cutting (e.g., Eq. 3.38 in [36]), i.e.,

$$\gamma_{\text{sh}} = \frac{\zeta^2 - 2\zeta \sin \lambda + 1}{\zeta \cos \gamma} \quad (1.16)$$

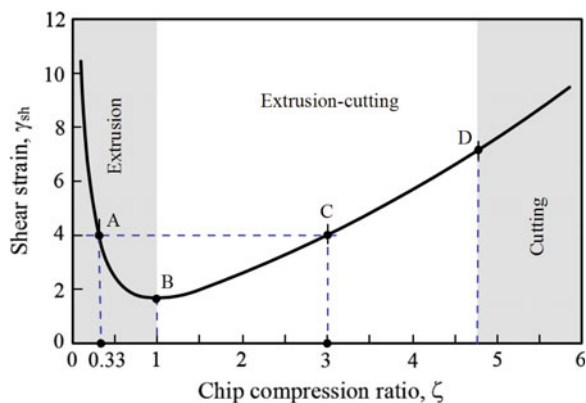
although the process differs essentially in terms of forces involved and deformation modes.

Shear strains calculated using the equation for ECAP (Eq. 1.2 when $\Psi_{dz} = 0^\circ$ and $N = 1$ (one pass as in extrusion-cutting)), and the equation for extrusion-cutting (Eq. 1.14 which is the same as for orthogonal cutting, i.e., Eq. 1.16) are shown in Table 1.1. As can be seen, the results are absolutely the same, although these equations were derived using considerably different models particular to considerably different processes. Moreover, it is not clear why the total force acting on the tool is almost twice greater in cutting-extrusion than that in orthogonal cutting under the same cutting conditions if the amount of plastic deformation is the same.

1.5.3 Detailed Analysis

A detailed analysis of extrusion cutting led to a conclusion that the process is a real cutting-extrusion process when the chip compression ratio is more than 1, i.e., when the chip deformation normal to the tool rake face is allowed, and less than that in

Fig. 1.22 Showing a zone of existence of extrusion-cutting



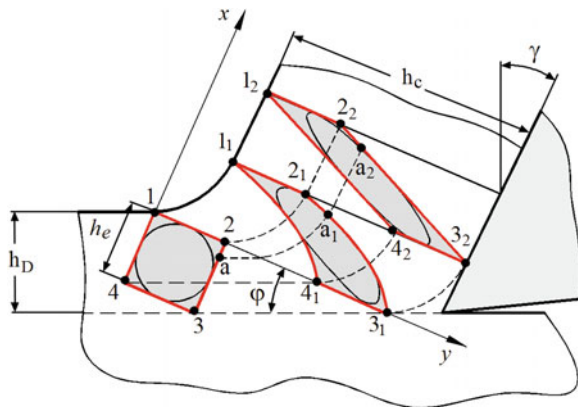
unrestricted cutting. To explain this statement, the deformation shear strain (γ_{sh}) is plotted as a function of the chip compression ratio (ζ) in Fig. 1.22. Three zones are distinguished in this graph. The zone of conventional (unconstrained) cutting (Zone 1) lies to the left from point D where ζ is equal to that in conventional cutting, i.e., corresponds to the model shown in Fig. 1.21d. The zone of extrusion-cutting (Zone 2) lies between points D and B. Point B in this graph corresponds to the chip compression ratio equal to 1, i.e., the chip and uncut chip thickness are equal. At this point, the process of extrusion-cutting is generally equivalent to an ECAP process. The extrusion zone (Zone 3) lies to the left of point B, as shown in Fig. 1.22. In this zone, the chip compression ratio is less than 1.

1.5.3.1 Zone 1—Unconstrained Cutting

Normally, in machining of metallic materials the chip thickness is greater than the uncut chip thickness. Therefore, the chip compression ratio is in the range 1.4–2.8 for steel machining and 2.5–6 (and over) for machining of soft aluminum, copper, and similar materials [55]. A particular value of chip compression ratio is defined by the properties of the work material, tool rake angle, tool material and coating (the tribological conditions over the tool–chip interface), coolant, machining regime, and so on [56]. Although the state of stress on the deformation zone is complex, including a combination of the compression and being stress [36] that result in fracture in each cycle of the chip-formation process [57], earlier studies include the analysis of the chip formation using the slip-line method and upper-bound theorem. Such a simplification, however, allows for assessing the nature of chip deformation in metal cutting.

Figure 1.23 shows a simplified model of chip formation with the deformation zone having parallel boundaries [36, 58]. A square 1234 is selected in the layer being cut so that one of its sides coincides with a part of the lower boundary of the deformation zone. This boundary is inclined at shear angle ϕ to the direction of tool motion. The deformation zone is bounded by lines 1–3₁, 3₁–3₂, 3₂–1₁, and 1₁–1.

Fig. 1.23 Transformation of a square in the layer being cut in the deformation zone with parallel boundaries



Let us consider the transformation of square 1234 as it passes the deformation zone and then becomes a part of the chip. Point A is selected on side 23 to make it easy to understand transformation. The equations that govern transformation were considered by the author earlier [36]. As can be seen, square 1234 is transformed into curvilinear rectangular $1_2 2_1 3_1 4_1$ and a circle transforms, not into an ellipse, but into a more complicated shape as illustrated in Fig. 1.23. Because this transformation is not linear, the deformation does not correspond to simple homogeneous shear. Passing the upper boundary of the deformation zone, curvilinear rectangular $1_2 2_1 3_1 4_1$ transforms into the parallelogram $1_2 2_2 3_2 4_2$ and the inscribed circle, drawn in square 1234, transforms into an ellipse, because $h_c > h_e$, even the final deformation is not simple shear. Rather, it corresponds to the case where $0 < c < 1$ (Fig. 1.16), i.e., corresponds to intermediate deformation mode where the normal strains are involved in the shortening and thickening of the chip compared to the length of cut and uncut chip thickness, respectively. This presents a problem in the common considerations of the chip deformation: because the final shape of the deformed element resembles the simple shear, the corresponding formula to calculate the shear strain (Eq. 1.16) strain is used, forgetting that $h_c > h_e$.

As the deformation mode in metal cutting is not simple shear, the chip structure is not uniform, often containing cracks, shear bands, serrations, and so on [36, 55, 59]. Nevertheless, Chandrasekar et al. [47] suggested that the chip produced in metal cutting as a product with nanocrystalline structure. They obtained US patent No. 6,706,324 (2004) "Method of forming nano crystalline structures and product formed thereof" and patent No. US 7,628,099 (2009) "Machining method to controllably produce chips with determinable shapes and sizes." In US patent No. 6,706,324 (2004) it is explicitly stated that the chips produced by the machining operation have nanocrystalline structure. These chips are then used to form the product. The chips are either consolidated to form the product, such that the product is a monolithic material that may contain nanocrystals or the chips are dispersed in a matrix material, such that the product is a composite material in

which the chips serve as a reinforcement material. US patent No. US 7,628,099 (2009) introduces a method of controllably producing chips with a desired shape and size by superimposing modulation on the cutting tool. Unfortunately, examples of superior properties of products made with the chips are not presented.

According to US patent No. 6,706,324 (2004), the major limitation of ECAP is inability to induce large strains in very strong materials, such as tool steels. As a result, metal cutting and particularly hard turning was suggested as the process of choice capable to deal with such materials in producing the chips having nano-structure. Bearing AISI 52100, low-alloy medium-carbon 4340, and high-carbon HSS M2 steels heat-treated by through-hardening and tempering to hardness values of about HRC 60–62, about 56–57, and about 60–62, respectively, were used in the confirmation tests. According to the patent description, the initial microstructures of the steels prior to machining were tempered martensite of relatively large grains prior to machining (ranging from about 55 to about 170 μm).

The described structure and pointed grain size of the steels prior to machining raise reasonable doubts. The problem is that, according to ASTM E 112 Committee E-4 on metallography (<http://www.metallography.com/grain.htm>), in heat-treated steels, it is recognized that the grain size of the product of the heat treatment, usually martensite, is not measured or cannot be measured. For low-carbon steel, the martensite forms in packets within the parent austenite grains. In high-carbon martensites, any convenient structural shape that can be measured has never been observed. In most cases, attempts are made to measure the size of the parent austenite grains that were formed during the high temperature hold during heat treatment. This is usually referred to as the “prior-austenite grain size” and it has been widely correlated to the properties of heat treated steels. The most difficult process here is the etching procedure needed to reveal these prior boundaries. Sometimes they cannot be revealed, particularly in low-carbon steels. In this case, it may be possible to measure the low-carbon lath martensite packet size, which is a function of the prior-austenite grain size.

It is not a surprise that the grain sizes of the chips obtained in cutting these materials are not reported. For example, the most important parameter that characterizes the obtained microstructure, namely the distributions of particulate sizes, is not mentioned. No relevant tests (discussed in great detail in [4]) and their results confirming that the objective of grain refinement (producing essentially equiaxed grains separated by reasonably straight grain boundaries [8]) are discussed.

1.5.3.2 Zone 2—Extrusion-Cutting

In Zone 2, the deformation takes place under a complex state of stress, which includes a combination of bending and compressive stresses, so the deformation mode is not simple shear. While moving from point D to point B, the contribution of the bending stress decreases, becoming zero at point B. As such, the total force, and thus energy needed to accomplish the process, increases as additional energy is required to reduce the chip thickness from that obtained in unrestricted cutting (point D) to that equal to

uncut chip thickness (point B). As such a reduction involved severe plastic deformation of the chip, the process temperature also increases.

1.5.3.3 Zone 3—Extrusion

The extrusion zone lies to the left of point B as shown in Fig. 1.22. Plastic deformation in this zone also takes place under a complex state of stress that includes compression. Because the chip becomes longer than the length of cut and its thickness becomes smaller than that of the undeformed chip thickness, normal strains are involved so the deformation mode is not simple shear. As no bending stresses involved in the state of stress, to achieve the same shear strain in the chip as in Zone 2, for example 4 as shown in Fig. 1.22, significantly greater energy (and thus force) is needed. In experimental study using 63 % Cu–brass alloy at different raw conditions (rolled and as-casted plates), De Chiffre was not able to achieve even the condition of ECAP, i.e., when the uncut chip thickness is equal to the chip thickness. He explained this by the lack of stiffness of the experimental setup because of the energy (force) needed to accomplish the process was significantly increased. Moreover, a simple comparison of the chip shape (considerable wrinkling and side cracks) when the chip compression ratio equal or less than 1 with defects found in ECAP (shown in Fig. 1.24) also reveals the problem with an increased energy (force). It is to say that the chip/extrusion wrinkles and cracks

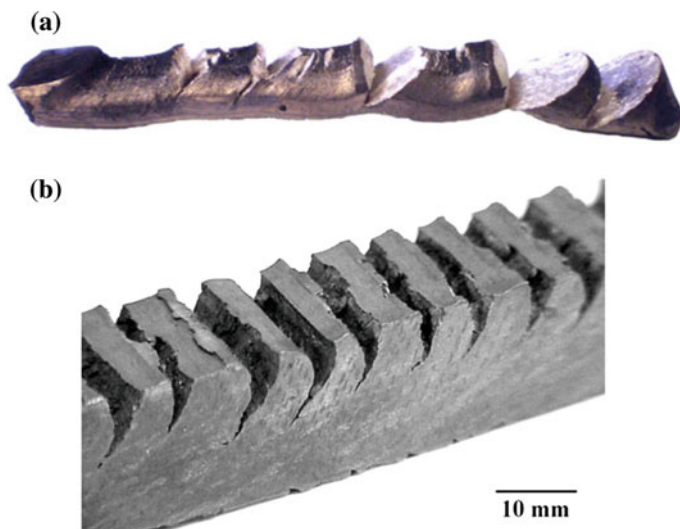


Fig. 1.24 ECAP defects: **a** magnesium alloy AZ31 (Mg–3 wt% Al–1 wt% Zn) processed by ECAP using solid dies with angle 90° at temperature 473 K at a pressing speed of 0.3 mm/s, **b** as-cast Pb–4.5 wt% Sb alloy processed by ECAP at room temperature at pressing speed of 5 mm/s

when the process strain exceeds that at fracture determined for the work (billet) material at the temperature used in cutting/extrusion under the state of stress imposed by the setup/die arrangement. This unavoidably happens no matter what deformation process is used or how one calls this process.

A good experimental confirmation to the discussed zones can be found in the paper by Cai and Dai [60]. In this paper, the evaluation of the structure of the titanium chip. It was found that this structure changes from the serrated chip with profound adiabatic shear bands in Zone 1 where unrestricted cutting takes place, to the combination of the heavily deformed grains and shear bands in Zone 2 where the combination of the cutting and extrusion takes place, and to the heavily deformed chip structure with no shear bands in Zone 3 where pure extrusion is the case.

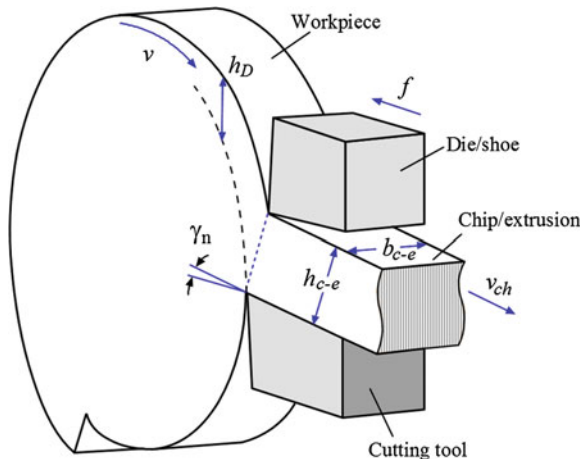
1.5.4 Large Strain ExtrusionMachining (LSEM)

Revisiting of extrusion cutting was attempted in the beginning of the twenty-first century [61–68]. A research team from Purdue University obtained patent US 7,617,750 (2009) “Process of producing nanocrystalline bodies” and filed patent application US 2014/0017113 (2014) “Large strain extrusion machining processes and bulk forms produced therefrom.” In the author’s opinion, however, the essence of ECAP was not revealed in these publications. As a result, a need for multi-pass processing is not clearly understood so that the obtained material structure and properties evaluations as in studies of ECAP were not attempted. Note, in modern publications on the subject the term Large-Strain Extrusion Machining (LSEM) is used instead of “extrusion-machining.”

To show that this is the case, consider the developments and results presented in patent US 7,617,750 (2009), patent application US 2014/0017113 (2014) and paper [66] by essentially the same team of researchers. The patented equipment shown in Fig. 1.25 is essentially the same as that used by De Chiffre (Fig. 4 in [54]). It is stated in these publications that multi-stage deformation processing is one of the most widely used experimental SPD techniques for studying microstructural changes produced by very large strain deformation. Notable examples include rolling, drawing, high pressure torsion (HPT), and ECAP processes. Analyzing ECAP, the authors pointed out that, in their opinion, there are significant limitations and disadvantages of this process such as:

- Inability to induce large strains in high-strength materials, such as nickel-based high-temperature alloys and tool steels;
- The difficulty of imposing strains much greater than one and inability to impose strains much greater than two in a single stage of deformation;
- Considerable uncertainty of the deformation field and minimal control over the important variables of deformation field such as strain, temperature, strain rate, and phase transformations, which are ‘expected’ to have a major influence on the evolution of microstructure and material properties.

Fig. 1.25 Schematic representation of a cutting tool adapted for both cutting and simultaneously extruding a chip produced during machining of a body in accordance with US patent 7,617,750 (2009) and described in [66, 68]



As discussed in Sect. 1.3 “Addressing common concerns: multi-pass, materials used, and strain achieved,” none of the listed disadvantages/limitations is actually the case in ECAPs. ECAP is used because simple shear is the deformation mode in this process so that the above-discussed advantages of grain refinement can be achieved (see Figs. 1.1 and 1.11). Multi-pass ECAP process is used not because it is impossible to achieve high strains in one pass, but rather to obtain smaller grains. To achieve pre-nano grain sizes (Fig. A4.20), 8–10 passes are needed. Optical metallography was conducted on billets of the alloy subjected to ECAP using either the die-set with $\Phi_{\text{die}} = 135^\circ$ after 12 passes or the die-set with $\Phi_{\text{die}} = 120^\circ$ after 8 passes. These results, shown in Fig. 1.26a, b, reveal a significant refinement of the grain structure of the α -phase in both the longitudinal direction and in the cross-section [4, 8]. Furthermore, the initial boundaries of the α -phase are no longer visible and uniform etching of the section area demonstrates the homogeneous nature of the processed structure.

The strain analysis presented in patent US 7,617,750 (2009), patent application US 2014/0017113 (2014), and papers [63, 66] is based on the “cutting (extrusion) ratio” defined as the ratio of the unreformed chip thickness and chip thickness, i.e., reciprocal to the chip compression ratio defined by Eq. (1.15) and used by De Chiffre in its modeling and experimental studies of extrusion-cutting [52, 54], introduced in metal cutting by Time [69] and then used by many researchers [36, 70]. The graphical representation of the results of this analysis, however, is obviously using the chip compression ratio that creates confusion in the description of LSEM (see for example Fig. 5 in [63], Fig. 7 in [66], and Fig. 3 in US 7,617,750 (2009)).

Inspired by the above-cited publication on extrusion-machining, other research teams investigated the LSEM process, particularly its ability to refine grains. Somewhat mixed results are reported. Some papers report insignificant grain refinement, whereas others reported grain retirement to the nano level. None of these papers, however, investigate/discuss the properties of the product obtained in

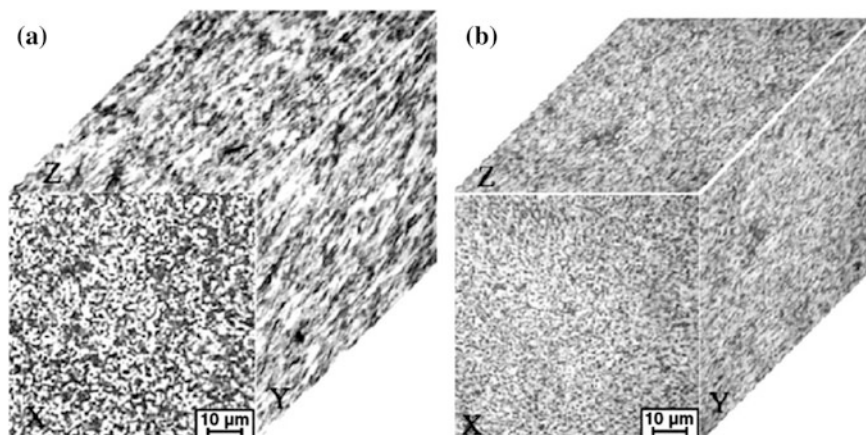


Fig. 1.26 Optical micrographs showing the structure of Ti6Al4V alloy after ECAP using route B_C at 700 °C: **a** with $\Phi_{\text{die}} = 135^\circ$ for 12 passes and **b** with $\Phi_{\text{die}} = 135^\circ$ for 8 passes

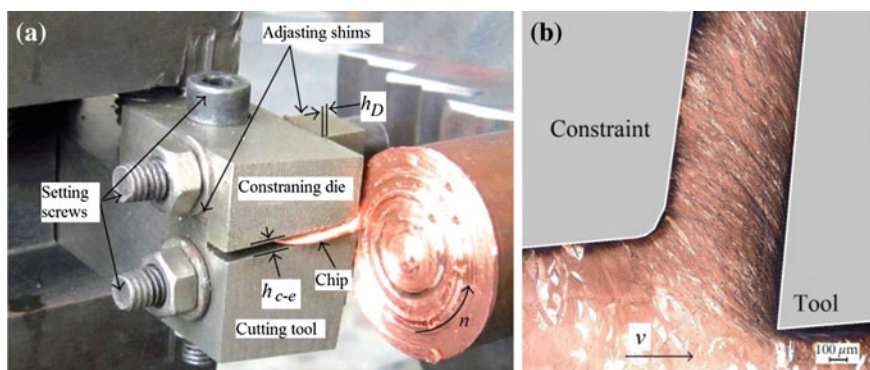
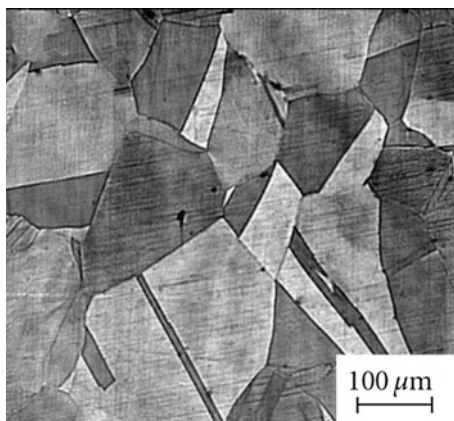


Fig. 1.27 LSEM of pure copper studies by Den et al. [71]: **a** experimental setup and **b** the macrostructure of the chip-extrusion (Figs. 3 and 8 in [71])

terms of the objective of grain refinement in the manner shown in Figs. 1.1 and 1.11, and discussed in Sect. 1.1, i.e., strength enhancement while preserving reasonable plasticity, superplasticity, improved creep resistance, etc.

The most noticeable paper in this respect is that by Den et al. [71]. The experimental setup used in their study is shown in Fig. 1.27a. As can be seen, it differs from those used by De Chiffre, in patent US 7,617,750 (2009), patent application US 2014/0017113 (2014), and papers [63, 66] in one, but essential, aspect, namely face cutting instead of disk cutting (as shown in Fig. 1.25) is used. In the latter case, the cutting speed decreases as tool progresses if the workpiece rotates at the same rotational speed as the diameter of the workpiece decreases.

Fig. 1.28 Grain structure of the bulk material (Fig. 7d in [71])



In the setup used by Den et al. [71], there is no cutting speed variation as this speed is defined by the rotational speed of the workpiece, n (rpm) and workpiece diameter which does not change.

The machining conditions used in the tests were as follows: the cutting speed velocity was 0.052 m/s. Such a low cutting velocity was selected to ensure quasi-static deformation and to minimize temperature effects; the undeformed chip thickness was 0.2 mm; the width of the cut was 1 mm; the rake angle was 10° ; the chip compression ratio was set to be 1. The work material was pure copper. The bulk material microstructure included equiaxed grains with an average size greater than of 0.1 mm as shown in Fig. 1.28.

Figure 1.27b shows the typical morphology (at macrolevel) of a chip of pure copper produced by LSEM when the chip compression ratio was set to be 1.9 and the uncut (undeformed) chip thickness (h_D) of 0.1 mm. As can be seen, this structure differs from that of the bulk material as deformation bands in the direction of deformation can be readily observed.

Figure 1.29a, b show the microstructure of the chip obtained in conventional cutting and in LSEM, respectively. The sizes of the grains range between 200 and 800 nm, with a mean diameter of about 400 nm. A comparison of these structures reveals the following:

- The structures and the ranges of grain sizes are essentially the same;
- Neither conventional machining nor LSEM result in the formation of equiaxed grains as in ECAP.

Garcia-Gonzalez et al. [72] attempted to use LSEM for grain refinement in steel AISI 1020. The setup used in their tests was similar to that shown in Fig. 1.25; the typical test results are shown in Fig. 1.30. The test results showed that the pearlite regions (Fig. 1.30) resemble those observable in the “as received” material. The ferritic grains appear elongated (with mean width $\sim 10 \mu\text{m}$). This microstructure is

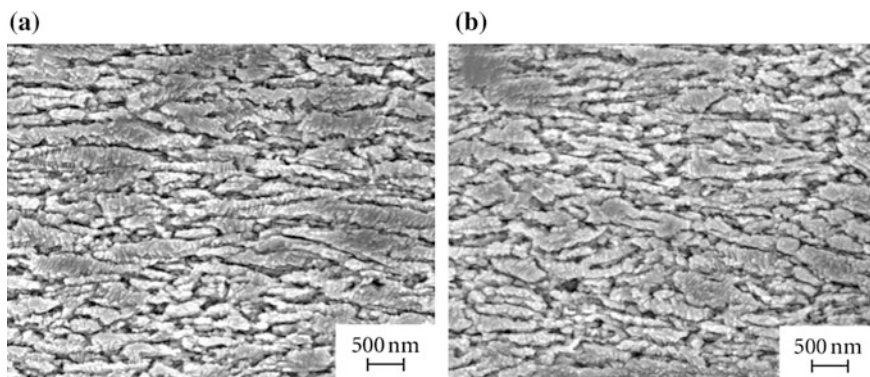


Fig. 1.29 Grain structure of the chip: **a** conventional machining, and **b** LSEM (Fig. 7a, c in [71])

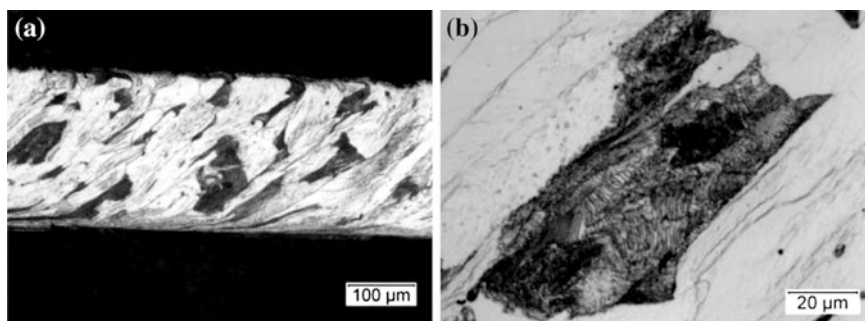


Fig. 1.30 Microstructure of AISI 1020 steel (at two different magnifications) produced in LSEM with strain $\gamma_{sh} = 2$

found to be consistent with the hardness measurement data. The high hardness of the material right after processing by LSEM is associated with high strength; the ductility of the material is low, as evidenced by the fact that the obtained strip did not bend past a few degrees before cracking.

A comprehensive study of strains imposed in LSEM was carried out by Cai et al. [73]. The work material used in the experiments is oxygen-free high-conductivity (OFHC) copper (99.95 %). The test pieces were cut from OFHC copper bar and their microstructures in three perpendicular section planes were assessed in the manner common in ECAP. A tensile testing machine was used in the test to provide the cutting motion as shown in Fig. 1.31. This allowed to carry the tests using orthogonal cutting where a wedge-shaped tool with a rake angle γ is static, and the workpiece with a preset uncut chip thickness t_D is moving toward the tool at the cutting speed, v . The chip thickness h_{c-e} was controlled by the constraint. The cutting tool with rake angle $\gamma = 10^\circ$ and clearance angle of 5° was used. The uncut

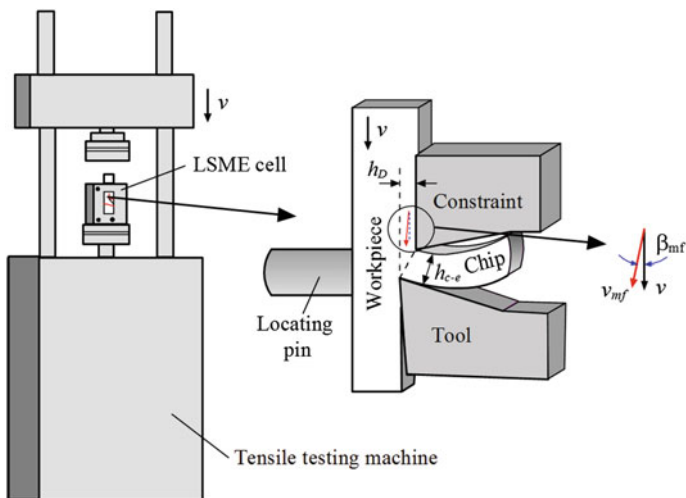


Fig. 1.31 Schematic of the experimental setup

chip thickness $h_D = 0.2$ mm was kept the same in the tests. The cutting width was 5 mm. The cutting speed was $v = 10$ $\mu\text{m/s}$.

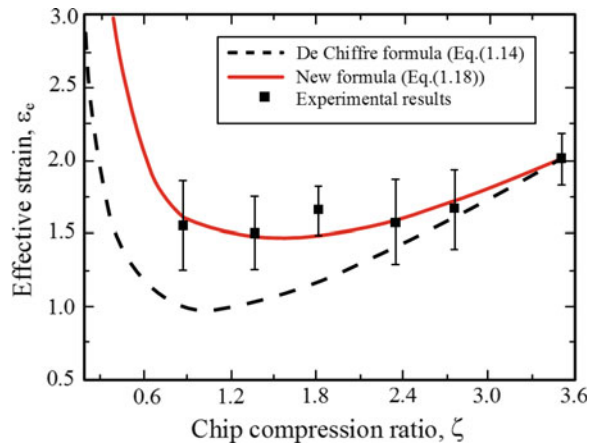
Using the information provided in books by Oxley [35] and Shaw [74], the authors in their analysis assumed that the single-shear plane model is valid and that metal cutting is accomplished by pure plastic deformation. In the author's opinion, however, it presented a number of problems in the analysis and led to unexplained experimental results.

Analyzing modeling of strains in LSEM Cai et al. [71] shows that the formula for strains in LSEM proposed by De Chiffre (Eq. 1.15) is the same as that for orthogonal cutting Eq. 1.16) so that the effect of the constraint is ignored. However, the presence and thus the role of the constraint is the most prominent difference between LSEM and orthogonal cutting. Based on the experimental results obtained using a digital correlation system and microscopic observations, Cai et al. [71] suggested that the work material flows into the deformation zone (the shear plane) not along the direction of the cutting speed as in orthogonal cutting but at a certain angle, termed as the deviating angle β_{mf} (see Fig. 1.31), to this direction. This deviating angle is calculated as

$$\tan \beta_{mf} = \frac{(\zeta_{oc} - \zeta_{em})^2 \cos \gamma}{\zeta_{em}(\zeta_{oc} - \sin \gamma)^2 + (\zeta_{em} - \sin \gamma)(\zeta_{oc} - \zeta_{em})^2} \quad (1.17)$$

where ζ_{oc} is the chip compression ratio in unconstrained (conventional orthogonal) cutting and ζ_{em} is the chip compression ratio in LSEM.

Fig. 1.32 Effective strain versus chip compression ratio according to the De Chiffre formula (Eq. 1.14), new formula (Eq. 1.18), and experimental results



The shear strain imposed in LSEM is calculated as

$$\gamma_{sh} = \frac{\zeta_{em} - \sin \gamma + \cos \gamma \tan \beta}{\cos \gamma - (\zeta_{em} - \sin \gamma) \tan \beta} + \frac{1}{\zeta_{em} \cos \gamma} - \tan \gamma \quad (1.18)$$

When $\zeta_{em} = \zeta_{om}$, i.e., when non-constrained orthogonal cutting is the case, Eq. (1.18) becomes the same as that for strain in orthogonal cutting (Eq. 1.16).

Figure 1.32 shows a comparison of the results of calculation using De Chiffre formula (Eq. 1.14), new formula (Eq. 1.18), and experimental results. As can be seen, the effective strains ($\epsilon_e = \gamma_{sh}/\sqrt{3}$) in LSEM calculated using Eq. (1.18) are much greater than those calculated using the De Chiffre formula (Eq. 1.14) used by other researches on LSEM.

Although the results of the tests shown in Fig. 1.32 are in good agreement with that calculated using the new formula, a reasonable doubt arises from the model it was derived. Moreover, it is not clear why the work material flows into the deformation zone (the shear plane) not along the direction of the cutting speed.

Cai et al. [71] did not analyze chip structure refinement. Nevertheless, from the micrograph of the partially formed chip presented in the paper, it may be concluded that the chip has the structure similar to that obtained by Den et al. [71] (see Figs. 1.27b and 1.29a).

References

- Altan BS (2006) Severe plastic deformation: toward bulk production of nanostructured materials. Nova Science, New York
- Hahn H (2002) Unique features and properties of nanostructured materials. In: Proceedings of the conference "nanomaterials by severe plastic deformation-NANOSPD2". Wiley-VCH, Vienna

3. Horita Z, Fujinami T, Nemoto M, Langdon TG (2000) Equal-channel angular pressing of commercial aluminum alloys: grain refinement, thermal stability and tensile properties. *Metall Mater Trans* 31A:691–701
4. Valiev RZ, Langdon TG (2006) Principles of equal-channel angular pressing as a processing tool for grain refinement. *Prog Mater Sci* 51:881–981
5. Figueiredo RB, Langdon TG (2009) Principles of grain refinement and superplastic flow in magnesium alloys processed by ECAP. *Mater Sci Eng A* 501:105–114
6. Kawasaki M, Mendes AA, Sordi VL, Ferrante M, Langdon TG (2011) Achieving superplastic properties in a Pb-Sn eutectic alloy processed by equal-channel angular pressing. *J Mater Sci* 46:155–160
7. Musin F, Kaibyshev R, Motohashi Y, Sakuma T, Itoh G (2002) High strain rate superplasticity in an Al-Li-Mg alloy subjected to equal-channel angular extrusion. *Mater Trans* 43:2370–2377
8. Valiev RZ, Zhilyaev AP, Langdon TG (2013) Bulk nanostructured materials: fundamentals and applications. Wiley, Somerset
9. Bertram A (2012) Elasticity and plasticity of large deformations: an introduction. Springer, Berlin
10. Dieter G (1976) Mechanical metallurgy, 2 edn. McGraw-Hill, New York
11. Schiotz J, Jacobsen KW (2003) A maximum in the strength of nanocrystalline copper. *Science* 301:1357–1359
12. Budrovic Z, Van Swygenhoven H, Derlet PM, Van Petegem S, Schmitt B (2004) Plastic deformation with reversible peak broadening in nanocrystalline nickel. *Science* 304:273–276
13. Olejnik L, Rosochowski A (2005) Methods of fabricating metals for nano-technology. *Bull Polish Acad Sci (technical sciences)* 53(4):413–423
14. Lowe TC, Valiev RZ (2004) The use of severe plastic deformation techniques in grain refinement. *J Miner Metals Mater Soc* 56(10):64–77
15. Furukawa M, Horita Z, Nemoto M, Langdon TG (2001) Review: processing of metals by equal-channel angular pressing. *J Mater Sci* 36:2835–2843
16. Nakashima K, Horita Z, Nemoto M, Langdon NG (1998) Influence of channel angle on the development of ultrafine grains in equal-channel angular pressing. *Acta Mater* 46(5):1589–1599
17. Chandrasekar S, Trumble K, Moscoso W, Efe M, Sagapuram D, Saldana CJ, Mann JB, Compton WD (2014) Large strain extrusion machining processes and bulk forms produced therefrom, US Patent Application 2014/0017113 A1
18. Liu ZY, Liang GX, Wang ED, Wang ZR (1998) The effect of cumulative large plastic strain on the structure and properties of a Cu-Zn alloy. *Mater Sci Eng A* 242(1):137–140
19. Saito S, Mabuchi M, Nakanishi M, Shigematsu I, Yamauchi G, Nakamura M (2001) Application of equal channel angular extrusion on strengthening of ferritic stainless steel. *J Mater Sci* 36(12):3229–3232
20. Vrátná J, Hadzima B, Bukovina M, Janeček M (2013) Room temperature corrosion properties of AZ31 magnesium alloy processed by extrusion and equal channel angular pressing. *J Mater Sci* 48(13):4510–4516
21. Shaban MG, Eghbali B (2011) Effect of integrated extrusion–equal channel angular pressing temperature on microstructural characteristics of low carbon steel. *Mater Sci Technol* 27(11):1802–1808
22. Semiatin SL, DeLo DP, Segal VM, Goforth RE, Frey ND (1999) Workability of commercial-purity titanium and 4340 steel during equal channel angular extrusion at cold-working temperatures. *Metall Mater Trans A* 30(5):1425–1435
23. Luo P, McDonald DT, Palanisamy S, Dargusch MS, Xia K Ultrafine-grained pure Ti recycled by equal channel angular pressing with high strength and good ductility. *J Mater Process Technol* 213:469–476
24. McDonald DT, Lui EW, Palanisamy S, Dargusch MS, Xia K (2014) Achieving superior strength and ductility in Ti-6Al-4V recycled from machining chips by equal channel angular pressing. *Metall Mater Trans A* 45(9):4089–4102

25. Valiev RZ, Alexandrov IV, Lowe TC, Zhu YT (2002) J, Mater Res 2002;17:5., Paradox of strength and ductility in metals processed by severe plastic deformation. J Mater Res 17 (01):5–8
26. Nishida Y, Arima H, Kim J-C, Ando T (2001) Rotary-die equal-channel angular pressing of an. Al–7 mass% Si–0.35 mass% Mg alloy. Scripta Mater 45:261–266
27. Jining Q, Han J-H, Guoding Z, Lee J-C (2004) Characteristic of textures evolution induced by equal channel angular pressing in 6061 aluminum sheets. Scripta Mater 51:185–189
28. Segal VM (2002) Severe plastic deformation: simple shear versus pure shear. Mater Sci Eng A 338:331–344
29. Hill R (1950) The mathematical theory of plasticity. Oxford University Press, London
30. Borja RI (2013) Plasticity: modeling & computation. Springer, Berlin
31. Piispanen V (1937) Lastunmuodostumisen teoriaa. Teknillinen Aikakauslehti 27: 315–322
32. Piispanen V (1948) Theory of formation of metal chips. J Appl Phys 19(October):876–881
33. Merchant ME (1945) Mechanics of the metal cutting process. II. Plasticity conditions in orthogonal cutting. J Appl Phys 16:318–324
34. Lee EH, Shaffer BW (1951) The theory of plasticity applied to a problem of machining. J Appl Mech 18:405–413
35. Oxley PLB (1989) Mechanics of machining: an analytical approach to assessing machinability. Wiley, New York
36. Astakhov VP (1998/1999) Metal cutting mechanics. CRC Press, Boca Raton
37. Johnson W, Mellor PB (1983) Engineering plasticity. Wiley, New York
38. Slater RAS (1977) Engineering plasticity: theory and application to metal forming processes. MacMillan Press, London
39. Hughes DA, Hansen N (1997) High angle boundaries formed by grain subdivision mechanisms. Acta Mater 45:3871–3886
40. Malin AS, Hatherly M (1979) Microstructure of cold-rolled copper. Metal Sci 8:463–472
41. Kuhlmann-Wilsdorf D, Hansen N (1991) Geometrically necessary, incidental and subgrain boundaries. Scr Metall Mater 25:1557–1562
42. Nabarro FRN, Duesbery MS (ed) (2002) Dislocations in solids, vol. 11. Elsevier, Amsterdam
43. Mataya MC, Carr MJ, Krauss G (1982) Flow localization and shear band formation in a precipitation strengthened austenitic stainless steel. Metall Trans A 13(7):1263–1274
44. Harren SV, Deve HE, Asaro RJ (1988) Shear band formation in plane strain compression. Acta Metall 36:2435–2480
45. Asaro RJ (1983) Crystal plasticity. J Appl Mech 50:921–934
46. Hirsch J, Lucke K, Hatherly M (1988) Mechanism of deformation and development of rolling textures in polycrystalline fcc metals-3. The influence of slip inhomogeneities and twinning. Acta Metall 36:2905–2927
47. Korbel A, Richert M (1985) Formation of shear bands during cyclic deformation of aluminum. Acta Metall 33:1971–1978
48. Thuillier S, Rauch EF (1994) Development of microbands in mild steel during cross loading. Acta Metall Mater 42:1972–1983
49. Gasperini M, Pinna C, Swiatnicki W (1996) Microstructural evolution of an aluminium alloy during high shear deformation. Acta Mater 44:4195–4208
50. Baygilzimer YI (2010) Simple shear pof metals: What is that? (in Russian). Phys Technol High Press 10(4):40–52
51. Ahmad Z (ed) (2012) Aluminium alloys: new trends in fabrication and applications. InTech, Rijeka
52. De Chiffre L (1976) Extrusion-cutting. Int J Mach Tool Des Res 16:137–144
53. Outeiro JC, Umbrello D, M'Saoubi R (2006) Experimental and numerical modeling of residual stresses induced in orthogonal cutting of AISI 316L steel. Int J Mach Tools Manuf 46:1786–1794
54. De Chiffre L (1983) Extrusion cutting of brass strips. Int J Mach Tool Des Res 23:141–151
55. Astakhov VP (2004) Tribology of metal cutting. Marcel Dekker, New York, pp 307–346

56. Astakhov VP (2012) Tribology of cutting tools. In: Davim PJ (ed) Tribology in manufacturing technology. Springer, New York, pp 1–66
57. Abushawashi Y, Xiao X, Astakhov VP (2013) A novel approach for determining material constitutive parameters for a wide range of triaxiality under plane strain loading conditions. *Int J Mech Sci* 74:133–142
58. Astakhov VP, Osman MOM (1996) An analytical evaluation of the cutting forces in self-piloting drilling using the model of shear zone with parallel boundaries. Part 2: application. *Int J Mach Tools Manuf* 36(12):1335–1345
59. Astakhov VP, Svets SV, Osman MOM (1997) Chip structure classification based on mechanics of its formation. *J Mater Process Technol* 71(2):247–257
60. Cai SL, Dai LH (2014) Suppression of repeated adiabatic shear banding by dynamic large strain extrusion machining. *J Mech Phys Solids* 73:84–102
61. Shankar MR, Chandrasekar S, King AH, Compton WD (2005) Microstructure and stability of nanocrystalline aluminum 6061 created by large strain machining. *Acta Materialia* 53:4781–4793
62. Sevier M, Lee S, Shankar MR, Yang HTY, Chandrasekar S, Compton WD (2006) Deformation mechanics associated with formation of ultra-fine grained chips in machining. *Mater Sci Forum* 503–504:379–384
63. Sevier M, Yang HTY, Lee S, Chandrasekar S (2007) Severe plastic deformation by machining characterized by finite element simulation. *Metall Mater Trans B* 38(6):927–938
64. Swaminathan S, Shankar MR, Rao BC, Compton WD, Chandrasekar S, King AH, Trumble KP (2007) Severe plastic deformation (SPD) and nanostructured materials by machining. *J Mater Sci* 42(5):1529–1541
65. Sevier M, Yang HTY, Moscoso W, Chandrasekar S (2008) Analysis of severe plastic deformation by large strain extrusion machining. *Metall Mater Trans A* 39:2645–2655
66. Saldana C, Swaminathan S, Brown TL, Mann JB, Compton WD, Chandrasekar S (2010) Unusual applications of machining: controlled nanostructuring of materials and surfaces. *J Manuf Sci Eng* 132:030908
67. Wiezorek JMK, Facco G, Idell Y, Kulovits A, Shankar MR (2014) Nano-structuring of 316L type steel by severe plastic deformation processing using two-dimensional linear plane strain machining. *Mater Sci Forum* 783–786:2720–2725
68. Efe M, Trumble KP, Compton WD, Chandrasekar S (2012) Mechanics of large strain extrusion machining and application to deformation processing of magnesium alloys. *Acta Materialia* 60:2031–2042
69. Time I (1870) Resistance of metals and wood to cutting (in Russian). Dermacow Press House, St. Petersburg
70. Zorev NN (1966) Metal cutting mechanics. Pergamon Press, Oxford
71. Deng WJ, Lin P, Xie ZC, Li Q (2012) Analysis of large-strain extrusion machining with different chip compression ratios. *J Nanomater* 2012:12. Article ID 851753
72. Garcia-Gonzalez JC, Sagapuram D, Efe M, Chandrasekar S, Moscoso-Kingsley W (2014) Steel strips made directly from bulk material by large strain extrusion machining. In: Twelfth LACCEI Latin American and Caribbean conference for engineering and technology (LACCEI'2014) "Excellence in engineering to enhance a country's productivity", Guayaquil, pp 1–9
73. Cai SL, Chen Y, Ye GG, Jiang MQ, Wang HY, Dai LH (2015) Characterization of the deformation field in large-strain extrusion machining. *J Mater Process Technol* 216:48–58
74. Shaw MC (2004) Metal cutting principles, 2nd edn. Oxford University Press, Oxford

Chapter 2

Cross Rolling: A Metal Forming Process

Matruprasad Rout, Surjya K. Pal and Shiv B. Singh

Abstract The chapter deals with cross rolling where the workpiece is rotated by 90° in the rolling plane after each rolling pass. The chapter begins with basics of metal rolling, and later on focuses on cross rolling. A short introduction to texture and its representation is presented followed by an overview of the formation of deformation texture in various materials after cross rolling. Review of some of the research works on cross rolling in last few decades has also been included. A case study has been provided at the end of this chapter.

2.1 Introduction

Rolling is one of the bulk metal forming processes, where metal is deformed plastically by allowing it to flow between two rollers, rotating in opposite directions. Plastic deformation reduces the initial thickness of the workpiece to a pre-defined final thickness, and the gap between the two rotating rolls, which is less than the initial thickness, determines the final thickness. Because of the constancy of volume of material before and after rolling, the amount of reduction in material thickness governs the elongation in length. The change in width is negligible since it is much larger as compared to its thickness. Frictional force, f between workpiece and rolls is responsible for dragging the workpiece into the roll gap. Rolling process not only reduces the thickness, but also enhances material properties like strength, toughness, surface morphology, etc. Contour of the rolls governs the shape of the rolled product. Rolling is the most widely used forming process, which produces

M. Rout · S.K. Pal (✉)

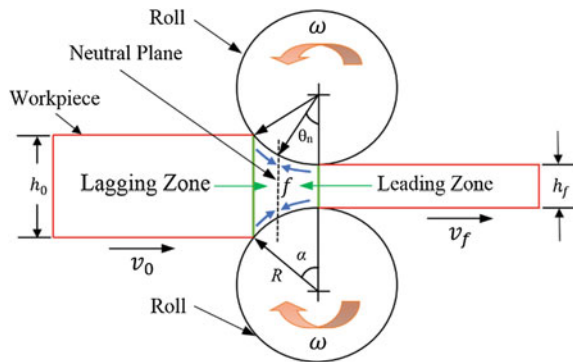
Department of Mechanical Engineering, Indian Institute of Technology,
Kharagpur 721302, India
e-mail: skpal@mech.iitkgp.ernet.in

S.B. Singh

Department of Metallurgical and Materials Engineering,
Indian Institute of Technology, Kharagpur 721302, India

© Springer International Publishing Switzerland 2015
J.P. Davim (ed.), *Modern Manufacturing Engineering*, Materials Forming,
Machining and Tribology, DOI 10.1007/978-3-319-20152-8_2

41

Fig. 2.1 Flat rolling process

products like bloom, billet, slab, plate, strip, sheet, etc. In order to increase the flowability of the metal during rolling, the process is generally performed at high temperature and consequently the load requirement reduces. Figure 2.1 shows a schematic diagram of a rolling process, where a strip of thickness, h_0 enters the roll gap and is reduced to h_f by a pair of rolls, rotating in opposite directions. The surface speed of the roll is $V_r (= \omega \times R)$. The linear speed of the workpiece increases from its initial value, V_0 as it moves through the roll gap and attains a highest value, V_f at the exit of the roll gap.

Friction plays an important role in rolling as it always opposes relative movement between two surfaces sliding against each other. At the point where workpiece enters the roll gap, the surface speed of the rolls is higher than that of the workpiece. So, the direction of friction is in the direction of the workpiece movement and this friction force drags it into the roll gap. During rolling, velocity of the workpiece increases as material flow rate remains same all throughout the deformation. Material velocity is equal to the surface speed of the rolls at a plane, called the *neutral plane*. From the entry point to the neutral point, the deformation zone is named as the *lagging zone*. Beyond the neutral plane, i.e., in the *leading zone*, the speed of the deforming workpiece is faster than the peripheral speed of the rolls and direction of friction quickly changes to oppose this. In order to make the analysis of flat rolling process simple, assumptions like plane strain deformation, volume constancy principle, constant coefficient of friction, constant surface velocity of the rolls, etc., are considered. Out of all varieties of the rolling processes, the flat rolling is the most practical one which produces around 40–60 % of the total rolled products [1]. This attracts several researchers to work in this area to improve the quality and quantity of products through optimizing the process parameters. Cross rolling, by changing the workpiece orientation and hence changing the deformation path, is a way of tailoring texture development to reduce the anisotropic properties of the workpiece.

2.1.1 Cross rolling

Cross rolling (CR) is normally done on samples of comparatively lesser dimension, by changing the rolling direction (RD). The sample, on the rolling plane, is rotated by 90° about the normal direction (ND). There is no standardized sequence of stages of cross rolling but the sequences followed by most of the researchers are mainly of two types: Two-step cross rolling (TSCR), also known as pseudo-cross-rolling, where direction is changed after achieving 50 % of the total reduction (Fig. 2.2a). Second, Multistep cross rolling (MSCR), also known as true cross rolling, where direction is changed after each pass (Fig. 2.2b) [2]. Clock rolling (Fig. 2.2c) may be one more way of achieving cross rolling, by continuously changing the rolling direction by 90° about ND, and if the rotation is 180° instead of 90° , it is called as reverse rolling. Change in rolling direction or deformation path changes the substructure formed in the previous path of deformation, and hence affects the deformation texture. Cross rolling leads to rolled product of comparatively uniform mechanical properties in all directions (Fig. 2.3).

Schmitt et al. [3] have studied the effect of critical resolved shear stress (CRSS) value on yield locus for polycrystalline material. Different values of CRSS were obtained by prestraining the material in different directions and the degree of change in strain path, is defined by a scalar parameter, $\alpha = d\varepsilon_p \cdot d\varepsilon$, where $d\varepsilon_p$ and $d\varepsilon$ are the unit vectors in two different strain paths. They have observed that the yield stress value increases with α varying from 1 to 0 and decreases when α varies from 0 to -1 . Gurao et al. [4] defined the above-mentioned parameter in a different way as $\theta = (\varepsilon_p : \varepsilon) / (\|\varepsilon_p\| \|\varepsilon\|)$, where ε_p is strain tensor in the prestrain path and ε

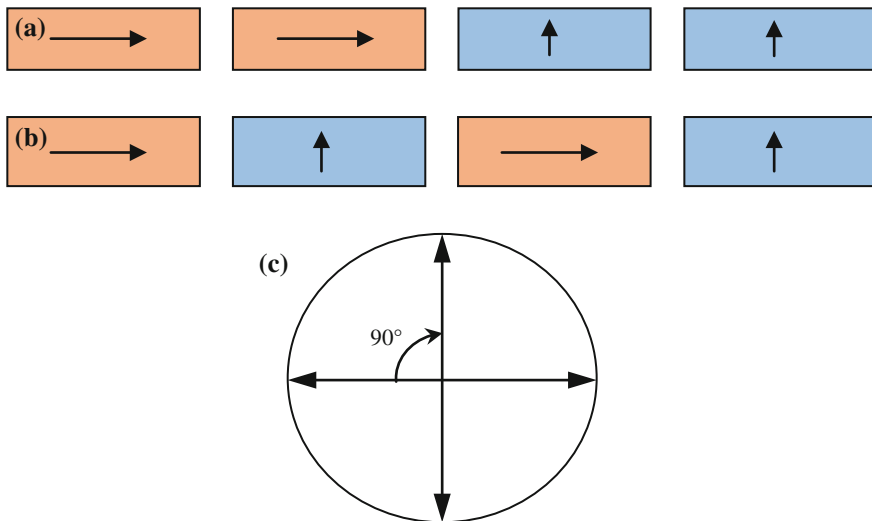
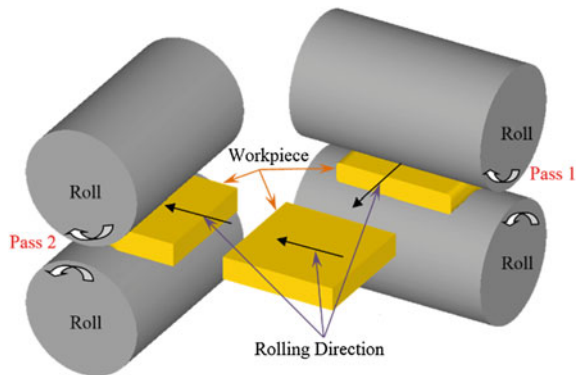


Fig. 2.2 Cross rolling sequences; **a** Two-step cross-rolling (TSCR), **b** Multistep cross-rolling (MSCR) and **c** Clock rolling

Fig. 2.3 Rolling mill arrangement for cross rolling



is the strain tensor in successive strain path. For no change in strain path, $\varepsilon_p = \varepsilon$ and $\theta = 1$, while $\theta = 0$ corresponds to orthogonal strain path change. As the parameter θ is defined for change of strain path during rolling, it leads to a value of 0.5 for both MSCR, TSCR and 1 for reverse rolling, as reported by Suwas and Gurao [5].

For unidirectional or straight rolling, where it is considered as a plane strain deformation, the sample has an orthorhombic symmetry. Symmetry is something that when certain operations are performed on the sample it will bring the sample into coincidence with itself. Orthorhombic symmetry means all the three viz. rolling, transverse, and normal directions of the sample are axes of twofold symmetry. Now, for cross rolling, where the sample is rotated by 90° after each pass, the sample symmetry becomes tetragonal having one fourfold axis which is parallel to the normal direction [2, 6].

2.1.1.1 Applications

Cross rolling is a way of reducing the directional dependency of different properties of the rolled plate. An application of this process can be for the sheets used for making cup by deep drawing processes. The value of \bar{R} and ΔR (described in Sect. 2.1.2.2) can be controlled by cross rolling, which may be needful in reducing the ear formation during a deep drawing process. In another application, it can be used for producing non-grain-oriented electrical steels used in transformers, motors, generators, etc., to get similar magnetic properties in all directions. Bohler-Uddeholm of USA is one of the industries [7] which is currently using this process to make stainless steel sheets for manufacturing of knives.

2.1.1.2 Limitations

As the plate is rotated, i.e., width and length of the plate are altered, it cannot be applicable for products of longer dimensions. Initial cost of the set up may increase

due to the placing of the rolls in two different angles and due to the required material handling equipment.

2.1.2 Effects of Cross Rolling

Cross rolling can affect the material properties in many ways; possible effects on the material due to change in rolling directions are

- Microstructural changes and changes in crystallographic texture
- Changes in plastic anisotropy
- Changes in residual stress distribution

2.1.2.1 Crystallographic Texture

Almost all materials of interest are made up of aggregates of single crystals (also known as grains). Single crystals are solid aggregates where the crystal lattice is continuous, i.e., without grain boundaries. Most commercial metals are polycrystals, composed of aggregates of single crystals, with different atomic orientations with respect to a predetermined external frame of reference and hence have the grain boundaries. The main differences among the grains of the polycrystalline materials are: the shape and the orientation. Shape of the grains depends on type of the solidification and the subsequent thermomechanical processes, whereas orientation largely depends on the processing that a material experiences during deformation. In a plastic deformation process of polycrystalline metals, crystallographic orientation of each grain changes which is known as texture evolution. This texture evolution needs to be controlled as it has a significant effect on the anisotropy of the properties [8]. Texture, generally characterized by a crystallographic plane and a crystallographic direction, can be represented graphically in pole figures and orientation orientation distribution functions (ODF). Basically this representation indicates the intensity of an orientation or texture component, which depends on the number of grains having same orientation [9].

2.1.2.2 Plastic Anisotropy

Plastic anisotropy means that in plastic deformation materials are not isotropic, which is normally the directional independency of the properties. Most of the materials available are polycrystalline and exhibit anisotropic behavior. During manufacturing, some forms of textures are developed in the material and it may enhance anisotropy. The form of texture pattern depends on the type of deformation and depending on that it may enhance or reduce the level of anisotropy. In case of rolling, high intense textures are formed in the direction of rolling, which may lead to significantly different properties in the rolling and transverse directions.

Lankford coefficient, R , defines plastic anisotropy by the ratio of strain in width direction (ε_w) to the strain in thickness direction (ε_t) in the uniaxial tensile test. Higher value of R indicates high resistance of the material to thinning and hence the material can be drawn into a greater height. The Lankford coefficient depends on the orientation of tensile axis with reference to the rolling direction, in the rolling plane and defined by the angle α , and hence $R = R_\alpha$. In general, materials are anisotropic and defined by average \bar{R} (ASTM E517):

$$\bar{R} = \frac{1}{4} (R_{0^\circ} + 2R_{45^\circ} + R_{90^\circ}) \quad (2.1)$$

Variation of the R_α in the plane of the sheet is also important and it is described by the coefficient of planar anisotropy,

$$\Delta R = \frac{1}{2} (R_{0^\circ} - 2R_{45^\circ} + R_{90^\circ}) \quad (2.2)$$

Planar anisotropy relates to the formation of ears in deep drawn cups or in other words ΔR is the degree of the tendency of the sheet to form ears. If $\Delta R > 0$, then ears form at 0° and 90° to the rolling direction, and if $\Delta R < 0$, ears form at 45° . These two coefficients are dependent on crystallographic texture.

2.1.2.3 Residual Stress

Stresses which remain in the solid material even after the removal of the cause of stress are called as residual stress. The cause of the stress may be external mechanical load or it may be the thermal load and for the latter case, the residual stress is normally called as thermal stress. During hot rolling, the material is subjected to both the types of loading; and due to the nonuniformity in deformation and presence of temperature gradients; the residual stress distribution in the material after rolling is not uniform. Residual stress may distort the shape of the rolled material and it also has significant effect on further processing of the rolled product. Thus, the residual stresses distribution in rolled sheet cannot be ignored. Residual stresses, which may be a compressive or a tensile type, are sometimes desirable also. For brittle fracture by crack propagation in a material having compressive residual stress is little difficult. Now for cross rolling, where the deformation path changes, the temperature and plastic strain distribution in the material will be different to that of a material rolled in a single direction and hence the residual stress distribution will also change. Very few literatures are available on residual stress distribution for the cross-rolled material. Nature of the residual stress developed in the rolled product can be changed, i.e., from tensile to compressive, by cross rolling [10].

2.2 Texture or Preferred Orientation

Texture is a measure of the similarity in orientation of the crystal lattice within the constituent grains of a polycrystalline. In simple words, texture is the orientation or arrangement of the grains in the material with respect to a fixed coordinates. This can be clarified using the following figures. In Fig. 2.4a, the grains in the plate are placed randomly and gives rise to a random texture, whereas in Fig. 2.4b the grains are arranged in a similar fashion and forms a preferred orientations, as normally seen in the rolled sheets made through unidirectional rolling.

Texture development or changes in texture in a material normally occurs due to any one or combination of any of the reasons; (i) solidification, (ii) plastic deformation, (iii) annealing, and (iv) phase transformation. This chapter deals with deformation texture (rolling texture). Texture or orientation of grains, in rolling, is normally represented by set of Miller indices $\{hkl\}\langle uvw \rangle$, where $\{hkl\}$ specifies the crystallographic planes of the grains parallel to the plane of the sample and $\langle uvw \rangle$ shows crystallographic direction parallel to the rolling direction. For polycrystalline material, different grains have different orientations which give rise to a complex texture. In such cases, the overall texture can be statistically represented by the following fundamental equation [11]:

$$\text{Texture}_{\text{Overall}} = \sum w_i \{hkl\}_i \langle uvw \rangle_i, \quad (2.3)$$

where w_i is a weighting factor. Texture can be broadly classified into two types: macrotexture and microtexture. Macrotexture gives information about how much volume fraction of the sample has a specific orientation and does not give any idea about how the grains are spread within the sample. Microtexture is the combination of microstructure and texture. It gives information about the orientation of an individual grain and its neighbors as well. X-ray diffraction is the commonly used method for bulk texture measurement; whereas, electron back scatter diffraction (EBSD) is used for microtexture measurement. The other method used for texture measurement is by Neutron diffraction. Details regarding texture formation, measurement, and representation can be found elsewhere (Engler and Randle [12]; Kocks et al. [9]). In this chapter, a brief introduction of how to represent texture is presented.

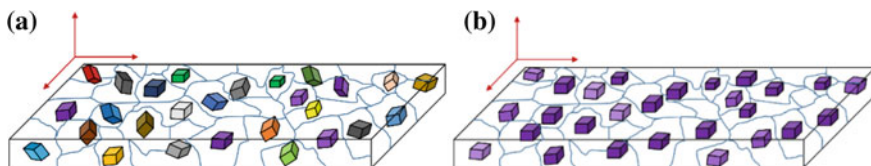


Fig. 2.4 Crystal orientations in a plate; **a** random orientation and **b** preferred orientation

2.2.1 Reference System

Reference system is an important parameter for representing crystal orientation. It may be sample reference system or crystal reference system. In sample reference system, the three mutually perpendicular axes of sample are taken as reference. But, in crystal reference system the three mutually perpendicular crystallographic axes of a unit cell are considered as reference and the same axes are considered for all the crystals within the sample, irrespective of their orientations. Generally for sample reference system, the axes were fixed, i.e., RD, TD, and ND; but for crystal reference system, the axes can be chosen arbitrarily. In Fig. 2.5a both the sample and crystal/unit cell have same orientation with respect to an external frame, and in Fig. 2.5b, the orientation gets changed but still both have same orientation. But in Fig. 2.5c the crystal has completely different orientation to that of the sample.

While representing orientation, it is necessary to transfer the sample reference system to crystal reference system or the vice versa.

2.2.2 Euler Angle

The Euler angles are the angles of rotation, which when performed in correct order, transforms the specimen coordinate system onto the crystal coordinate system. Bunge [13], Roe [14] and Williams [15] proposed different ways of transforming sample frame to the crystal frame. Out of these three ways, the one proposed by Bunge is commonly used [11]. The sequence of rotation given by Bunge is given below:

1. Rotation about the ND (normal direction) by an amount φ_1 , changing the TD (transverse direction) into TD' and the RD (rolling direction) into RD'
2. Rotation about the new RD axis, i.e., RD' by an amount Φ , converting TD' to TD'' and ND' to ND''
3. Rotation about the new ND, i.e., about ND'' by an amount φ_2

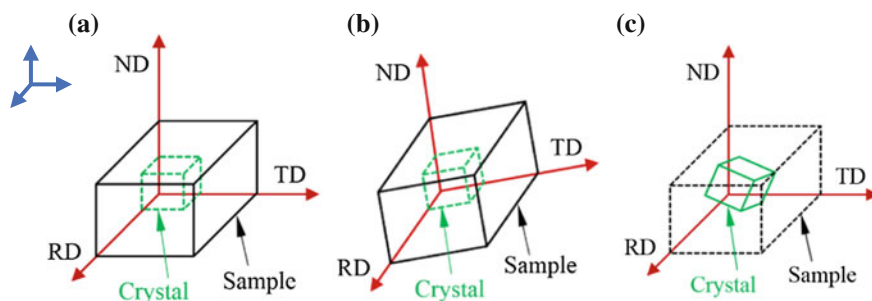
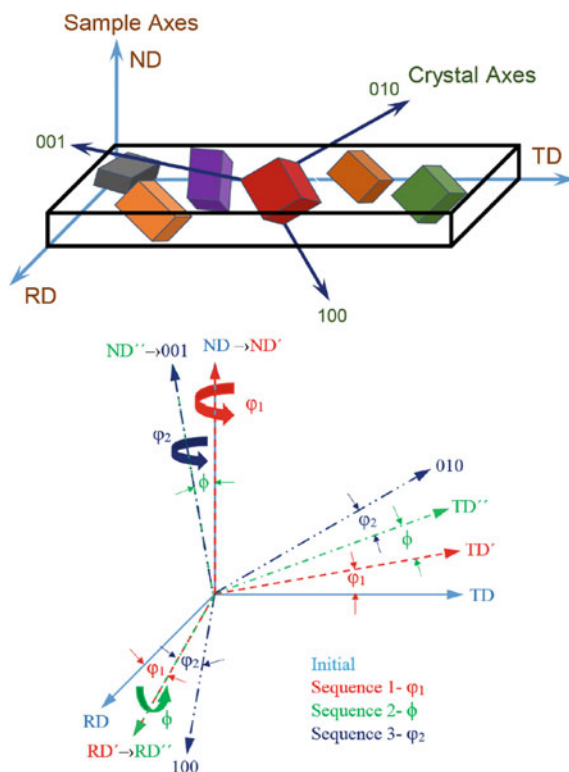


Fig. 2.5 Reference System

Fig. 2.6 Euler angles proposed by Bunge [13]



where ϕ_1 , Φ and ϕ_2 are the Euler angles. The sequence of rotation is represented graphically in Fig. 2.6 [16].

2.2.3 Representation of Texture

Graphically, texture can be represented by any of the following ways: pole figure showing the distribution of a specific crystallographic direction in the assembly of grains of the specimen in sample reference system; inverse pole figure (IPF) showing the frequency with which a particular crystallographic direction coincides with axes of the specimen; and orientation distribution function (ODF) which shows the full 3D representation of crystallographic texture calculated from a set of pole figures.

2.2.3.1 Pole Figure

Orientation of a plane can be represented by a line normal to it. If a sphere, termed as reference sphere, is drawn with the center on the plane, then the circle formed at the intersection of the plane and the sphere is called trace [17]. Now, if the line normal to

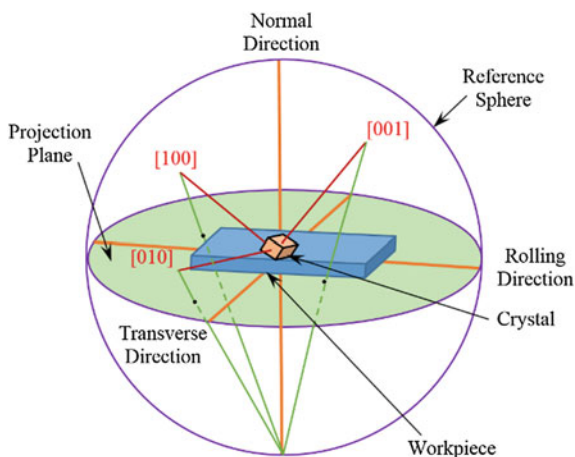
the plane is extended to the sphere, the intersection point will be the pole. The indices of these poles are same as that of the planes, to whom they are perpendicular. These formed poles, either on upper hemisphere or on lower hemisphere, are then mapped to a plane called as the projection plane. The formed circle with projected poles is called pole figure. Stereographic projection is the well-known mapping method used by metallurgists to map the hemisphere to a plane. Figure 2.7 shows the schematic diagram representing the formation of a pole figure. For material with high texture, poles are normally accumulated about a particular direction.

The projection of normal to the three mutually perpendicular planes viz. 100, 010, and 001, of a single unit cell, on the projection plane is represented in Fig. 2.7. Now, if we consider the same planes or poles for other grains, then they may be formed near to the same location as that of initial one or may be scattered on the projection plane depending on the orientation of the grains. If the poles are formed close to each other, forming cluster, they indicate a strong texture in the sample. But, if the poles are scattered in the projection plane, then it indicates random texture in the sample. Normally, pole figure is drawn for a single plane or pole, which indicates how the plane is oriented, with respect to the sample frame, in the considered scanned area of the sample. Pole figures can be represented by using the projected individual poles or by contour plot for overlap poles. In contour plot, the number near to contour line indicates the density of the pole with respect to that of a sample having random texture [11].

2.2.3.2 Inverse Pole Figure

Inverse pole figure (IPF) is the inverse or opposite of the pole figure. In pole figure, crystallographic orientations are represented with respect to an external, i.e., sample reference system but in IPF the sample directions (i.e., RD, TD, and ND) are represented with respect to the crystallographic axes. In other words, IPF represents

Fig. 2.7 Pole figure



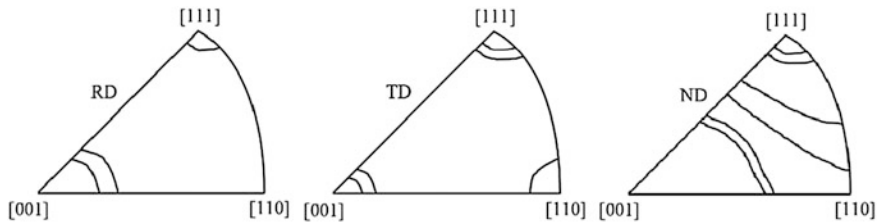


Fig. 2.8 Inverse pole figure

the frequency with which the sample axes coincide with the crystallographic axes. Stereographic projection has been made for crystallographic direction parallel to RD, TD, or ND, but due to the crystal symmetry a part of the projection is represented as IPF. Figure 2.8 shows a representation of IPF.

2.2.3.3 Orientation Distribution Function

To completely describe a polycrystalline structure, orientation, form, and position of each crystal is necessary, which is very complicated. So, relatively simplified statistical parameters are used to describe a polycrystalline structure. Orientation distribution function (ODF) is one of those statistical parameters, which is defined by only considering the orientation of the crystallographic axes with respect to the sample axes [13]. Mathematically,

$$\text{ODF} = f(g)dg = \frac{\Delta v(g)}{v}, \quad (2.4)$$

where, v = volume of whole sample, $\Delta v(g)$ = volume of all the crystallites having orientations in the range of $g + \Delta g$ and g is the orientation of the crystallite in terms of Euler angles, i.e., $g = g(\varphi_1, \Phi, \varphi_2)$. The texture details obtained from pole figure are in 2D as it is projecting the poles to a plane and hence has some limitations. Whereas, ODF can give a full 3D representation of the crystallographic texture of a polycrystalline material. Mathematical models, which take numerical data from several pole figures as input, are used to get a complete 3D ODF. Three-dimensional ODF is represented in a space having φ_1, Φ and φ_2 as the Cartesian coordinates. A point on this space gives a particular value of φ_1, Φ and φ_2 . If a number of crystals have same orientation, i.e., same value of φ_1, Φ and φ_2 then they will form a cluster in the 3D ODF, and hence represents the existence of a texture. Normally, ODF is represented by slicing the Euler space on any one of the three axes. If slicing is done on φ_1 axis, i.e., ODF is represented on constant φ_1 section, then it is called as sample orientation distribution (SOD). Whereas, if it is represented on constant φ_2 section, it is termed as crystal orientation distribution (COD).

As per Bunge, an orientation distribution function can be described by following series [5]:

$$f = (\varphi_1, \Phi, \varphi_2) = \sum_{l=0}^{\infty} \sum_{m=-1}^{+1} \sum_{n=-1}^{+1} C_1^{mn} P_1^{mn}(\Phi) \times \exp(im \varphi_2) \exp(in \varphi_1), \quad (2.5)$$

where C_1^{mn} is the series coefficients and $P_1^{mn}(\Phi)$ are certain generalizations of associated Legendre functions.

2.2.4 Ideal Orientations

Ideal orientations are the orientations of the grains or texture components, which are normally observed in rolled materials. Some of these components are named after the metal or alloys in which they were observed for the first time. Apart from the ideal orientations, there are some texture fibers, which are nothing but the lines joining the texture components having a range of orientations with a single degree of freedom about a fixed axis, has also been observed [9]. Followings are the list of ideal orientations for materials with different crystal structures presented in tabular forms (Tables 2.1, 2.2).

2.2.5 Prediction of Texture

Various mathematical models are used to predict the deformation mechanism and hence deformation texture during rolling. Basically these models consider the

Table 2.1 Ideal orientations in BCC materials [5]

Components	Miller indices $\{hkl\}\langle uvw \rangle$	Euler angles (°) ($\varphi_1, \Phi, \varphi_2$)
Cube (C)	$\{100\}\langle 001 \rangle$	45, 0, 45
Rotated cube	$\{001\}\langle 110 \rangle$	0, 0, 45
Goss (G)	$\{110\}\langle 001 \rangle$	90, 90, 45

Table 2.2 Ideal orientations in FCC materials [5, 9]

Components	Miller indices $\{hkl\}\langle uvw \rangle$	Euler angles (°) ($\varphi_1, \Phi, \varphi_2$)
Copper (Cu)	$\{112\}\langle 111 \rangle$	90, 35, 45
Brass (Bs)	$\{110\}\langle 112 \rangle$	35, 45, 0
Cube (C)	$\{100\}\langle 001 \rangle$	0, 0, 0
Goss (G)	$\{110\}\langle 001 \rangle$	0, 45, 0
S	$\{123\}\langle 634 \rangle$	59, 29, 63

behavior of the materials, which are normally polycrystalline, as a statistical function of the behavior of distinct grains. Some of the models are: Taylor model, Sachs' model, LAMEL, ALAMEL, GIA, CPFEM, viscoplastic self-consistent model and many more. The basics of these models start with deriving mathematical equation which transfers or relates the stresses and strains, the sample is subjected to, at the grain level. Now, these microlevel stresses and strains are linked to slip and twinning systems, by some constitutive equations, for the initiation of plastic deformation. The fundamental equation is shown below [11]

$$D^C = \dot{\epsilon} \sum_s \left| \frac{m^s : \sigma^C}{\tau^s} \right| m^s \operatorname{sgn}(m^s : \sigma^C) \quad (2.6)$$

where

D^C : Strain rate in a crystal

$\dot{\epsilon}$: Scaling factor

σ^C : Stress in a crystal

τ^s : Critical resolved shear stress (CRSS)

m^s : Schmid tensor

$$m^s = \left(\frac{1}{2} \right) \left(b_i^s n_j^s + b_j^s n_i^s \right) \quad (2.7)$$

s : slip and twinning systems

b : Slip direction

n : Normal to the slip plane

Slip in a system will occur when the resolved shear stress $m^s : \sigma^C$ approaches τ^s and the plane on which slip occurs, which were identified by simultaneously solving the equation for a single crystal as well as interaction between the crystals. Plastic deformation causes lattice rotation and can be calculated after inputting the activated slip system which is well known for different crystal structure materials. The obtained lattice rotations are used in deriving the deformation texture. These deformation models are also implemented to cross rolling to predict the deformation texture, by different authors, but the number of research papers available on this is not too high. Some of the works on the predicted deformation texture for cross rolling is given in Sect. 2.3.2.

2.3 Cross Rolling Texture: An Overview

2.3.1 Experimental Observation

Texture or preferred orientation, which affects material properties, contains information about the interrelation between processing parameters and material performance. It provides essential feedback for tuning the thermomechanical history to

get desired properties in the finished product [9]. This makes texture development an important field of research for researchers. Changing the deformation path by changing the rolling direction may be one way of tuning the thermomechanical processing route to get the required orientation, and hence required properties. Some of the available earlier articles on cross rolling are by, Custers and Riemersma [18], Merlin and Beck [19], Wassermann and Grewen [20], Yeung and Duggan [21], on materials with face centered cubic (FCC), body centered cubic (BCC), and hexagonal close packed (HCP) crystal structures. But it is in the last few decades, where there is a significant progress in the research on cross rolling, which is mainly due to the advancement in technology to detect and analyze textures in materials. Recently, some research works have been carried out using crystal plasticity finite element models to simulate the deformation mechanism during the process. Literatures are available where rolling has been done by placing the work-rolls at some angle in the rolling plane and termed as cross rolling. This type of rolling has not been discussed in the current chapter. Some of the research works, which are experimentally carried out on cross rolling, are discussed below.

2.3.1.1 Body Centered and Face Centered Cubic Materials

Due to the wide industrial application of BCC and FCC structure metals and alloys, a lot of research works has been carried out for texture evolution. Vanderschueren et al. [22] experimentally studied the effect of change in rolling direction on the magnetic properties of nonoriented 0.6 % Si steel. Nonoriented electrical steels, which are normally used in rotor and starter of comparatively smaller electrical machines, requires low core loss and high permeability to give an efficient performance to the machine. Hysteresis loss and eddy current loss are the two which mutually do the core loss. Eddy current loss is related to resistivity and can be controlled by the composition of the material but the hysteresis loss depends on the magnetic anisotropy, which depends on the orientation or texture of the material and can be modified during the processing of the material. The authors have studied the direction effect by changing the rolling direction to 90°(TD) during cold rolling and after which the sheets were subjected to annealing and decarburization. Cross-cold rolling changes the initial hot-rolling texture components and produces a strong $\{001\}\langle 110 \rangle$ component. The texture data were correlated to the magnetic properties, and found that, hysteresis loss was 80 % of the total loss and it was due to texture and grain size. Bocker et al. [2, 6] reported the texture development, through ODF, for two different materials namely Armco iron (BCC) and AlMn1 alloy (FCC) in two separate articles. The same rolling sequence consisting of a MSCR and TSCR was followed for both the materials. They concluded that for MSCR, the deformation path follows a tetragonal symmetry; whereas for TSCR, it is a broken path as the deformation path changes at 50 % of total reduction but both the parts of deformation has orthorhombic symmetry. For AlMn1, they found that, TSCR produces texture which has tube orientation extending between orientation A and B, whereas MSCR gives rise texture with ideal orientation C.

The high-temperature withstanding capacity of molybdenum (Mo) makes it an excellent refractory material and find its application in furnace, nuclear industry, etc. It is a well-known fact that rolling produces preferred orientation in the material in the rolling direction and molybdenum (BCC) is not an exception. Oertel et al. [23] investigated the influence of cross rolling as well as heat treatment on texture and formability of Mo sheet. The investigations were made at different stages (early stage and late stage) of the processing route and the rolling direction was changed in larger varieties, like 45° , 90° , and 135° . Texture produced in different sheets made by different rolling sequences are independent of cross-rolling steps and gives rise to an incomplete α -fiber with maximum strengths sited at the rotated cube component. However, the intensities of the texture for sheets with complex rolling sequences are much less as compared to others. Cross rolling done at the early stage, produces sheets with high mechanical anisotropy as compare to the sheets produced by processing where cross rolling is implemented at the later stage. This indicates the disappearance of effect of cross rolling, which is due to the subsequent rolling in one direction. Sheets produced by changing the rolling direction in complex manner give lower planar anisotropy (ΔR). The reported value shows the parameter Z, which is related to the earing formed during deep drawing, increases with the increase in ΔR value.

Aluminum alloys found a wide application due to its good strength, high ductility, high corrosion resistance, and low weight. But while doing sheet metal forming, like deep drawing of aluminum alloys, the chances of formation of earing is quite high due to its high plastic anisotropic properties. A good number of researchers have done cross rolling on various aluminum alloys to study this anisotropy parameter, as well as deformation texture. Liu et al. [24] studied the texture development in AA 3105 aluminum alloy (FCC), which has a strong β fiber rolling texture. They used a two-stage cross-cold-rolling process, where the rolling was done in original TD and reduced the 2 mm sheet to different thickness, maximum up to 90 %. The initial texture components present in the materials like B, S, and C get rotated and transform to B', S', and C', respectively. With increase in rolling reduction, intensities of components like B and S get increased, whereas there is no significant increase in the component C. They also made a quantitative analysis for texture by calculating the volume fraction of different texture components and correlated them with true rolling strain. In another paper, Liu et al. [25] reported the recrystallization texture of continuous cast AA 5005 aluminum alloy, where, the samples were annealed after rolled by pseudo-cross-cold-rolling process. Mondal et al. [26] makes a detailed analysis of cross rolling on AA 7010 aluminum alloys. They concluded that, cross rolling leads to the formation of β fiber in the aluminum alloy and with increasing number of cross rolling steps, the strength of the rotated-Bs component increases while that of rotated-Cu component reduces. In another study [27], made by same authors for a different kind of aluminum alloy, the authors found a strong rotated-Bs texture in the hot cross-rolled alloy.

Wronski et al. [10] studied the effect of cross rolling for pure copper (FCC) and low carbon ferritic steel (BCC), by increasing the strain level for the second pass, where it is rotated by 90° . Texture formation by cross rolling gets symmetrized with increase in strain value and becomes highest, when the amount of strain in both the

direction becomes equal. Symmetrization of the texture forms two more new axes of symmetry. With further increase in strain value, the symmetry of texture get reduced and start to form textures with characteristic same as that formed when rolled in one direction, i.e., the effect of cross rolling disappears. Due to the different slip system, the obtained rolling textures were different from each other. The ideal texture components which were observed for straight rolling of copper are S, C, B, and G, whereas for cross rolling, the B component becomes stable and the others are absent. Similarly for ferritic steel, straight rolling produces components like RW, A, Y, and Z, whereas in cross rolling, except component A all other components remain stable, but with different intensities. The authors also studied the plastic anisotropy parameter for cross-rolled plate. For copper, cross rolling makes the material more isotropic as the normal anisotropy approaches 1 and planar anisotropy reduces from 0.54 to 0.3 which is beneficial for deep drawing. But for ferritic steel, cross rolling causes increase in anisotropy which was due to the formation of α - fiber texture.

2.3.1.2 Hexagonal Close Packed Materials

A few literature is available on the study on texture development for HCP structure materials, as a function of rolling mode, as compared to BCC and FCC structure materials. Texture development in these materials depends on the c/a ratio; and commonly observed textures are R-type and T-type. Magnesium, which has a HCP structure and normally forms basal texture in rolling, is difficult to be deformed plastically as the resolve shear stress value is basically zero in the basal plane [26, 27]. It also has a high anisotropy as compared to aluminum. Al-Samman and Goststein [28], demonstrated for AZ31 magnesium alloy with initial basal texture, formation of basal texture in rolling was independent of the path of deformation (CR & UR), but cross rolling can reduce the strength of the developed basal texture. In cross rolling, due to continuous change in rolling direction, the samples obtained have lesser internal misorientation than that obtained in unidirectional rolling. They also concluded that, for high reduction per pass, cross rolling gives high surface quality and greater rollability, whereas for unidirectional rolling with the same reduction per pass surface cracks are observed. Li et al. [30] also observed same kind of results for ME20 magnesium alloy. The intensity ratio of the basal and non-basal textures reduced in cross rolling, and thus enhances the formability of the sheet. Cross rolling gives rise to sheets of finer microstructure but of lower yield strength, which is due to the weaker texture where basal poles get scattered from ND. Plastic anisotropy also got improved by CR. Xing-pin et al. [29] did experimental investigation on AZ31 magnesium alloy by rotating the plate by 90° after every five passes, with intermediate heating. For this rolling schedule, cross rolling gives symmetric but high intensity basal texture. Cross-rolling produces magnesium sheets with high and more uniform yield strength and percentage elongation; whereas for unidirectional rolling, the material shows high anisotropy with reasonably different percentage elongation, in all three principle directions. The difference in percentage elongation, for

unidirectional rolling, is basically due to the distribution of basal poles which are much closer to RD than TD. Xiong et al. [31] investigated the effect of cross rolling for Mg 0.6 wt% Zr sheet and compared with that of unidirectional. In both the modes of deformation, Schmid factor has higher value along RD but gradually reduces toward TD. This gives lower yield strength along RD. The other reported results are of similar kind to that of observed by other researchers for different Mg alloys.

Gurao et al. [32] studied texture evolution for metastable β titanium alloy using unidirectional and multistep cross rolling, with a constant true strain/pass. Along with different mode of rolling, they did recrystallization and aging of the rolled sample to study all types of texture evolution, viz. deformation texture, recrystallization texture, and transformation texture. Premkumar et al. [33] did experimental study on different sequences of rolling, including unidirectional rolling and different cross rolling, on multifunctional β titanium alloy (HCP) and reported the resulting texture as well as yield locus anisotropy. The developed textures were represented by two fiber textures; viz. α and γ . With the increase in rolling reduction, the intensities of γ fiber for all modes of rolling, i.e., two-step, multistep, and clock rolling, decrease. The intensity distribution is also not the same for all the cases. The authors conducted tensile as well as compression tests to get the yield loci of the rolled samples. Obtained anisotropy is minimum for clock rolling, whereas, it is maximum for multistep cross rolling. Moreover, the type of deformation texture components formed by rolling may remain the same but the intensities and distribution of these components get changed, in cross rolling, due to the rotation of the plate and these variations are functions of amount reduction per pass and the cross rolling sequences.

2.3.2 Prediction of Cross Rolling Texture

One of the earliest available researches on this field is by Wierzbowski in 1979 [34]. He predicted the texture of FCC and BCC materials during cross rolling as well as under compression, by using Sachs model and Taylor model. Both the models gave a close prediction to experimental results. He found that, due to cross rolling some new orientation, like $\{001\}\langle 100 \rangle$ orientation, was introduced for FCC material, as this was not observed for simple rolling; and the predicted textures were highly symmetric. Yeung and Duggan [21] studied the texture development due to cross rolling in α brass. They used the program written by Dillamore [35] with a slip system of $\{111\}\langle 110 \rangle$ for the FCC material, as used in Taylor-Bishop-Hill theory. The simulated result shows the stability of $\{110\}\langle 223 \rangle$ component in cross rolling, whereas, the same component was unstable for straight rolling. Stability of the component was studied by plotting Euler angles for different rolling strains. Liu and Houthe [36] implemented full constraint and relaxed constraint Taylor-Bishop-Hill models to predict the deformation texture developed by cross-cold rolling, as well as by simple cold rolling, for molybdenum sheet. The considered slip systems were $\{110\}\langle 111 \rangle$ and $\{112\}\langle 111 \rangle$, for the BCC structure material. For cross rolling, in

order to get the input texture, the texture of previous pass was taken with respect to a new sample frame, obtained by rotating the sample reference frame about ND by 90° . In relaxed constraint model, they have considered different version of Taylor model, viz. the lath model, the Pancake model, and the three relaxations models [37] and found that Pancake model gave much more accurate result than the other models; whereas, for lower % reduction, the effect of cross rolling was not significant for full constrained model.

Suwas and Singh [38] used the relaxed constraint Taylor model to predict the texture obtained by a two-step cross rolling and unidirectional rolling for Cu alloys. The predicted results show instability of β fiber due to cross rolling. In case of cross rolling, texture intensity does not depend too much on % reduction per pass. This has been reported earlier by Al-samman and Gottestien [28]. They considered full constraint Taylor model with ratios of critical resolved shear stress as 1:38:50 (basal: prismatic: pyramidal) and simulated the rolling texture for both unidirectional and cross-rolling operations of magnesium alloy, with different reductions per pass. They compared results for both the modes of rolling, by plotting intensity of formed texture with respect to reduction per pass, and demonstrated that as compared to unidirectional rolling, cross rolling has low intensity texture and also does not depend on reduction per pass. The said model for texture prediction does not accommodate microstructure part like recrystallization, recovery, etc., due to which there is a difference between computed and experimental results as well. For cross rolling, the input texture was taken by changing the strain tensor of previous path; whereas for unidirectional rolling, it was taken without any change. Wronski et al. [10] predicted cross rolling as well as unidirectional rolling textures for low carbon steel and copper, by considering a deformation model with the interaction between grain and its surrounding as elasto-plastic. The plastic stress and strain at grain level were correlated to that of sample. Plastic deformation was initiated by slip, at planes where the values of shear stresses cross the critical resolved shear stress value. Slip systems considered were $\{111\}\langle 110 \rangle$ for copper and $\{110\}\langle 111 \rangle$ for steel. The model also considers hardening during deformation which is due to the interactions of slip systems. Stability of the texture components was also examined by the deformation model. Gurao et al. 2011 [4] used viscoplastic self-consistent formulation to study texture development by different modes of rolling for copper and nickel. A rate-dependent viscoplastic law, which correlates strain rate in grain to grain stress, was used.

2.4 Case Study

A case study for cross rolling on AISI 304 stainless steel is presented in this chapter. For better understanding, cross rolling is compared with the unidirectional rolling. The effect of change in direction is a function of percentage reduction per pass and the sequences in which the rolling is carried out. This case study is done for a three-pass rolling with equal amount of reduction in each pass.

2.4.1 Rolling

Samples were heated to the required temperature in the muffle furnace and the hot rolling was carried out on a 2-HI reverse rolling mill of capacity 75 ton. A total of 50 % reduction has been achieved in three passes. After rolling, the samples were left for air cooling. Experimental details and rolling schedule, used for the current study, is shown in Table 2.3 and Fig. 2.9, respectively. Figure 2.10 shows the 2-HI rolling mill and the samples obtained after rolling.

2.4.2 Tensile Test

2.4.2.1 Strength

Tensile specimens of 25 mm gauge length (ASTM E8 sub size specimen) were cut from the rolled sample in three different directions, as shown in Fig. 2.11a, and tested at room temperature in Universal Testing Machine (INSTRON 8862) with a cross-head velocity of 1 mm/min (Fig. 2.11b). Two samples from each direction were tested; one for determination of tensile properties and the other for determination of anisotropy parameter.

Table 2.3 Experimental details

Sample		Work-roll		Pass	
Material	304 SS	Speed	10 m/min	Number of pass	3
Initial thickness	12 mm	Diameter	320 mm	Reduction/Pass	2 mm
Initial temperature	1100 °C	Length	300 mm		

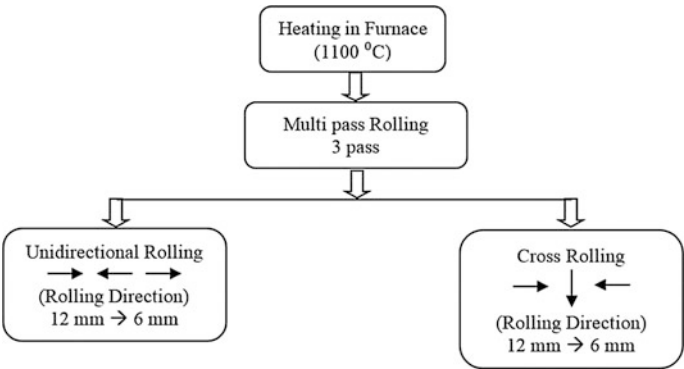


Fig. 2.9 Rolling schedule

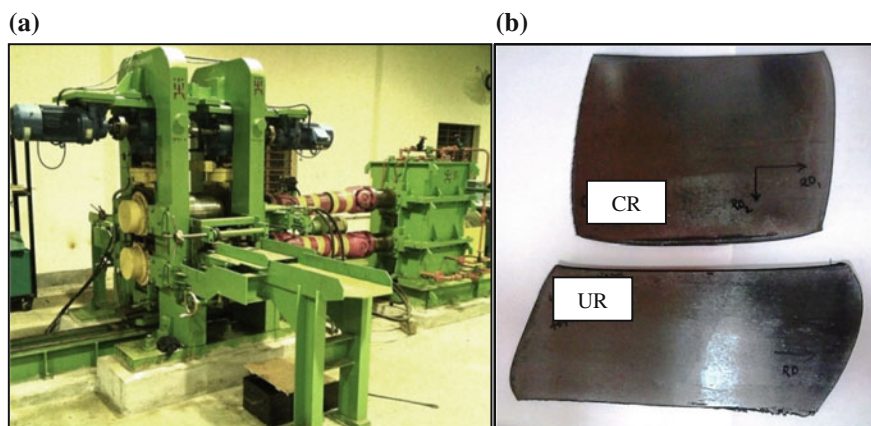


Fig. 2.10 a 2-HI Rolling mill and b Rolled samples

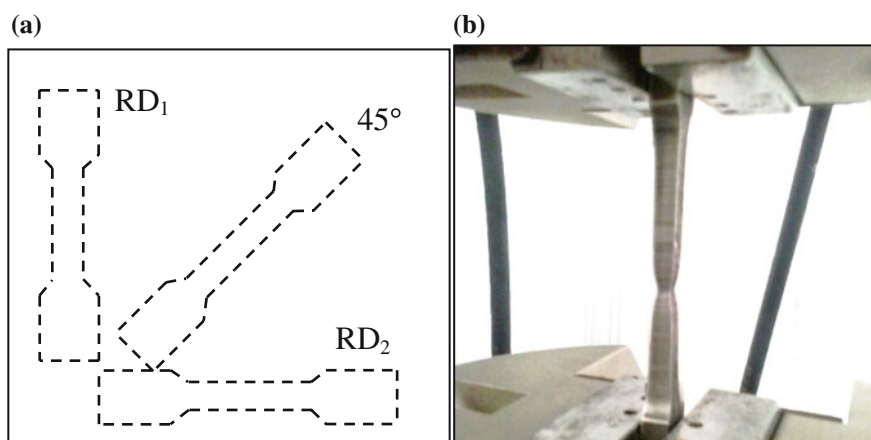
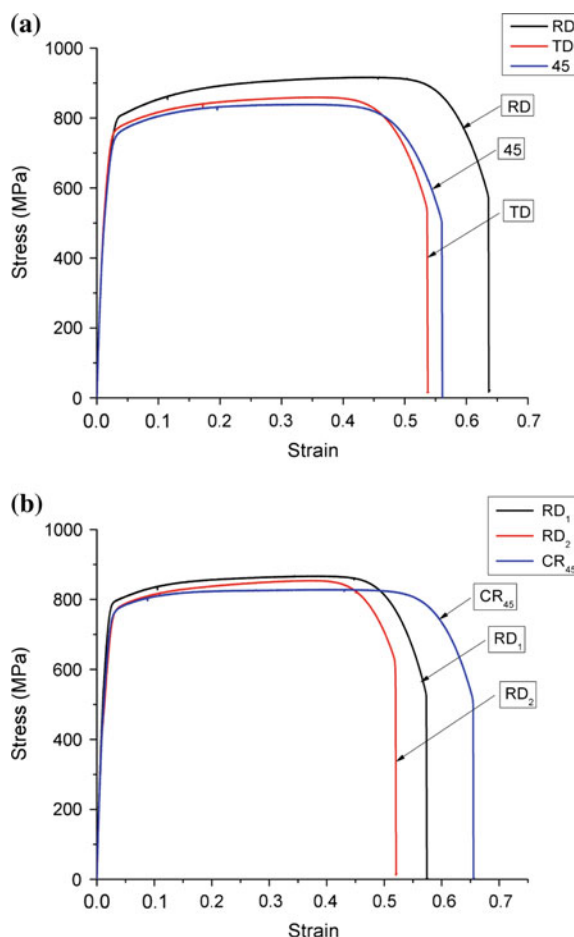


Fig. 2.11 a Tensile sample orientation and b Sample during testing on INSTRON

For Cross Rolling (CR), RD_1 = Rolling Direction (RD) of Unidirectional Rolling (UR), and RD_2 = Transverse Direction (TD) of Unidirectional Rolling.

Figure 2.12a, b show the Stress–Strain (engineering) plot for UR and CR. The results of the tensile tests are summarized in Tables 2.4, 2.5. By changing the rolling direction UTS reduces (in RD direction) from 916 MPa, as in unidirectional rolling, to 867 MPa. But it increases the % elongation along 45° direction from 56 to 65 %. In brief, it can be mentioned that cross rolling produces a plate with more isotropic properties in different directions as compared to unidirectional rolling.

Fig. 2.12 Stress–Strain (engineering) curve
a Unidirectional rolling and
b Cross rolling



2.4.2.2 Anisotropy

To find out plastic anisotropy parameter, uniaxial tensile tests were conducted on samples of 25 mm gauge length. Loading on the samples was stopped, as the elongation value reached to 20 %. Table 2.6 shows the values of average anisotropy parameter and planar anisotropy for CR and UR. Cross rolling increased the value of \bar{R} from 0.78 to 0.85, and also the absolute value of planar anisotropy decreased from 0.12 to 0.06. This result indicates that cross-rolling reduces plastic anisotropy of the rolled sample.

Table 2.4 Yield strength and ultimate tensile strength

Direction	Unidirectional rolling		Cross rolling	
	UTS (MPa)	YS (MPa)	UTS (MPa)	YS (MPa)
RD	916	427	867	502
45°	839	442	828	431
TD	860	518	854	432

Table 2.5 Percentage elongation

Direction	Unidirectional rolling		Cross rolling	
	TE (%)	UE (%)	TE (%)	UE (%)
RD	63	44	57	34
45°	56	32	65	43
TD	53	35	52	38

TE: Total Elongation, UE: Uniform Elongation

Table 2.6 Plastic anisotropy

Plastic anisotropy	Cross rolling	Unidirectional rolling
\bar{R}	0.85375	0.78625
ΔR	0.0695	-0.1275

2.5 Conclusion

Change in the direction of rolling during rolling is not a new process and it has been studied for many decades. However, it is only in the last two decades that extensive research work has been done in this area and thanks to the development of new technologies to detect and analyze the texture of a material very critically. Still, there are many areas which need to be explored further so that the application of cross-rolled material can be extended to a much wider field. An in-depth study of the correlation among microstructure, texture, and material properties is obviously required for successful commercial exploitation of the process. Moreover, the application of cross rolling to different alloys as well as composites can be studied in future.

References

1. Shahani AR, Setayeshi S, Nodamaie SA, Asadi MA, Rezaie S (2009) Prediction of influence parameters on the hot rolling process using finite element method and neural network. *J Mater Process Technol* 209(4):1920–1935
2. Bocker A, Klein H, Bunge HJ (1990) Development of cross-rolling textures in ARMCO-IRON. *Textures Microstruct* 12:103–123

3. Schmitt JH, Aernoudt E, Baudelet B (1985) Yield loci for polycrystalline metals without texture. *Mater Sci Eng* 75:13–20
4. Gurao NPP, Sethuraman S, Suwas S (2011) Effect of strain path change on the evolution of texture and microstructure during rolling of copper and nickel. *Mater Sci Eng A* 528(25–26):7739–7750
5. Suwas S, Gurao NP (2014) Development of microstructures and textures by cross rolling. *Compr Mater Process* 3(30):81–107
6. Bocker A, Klein H, Bunge HJ (1990) Development of cross-rolling textures in AlMn1. *Textures Microstruct* 12:155–174
7. Bohler-Uddeholm U.S.A. <http://www.bucorp.com/index.htm>. Accessed 12 Mar 2015
8. Davenport SB, Higginson RL (2000) Strain path effects under hot working: an introduction. *J Mater Process Technol* 98:267–291, Feb 1998
9. Kocks UF, Tome CN, Wenk HR (1998) Texture and anisotropy
10. Wronski S, Wrobel M, Baczmanski A, Wierzbanski K (2013) Effects of cross-rolling on residual stress, texture and plastic anisotropy in f. c. c. and b. c. c. metals. *Mater Charact* 77:116–126
11. Suwas S, Ray RK (2014) Crystallographic Texture of Materials. Springer, New York, p 260
12. Engler O, Randle V (2010) Introduction to texture analysis. CRC Press, Florida p 490
13. Bunge HJ, Morris PR (1982) Texture Analysis in Materials Science. Butterworths, London p 602
14. Roe RJ (1965) Description of crystallite orientation in polycrystalline materials. III. General solution to pole figure inversion. *J Appl Phys* 36(1965):2024–2031
15. Williams RO (1968) Analytical methods for representing complex textures by biaxial pole figures. *J Appl Phys* 39(1968):4329–4335
16. Rollett AD (2014) Texture, microstructure & anisotropy. <http://neon.mems.cmu.edu/rollett/27750/27750.html>. Accessed 23 Mar 2015
17. Cullity BD (1957) Elements of X-ray diffraction. Addison Wesley Publishing Company, London p 514
18. Custers JFH, Riemersma JC (1946) The textures of straight-rolled and of cross-rolled molybdenum. *Phys XII* 4:195–208
19. Merlini A, Beck PA (1953) Study of the origin of cube texture. *Acta Metall* 1:598–606
20. Wassermann G, Grewen J (1962) Texturen metallischer Werkstoffe. Springer, Heidelberg, p 808
21. Yeung WY, Duggan BJ (1986) Texture and structure development in cross-rolled α brass. *Acta Met* 34(4):653–660
22. Vanderschueren D, Kestens L, Van Houtte P, Aernoudt E, Dilewijns J, Meers U (1991) The effect of cross rolling on texture and magnetic properties of non oriented electrical steels. *Textures Microstruct* 14–18:921–926
23. Oertel C, Hünsche I, Skrotzki W, Lorch A, Knabl W, Resch J, Trenkwalder T (2010) Influence of cross rolling and heat treatment on texture and forming properties of molybdenum sheets. *Int J Refract Met Hard Mater* 28(6):722–727
24. Liu W, Kong X, Chen M, Li J, Yuan H, Yang Q (2009) Texture development in a pseudo cross-rolled AA 3105 aluminum alloy. *Mater Sci Eng A* 516(1–2):263–269
25. Liu W, Li X, Meng X (2009) Effect of pseudo cross-rolling on the recrystallization texture of a continuous cast Al–Mg alloy. *Scr Mater* 60(9):768–771
26. Mondal C, Singh AK, Mukhopadhyay AK, Chattopadhyay K (2013) Effects of different modes of hot cross-rolling in 7010 aluminum alloy: Part I. Evolution of microstructure and texture. *Metall Mater Trans A* 44(6):2746–2763
27. Mondal C, Singh AK, Mukhopadhyay AK, Chattopadhyay K (2011) Formation of a single, rotated-Brass {110} $\langle 5\ 5\ 6 \rangle$ texture by hot cross-rolling of an Al–Zn–Mg–Cu–Zr alloy. *Scr Mater* 64(5):446–449
28. Al-Samman T, Gottstein G (2008) Influence of strain path change on the rolling behavior of twin roll cast magnesium alloy. *Scr Mater* 59(7):760–763

29. Xing-pin C, Du S, Rui X, Guang-jie H, Qing L (2010) Influence of rolling ways on microstructure and anisotropy of AZ31 alloy sheet. *Trans Nonferrous Met Soc China* 20: s589–s593
30. Li X, Al-Samman T, Gottstein G (2011) Mechanical properties and anisotropy of ME20 magnesium sheet produced by unidirectional and cross rolling. *Mater Des* 32(8–9):4385–4393
31. Xiong J, Chen Z, Yi L, Hu S, Chen T, Liu C (2014) Microstructure and mechanical properties of annealed Mg–0.6 wt % Zr sheets by unidirectional and cross rolling. *Mater Sci Eng A* 590:60–65
32. Gurao NP, Ali AA, Suwas S (2000) Study of texture evolution in metastable β -Ti alloy as a function of strain path and its effect on α transformation texture. *Mater Sci Eng A* 504 (1–2):24–35
33. Premkumar M, Himabindu VS, Banumathy S, Bhattacharjee A, Singh AK (2012) Effect of mode of deformation by rolling on texture evolution and yield locus anisotropy in a multifunctional β titanium alloy. *Mater Sci Eng A* 552:15–23
34. Wierzbanski K (1979) Numerical prediction of cross rolling and compression textures. *Scr Mater* 13:1117–1120
35. Dillamore IL, Roberts WT (1965) Preferred orientation in wrought and annealed metals. *Metall Rev* 10(39):271–380
36. Liu YS, Van Houtte P (2001) Simulation of deformation textures in cold-rolled molybdenum sheets by the taylor–bishop–hill theory. *Int J Refract Met Hard Mater* 19(3):209–216
37. Van Houtte P (1982) On the equivalence of the relaxed taylor theory and the bishop–hill theory for partially constrained plastic deformation of crystals. *Mater Sci Eng* 55:69–77
38. Suwas S, Singh AK (2003) Role of strain path change in texture development. *Mater Sci Eng A* 356(1–2):368–371

Chapter 3

Finite Element Method in Machining Processes: A Review

Carlos H. Lauro, Lincoln C. Brandão, Sergio L.M. Ribeiro Filho,
Robertt A.F. Valente and J. Paulo Davim

Abstract An ecological production and low cost is the target of several industries. Increasingly, the product development is critical stage to obtain a great quality and fair price. This stage will define shapes and parameters that will able to reduce wastes and improve the product. However, the expense of prototypes also should be reduced, because, in general, the prototypes are more expensive that final product. The use of finite element method (FEM) can avoid much tests that reduce number of prototypes, and consequently the project cost. In the machining processes simulation, several cutting conditions can be reproduced to define the best tool and parameters in function of analyzed forces, stress, damages and others. This paper debates the use of FEM in the machining processes, shows some researches and indicates the main attributes to develop simulation studies for conventional machining and micromachining.

C.H. Lauro (✉) · R.A.F. Valente · J. Paulo Davim
Department of Mechanical Engineering, University of Aveiro, Campus Santiago,
3810-193 Aveiro, Portugal
e-mail: carlos.lauro@ua.pt

R.A.F. Valente
e-mail: robertt@ua.pt

J. Paulo Davim
e-mail: pdavim@ua.pt

L.C. Brandão · S.L.M. Ribeiro Filho
Department of Mechanical Engineering, Federal University of São João del-Rei,
Praça Frei Orlando 170, Centro, São João del-Rei 36307-352, Brazil
e-mail: lincoln@ufsj.edu.br

S.L.M. Ribeiro Filho
e-mail: sergiolmrf@gmail.com

© Springer International Publishing Switzerland 2015
J.P. Davim (ed.), *Modern Manufacturing Engineering*, Materials Forming,
Machining and Tribology, DOI 10.1007/978-3-319-20152-8_3

65

3.1 Introduction

The development of products with highest quality and lower cost are goals of many industries. New techniques to inspect and control the products are employed attempting to achieve these goals. However, the first step to reach these goals should happen still in the project conception. The materials, machines, tools, workers and others factors should be tightly defined, qualified and quantified avoiding damages, rework and wastes. Thus, the usage of computer means to concept the best shapes, material, manufacture process and others is commonly used in the industries as well as academic research, sport competition and others.

Engineering enables to find several softwares with this purpose. There are CAD's software that allow optimize the amount of material and check the interferences of components. However, among the computer mean applied in the mechanical engineering, the numerical simulation is the most widely applied to obtain specific characteristic in the components or devices. This technique is used to define dimensions, shapes, material and others variables on the single component (such as shaft, nut, bolt and others) or in complex equipment (such as aircraft, space shuttles, F1 cars and others).

The finite element method (FEM) is a numerical simulation technique, which when used presents an advantage of decreasing the number of produced prototypes. This technique allows eliminating prototypes that would be produced to analyze phenomena resultant of several manufacture processes and their respective parameters to chosen the better conditions. Liu and Zheng [1], used the 2D analysis in their investigation about composite used in vessels for hydrogen storage (aluminium liner and carbon fibre/epoxy composite layers). After simulation, they used a high-pressure pump to fill the vessels and observed the finite element results were in good agreement with the experimental values. In their investigation, Silva et al. [2] have used the FEM to evaluate the effect of the elastic properties variation on auxetics geometries. They studied eight geometries using FEM to select the two extremes conditions to validation.

According to Özel and Altan [3], FEM is developed for large deformation processes, such as metal cutting process that has been considered as a deformation process where the deformation is highly concentrated in a small zone. It is used to predict chip flow, cutting forces and especially the temperatures in the tool and the cutting stress during various machining conditions.

Thus, the FEM can be advantageous in the machining processes. The FEM helps to define parameter that can increase the tool life, improve the residual stresses and others. The objective of this section is to present the usage of the FEM in machining processes studies. Furthermore, this section indicates the attributes and modelling that are important to obtain great results of machining processes simulations.

3.2 Finite Element Method in Machining

A simple engineering problem involves several variables (sometime ignored or not observed) that complicate the reproduction of responses. Thus, the repeating same event will not result in obtaining the same measured values, which rarely will occurs. According to Fish and Belytschko [4], engineering phenomenon can be represented by partial differential equations, although these equations can be very difficult to solve by analytical methods.

The solution is by creating a numeric technique that is based on the study of Richard Courant, in 1943, who used triangular elements with variational principles to solve vibration problems, which some investigators claim to be the discovered this technical. In the 1950s, this technique was employed in the aerospace industry (Boeing, Bell Aerospace and Rolls Royce). In the 1960s, this technic was called "Finite Element" and E. Wilson developed one of the first finite element programs, limited to two-dimensional stress analysis that was widely used [4].

Shaw [5] affirmed that it was not viable until digital computers and suitable software became available in the 1960s due to the simultaneous solution of a large number of equations. According to Childs et al. [6], the studies applying FEM in chip formation began with Zienkiewicz and with Kakino, both in 1971, that simulated the loading of a tool against a pre-formed chip. However, it presented a number of limitations, such as disregard of the friction between the chip and tool, strain rate, temperature, the variations of material flow stress and its purposed the shape of the chip. These limitations were removed in 1976 by Shirakashi and Usui that included chip/tool friction conditions, the temperature and material flow stress variations with strain, strain rate and temperature, thus it was possible to keep computational advantages in the simulation during chip formation and the influence of tool. In the 1980s, arose the first non-steady chip formation analysis and following the development of a chip formation with a first contact between the cutting edge and the work piece, similar to real conditions. In the 1990s, the non-steady analysis from transient to discontinuous chip formation and the first three-dimensional analysis and the introduction of adaptive meshing techniques particularly to cope with flow around the cutting edge of a tool was developed.

The FEM is a suitable alternative to reduce the long time and high cost in machining experimental. Furthermore, the experimental tests are valid alone in the condition tested and they depend on the precision of the equipment used [7]. Arrazola et al. [8] emphasize the need for continued fundamental modelling efforts. They affirmed that the prediction models have continued to make significant progress, but its end goal is to predict industry-relevant outcomes to improve the productivity. These models include cutting parameters (tool geometry, workpiece and tool materials) to calculate intermediary fundamental physical variables and obtain machining performance outcomes, such as tool life modelling. However, while input variables appear to remain unchanged, process outcomes can still change drastically.

Table 3.1 Some machining researches using finite element method

Researcher	Software	Process	Material
Zanger and Schulze [14]	Abaqus TM	Turning	Ti-6Al-4V titanium alloy
Dandekar et al. [15]	AdvantEdge TM	Turning	Ti-6Al-4V titanium alloy
Muhammad et al. [16]	MSC-MARC TM	Turning	Ti15V3Cr3Al3Sn titanium alloy
Maranhão and Davim [17]	AdvantEdge TM	Turning	AISI 316
Amini et al. [13]	MSC-MARC TM	Turning	Inconel 738
	ANSYS TM		7075 aluminium alloy, AISI 1045
John et al. [18]	DEFORM TM	Turning	AISI 1020
Lauro et al. [19]	ANSYS TM	Drilling	AISI H13
Isbilar and Ghassemieh [20]	Abaqus TM	Drilling	Ti-6Al-4V titanium alloy
Schulze et al. [21]	Abaqus TM	Broaching	SAE 5120

The cutting metal process simulation is a useful technique to extend the tool life prevising the temperature and stress in the tool [9]. Elbestawi et al. [10] also affirmed the usage of the FEM to understand the tool wear. Stenberg and Proudian [11] studied the residual stresses in the turning using 2D simulations because the simulations are relatively lower in calculation cost and it is fastest than 3D simulations.

Different packages have different capabilities and it is critical to select the package with the appropriate feature set to perform type of analysis with quality of the results. The results are influenced by the assumptions and solver techniques used in the package [12]. Amini et al. [13] used two different packages software in their investigation. A package was employed to analyze the process where the tool is considered to vibrate with an ultrasonic frequency and other package to model the horn and cutting tool. In the literature, it is possible to find many publications that report a various machining process simulation using different softwares, dimensions and others aspects, see Table 3.1.

Machining simulation has the advantage to predict thermal and mechanical behaviour of both material and tool, without spending time and money with experimental procedures that can improve productivity and reduced costs. However, it requires a great understanding of how the input data affect the prediction. The reason is that the reliability in the machining simulation is ensured by accuracy of the input values [22]. The input parameters cover the mechanical and the thermal properties of the workpiece, the cutting tool geometry, cutting speed, mesh definition and other, [23]. Astakhov and Outeiro [7] affirmed that the usage of FEM in process of chip removal presents several difficulties, mainly the high processing time, but it can result in a reliability of 95 %.

Ali et al. [24] analyzed the research review that used several software on the machining simulation of Ti-6Al-4V titanium alloy. They observed that machining process of Ti-6Al-4V titanium alloy is in agreement with the simulation values of

FEM. According to the authors, the accuracy based on the most of researchers between the experimental data and simulation showed results with more than 90 %.

John et al. [18] applied the FEM to study the effect on the surface roughness of the AISI 1020 using single-point tool (HSS) and insert tool (CNMA WC). They compared the FEM results with experimental tests, analyzing the influence of feed rate [deviation between 7.5 and 18.9 % (HSS) and 1.46 and 8.3 % (CNMA WC)], depth of cut [deviation between 3.74 and 18.5 % (HSS) and 2.9 and 4.9 % (CNMA WC)], cutting speed [deviation between 1.5 and 11.8 % (HSS) and 2.9 and 4.9 % (CNMA WC)] and tool geometry.

The comparison between FEM and experimental results in the turning of AISI 316 study, Maranhão and Davim [17] observed a difference in the cutting force (7.0, 12.6 and 8.9 %), feed force (15.4, 13.5 and 13.5 %), cutting power (2.5, 13.2 and 10.1 %), maximum cutting temperature (19.6, 24.4 and 24.6 %) and plastic strain (15.0, 19.9 and 1.3 %) when the feed rate was varied (0.05, 0.1 and 0.2 mm/rev).

However, the FEM has most relevant criticisms involve material characterization (strain, strain rate, material hardness and temperature) and machining data (friction data at the tool–workpiece interface, chip formation and heat transfer conditions) that influence the effectiveness of the results [25]. Doman et al. [26] researched in the literature the usage of FEM in the grinding process to model approaches at the macro- and micro-scales. They found models still based on the modelling approach that is thermal structural with triangular heat flux, normal pressure and tangential stress inputs. The effect of coolant by convection cooling boundary conditions and constitutive material model employed was the thermo-elastoplastic type. However, they sustain the experimental tests to validate the results, because without broader validation these results and their applicability may be limited.

3.2.1 FEM Types

According to Özel and Zeren [27], the types of analyses in the FEM modelling of deformation processes can be described as Eulerian analysis, it is fixed in space, and Lagrangian analysis, the computational grid deforms with the material.

Benson and Okazawa [28] affirmed that Eulerian analysis is effective for the machining calculations, except the simplest formulations, because its mesh is fixed in space, eliminating the element distortion problems that can generate new free surfaces without a special algorithm. Furthermore, this analysis avoids a special algorithm because it can generate new free surfaces naturally. However, the problem proved not to be a sensitive benchmark calculation for evaluating the accuracy of the contact methods.

Carroll and Strenkowski [29] cited that the mainly advantages are that no explicit material failure criterion is required and that the elements cannot become overly distorted. This approach requires boundaries of the chip-free surface known in advance or adjusted interactively during the simulation and it eliminates the lengthy

transition to steady-state cutting and the need for an explicit material failure or separation criterion. However, an obvious drawback of neglecting workpiece's elasticity is that residual stresses cannot be predicted with the model. The model based on an Eulerian reference frame was developed which mesh with good elements that was defined in a control volume through which the workpiece material flowed.

The Lagrangian analysis embeds a computational mesh in the material domain and solves the position of the mesh at discrete points in time, which is relied by majority numerical models. This requires a criterion for the separation of the undeformed chip from the workpiece using several chip separation criteria. Lagrangian analysis can be utilized in the implicit technique (more applicable to solving linear static problems) and the explicit time method (more suitable for non-linear dynamic problems) [27].

The usage of implicit methods could be found in few studies in the literature. In the implicit integration, the global/structural matrices have to be formulated and inverted integration; and the whole system of differential equations has to be solved simultaneously. Besides, the implicit integration is unconditionally stable and the only limitation on Δt is the convergence of the solution, which is based on a pre-defined criterion [30].

Bäker et al. [31] decided to use an implicit method because it has a better scaling behaviour when local mesh refinement is needed. This method allows a greater range of flexible user-defined subroutines to be introduced in the simulation, with routines that can be used to implement complicated material separation criteria. Mamalis et al. [32] used the implicit method to model the precision hard cutting of AISI 52100 using the PcBN tool to analyze the cutting forces and temperatures.

In explicit method, a system of de-coupled differential equations is solved based on element-by-element basis, thus, only the elements' stiffness and mass matrices need to be formulated and inverted. The only concern is its conditional stability and the need to use very small Δt [32]. According to Coelho et al. [33], the explicit method is more suitable for events with large non-linear deformations at high strain rates and temperatures with complex contacts between surfaces, conditions typically expected in chip formation.

The application of Lagrangian or Eulerian analysis presents shortcomings, but a technique has been developed combining the best features of both analyses that succeed to a certain extent. It is known as the Arbitrary Lagrangian-Eulerian (ALE). Although this method is embedded in the finite element analysis software, it is very necessary to master the technique details, mainly to algorithms of mesh rebuilding and element variables remapping are affected by many factors [34].

Özel and Zeren [27] utilized the explicit dynamic ALE method with adaptive meshing capability and developed a simulation model for the orthogonal cutting of AISI 4340 that presented results in better predictions for machining-induced stresses, without re-meshing and without using a chip separation criterion.

3.3 Material and Tool Modelling

To obtain great results using FEM, it is necessary to assign material the desired properties using higher accuracy values. Simoneau et al. [35] affirmed that material properties used for metal cutting should be determined under situations involving large strains, high strain rates and elevated temperatures.

According to Buchkremer et al. [36], the material models can be categorized into two groups, the interaction between damage and plasticity. The machining simulations can be applied to one of several of constitutive equations to describe the material behaviour. It is essential to implement a plasticity model that describes the thermo-mechanical conditions under which the material deforms plastically, whose quality of the majority of proposed sub-models depends on the accuracy of the applied material model.

3.3.1 Johnson–Cook Model

In the FEM models of cutting an essential and desired attribute, the material model should satisfactorily represent elastic, plastic and thermo-mechanical behaviour. Based on this, the deformations on work material were observed and highlighted have great importance in the accurate flow stress models to represent work material constitutive behaviour under high strain rate deformation conditions [27]. The authors used a Johnson–Cook (J–C) model, Eq. 3.1, to define the flow stress in the machining of AISI 4340 steel in annealed condition simulation. One of first usage of this model was published by Johnson and Cook [37]. They develop a cumulative-damage fracture model to determine the characteristics of OFHC copper, Armco iron and 4340 steel, which was observed a very dependent trend on the state of hydrostatic pressure, and less dependent on the strain rate and temperature.

$$\bar{\sigma} = \underbrace{[A + B \cdot \varepsilon^n]}_{\text{Elasto-Plastic term}} \cdot \underbrace{\left[1 + C \cdot \ln\left(\frac{\dot{\varepsilon}}{\dot{\varepsilon}_0}\right)\right]}_{\text{Viscosity term}} \cdot \underbrace{\left[1 - \left(\frac{T - T_{\text{room}}}{T_{\text{melt}} - T_{\text{room}}}\right)^m\right]}_{\text{Thermal softening term}} \quad (3.1)$$

where

$A \leftrightarrow$ yield stress of the material under reference deformation conditions (MPa)

$B \leftrightarrow$ strain hardening constant (MPa)

$n \leftrightarrow$ strain hardening coefficient

$C \leftrightarrow$ strain rate strengthening coefficient

$m \leftrightarrow$ thermal softening coefficient

$T \leftrightarrow$ deformation temperature

$T_{\text{room}} \leftrightarrow$ room temperature

$T_{\text{melt}} \leftrightarrow$ melting temperature of the material

$\dot{\varepsilon}_0 \leftrightarrow$ reference strain rate (1/s)

$\dot{\varepsilon} \leftrightarrow$ equivalent plastic strain normalized with a reference strain rate

$\varepsilon \leftrightarrow$ plastic equivalent strain

According to Dandekar and Shin [38], the Johnson–Cook model, that has been used in many studies, is based on experimentally determined flow stresses as a function of strain, temperature and strain rate in separate multiplicative terms. Sartkulvanich et al. [39] present two equations that were modified from J–C model. The first modified model takes the blue brittleness effect in low carbon steel into account, Eq. 3.2, and the second model is used for materials that do not exhibit blue brittleness, Eq. 3.3. The authors affirmed that these models assume to have no effect of coupling and reduce the problem of non-uniqueness. Furthermore, a small number of parameters are preferred for reducing computational time and promoting computational robustness. The parameter ‘A’ is disregarded due to no initial stress assumption used in Oxley’s theory.

$$\bar{\sigma} = B \cdot \varepsilon^n \cdot \left[1 + C \cdot \ln\left(\frac{\dot{\varepsilon}}{\dot{\varepsilon}_0}\right) \right] \cdot \left[\left(\frac{T - T_{\text{room}}}{T_{\text{melt}} - T_{\text{room}}} \right) + a \cdot e^{-0.00005 \cdot (T - 700)^2} \right] \quad (3.2)$$

$$\bar{\sigma} = B \cdot \varepsilon^n \cdot \left[1 + C \cdot \ln\left(\frac{\dot{\varepsilon}}{\dot{\varepsilon}_0}\right) \right] \cdot \left[1 - \left(\frac{T - T_{\text{room}}}{T_{\text{melt}} - T_{\text{room}}} \right)^m \right] \quad (3.3)$$

Besides usage of elastic, plastic and thermo-mechanical behaviour modelling, it is necessary to assign a damage model. Chen et al. [40] used an energy-based ductile failure criterion to simulate HSM of Ti-6Al-4V titanium alloy. According to Ambati and Yuan [41], the damage modelling in orthogonal cutting has significant importance because the most part of the failure occurs due to thermal softening and to form the chip. It should be detached from the workpiece material to which fracture criterion should be applied. The Johnson–Cook damage criterion, Eq. 3.4, is found in the literature used by several researches. Duan and Zhang [42] cited that the damage parameters can be uniquely determined independent of the cutting conditions and its usage as criterion for chip separation in HSM can avoid the problems in the simulations using other criteria.

$$\bar{\varepsilon}_f = \left[D_1 + D_2 \cdot e^{(D_3 \cdot \frac{p}{\sigma_e})} \right] \cdot \left[1 + D_4 \cdot \ln\left(\frac{\dot{\varepsilon}^p}{\dot{\varepsilon}_0^p}\right) \right] \cdot \left[1 + D_5 \cdot \left(\frac{T - T_{\text{room}}}{T_{\text{Melt}} - T_{\text{room}}} \right) \right] \quad (3.4)$$

where

$D_1 \leftrightarrow$ Initial failure strain

$D_2 \leftrightarrow$ Exponential factor

$D_3 \leftrightarrow$ Triaxiality factor

$D_4 \leftrightarrow$ Strain rate factor

$D_5 \leftrightarrow$ Temperature factor

$T \leftrightarrow$ deformation temperature

$T_{\text{room}} \leftrightarrow$ room temperature

$T_{\text{melt}} \leftrightarrow$ melting temperature of the material

$\bar{\epsilon}_f \leftrightarrow$ failure plastic strain for damage initiation

$\dot{\epsilon}^p \leftrightarrow$ equivalent plastic strain rate

$\dot{\epsilon}^0 \leftrightarrow$ plastic strain rate

$\frac{p}{\sigma_e} \leftrightarrow$ ratio between hydrostatic pressure to equivalent stress

Shrot and Bäker [43] proposed a method for inverse determination of J–C constants using the chip morphology and the cutting force encountered during the high-speed cutting process. They found an optimal parameter set returned by the simulation produces results which are indistinguishable from the results produced by the original set, although it is possible to re-identify J–C parameters by inverse methods and the existence of noise in the error function poses a hurdle in re-identifying the original J–C constants.

Umbrello et al. [44] investigated the influence of the constants used in the J–C model on the forces, temperatures, chip morphology and residual stresses in the machined components of AISI 316L steel, comparing with experimental data. They applied five different sets where two sets were used with high strain rate mechanical. The tests were carried out on hat-shaped specimens applying the Split Hopkinson's Pressure Bar (SHPB) method. Moreover, instrumented orthogonal milling tests were carried out to generate information about material flow stress in machining based on different analytical chip formation models. One set identified using SHPB tests that were carried on cylindrical compression specimens. One set based on SHPB experiments using hat-shaped specimens and the last one set determined using a methodology based on analytical modelling of the orthogonal cutting process along with metal cutting experiments.

Yan et al. [45] studied an approach to characterize the stress response of workpiece in hard machining of AISI H13 die steel (30–60 HR_C). They presented a methodology expressed by coupling the reference flow stress curve at the certain workpiece hardness that taken an advantage of the form of the Johnson–Cook model, incorporating strain, strain rate and thermal softening effects. This isotropic thermal-elastic-plastic model, which considers the influence of the workpiece hardness on the flow stresses, is showed by the Eq. 3.5.

$$\bar{\sigma} = [A + B \cdot \epsilon^n + C \cdot \ln(\epsilon_0 + \epsilon) + D] \cdot \left[\left(1 + E \cdot \ln\left(\frac{\dot{\epsilon}}{\dot{\epsilon}_0}\right) \right) - \left(1 - \left(\frac{T - T_{\text{room}}}{T_{\text{melt}} - T_{\text{room}}} \right)^m \right) \right] \quad (3.5)$$

where the C and D are the function of the initial workpiece hardness accounted for the influence of hardness, which are determined by Eqs. 3.6 and 3.7, respectively. The E is the strain rate strengthening coefficient (C in the Eq. 3.1). The ϵ_0 is the reference strain and is taken to be 10^{-3} . The other variables are described in the Eq. 3.1.

$$C = 0.0576 \cdot (HR_C)^2 - 3.7861 \cdot (HR_C) + 52.82 \text{ (MPa)} \quad (3.6)$$

$$D = 0.6311 \cdot (HR_C)^2 - 12.752 \cdot (HR_C) - 727.5 \text{ (MPa)} \quad (3.7)$$

3.3.2 Zerilli–Armstrong Model

The Zerilli–Armstrong (Z–A) model was developed for relatively simple materials where the dislocation slip in several kind of crystal structures was considered. This formulation considers slip based on dislocation physics, which can describe the flow stress as appropriate for the Johnson–Cook model. The Z–A not take into account the damage induced by secondary phase particles due to be a failure mechanism based solely on the constitutive law. The comparison between the Z–A and J–C models for the AISI D2 steel and observed that the Z–A showed a more accurate estimate for higher temperature range and is less accurate for low temperatures [46].

According to Liu et al. [47], the Z–A model is derived from the thermal activation theory of dislocations and widely used for analyzing the dynamic response of metals over a range of temperatures and strain rates. The authors affirmed that there are two physical sources of flow softening at high strains. The first is due to the material failure in the shear band because of the void and crack formation, which depends on both strain and the strain rate. The second is due to the dynamic recovery, which causes flow softening at high strains and is captured by the square root term in the Z–A model.

Moćko and Kowalewski [48] cited that Z–A model compared to J–C model is that reflects the coupled influence for both temperature/strain and strain rate/temperature on the mechanical characteristics. In the X4CrMnN16-12 austenitic steel modelling, they observed that the Z–A model gave the worst results related to a phase transformation during plastic deformation process.

Zerilli and Armstrong [49] presents a description of stress components that combine to determine the plastic flow stresses showing two separate reasonably explicit expressions for their constitutive behaviour. One is for the body-centred cubic material (bcc), where the temperature softening and strain-rate hardening depends on “ u ” and are higher with the increase of strain hardening, as can be seen in Eq. (3.8). The other is face-centred cubic (fcc), which exhibits dependencies uncoupled of the strain hardening factor from the strain-rate hardening, thermal softening and the grain size, according to Eq. (3.9). The authors also showed a model where the thermal activation stress and the effect of yield stress on grain size are considered due to the requirement of slip band-stress concentrations at grain boundaries being needed for the transmission of plastic flow between the polycrystal grains.

$$\sigma_{th} = C_1 \cdot e^{-C_3 \cdot T + C_4 \cdot T \cdot \ln \dot{\epsilon}} \quad (3.8)$$

$$\sigma_{th} = C_2 \cdot \epsilon^{1/2} \cdot e^{-C_3 \cdot T + C_4 \cdot T \cdot \ln \dot{\epsilon}} \quad (3.9)$$

where

$\sigma_{th} \leftrightarrow$ thermal component of the shear stress

C_1, C_2, C_3 and $C_4 \leftrightarrow$ undetermined coefficients

$T \leftrightarrow$ current temperature minus reference temperatures

$\dot{\epsilon} \leftrightarrow$ being the strain rate

3.3.3 Others Models

Buchkremer et al. [36] presented in their paper the modified Bai-Wierzbicki (MBW) material model to simulate the longitudinal turning processes with steel AISI 1045. The MBW model integrates a damage variable into the yield potential for the description of material degradation. The MBW model shows great potential to predict the softening behaviour of the material and the damage approach enables the prediction of possible failure behaviours like serrated chip formation or chip breakage. Furthermore, it is further extended with the consideration of temperature and strain rate effects, whose influences are significant in machining. The validation tests showed that the chip formation, cutting temperatures, and mainly, the cutting forces were in close agreement with each other.

Besides J-C and Z-A models, the Rusinek and Klepaczko (RK) model, Eq. (3.10) can be much more precise description of the mechanical properties variation of materials, in question, particularly under dynamic loads. This model decomposes the equivalent stress into internal stress, effective stress and viscous-drag stress. In addition, the model considers the effective stress and it presented coupled relationships between strain rate and temperature. The use of the RK model showed best results [48].

$$\bar{\sigma}(\bar{\epsilon}_p, \dot{\bar{\epsilon}}_p, T) = \frac{E(T)}{E_0} [\sigma_\mu(\bar{\epsilon}_p, \dot{\bar{\epsilon}}_p, T) + \sigma^*(\dot{\bar{\epsilon}}_p, T)] + \bar{\sigma}_{vs}(\dot{\bar{\epsilon}}_p) \quad (3.10)$$

where

$\bar{\sigma}(\bar{\epsilon}_p, \dot{\bar{\epsilon}}_p, T) \leftrightarrow$ overall flow stress

$\sigma_\mu(\bar{\epsilon}_p, \dot{\bar{\epsilon}}_p, T) \leftrightarrow$ internal stress component

$\sigma^*(\dot{\bar{\epsilon}}_p, T) \leftrightarrow$ effective stress component

$\bar{\sigma}_{vs}(\dot{\bar{\epsilon}}_p) \leftrightarrow$ drag stress component

$E(T) \leftrightarrow$ temperature dependence of the Young's modulus

$E_0 \leftrightarrow$ Young's modulus at $T = 0$ K,

$T \leftrightarrow$ temperature

$\dot{\bar{\epsilon}}_p \leftrightarrow$ strain rate

$\bar{\epsilon}_p \leftrightarrow$ inelastic strain

3.3.4 Tool

Generally, the tools are not applied in complex model to characterize the material. In some studies, the tool material is defined by thermal and/or mechanical properties. Tang et al. [50] considered the thermal (thermal conductivity, thermal expansion, specific heat capacity) and mechanical properties (Young's modulus, Poisson's ratio, density, tensile strength) properties to cBN tool. Fathipour, Hamed and Yousefi [51] used only density and Young's modulus to characterize the tool. Santiuste et al. [52], Shrot and Bäker [43], Manikandan et al. [53] considered the tool as rigid body, which is not applied to the properties. Based on this, the results obtained by these preliminary studies show that more researches about tool modelling should be developed to complete the total understanding about machining process using finite element methods.

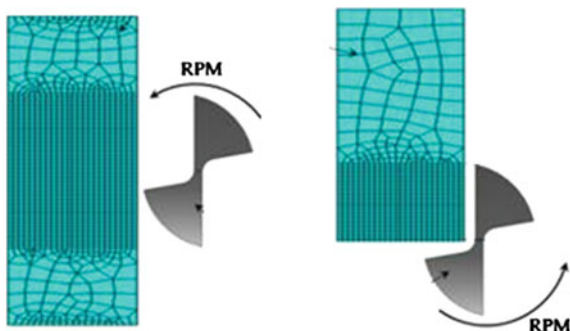
3.4 Meshing and Re-meshing

The definition of meshing requires great caution, because of the element type and element size interference in the results and also due to computational effort. Ambati and Yuan [41] emphasized that numerical simulations are verified with measured cutting force that is insensitive to the element size. In their work, they studied the chip formation from computational simulation analyzing the effect of element size that leads to a direct modification in failure criterion. They observed that the finite element size changes chip morphology significantly and a failure model can transform the chip from continuous to segment. Furthermore, the dependence on element size can be eliminated by a simple non-local damage model based on characteristic element length, generating a unique solution of cutting chip if the temperature can be neglected.

To model the turning process of Ti-6Al-4V titanium alloy, Dandekar et al. [15] used an updated-Lagrangian FEM along with continuous re-meshing. They adopted tetrahedral finite elements, 4-node and 12 degree of freedom and the minimum element edge length for the chip bulk of 0.0198 mm, cutter edge of 0.01 mm and the radius of refined region was set as 0.075 mm. Santiuste et al. [52] used a medium element size at this zone, and this size was 5 μm in the orthogonal cutting of glass and carbon fibre composites developed with plane stress, quadrilateral, linearly interpolated, elements, with reduced integration and automatic hourglass control.

Shrot and Bäker [43] used a plane strain elements with 4-node bilinear and reduced integration applying the hourglass control to simulate orthogonal cutting of AISI 52100. Zanger and Schulze [14] defined the coupled temperature-displacement using plane strain elements with 4-node bilinear displacement and temperature to simulate the cutting of Ti-6Al-4V titanium alloy. Seshadri et al. [54] modelled the workpiece (6 mm \times 2 mm) using of iso-parametric quadrilateral element type with size of 0.057 mm, 4,680 nodes and 4,500 elements.

Fig. 3.1 Example of workpiece meshing (Adapted from [56], with permission from Springer)



According to Bäker et al. [31], the simulation has to meet the following requirements as usage of quadrilateral elements (as regular as possible, avoiding extremely distorted meshes); high mesh density in the shear zone; discontinuous deformation (segmentation) of the chip; convergence of the implicit algorithm; and usage of standard software for portability and flexibility.

It is known that a refined meshing will improve the results, but it will need high investments in computer and time. Many researchers use the deformation section a meshing more refined than the workpiece rest, it decrease the elements number and the simulation time, Fig. 3.1. Kouadri et al. [55] defined a coupled displacement–temperature four nodes element with minimum element, sized about $10\text{ }\mu\text{m}$, in the chip zone that was chosen after mesh convergence tests and a compromise between result accuracy and reasonable CPU time.

The cutting simulation presents an additional degree of complexity due to need of a proper modelling of both large plastic deformations. This should be considered from the mathematical point of view and because it cause rapid solution degradation due to element distortion and material removal. In spite of a problem be tackled using pre-distorted meshes, this technique was essential to obtain reliable numerical solutions, thus it was adapted of adaptive re-meshing techniques, which encompass three main aspects: Meshing techniques, Error and distortion metrics guiding the re-meshing, and Data transfer from old to new mesh [57]. Schulze et al. [58] considered the high mesh deformations in the material separation zone to simulate the broaching process, however, as example, it can be commented that the separation of the material lead to a loss of information due to the deletion of element or nodes.

Saffar et al. [59] affirmed that the meshing nodes are moved to more favourable positions to improve mesh distortion. The solution-dependent meshing is supplied to concentrate mesh towards with the developing boundary concave, aiming the chip separation area approximately in the cutting edge with generating local mesh refinement in this area. Furthermore, the authors cited that the mesh is adaptively designed to create a new spatial discrimination and the mesh quality is improved: *h*-adaptively, *p*-adaptively and *r*-adaptively.

According to Vaz et al. [57], the *h*-adaptivity consists of changing the element size *h* that can be used to generate well-shaped elements. The new mesh has a

Table 3.2 Comparison of re-meshing methods [57]

Methods	Advantages	Disadvantages
General <i>h</i> -method	The most general and flexible method	Requires more elaborate algorithms
Hierarchical <i>h</i> -method	Fast method. Easy to implement for regular mesh	Difficult to implement for irregular mesh. Will not reduce element distortion
<i>r</i> -Method	Easy to implement. Inexpensive	Limited capacity to improve mesh
<i>p</i> -Method	Fast and simple	The degree in the shape functions cannot be increased too much so the improvement is limited. Cannot reduce element distortion

different number of elements and the connectivity of the nodes is changed. The authors also highlighted the hierarchical *h*-method, which is a hierarchy between old and new elements and the approach. The *r*-adaptivity consists of relocation of the nodes without changing the mesh connectivity, which is called smoothing when used to improve the shape of elements. In the *p*-adaptivity, the degree of the interpolating polynomials is changed in order to increase the accuracy of the solution. A comparison of these methods is presented in the Table 3.2.

3.5 Boundary Conditions

The boundary conditions can be defined in two types, the first was a mechanical condition applied on the bottom face of the workpiece fixed in the feed and cutting directions. The second showed a condition where the cutting speed is applied to the rigid tool and a thermal condition with initial configuration an initial temperature that considered the workpiece–tool couple. Both conditions were considered during the chip formation at the tool–workpiece contact zone [55]. These authors also neglected heat exchange with the environment to obtain a significant heat exchange with environment that can influence the chip formation process due to the simulated cutting duration is very short, few microseconds.

Vaz et al. [57] highlighted the great importance of contact due to the important effects associated with the tool–chip interface, which is commonly solved by penalty approach, such as method of Lagrangian multipliers or a combination of penalty and Lagrangian multiplier methods. The latter is as in the augmented Lagrangian technique, with the aim of retaining the merits of each approach. Saffar et al. [59] highlighted the high stresses, high strain rates and high temperatures can cause a high mechanical power which is dissipated in the tool–chip interface leading to many structural modifications of the contacting pieces. Thus, there is no law for universal contact which can predict friction forces among a wide range of cutting conditions.

In their study of the cutting modelling, Malakizadi et al. [60] assumed that the workpiece material was a rigid-perfectly plastic. The tool was considered a rigid

body, where the heat transfer within the tool was allowed. Beyond the heat transfer coefficient between the tool and chip interface was assumed to be $10^5 \text{ N/s}\cdot\text{mm}\cdot\text{C}$ to ensure that the heat transfer reaches steady-state condition at the end of the simulations.

3.5.1 Chip Separation

Saffar et al. [59] affirmed that the chip formation occurs due to chip separation (geometrical and physical) criterion and model realization. The geometry of chip separation occurs when the distance between the nearest workpiece's node on the moving path of the cutting edge and the cutting edge is equal to or smaller than this given distance value. For the physical criteria, the magnitude of distribution of shear stress, effective stress or effective plastic strain has a major effect on mesh distortion together with the value of maximum shear stress, and the effective stress in the machined surface. According these authors, the model realization is related to the software applied and there are several methods in a finite element mesh, as:

- Element removal: when the physical criterion is reached, the material failure happens and the element carries no stress any more as if it does not exist. Such elements can be removed and will not be displayed.
- Node debond: the chip and the workpiece are two separated parts. They are perfectly bonded together through some pair of nodes along the prospective parting line.
- Node splitting: the front of cutting edge separates the element and creates new nodes at this region. Through the further movement of the cutting tool, the two elements move in different directions and lose contact.
- Mesh adaptively: Chip separation is performed by mesh refinement in the separation zone by increasing the number of elements or relocation of the nodes.

For Vaz et al. [57], the chip formation can be reproduced in continuous, discontinuous and intermediate forms that follow three basic strategies: continuous chip separation along a pre-defined cutting plane; chip separation and breakage; no chip separation. They mentioned that most common approach predefines a chip separation line (or plane), along which a separation indicator is computed. Also, they highlighted several chip separation as Nodal distance, Equivalent plastic strain, Energy density, Tensile plastic work, Stress index, Maximum principal stress, Johnson–Cook, Damage considerations and others.

Özel and Zeren [27] affirmed that the FEM models should not require chip separation criteria that highly deteriorate the physical process simulation around the tool cutting edge, especially in the presence of dominant tool edge geometry. Duan and Zhang [42] suggest the use of Johnson–Cook models for chip separation and the modified Zorev model for tool-chip friction description to predict precisely the serrated chip formation and cutting force in HSM.

In their paper, Chen et al. [40] analyzed the variations of chip morphology with cutting speeds and feed rates in the HSM of Ti-6Al-4V titanium alloy, which observed that the dimensions of segment chip morphology increase with feed rate and the degree of segmentation is more obvious under higher cutting speeds. Pu et al. [61] used the chip morphology to calibre their numeric tests that showed a differences range from 10 to 20 % to the experimental results.

3.6 Friction

Besides the material characterization, another aspect that is important in the cutting simulation is determining the friction coefficient. According to Isbilir and Ghassemieh [20], the contact and the friction parameters between the tool and workpiece are influenced by the cutting speed, feed rate, geometry and the surface properties. Özel and Zeren [27] emphasized that the interfacial friction characteristics on the tool/chip and tool/work contacts should be modelled with high accuracy in order to account for additional heat generation and stress developments due to friction.

Arrazola and Özel [62] studied the importance of detailed friction model to improve the results. They observed differences between predicted and experimental forces when comparing the forces between the Coulomb friction and the sticking-sliding friction reveals important findings. It exhibited the influence is larger over the thrust force since it decreases by 35 %, while the cutting force decreases only by 11 %. In the literature it is possible to find several models to determine the friction coefficient. The usage of the Coulomb's law is employed to determine the friction coefficient. Coulomb's law was generally used in the sliding region that is located next to the sticking region up until the point where the chip leaves the tool, Eq. (3.11). The relatively low normal stresses and small plastic deformation, friction behaviour in this region is characterized by the real area of contact. Thus, the frictional stress can be assumed to be dependent of the normal stress. The shear stress decreases from a constant value at the sticking region to zero at the location where the chip leaves from the tool rake face.

$$\tau = \mu \cdot \sigma_n \quad (3.11)$$

where

$\tau \leftrightarrow$ frictional stress

$\mu \leftrightarrow$ coefficient of friction

$\sigma_n \leftrightarrow$ normal stress

According to Isbilir and Ghassemieh [20] Coulomb friction model is used and a constant friction coefficient of 0.5 is used in the analysis. Maranhão and Davim [17] simulated the turning of AISI 316 using a cemented carbide tool with a chip breaker and coating of TiCN-Al₂O₃-TiN. They applied the Coulomb model, Eq. (3.12), to provide a first approach to the friction value (0.89, 0.80 and 0.53) and time later,

they needed several iterations must be carried until the results are satisfactory (1.1, 1.0 and 0.95). The authors justified this correction due to a change of friction coefficient is a fast and reliable way to minimize differences between experimentation and simulation. Besides, the software did not allow a change of Johnson–Cook coefficients, which could allow a disagreement between numerical and analytical results due to the critical friction coefficient.

$$\mu = \frac{F_T + F_c \cdot \tan \gamma}{F_c - F_T \cdot \tan \gamma} \quad (3.12)$$

where

$F_T \leftrightarrow$ thrust (feed) force

$F_c \leftrightarrow$ cutting force

$\gamma \leftrightarrow$ tool rake angle

Özel [63] cited that in the first simulations, the friction in the metal cutting was largely ignored or assumed to be constant based on Coulomb's law at the entire tool–chip interface. Many researchers utilized Zorev's model in simulations of orthogonal cutting. They studied the influence of implementing different friction models in the simulation for orthogonal cutting of low-carbon free-cutting steel with P20 carbide cutting tool by comparing the output variables (cutting force, thrust force, chip-tool contact length, shear angle and maximum temperature at tool–chip interface) to experimental results. These comparisons showed that the friction models had a significant influence in predicting chip geometry, forces, stresses on the tool and the temperatures at the tool–chip interface. The predictions are clearly found to be most accurate when utilizing friction models based on the measured normal and frictional stresses on the tool rake face and when implemented as variable.

According to Manikandan et al. [53], the friction condition is an important factor that influences the chip formation, cutting load and surface finish quality. They used the combination of the Coulomb's friction model and shear (sticking) friction model, Eq. (3.13).

$$\tau = \begin{cases} \mu\sigma & \tau < k \\ k & \tau \geq k \end{cases} \quad (3.13)$$

where

$\tau \leftrightarrow$ surface friction stress

$\mu \leftrightarrow$ friction coefficient

$k \leftrightarrow$ surface normal stress and shear flow stress

Duan and Zhang [42] proposed the modified Zorev's model to describe the chip-tool friction, which was used to analyze the friction influence related to the tool rake angle with an inverse relation. According to Haddag et al. [64], the contact zone a part of the heat flux q is generated by friction that can be written as the sum of inelastic work heat flux due and friction work heat flux. They applied the Eq. (3.14)

to evaluate the heat flux generated by friction at the contact interface. In the orthogonal cutting of Al 2024-T351 aluminium alloy, applying a cutting speed of 60 m/min, feed of 0.4 mm/rev and depth of cut of 0.5 mm, they assumed that the frictional work converts into heat (η_f) was 1. The fraction of the thermal energy conducted into the chip (f_f), which depends on the thermal properties of the tool and workpiece material as well as the temperature gradient near the chip/tool interface was 0.5.

$$\dot{q}_f = f_f \cdot n_f \cdot \tau \cdot \dot{\gamma} \quad (3.14)$$

where

$\dot{q}_f \leftrightarrow$ friction work heat flux

$f_f \leftrightarrow$ fraction of the thermal energy conducted into the chip

$\eta_f \leftrightarrow$ frictional work conversion factor

$\tau \leftrightarrow$ friction stress given by Eq. (3.10)

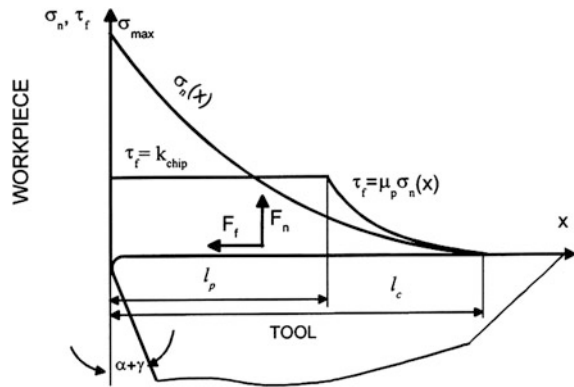
$\dot{\gamma} \leftrightarrow$ slip rate

Knowing that the friction is an important aspect in machining processes (experimental or modelling), especially during dry condition, Ulutan and Özel [65] developed a new methodology to determine tool friction on orthogonal cutting of Ti-6Al-4V titanium and IN-100 nickel-based alloys using uncoated tungsten carbide (WC/Co) tool. In this study, they considered unworn and worn tool geometry. They observed that the friction coefficients did not depend on most of the cutting parameters in machining titanium and nickel-based alloys and slightly with cutting edge geometry.

According to Özel and Altan [66], the friction conditions at the chip–tool contact can be interpreted in terms by shear friction and friction coefficient, Fig. 3.2. They used an appropriate initial value for the friction coefficient ($\mu_{p,initial}$) selecting as the ratio of the frictional force (F_f) and normal force (F_n) acting on the tool rake face that were calculated from the measured force components at the given rake angle.

Malakizadi et al. [60] developed a subroutine to include pressure dependencies on shear friction model at chip/tool interface using the Eq. (3.15). They affirmed

Fig. 3.2 The normal and frictional stress distributions (Adapted from [66], with permission from Elsevier)



that, for the aluminium alloy and Grey Cast Iron, the constants of the model, α (0.012 and 0.0035) and m_0 (1), were kept constant.

$$\tau = m_0 \cdot [1 - \exp(\alpha \cdot P)] \cdot k \quad (3.15)$$

where

$\tau \leftrightarrow$ frictional shear stress

$K \leftrightarrow$ shear strength of the workpiece material

$P \leftrightarrow$ pressure

m_0 and $\alpha \leftrightarrow$ model constants.

Muhammad et al. [16] affirmed that the effect of friction on the tool–workpiece interface is accounted for its effect on the cutting forces. They used a modified shear friction model to adequately represent the friction behaviour at the tool–workpiece interface, Eq. (3.16).

$$\sigma_{fr} \leq -m_{fr} \cdot \frac{\bar{\sigma}}{\sqrt{3}} \cdot \frac{2}{\pi} \cdot \text{sgn}(V_r) \cdot \arctan\left(\frac{V_r}{V_{cr}}\right) \quad (3.16)$$

where

$\sigma_{fr} \leftrightarrow$ friction stress

$\bar{\sigma} \leftrightarrow$ equivalent stress

$V_r \leftrightarrow$ relative sliding velocity

$V_{cr} \leftrightarrow$ critical sliding velocity

$m_{fr} \leftrightarrow$ friction coefficient

$\text{sgn}(x) \leftrightarrow$ signum function of x

According to Özel [67], the constant friction models may not represent the sophisticated contact conditions that exist in the 3D engagement of the micro-geometry tool edge and the workpiece. The friction zones are also difficult to be implemented in 3D problems. According to the literature, it can be found several friction values to different machining processes types. Coelho et al. [33] cited that the FEM software used does not allow the shear stress limit to vary, therefore, the value of 329 MPa was set, using the initial equivalent stress of 950 MPa and an average friction coefficient of 0.60 and suggests to uncoated PcBN a coefficient of 0.35.

Rotella et al. [68] compared the experimental and numeric results of turning of Al 7075-T651 aluminium alloy that showed differences between the values, especially for the radial force. These differences can be justified by use of 3D FEM model that has still problem as friction models. These models were well tested in orthogonal machining, but in the 3D model have taken into account the influence of tool geometry parameters (tool nose radius, angles, etc.), as well as the grain size.

In the composite cutting, although the friction model between workpiece and tool is required, an accurate value remains an issue for several reasons [69]. To simplify the process, Mahdi and Zhang [70] ignored friction in the orthogonal cutting of the fibre-reinforced composite. Phadnis et al. [71] considered the 0.03 the friction coefficient at the interface between cutting edge and laminate in the

Table 3.3 Same values of friction coefficient using in machining researches

Researcher	Tool material	Workpiece material	vc (m/min)	Feed ($\mu\text{m}/\text{rev}$)	Depth (mm)	Friction
<i>Turning</i>						
Özel and Altan [66]	Uncoated carbide	AISI P20 (30 HR _C)	200, 300 and 550	51, 75, 100	1	0.5–0.7
				25		1
Seshadri et al. [54]	WC-Co/TiAlN	2024-T351 aluminium alloy	66, 102, 157	102, 205, 318	1	0.43
Kouadri et al. [55]	WC-Co	2024-T351 aluminium alloy	30–500	50, 300	4	0.2
<i>Milling</i>						
					ap	ae
Saffar et al. [59]	HSS ($\phi 6$ mm)	AISI 1045	47.12	ago/40	4–7.5	2.5
	HSS ($\phi 3$ mm)		23.56	ago/50	1.5–5	1.5
<i>Drilling</i>						
				f (mm/min)	Diameter	
Isbilar and Ghassemieh [20]		Ti-6Al-4V	35.2	95–171	8 mm	0.5
<i>Broaching</i>						
Schulze et al. [21]		SAE 5120	30, 60, 90	40 μm		0.35, 0.50

ultrasonically assisted drilling of CFRP composite. To model the drilling on CFRP composite, Phadnis et al. [72] used a coefficient of friction of 0.3. Santiuste et al. [52] assumed a constant coefficient of friction equal to 0.5 in the orthogonal cutting of glass and carbon fibre reinforced polymer composite. In the orthogonal cutting of metal matrix composite (MMC), Al 6061 aluminium alloy reinforced with silicon carbide particles, Pramanik et al. [73] employed a coefficient of friction of 0.62. The Table 3.3 shows the friction values applied in some machining researches.

3.7 Examples of Employments

The cutting metal simulation is commonly employed to predict the phenomena and events in the machining. One of reasons to this is the facility to measure machining phenomena. Arrazola and Özel [62] affirmed that it is very costly and difficult to

measure stresses and temperatures in high-speed machining using experimental tests. Umbrello et al. [44] cited that the good agreement obtained between the experimental and numerical results indicate that the proposed FEM model appears to be suitable for studying the influence of cutting parameters on residual stress. Manikandan et al. [53] used orthogonal cutting to analyze plane strain-coupled thermo-mechanical.

To understand the influence of cutting speed and feed conditions in the built-up edge (BUE) formation in machining carbon steels based, Childs [74] analyzed flow stress in the absence of failure depending of the strain, strain-rate and temperature. The modelling and simulations confirm the importance of the blue-brittle effect for BUE formation in steel machining. In the agreement between predicted and experimental BUE speed ranges it was necessary to reduce the temperature for maximum blue-brittle effect from the expected 600 to 400 °C and a need for more data on or understanding of ductile shear failure of steels in the compressive (pressure from 0 to 0.75 of flow stress) and temperature (up to 600 °C) conditions of chip formation in BUE conditions.

Buchkremer et al. [36] highlight that the cutting force is the integral representations of the calculated flow stresses in the primary shear zone, showed excellent results for a broad range of cutting conditions.

The usage of FEM to resolve machining operation is generally applied due to it involves intense thermo-mechanical phenomena. Each material point in the cutting tool and the workpiece should satisfy simultaneously the Mechanical (3.17) and Thermal (3.18) equilibrium equations that are strongly coupled, since the stress tensor (σ), in the mechanical equilibrium equation, depends on the temperature variable (T). Furthermore, a part of the mechanical inelastic work transforms to heat, so a part of the heat flux q is a function of the flow stress and the plastic strain [64].

$$\text{div } \sigma + f_v = p\ddot{u} \quad (3.17)$$

where

$\sigma \leftrightarrow$ Cauchy stress tensor

$f_v \leftrightarrow$ body forces

$\ddot{u} \leftrightarrow$ acceleration

$$k\nabla^2 T - \rho \cdot c_p \cdot \dot{T} + \dot{q} = 0 \quad (3.18)$$

where

$k \leftrightarrow$ thermal conductivity

$T \leftrightarrow$ temperature

$\rho \leftrightarrow$ material density

$c_p \leftrightarrow$ thermal capacity

$q \leftrightarrow$ heat flux

Weinert and Schneider [75] affirmed that FEM has proven to be advantageous for describing the thermal and thermo-mechanical stress and can establish a direct link between the thermal stress and the application properties of the tool during grinding. The use of FEM in cutting processes are emerging as useful techniques for predicting tool temperatures and stresses and for extending tool life [9].

According to Rizzuti et al. [25], besides the 2D model, the few milliseconds of cutting time are one of the main problem in temperature modelling because there are several problems related to heat generation and diffusion into the tool. In fact, no steady-state conditions are reached during the numerical simulation.

Rotella et al. [68] studied the effects of cutting speed and tool geometry on the grain size evolution in the turning of Al 7075-T651 aluminium alloy. After the calibration to determine the frictions values (m and μ), they applied a subroutine to predict the dynamic recrystallization process by Zener–Hollomon equation and the hardness modification using the Hall–Petch equation. This proposal provided a good prediction of the microstructural alteration that was affected by cutting speed and the tool nose radius.

Pu et al. [61] used a 2D model to predict grain size in turning of AZ31B magnesium alloy on the dry and cryogenic cooling system. They developed a subroutine applying the Zener–Hollomon equation that showed a successfully predicted the grain refinement on the surface and sub-surface.

Duan et al. [76] used the FEM simulation to study the thickness of white layer based on phase transformation mechanism. They analyzed the effects of mechanical factors on transition temperature were taken into account explicitly. They observed an influence of cutting parameters on the thickness of white layer, i.e. the thickness of white layer varies significantly with the variations of cutting speed, depth of cut, flank wear and chamfer geometry of tool.

Attanasio et al. [77] used numeric (2D and 3D) and experimental tests to study the formation of layers on the orthogonal hard turning of AISI 52100. They found that the thickness of white and dark layers increases with increasing of tool flank wear and higher cutting speed generates thicker white layers and thinner dark layers. A small feed rate increases the white layers thickness; on the other hand, the high feed rate decreases the dark layer thickness.

Ramesh and Melkote [78] used the FEM to study the white layer formation in orthogonal machining of AISI 52100 (62 HRC) using the cBN tool. They used a model explicitly incorporates the effects of stress and strain on the transformation temperature, volume expansion and transformation plasticity that showed predicted values and trends of white layer thickness. These effects are in good agreement with the measured values and trends when compared to experimental validation.

Sometime, many investigators using the FEM to study the residual stress behaviour on the machining processes. Thus, for example, Ee et al. [79] used a 2D model to study the residual stresses induced by orthogonal machining. Valiorgue et al. [80] used a 3D model to study the residual stresses in finish turning of AISI 304L stainless steel with a TiN coated carbide tool. They proposed a model that does not simulate the chip formation and the material separation around the cutting

edge, but only onto the thermo-mechanical loadings applied onto the machined surface.

Rizzuti et al. [25] affirmed that the residual stresses are generated by the material deformation and by the thermal cycle and both phenomena occur during the cutting process. The components of the residual stresses can be the axial and the circumferential. They measured the circumferential stress using the numerical procedure of orthogonal cutting of AISI 1045, which observed agreement was obtained between the numerical predicted residual stresses and those experimentally measured.

Özel and Zeren [27] used the FEM to study machining with round edge cutting tools in the HSM of AISI 4340 and they compared with experimentally measured residual stresses obtained from the literature, which indicated an influence the stress and temperature fields greatly. These predictions combined with the temperature field predictions are highly essential to further predict surface integrity and thermo-mechanical deformation related property alteration on the microstructure of the machined surfaces.

Ji et al. [81] modelled the orthogonal cutting of TC4 alloy applying MQL effects and they analyzed the heat transfer coefficient that are all considered in the residual stress prediction model. Their model gives a relationship between the flow rate of oil and the average residual stresses. They observed that the increasing the flow rate of oil, the lubricant film thickness and the heat transfer coefficient increase, while the friction coefficient decreases.

3.8 FEM in Micromachining

In some case, to predict the temperature in the tool–chip interface, for example, the use of FEM in machining studies is widely recommended. It is more applied in the micromachining studies due to the smaller dimensions that may complicate the observation of events during the metal cutting. However, while the investigation using FEM in the conventional machining is increasing in the last times; the investigation using FEM in the micromachining is still modest. A search in the Engineering Village database using the word “Finite Element” AND “machining OR milling OR turning or drilling” limited to “Subject/Title/Abstract” was presented an average value of 22,089 publications with this matchup. Replacing the “machining OR milling OR turning OR drilling” by “micromachining OR micro-milling OR micro-turning or micro-drilling”, the result was an average of 183 publications, Fig. 3.3.

Although the micromachining processes present many researches employed experimental or numeric test, this theme has already several gaps to fill out. FEM is used in nanoscale cutting simulation to clarify the chip removal of nanoscale cutting and to re-examine the cutting process in general, that is necessary to understanding of physic of micro-cutting to develop and improve the process of ultra-precision metal cutting technology [83].

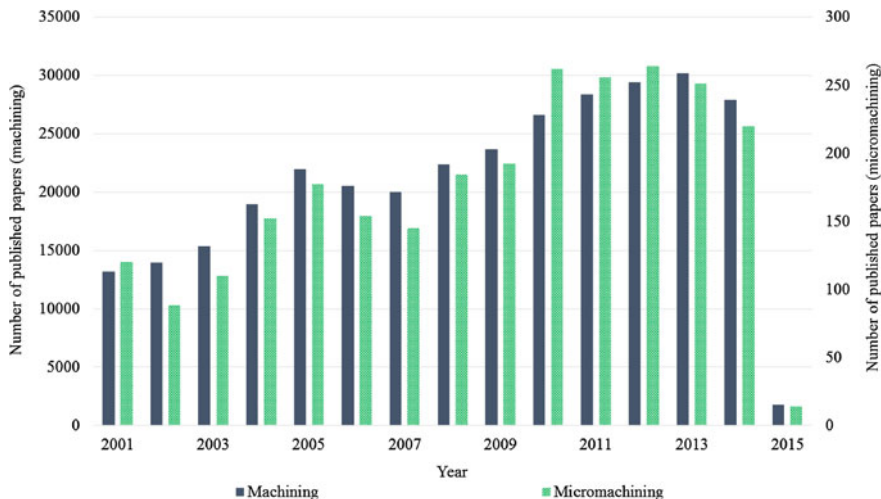


Fig. 3.3 The usage of FEM in conventional and micromachining [82]

Woon et al. [84] cited the first difficulties to simulate micromachining process using FEM, which were technically infeasible due to computing resources required are too intensive becoming this modelling did not too reliable for machining:

- the inabilities of pure Lagrangian solution to manage large element distortions without using unrealistic chip separation criteria, while pure Eulerian solution is impractical for chip formation study as prior assumptions of the chip flow and shape are required to be determined;
- the numerical methods were unable to describe severe plastic deformation in micromachining because accurate solution methods, frictional and material models were not available;
- FEM of micromachining requires large amount of elements at sub-micron to generate an extremely fine mesh to capture insightful transient behaviour of the process.

Maybe because the tool and workpiece size is smaller, some researchers choose to work with FEM. Ding et al. [85] used the FEM to observe in difficult-to-machine materials (Ti-6Al-4V, Inconel 718 and stainless steel AISI 422SS) the application of laser-assisted micro-milling that can eliminate or reduce built-up edge formation.

The micromachining processes are applied to study influence of parameters, events and/or phenomena during or after the cutting. Wang et al. [86] developed a study quantitatively of the chip formation mechanism in micro-milling of Al6061-T6 alloy with a carbide tool using a hybrid FEM analytical approach. They observed that the simulated chip morphology, segment length and cutting force matched the experimental results with acceptable error.

Chen et al. [87] used an energy density-based ductile failure model to study the temperature of tool and workpiece in the micro-cutting of 2A12-T4 aluminium

alloy. The energy density-based ductile failure material model was developed to maintain material deformation behaviour at different mesh distribution in micro-cutting simulation. Furthermore, they observed maximum relative errors between the experimental and simulated temperatures of tool tip and workpiece surface lie between 10 and 20 % under different conditions.

In the laser-assisted micro-milling (LAMM) study, Ding et al. [85] used a 3D finite volume prismatic thermal model to accurately predict the temperature distribution due the laser heating in different LAMM configurations. They also used a 2D finite element models to simulate the continuous chip formation with varying chip thickness in LAMM side cutting with the strain gradient material constitutive models. Among the results, the FE model simulations showed that LAMM could eliminate or reduce the BUE formation in micromachining of difficult-to-machine materials.

To simulate the 2-D micro-milling of Ti-6Al-4V alloy titanium model with feed rate of 4.5 $\mu\text{m}/\text{tooth}$, Özel et al. [88] considered a workpiece with the undeformed chip geometry with a mesh containing 25,000 quadrilateral elements and element size ranging from 0.1 to 3 μm and a micro-tool with a mesh containing 2,500 elements with minimum element size of 0.1 μm .

Huang and Hu [89] cited that the micro-turning process simulation can help observe events that in the experimental during micro-turning are the difficult to observe. They used a 3D model to study the single-grain ceramic influences in the forces, temperature and tool wear.

Maranhão et al. [90] studied the orthogonal cutting of the AISI 1045 with a ISO K10 tool without coating that analyzed the cutting forces, temperature, stresses and displacements. To valid the experimental, they compared the cutting force with experimental results and found an error between 1.89 and 6.18 %. In the temperature analysis, they observed the increase of temperature from 320 to 522 $^{\circ}\text{C}$ with an increase of the feed from 10 to 80 $\mu\text{m}/\text{rev}$. It can be justified as the quantity of energy needed to shear a higher material volume.

Woon et al. [84] used the FEM in micro-milling to investigate the tool edge radius effect, whose the central idea was understand the size differences between the cutting magnitude and tool edge radius rather than emphasizing solely on either one of the parameters separately. In the study of performance of uncoated and cBN coated micro-tools, Özel et al. [88] used the FEM to predict the temperatures and wear development in micromachining of Ti-6Al-4V titanium alloy.

3.8.1 MaterialModelling

The usage of FEM in machining requires much attention. The application the Johnson-Cook (JC) and Coulomb's friction models present good results [86]. However, the material can be of the same order as the grain size and cannot be treated as isotropic and homogeneous, moreover, the FE modelling of micromachining has to be taken into account the size effect [91].

Abouridouane et al. [92] used a 3D thermo-mechanically model to understand the size effects occurring in micro-drilling of AISI 1045 carbon steel. The material modelling was constituted by two-phase (ferrite-pearlite). They affirmed that the cutting process in the micro scale is very complicated and the most model developed considering the heterogeneous materials are still limited currently to two-dimensional orthogonal cut and only give a qualitative prediction of simple plane strain cutting processes.

Bajpai and Singh [93] developed a model of orthogonal machining of Pyrolytic Carbon (PyC) that was constituted by layered anisotropic material presenting errors in the prediction of cutting/thrust forces lie between 9 and 27 %. The damage model used in this paper considered the material response below the elastic limit as well as the post-failure response beyond cracking strain in the strain softening regime in tension.

Zahedi et al. [94] developed a smoothed Particle Hydrodynamic (SPH) approach, which is known as an efficient and numerically robust way for solving large-deformation problems, in modelling micro-turning of single-crystal copper. In this paper, the authors calculated the influence of the anisotropic crystallographic orientations on cutting energy. The variation of cutting energy with different crystallographic orientations can vary up to 400 % for micromachining process of crystalline copper.

According to Zahedi et al. [95], the importance of grain orientation and direction of micromachining on the overall cutting forces, chip morphology was demonstrated together with propensity of the workpiece material to generate slips when its grains undergo rotations. They observed that total difference in force for the chosen orientations was 33 %, signifying the strength of the effect of crystal orientation in micromachining process.

To study the micro-milling of AISI H13 with different hardness, Afazov et al. [96] applied the proposed method by Yan et al. [45]. They implemented into software a subroutine that needs to be defined for each integration/material point of the FE model. They observed that this methodology had been successfully developed to predict the relationship between cutting forces, uncut chip thickness and cutting velocity with material with different hardness.

3.8.2 Friction

An aspect that requires great attention is the friction coefficient that generally in the macromachining; the friction coefficient is around of 0.5. However, in the micromachining literature is possible to find a high range of friction coefficient. The Table 3.4 exhibits some values found in the literature.

Özel et al. [88] assigned on the micro-milling of Ti-6Al-4V alloy titanium with speed cutting of 75 m/min and a feed per tooth of 4.5 $\mu\text{m}/\text{tooth}$ a sliding friction contact (μ) of 0.7 for WC/Co and 0.4 for cBN coating. They perceived that the lowest temperature rise in the cBN coated WC/Co tool due to a lower friction coefficient and higher effective thermal conductivity.

Table 3.4 Friction coefficient applied in micromachining

Researcher	Process	Material	Friction
Woon et al. [84]	Orthogonal cutting	AISI 4340 steel (HRC 33)	0.1
Abouridouane et al. [92]	Drilling	AISI 1045	0.2
Moriwaki et al. [97]	Orthogonal cutting	Copper	0.7
Wang et al. [86]	Milling	Al 6061-T6 Aluminium alloy	0.7
Ding et al. [85]	Milling	Ti6Al4 V, Inconel 718, AISI 422	0.65

3.9 Remarks

The FEM can be considered a fundamental tool to develop product, mainly to define manufacturing conditions. To employ the FEM to study the machining processes can help to explain several issue through the important information about the cutting, as temperature, residual stress, force and others. Thus, although the simulation tests consume more time than experimental tests, the FEM can be considered an excellent tool to study machining processes because these tests are more inexpensive and provide more information than experimental tests.

However, the users should take care with the input and output in their tests. They should define warily the attributes, mainly the friction and the material modelling, to obtain reliable results. They also should be borne in mind that the FEM provides approximate results and the experimental results, “reals” values, can vary due to not assigned variables, as the variation of the cutting tool geometry, material porosity, variation of the material structure and others. Ashtakhov [98] affirmed that the advanced numerical methods, as FEM, are no more than a powerful tool that requires very skilful hands to handle and the computer’s apparent precision causes an unwarranted confidence in the validity of the resulting numbers. The author also highlighted that the software incorporates many not observed assumptions by the users that influence the validity of the results. This fact requires vigilance and the same visual knowledge and intuitive sense of fitness to obtain a successful computer-aided modelling.

Thus, despite computational advances and the software more friendly, FEM can be considered an excellent tool, but just another tool, to study machining processes and other engineering processes. This paper endorses the use of FEM in machining processes researches; nevertheless, it suggests that the users be wary with their results. To search similar experimental researches and confront the results, even the unwanted, can help the users have a perception of phenomenon that would improve her models.

Acknowledgments The authors would like to thank the Ministry of Education’s Coordination for the Improvement of Higher Education Personnel (CAPES). The author C.H. Lauro would like to thank Elsevier and Springer for granting permission for reuse of the published materials.

References

1. Liu PF, Zheng JY (2008) Progressive failure analysis of carbon fiber/epoxy composite laminates using continuum damage mechanics. *Mater Sci Eng A* 485:711–717. doi:[10.1016/j.msea.2008.02.023](https://doi.org/10.1016/j.msea.2008.02.023)
2. Silva TAA, Panzera TH, Brandão LC et al (2012) Preliminary investigations on auxetic structures based on recycled rubber. *Phys Status Solidi* 249:1353–1358. doi:[10.1002/pssb.201084225](https://doi.org/10.1002/pssb.201084225)
3. Özel T, Altan T (2000) Process simulation using finite element method—prediction of cutting forces, tool stresses and temperatures in high-speed flat end milling. *Int J Mach Tools Manuf* 40:713–738. doi:[10.1016/S0890-6955\(99\)00080-2](https://doi.org/10.1016/S0890-6955(99)00080-2)
4. Fish J, Belytschko T (2007) A first course in finite elements. doi:[10.1002/9780470510858](https://doi.org/10.1002/9780470510858)
5. Shaw MC (2004) Metal cutting principles, 2nd edn. Oxford University Press, New York
6. Childs THC, Maekawa K, Obikawa T, Yamane Y (2000) Metal machining theory and applications. Arnold, London
7. Astakhov VP, Outeiro JC (2008) Metal cutting mechanics finite element modelling. In: Davim JP (ed) *Machining. Fundamentals and recent advances*, 1st edn. Springer, London, pp 13–25
8. Arrazola PJ, Özel T, Umbrello D et al (2013) Recent advances in modelling of metal machining processes. *CIRP Ann Manuf Technol* 62:695–718. doi:[10.1016/j.cirp.2013.05.006](https://doi.org/10.1016/j.cirp.2013.05.006)
9. Fallböhmer P, Rodriguez CA, Özel T, Altan T (2000) High-speed machining of cast iron and alloy steels for die and mold manufacturing. *J Mater Process Technol* 98:104–115. doi:[10.1016/S0924-0136\(99\)00311-8](https://doi.org/10.1016/S0924-0136(99)00311-8)
10. Elbestawi MA, Chen L, Bezce CE, El-Wardany TI (1997) High-speed milling of dies and molds in their hardened state. *CIRP Ann Manuf Technol* 46:57–62. doi:[10.1016/S0007-8506\(07\)60775-6](https://doi.org/10.1016/S0007-8506(07)60775-6)
11. Stenberg N, Proudian J (2013) Numerical modelling of turning to find residual stresses. In: *Procedia CIRP 14th CIRP conference model machining operations*, vol 8, pp 258–264. doi:[10.1016/j.procir.2013.06.099](https://doi.org/10.1016/j.procir.2013.06.099)
12. Gardner JD, Vijayaraghavan A, Dornfeld DA (2005) Comparative study of finite element simulation software. In: *Lab Manuf Autom* <http://escholarship.org/uc/item/8cw4n2tf>. Accessed 19 Nov 2013
13. Amini S, Soleimanimehr H, Nategh MJ et al (2008) FEM analysis of ultrasonic-vibration-assisted turning and the vibratory tool. *J Mater Process Technol* 201:43–47. doi:[10.1016/j.jmatprotec.2007.11.271](https://doi.org/10.1016/j.jmatprotec.2007.11.271)
14. Zanger F, Schulze V (2013) Investigations on mechanisms of tool wear in machining of Ti-6Al-4V using FEM simulation. In: *Procedia CIRP 14th CIRP conference on modeling of machining operations*, vol 8, pp 158–163. doi:[10.1016/j.procir.2013.06.082](https://doi.org/10.1016/j.procir.2013.06.082)
15. Dandekar CR, Shin YC, Barnes J (2010) Machinability improvement of titanium alloy (Ti-6Al-4V) via LAM and hybrid machining. *Int J Mach Tools Manuf* 50:174–182. doi:[10.1016/j.ijmachtools.2009.10.013](https://doi.org/10.1016/j.ijmachtools.2009.10.013)
16. Muhammad R, Ahmed N, Roy A, Silberschmidt VV (2012) Numerical modelling of vibration-assisted turning of Ti-15333. *Procedia CIRP* 1:347–352. doi:[10.1016/j.procir.2012.04.062](https://doi.org/10.1016/j.procir.2012.04.062)
17. Maranhão C, Davim JP (2010) Finite element modelling of machining of AISI 316 steel: numerical simulation and experimental validation. *Simul Model Pract Theory* 18:139–156. doi:[10.1016/j.simpat.2009.10.001](https://doi.org/10.1016/j.simpat.2009.10.001)
18. John MRS, Shrivastava K, Banerjee N et al (2013) Finite element method-based machining simulation for analyzing surface roughness during turning operation with HSS and carbide insert tool. *Arab J Sci Eng* 38:1615–1623. doi:[10.1007/s13369-013-0541-1](https://doi.org/10.1007/s13369-013-0541-1)
19. Lauro CH, Brandão LC, Januário T et al (2013) An approach to define the heat flow in drilling with different cooling systems using finite element analysis. *Adv Mech Eng* 2013:9. doi:[10.1155/2013/612747](https://doi.org/10.1155/2013/612747)

20. Isbilir O, Ghassemieh E (2011) Finite element analysis of drilling of titanium alloy. In: *Procedia engineering—11th international conference on the mechanical behavior of materials*, vol 10, pp 1877–1882. doi:[10.1016/j.proeng.2011.04.312](https://doi.org/10.1016/j.proeng.2011.04.312)
21. Schulze V, Osterried J, Strauß T (2011) FE analysis on the influence of sequential cuts on component conditions for different machining strategies. *Procedia Eng* 19:318–323. doi:[10.1016/j.proeng.2011.11.119](https://doi.org/10.1016/j.proeng.2011.11.119)
22. Davim JP, Maranhão C, Jackson MJ et al (2007) FEM analysis in high speed machining of aluminium alloy (Al7075-0) using polycrystalline diamond (PCD) and cemented carbide (K10) cutting tools. *Int J Adv Manuf Technol* 39:1093–1100. doi:[10.1007/s00170-007-1299-y](https://doi.org/10.1007/s00170-007-1299-y)
23. Sartkulvanich P, Altan T, Göçmen A (2005) Effects of flow stress and friction models in finite element simulation of orthogonal cutting—a sensitivity analysis. *Mach Sci Technol* 9:1–26. doi:[10.1081/MST-200051211](https://doi.org/10.1081/MST-200051211)
24. Ali MH, Ansari MNM, Khidhir BA et al (2014) Simulation machining of titanium alloy (Ti-6Al-4V) based on the finite element modeling. *J Brazilian Soc Mech Sci Eng* 36:315–324. doi:[10.1007/s40430-013-0084-0](https://doi.org/10.1007/s40430-013-0084-0)
25. Rizzuti S, Umbrello D, Filice L, Settineri L (2010) Finite element analysis of residual stresses in machining. *Int J Mater Form* 3:431–434. doi:[10.1007/s12289-010-0799-](https://doi.org/10.1007/s12289-010-0799-)
26. Doman D, Warkentin A, Bauer R (2009) Finite element modeling approaches in grinding. *Int J Mach Tools Manuf* 49:109–116. doi:[10.1016/j.ijmachtools.2008.10.002](https://doi.org/10.1016/j.ijmachtools.2008.10.002)
27. Özel T, Zeren E (2007) Finite element modeling the influence of edge roundness on the stress and temperature fields induced by high-speed machining. *Int J Adv Manuf Technol* 35:255–267. doi:[10.1007/s00170-006-0720-2](https://doi.org/10.1007/s00170-006-0720-2)
28. Benson DJ, Okazawa S (2004) Contact in a multi-material Eulerian finite element formulation. *Comput Methods Appl Mech Eng* 193:4277–4298. doi:[10.1016/j.cma.2003.12.061](https://doi.org/10.1016/j.cma.2003.12.061)
29. Carroll JT, Strenkowski JS (1988) Finite element models of orthogonal cutting with application to single point diamond turning. *Int J Mech Sci* 30:899–920. doi:[10.1016/0020-7403\(88\)90073-2](https://doi.org/10.1016/0020-7403(88)90073-2)
30. Nasr MNA, Ng E-G, Elbestawi MA (2008) A modified time-efficient FE approach for predicting machining-induced residual stresses. *Finite Elem Anal Des* 44:149–161. doi:[10.1016/j.finel.2007.11.005](https://doi.org/10.1016/j.finel.2007.11.005)
31. Bäker M, Rösler J, Siemers C (2002) A finite element model of high speed metal cutting with adiabatic shearing. *Comput Struct* 80:495–513. doi:[10.1016/S0045-7949\(02\)00023-8](https://doi.org/10.1016/S0045-7949(02)00023-8)
32. Mamalis AG, Branis AS, Manolakos DE (2002) Modelling of precision hard cutting using implicit finite element methods. *J Mater Process Technol* 123:464–475. doi:[10.1016/S0924-0136\(02\)00133-4](https://doi.org/10.1016/S0924-0136(02)00133-4)
33. Coelho RT, Ng E, Elbestawi MA (2007) Tool wear when turning hardened AISI 4340 with coated PcBN tools using finishing cutting conditions. *Int J Mach Tools Manuf* 47:263–272. doi:[10.1016/j.ijmachtools.2006.03.020](https://doi.org/10.1016/j.ijmachtools.2006.03.020)
34. Hu F, Li D (2011) Modelling and simulation of milling forces using an arbitrary Lagrangian-Eulerian finite element method and support vector regression. *J Optim Theory Appl* 153:461–484. doi:[10.1007/s10957-011-9927-y](https://doi.org/10.1007/s10957-011-9927-y)
35. Simoneau A, Ng E, Elbestawi MA (2006) Chip formation during microscale cutting of a medium carbon steel. *Int J Mach Tools Manuf* 46:467–481. doi:[10.1016/j.ijmachtools.2005.07.019](https://doi.org/10.1016/j.ijmachtools.2005.07.019)
36. Buchkremer S, Wu B, Lung D et al (2013) FE-simulation of machining processes with a new material model. *J Mater Process Technol*. doi:[10.1016/j.jmatprotec.2013.10.014](https://doi.org/10.1016/j.jmatprotec.2013.10.014)
37. Johnson GR, Cook WH (1985) Fracture characteristics of three metals subjected to various strains, strain rates, temperatures and pressures. *Eng Fract Mech* 21:31–48. doi:[10.1016/0013-7944\(85\)90052-9](https://doi.org/10.1016/0013-7944(85)90052-9)
38. Dandekar CR, Shin YC (2012) Modeling of machining of composite materials: a review. *Int J Mach Tools Manuf* 57:102–121. doi:[10.1016/j.ijmachtools.2012.01.006](https://doi.org/10.1016/j.ijmachtools.2012.01.006)
39. Sartkulvanich P, Koppka F, Altan T (2004) Determination of flow stress for metal cutting simulation—a progress report. *J Mater Process Technol* 146:61–71. doi:[10.1016/S0924-0136\(03\)00845-8](https://doi.org/10.1016/S0924-0136(03)00845-8)

40. Chen G, Ren C, Yang X et al (2011) Finite element simulation of high-speed machining of titanium alloy (Ti-6Al-4 V) based on ductile failure model. *Int J Adv Manuf Technol* 56:1027–1038. doi:[10.1007/s00170-011-3233-6](https://doi.org/10.1007/s00170-011-3233-6)
41. Ambati R, Yuan H (2010) FEM mesh-dependence in cutting process simulations. *Int J Adv Manuf Technol* 53:313–323. doi:[10.1007/s00170-010-2818-9](https://doi.org/10.1007/s00170-010-2818-9)
42. Duan C, Zhang L (2012) A reliable method for predicting serrated chip formation in high-speed cutting: analysis and experimental verification. *Int J Adv Manuf Technol* 64:1587–1597. doi:[10.1007/s00170-012-4125-0](https://doi.org/10.1007/s00170-012-4125-0)
43. Shrot A, Bäker M (2012) Determination of Johnson-Cook parameters from machining simulations. *Comput Mater Sci* 52:298–304. doi:[10.1016/j.commatsci.2011.07.035](https://doi.org/10.1016/j.commatsci.2011.07.035)
44. Umbrello D, M'Saoubi R, Outeiro JC (2007) The influence of Johnson-Cook material constants on finite element simulation of machining of AISI 316L steel. *Int J Mach Tools Manuf* 47:462–470. doi:[10.1016/j.ijmachtools.2006.06.006](https://doi.org/10.1016/j.ijmachtools.2006.06.006)
45. Yan H, Hua J, Shivpuri R (2007) Flow stress of AISI H13 die steel in hard machining. *Mater Des* 28:272–277. doi:[10.1016/j.matdes.2005.06.017](https://doi.org/10.1016/j.matdes.2005.06.017)
46. Becze CE, Worswick MJ, Elbestawi M (2001) High strain rate shear evaluation and characterization of Aisi D2 tool steel in its hardened state. *Mach Sci Technol* 5:131–149. doi:[10.1081/MST-100103182](https://doi.org/10.1081/MST-100103182)
47. Liu R, Melkote S, Pucha R et al (2013) An enhanced constitutive material model for machining of Ti-6Al-4 V alloy. *J Mater Process Technol* 213:2238–2246. doi:[10.1016/j.jmatprotec.2013.06.015](https://doi.org/10.1016/j.jmatprotec.2013.06.015)
48. Močko W, Kowalewski ZL (2013) Perforation test as an accuracy evaluation tool for a constitutive model of austenitic steel. *Arch Metall Mater* 58:1105–1110. doi:[10.2478/amm-2013-0133](https://doi.org/10.2478/amm-2013-0133)
49. Zerilli FJ, Armstrong RW (1987) Dislocation-mechanics-based constitutive relations for material dynamics calculations. *J Appl Phys* 61:1816. doi:[10.1063/1.338024](https://doi.org/10.1063/1.338024)
50. Tang L, Huang J, Xie L (2010) Finite element modeling and simulation in dry hard orthogonal cutting AISI D2 tool steel with cBN cutting tool. *Int J Adv Manuf Technol* 53:1167–1181. doi:[10.1007/s00170-010-2901-2](https://doi.org/10.1007/s00170-010-2901-2)
51. Fathipour M, Hamed M, Yousefi R (2013) Numerical and experimental analysis of machining of Al (20 vol% SiC) composite by the use of ABAQUS software. *Materwiss Werkstsch* 44:14–20. doi:[10.1002/mawe.201300959](https://doi.org/10.1002/mawe.201300959)
52. Santiuste C, Soldani X, Miguélez MH (2010) Machining FEM model of long fiber composites for aeronautical components. *Compos Struct* 92:691–698. doi:[10.1016/j.compstruct.2009.09.021](https://doi.org/10.1016/j.compstruct.2009.09.021)
53. Manikandan G, Uthayakumar M, Aravindan S (2012) Machining and simulation studies of bimetallic pistons. *Int J Adv Manuf Technol* 66:711–720. doi:[10.1007/s00170-012-4359-x](https://doi.org/10.1007/s00170-012-4359-x)
54. Seshadri R, Naveen I, Srinivasan S et al (2013) Finite element simulation of the orthogonal machining process with Al 2024 T351 aerospace alloy. *Procedia Eng Int Conf Des Manuf* 64:1454–1463. doi:[10.1016/j.proeng.2013.09.227](https://doi.org/10.1016/j.proeng.2013.09.227)
55. Kouadri S, Necib K, Atlati S et al (2013) Quantification of the chip segmentation in metal machining: application to machining the aeronautical aluminium alloy AA2024-T351 with cemented carbide tools WC-Co. *Int J Mach Tools Manuf* 64:102–113. doi:[10.1016/j.ijmachtools.2012.08.006](https://doi.org/10.1016/j.ijmachtools.2012.08.006)
56. Ribeiro Filho SLM, Gomes MO, Lauro CH, Brandão LC (2014) Definition of the temperature and heat flux in micromilling of hardened steel using the finite element method. *Arab J Sci Eng* 39:7229–7239. doi:[10.1007/s13369-014-1281-6](https://doi.org/10.1007/s13369-014-1281-6)
57. Vaz M, Owen DRJ, Kalhori V et al (2007) Modelling and simulation of machining processes. *Arch Comput Methods Eng* 14:173–204. doi:[10.1007/s11831-007-9005-7](https://doi.org/10.1007/s11831-007-9005-7)

58. Schulze V, Zanger F, Boev N (2013) Numerical investigations on changes of the main shear plane while broaching. *Procedia CIRP* 8:246–251. doi:[10.1016/j.procir.2013.06.097](https://doi.org/10.1016/j.procir.2013.06.097)
59. Saffar RJ, Razfar MR, Zarei O, Ghassemieh E (2008) Simulation of three-dimension cutting force and tool deflection in the end milling operation based on finite element method. *Simul Model Pract Theory* 16:1677–1688. doi:[10.1016/j.simpat.2008.08.010](https://doi.org/10.1016/j.simpat.2008.08.010)
60. Malakizadi A, Sadik I, Nyborg L (2013) Wear mechanism of cBN inserts during machining of bimetal aluminum-grey cast iron engine block. In: 14th CIRP conference on modeling of machining operations, vol 8, pp 188–193. doi:[10.1016/j.procir.2013.06.087](https://doi.org/10.1016/j.procir.2013.06.087)
61. Pu Z, Umbrello D, Dillon OW et al (2014) Finite element modeling of microstructural changes in dry and cryogenic machining of AZ31B magnesium alloy. *J Manuf Process* 16:335–343. doi:[10.1016/j.jmapro.2014.02.002](https://doi.org/10.1016/j.jmapro.2014.02.002)
62. Arrazola PJ, Özel T (2010) Investigations on the effects of friction modeling in finite element simulation of machining. *Int J Mech Sci* 52:31–42. doi:[10.1016/j.ijmecsci.2009.10.001](https://doi.org/10.1016/j.ijmecsci.2009.10.001)
63. Özel T (2006) The influence of friction models on finite element simulations of machining. *Int J Mach Tools Manuf* 46:518–530. doi:[10.1016/j.ijmachtools.2005.07.001](https://doi.org/10.1016/j.ijmachtools.2005.07.001)
64. Haddag B, Atlati S, Nouari M, Znasni M (2010) Finite element formulation effect in three-dimensional modeling of a chip formation during machining. *Int J Mater Form* 3:527–530. doi:[10.1007/s12289-010-0823-z](https://doi.org/10.1007/s12289-010-0823-z)
65. Ulutan D, Özel T (2013) Determination of tool friction in presence of flank wear and stress distribution based validation using finite element simulations in machining of titanium and nickel based alloys. *J Mater Process Technol* 213:2217–2237. doi:[10.1016/j.jmatprotec.2013.05.019](https://doi.org/10.1016/j.jmatprotec.2013.05.019)
66. Özel T, Altan T (2000) Determination of workpiece flow stress and friction at the chip–tool contact for high-speed cutting. *Int J Mach Tools Manuf* 40:133–152. doi:[10.1016/S0890-6955\(99\)00051-6](https://doi.org/10.1016/S0890-6955(99)00051-6)
67. Özel T (2009) Computational modelling of 3D turning: influence of edge micro-geometry on forces, stresses, friction and tool wear in PcBN tooling. *J Mater Process Technol* 209:5167–5177. doi:[10.1016/j.jmatprotec.2009.03.002](https://doi.org/10.1016/j.jmatprotec.2009.03.002)
68. Rotella G, Dillon OW, Umbrello D et al (2013) Finite element modeling of microstructural changes in turning of AA7075-T651 alloy. *J Manuf Process* 15:87–95. doi:[10.1016/j.jmapro.2012.09.005](https://doi.org/10.1016/j.jmapro.2012.09.005)
69. Klinkova O, Rech J, Drapier S, Bergheau J-M (2011) Characterization of friction properties at the workmaterial/cutting tool interface during the machining of randomly structured carbon fibers reinforced polymer with carbide tools under dry conditions. *Tribol Int* 44:2050–2058. doi:[10.1016/j.triboint.2011.09.006](https://doi.org/10.1016/j.triboint.2011.09.006)
70. Mahdi M, Zhang L (2001) A finite element model for the orthogonal cutting of fiber-reinforced composite materials. *J Mater Process Technol* 113:373–377. doi:[10.1016/S0924-0136\(01\)00675-6](https://doi.org/10.1016/S0924-0136(01)00675-6)
71. Phadnis VA, Roy A, Silberschmidt VV (2013) A finite element model of ultrasonically assisted drilling in carbon/epoxy composites. *Procedia CIRP* 8:141–146. doi:[10.1016/j.procir.2013.06.079](https://doi.org/10.1016/j.procir.2013.06.079)
72. Phadnis VA, Roy A, Silberschmidt VV (2012) Finite element analysis of drilling in carbon fiber reinforced polymer composites. *J Phys: Conf Ser* 382:012014. doi:[10.1088/1742-6596/382/1/012014](https://doi.org/10.1088/1742-6596/382/1/012014)
73. Pramanik A, Zhang LC, Arsecularatne JA (2007) An FEM investigation into the behavior of metal matrix composites: Tool–particle interaction during orthogonal cutting. *Int J Mach Tools Manuf* 47:1497–1506. doi:[10.1016/j.ijmachtools.2006.12.004](https://doi.org/10.1016/j.ijmachtools.2006.12.004)
74. Childs THC (2013) Ductile shear failure damage modelling and predicting built-up edge in steel machining. *J Mater Process Technol* 213:1954–1969. doi:[10.1016/j.jmatprotec.2013.05.017](https://doi.org/10.1016/j.jmatprotec.2013.05.017)
75. Weinert K, Schneider M (2000) Simulation of tool-grinding with finite element method. *CIRP Ann Manuf Technol* 49:253–256. doi:[10.1016/S0007-8506\(07\)62940-0](https://doi.org/10.1016/S0007-8506(07)62940-0)

76. Duan C, Kong W, Hao Q, Zhou F (2013) Modeling of white layer thickness in high speed machining of hardened steel based on phase transformation mechanism. *Int J Adv Manuf Technol* 69:59–70. doi:[10.1007/s00170-013-5005-y](https://doi.org/10.1007/s00170-013-5005-y)
77. Attanasio A, Umbrello D, Cappellini C et al (2012) Tool wear effects on white and dark layer formation in hard turning of AISI 52100 steel. *Wear* 286–287:98–107. doi:[10.1016/j.wear.2011.07.001](https://doi.org/10.1016/j.wear.2011.07.001)
78. Ramesh A, Melkote SN (2008) Modeling of white layer formation under thermally dominant conditions in orthogonal machining of hardened AISI 52100 steel. *Int J Mach Tools Manuf* 48:402–414. doi:[10.1016/j.ijmachtools.2007.09.007](https://doi.org/10.1016/j.ijmachtools.2007.09.007)
79. Ee KC, Dillon OW, Jawahir IS (2005) Finite element modeling of residual stresses in machining induced by cutting using a tool with finite edge radius. *Int J Mech Sci* 47:1611–1628. doi:[10.1016/j.ijmecsci.2005.06.001](https://doi.org/10.1016/j.ijmecsci.2005.06.001)
80. Valiorgue F, Rech J, Hamdi H et al (2012) 3D modeling of residual stresses induced in finish turning of an AISI304L stainless steel. *Int J Mach Tools Manuf* 53:77–90. doi:[10.1016/j.ijmachtools.2011.09.011](https://doi.org/10.1016/j.ijmachtools.2011.09.011)
81. Ji X, Zhang X, Liang SY (2013) Predictive modeling of residual stress in minimum quantity lubrication machining. *Int J Adv Manuf Technol*. doi:[10.1007/s00170-013-5439-2](https://doi.org/10.1007/s00170-013-5439-2)
82. Engineering Village (2015) Number of published papers about finite element method in machining process. www.engineeringvillage.com
83. Mackerle J (1999) Finite-element analysis and simulation of machining: a bibliography (1976–1996). *J Mater Process Technol* 86:17–44. doi:[10.1016/S0924-0136\(98\)00227-1](https://doi.org/10.1016/S0924-0136(98)00227-1)
84. Woon KS, Rahman M, Fang FZ et al (2008) Investigations of tool edge radius effect in micromachining: a FEM simulation approach. *J Mater Process Technol* 195:204–211. doi:[10.1016/j.jmatprotec.2007.04.137](https://doi.org/10.1016/j.jmatprotec.2007.04.137)
85. Ding H, Shen N, Shin YC (2012) Thermal and mechanical modeling analysis of laser-assisted micro-milling of difficult-to-machine alloys. *J Mater Process Technol* 212:601–613. doi:[10.1016/j.jmatprotec.2011.07.016](https://doi.org/10.1016/j.jmatprotec.2011.07.016)
86. Wang J, Gong Y, Abba G et al (2009) Chip formation analysis in micromilling operation. *Int J Adv Manuf Technol* 45:430–447. doi:[10.1007/s00170-009-1989-8](https://doi.org/10.1007/s00170-009-1989-8)
87. Chen G, Ren C, Zhang P et al (2013) Measurement and finite element simulation of micro-cutting temperatures of tool tip and workpiece. *Int J Mach Tools Manuf* 75:16–26. doi:[10.1016/j.ijmachtools.2013.08.005](https://doi.org/10.1016/j.ijmachtools.2013.08.005)
88. Özel T, Thepsonthi T, Ulutan D, Kaftanoğlu B (2011) Experiments and finite element simulations on micro-milling of Ti–6Al–4 V alloy with uncoated and cBN coated micro-tools. *CIRP Ann Manuf Technol* 60:85–88. doi:[10.1016/j.cirp.2011.03.087](https://doi.org/10.1016/j.cirp.2011.03.087)
89. Huang W-J, Hu H-J (2014) Micro-turning of hard steel by single-grain ceramic cutter based on numerical simulations. *Ceram Int*. doi:[10.1016/j.ceramint.2014.05.002](https://doi.org/10.1016/j.ceramint.2014.05.002)
90. Maranhão C, da Silva LR, Davim JP (2013) Comportamento termo mecânico no micro-torneamento ortogonal do aço AISI 1045 (Ck45 - DIN): Simulação via elementos finitos e validação experimental. *Ciência Tecnol dos Mater* 25:57–66. doi:[10.1016/j.ctmat.2013.12.006](https://doi.org/10.1016/j.ctmat.2013.12.006)
91. Klocke F, Gerschwiler K, Abouridouane M (2009) Size effects of micro drilling in steel. *Prod Eng* 3:69–72. doi:[10.1007/s11740-008-0144-y](https://doi.org/10.1007/s11740-008-0144-y)
92. Abouridouane M, Klocke F, Lung D, Adams O (2012) Size effects in micro drilling ferritic-pearlitic carbon steels. 45th CIRP Conf. *Manuf Syst* 3:91–96. doi:[10.1016/j.procir.2012.07.017](https://doi.org/10.1016/j.procir.2012.07.017)
93. Bajpai V, Singh RK (2014) Finite element modeling of orthogonal micromachining of anisotropic pyrolytic carbon via damaged plasticity. *Precis Eng* 38:300–310. doi:[10.1016/j.precisioneng.2013.10.004](https://doi.org/10.1016/j.precisioneng.2013.10.004)
94. Zahedi SA, Roy A, Silberschmidt VV (2013) Modeling of micro-machining single-crystal f.c.c. metals. *Procedia CIRP* 8:346–350. doi:[10.1016/j.procir.2013.06.114](https://doi.org/10.1016/j.procir.2013.06.114)
95. Zahedi SA, Demiral M, Roy A, Silberschmidt VV (2013) FE/SPH modelling of orthogonal micro-machining of f.c.c. single crystal. *Comput Mater Sci* 78:104–109. doi:[10.1016/j.commatsci.2013.05.022](https://doi.org/10.1016/j.commatsci.2013.05.022)

96. Afazov SM, Ratchev SM, Segal J (2011) Prediction and experimental validation of micro-milling cutting forces of AISI H13 steel at hardness between 35 and 60 HR_C. *Int J Adv Manuf Technol* 62:887–899. doi:[10.1007/s00170-011-3864-7](https://doi.org/10.1007/s00170-011-3864-7)
97. Moriwaki T, Sugimura N, Luan S (1993) Combined stress, material flow and heat analysis of orthogonal micromachining of copper. *CIRP Ann Manuf Technol* 42:75–78. doi:[10.1016/S0007-8506\(07\)62395-6](https://doi.org/10.1016/S0007-8506(07)62395-6)
98. Ashtakhov VP (2002) Metal cutting theory—missed chances or a science without history: Part 2. In: *Pers. Vis. Viktor P. Astakhov*. <http://viktorastakhov.tripod.com/mc2.pdf>. Accessed 1 Jan 2015

Chapter 4

Machining and Machining Modeling of Metal Matrix Composites—A Review

Angelos P. Markopoulos, Ioannis S. Pressas, Ioannis G. Papantoniou,
Nikolaos E. Karkalos and J. Paulo Davim

Abstract This chapter reviews the most common machining processes used in metal matrix composites (MMCs), such as turning, milling, and drilling. Apart from the difficulties faced in each of these processes in the case of MMCs and some possible solutions, certain other important factors, such as tool wear mechanisms and the final surface quality, are discussed. Furthermore, the machinability of MMCs, in a number of different machining processes, is examined. Tapping, grinding, honing, sawing, and micro-machining are also considered. Additionally, the manufacturing of MMC products through nonconventional machining processes is discussed, as alternatives to the aforementioned processes. Finally, modeling of MMCs and their machining will be examined. The analysis will concentrate on the most popular methods used, namely finite elements method, molecular dynamics, and soft computing techniques.

4.1 Introduction

Over the past years there has been high utilization of composite materials in a large number of industrial applications. Some of the most notable industrial sectors that mainly incorporate composite materials include the aviation, automotive, aeronautical, sports equipment, and defense systems industries [1–3]. The reason for this increased interest is mainly due to the superior properties that the composite materials display, compared to their weight. Although the composition of these materials presents a vast variety in terms of the component materials used, metal

A.P. Markopoulos (✉) · I.S. Pressas · I.G. Papantoniou · N.E. Karkalos
Section of Manufacturing Technology, School of Mechanical Engineering,
National Technical University of Athens, Heroon Politechniou 9, 15780 Athens, Greece
e-mail: amark@mail.ntua.gr

J. Paulo Davim
Department of Mechanical Engineering, University of Aveiro, Campus Santiago,
3810-193 Aveiro, Portugal

© Springer International Publishing Switzerland 2015
J.P. Davim (ed.), *Modern Manufacturing Engineering*, Materials Forming,
Machining and Tribology, DOI 10.1007/978-3-319-20152-8_4

99

matrix composites (MMCs) seem to be especially popular in industrial applications. Generally, MMCs consist of a metallic matrix with the reinforcements presenting a larger variety in terms of materials and forms. This constitution allows MMCs to present a high strength-to-weight ratio and stiffness, increased wear resistance, as well as several other improved properties, in comparison to their respective common monometallic materials and alloys [3, 4].

Although MMCs seem to provide an optimal solution for many applications, their manufacture can be rather arduous. This is mainly because of the material differentiation presented in an MMC and as a result, because of the constantly differentiating material properties presented during a manufacturing process [3]. This fact can affect both the final outcome of a manufacturing process and the methods and tools needed to produce a certain item. For example, in the case of the traditional turning process of an Al-SiC MMC, very hard and expensive cutting tools, such as polycrystalline diamond (PCD) tools, are required to have the desired result. The cutting parameters of this process have to be carefully chosen, in order to prevent excessive wear of the tools or insert any dynamic loads in the manufacturing process, as a result of the material's variable strength during a cutting cycle [5]. It needs to be noted that the whole point of machining an MMC product is crucial for industrial applications, as in most cases near-net shape items produced via a number of different manufacturing processes, such as casting, forging, and rapid prototyping [1], require subsequent machining of the product in order to achieve their final form [3].

In the following sections a description of the most common machining processes used for processing MMCs will be discussed. Turning, milling, and drilling are mainly investigated, however, tapping, grinding, honing, and sawing are considered as well. A special paragraph is dedicated to micro-machining of MMCs, as a lot of improvements are anticipated in this field in the near future. In another section of the chapter, non-conventional machining processes such as electrical discharge machining (EDM), abrasive water jet (AWJ), laser, electrochemical, and ultrasonic machining (USM) are investigated, in connection to MMC processing. In the final section, modelling methods used for the simulation and optimization of MMCs machining are thoroughly discussed.

4.2 Conventional Machining Processes of MMCs

MMC materials constitute an optimal solution for a vast number of applications. The reason for this lies with the superior properties that these materials possess, mainly in terms of their mechanical and thermal attitude, in comparison to other metals and alloys [6]. Although the properties of MMCs can be quite desirable, they are proven to be an obstacle in the production of MMC components, especially when machining is considered.

As the machining process of an MMC proceeds, the cutting tool passes through the different phases of the material, i.e., the softer matrix phase and the harder

reinforcement phase. Although for most cases the softer phase can be easily penetrated by the cutting tools, the abrasive nature of the reinforcements leads to severe reduction of the cutting tool life [7]. This excessive tool wear renders the machining of an MMC as an overly expensive process, if not entirely unfeasible [8]. In order to cope with this problem, some extensive research has been conducted, so as to determine the optimum combination of the cutting parameters and tools needed for several MMCs. Furthermore, new research data continue to be published, in which the difficulties of machining newly manufactured and improved MMCs are being discussed, as a result of the continuous advances in tools and manufacturing processes.

Describing the optimum machining parameters for all MMCs is fairly difficult; in this section some general guidelines regarding this subject are defined. What is more, emphasis is given on the tool wear mechanisms that occur during the machining of an MMC, which is one of the most important factors in this type of manufacturing. Furthermore, some general information regarding the proper tool choice for machining an MMC is addressed. Finally, a brief reference to the loads that develop during machining is conducted, based on the orthogonal cutting model. It needs to be noted that, although most of the conducted research refers to either Al-based, SiCp, or Al_2O_3 reinforced MMCs or GrA-Ni[®] MMCs, the guidelines that are described below are generalized according to some common properties that all MMCs present.

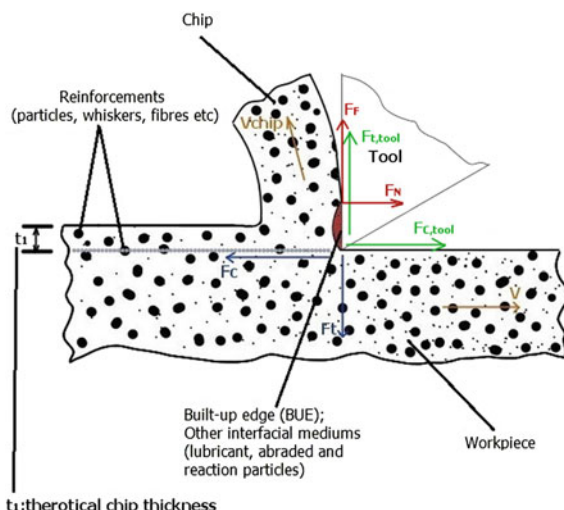
4.2.1 Loads During Machining of MMCs

In order to better clarify the tool wear mechanisms that occur in each machining process of MMCs, the loads on the tool and the workpiece should be defined. For this reason, the orthogonal cutting model is employed; the main forces are shown in Fig. 4.1.

As shown in Fig. 4.1 the main forces that affect the workpiece are the main cutting force F_c and the thrust force F_t . The reactions to these forces $F_{c, \text{tool}}$ and $F_{t, \text{tool}}$ developing on the tool are responsible, in combination with the excessive heat generated through friction, for the creation of the flank wear on the cutting edge [9]. From these two forces, the main contribution to the flank wear can be attributed to the reaction of the main cutting force, $F_{c, \text{tool}}$, as in the case of MMC machining, this particular force constantly differentiates from fairly low values to extremely high, when a particle of the reinforcement is met. The contact between the reinforcement particles and the cutting tool that occurs during a cutting route leads to the generation of certain mechanical and thermal loads, which heavily affect this type of tool wear. Generally, there seem to be a direct connection between the developing forces on the cutting tool and its flank wear [9].

In the case of forces that develop in the interface between the tool and the formed chip, F_F and F_N greatly contribute to the wear mechanisms that occur during MMC machining. Friction force F_F , is the main factor of the thermal loads generated

Fig. 4.1 Forces developing during machining of MMCs



during every machining process. This force is affected by the relative movement of the reinforcement particles in the tool–chip interface, something that further increases the wear of the cutting tool [10]. Moreover, the vertical tool–chip interface force, F_N , acts auxiliary to the friction force, enhancing the mechanical and thermal loads on the tool–chip interface. The combination of these two forces attributes to the majority of wear mechanisms that occur during this process, namely abrasion wear, flank wear, and built-up edge (BUE).

Generally, the dominant mechanical loads that strain the cutting tool in an MMC machining process, causing its wear, are summarized below [8, 11]:

- The contact between the reinforcement particles and the cutting edge causes the increase of abrasion in the tool.
- The reinforcement particles impacting on the cutting edge cause increased dynamic loads.
- The constantly differentiating material properties during the cutting route cause alternate stress in the tool.

At the same time, the main thermal loads straining the cutting tool are:

- The strenuous microcontact between the reinforcement particles and the cutting edge cause localized temperature increase, which results in high localized thermal loads.
- The main thermal load that is attributed to the increase of the cutting temperature during the machining process, is considered to be fairly low, as it is limited by the relatively low melt temperature of the matrix material.

As mentioned before, the developing forces during an MMC machining process account for a major part in the tool wear. For this reason, several researchers tried over the past years, to discover models that would predict the developing forces in

this process. For example, Sikder and Kishawy [12] tried to establish an analytical model to predict the contribution of several particle-induced forces to the friction force developing in the tool–chip interface. In another section of this chapter, a detailed presentation of models pertaining to MMC machining will be given.

4.2.2 Tool Wear Mechanisms

Extensive tool wear occurring during machining of an MMC is a main reason that limits a wider turn toward the mass MMC component production. Although use of harder tools and utilization of proper cutting parameters can provide the means for a successful machining process, in most cases the increased cost cannot justify mass production. Some extended research concerning tool wear mechanisms has been conducted over the past years, in order to discover possible solutions to the problem [6, 13]. Below, the main tool wear mechanisms that occur during machining of an MMC are introduced.

Abrasive wear is often considered as the dominant tool wear occurring during MMC machining [14]. This type of tool wear occurs as a result of the reinforcement particles impacting the cutting edge during the cutting of the MMC. Furthermore, the relative movement of these particles to the rake of the cutting tool seems to enhance the problem, as the cut-off particles maximize the mechanical and thermal loads on the tool [10]. Although abrasion seems rather easy to comprehend, the mechanisms behind this phenomenon are rather complicated and can be attributed to a combination of the properties of the cutting tool material and the MMC [8]. The most common mechanisms are microplowing, microfatigue, microcutting, and microcracking [15], with the dominant one to be defined by the above-mentioned material combination. In general, abrasive wear is attributed to increased hardness of the MMC reinforcements. In particular the shape, distribution, and volume fraction of the reinforcements inside an MMC are factors that affect the degree of abrasive wear in the tool [14]. This degree can be further enhanced if the concentration of the reinforcement in the MMC surpasses a certain value, which is related to certain properties of the reinforcement particles, such as their density and size [16]. Furthermore, the size of the material grains, as well as the chemical attitude of the tool can increase the implementation of one of the above-mentioned mechanisms over the other.

Flank wear is the most common type of tool wear in machining processes. It is a result of the combination of the thermal and mechanical loads that strain the cutting edge. In general, flank wear develops when the hard and abrasive particles of the workpiece impact on the softened from the increased heat cutting edge, causing its sections to chip-off. It is one of the most important types of tool wear, as many of the parameters of cutting, e.g., cutting forces, have a direct relationship to this wear type [9]. Should the flank wear increase above a certain value, the increasing forces cause the tool to fail. The size of flank wear is measured by its width, which is constantly increasing during the machining process. In the case of the machining an MMC, flank wear is affected by the chosen cutting parameters [16]. The main factor

that affects this type of wear is the cutting speed, as with its increase, the number of impacting particles on the cutting edge also increases. This fact is especially important in the case of MMC machining, as the impacting particles have an abrasive nature, thus straining the cutting edge significantly. Furthermore, the volume fraction of the reinforcement particles in the material is of high importance as well. In order to reduce the effect that the impacting particles cause, cutting tools of harder material are used. It is worth noting that, although in traditional machining the use of coolant can reduce the width of the flank wear, coolant usage in the machining of MMCs does not seem to provide such a result.

Built-up edge as a wear type provides both positive and negative results in the machining process. As a mechanism, this tool wear type is formed when some chipped-off particles of the chip adhere on the rake of the cutting tool. The main reason for this phenomenon lies with the increase of cutting speed, which results in higher thermal loads in the tool–chip interface. Thus, the chipped-off particles are able to gradually form an additional layer in this area of the tool, assisted by the increased mechanical loads developing due to the tool–chip contact [9]. Should BUE shear, as a result of the increased mechanical loads during the machining process, usually part of the tool rake chips-off as well, as a result of the unstable loads that develop at the time [9, 17]. Positive effects of BUE involve increased protection that is offered to the cutting edge. This is mainly due to the fact that as BUE is formed around the cutting edge, the abrasive particles of the workpiece, which would impact the cutting edge, end up impacting on BUE instead. This abrasion protection is generally considered to increase tool life. On the other hand, BUE is simultaneously rather unstable, thus resulting in an increase in cutting loads. This increase of cutting loads causes instabilities during the cutting route of the tool, thus reducing the resulting workpiece surface quality [14, 16].

Several researchers have investigated the parameters that affect BUE. The most important factor on the formation of BUE is the cutting speed. In most cases, a low cutting speed results in the formation of a well-developed BUE, while high cutting speed results in weaker and more fragile BUE [9]. It needs to be noted that even in high values of cutting speed, BUE is still formed, although to a lower extent [14]. Furthermore, other cutting parameters seem to play a significant role in the creation of BUE. In the case of feed rate, increasing its value above a certain limit results in the formation of BUE [18]. In both of the above cases, choosing machining parameters poorly results in an increase of the developing thermal loads, leading to increased possibility of particle adhesion. Because of the correlation between the thermal loads, and the BUE wear, the usage of coolant leads to a decrease of the material adhered to the tool and the minimization of the formed BUE [16].

4.2.3 Machinability

There is no accurate definition that characterizes the term machinability. In most cases, machinability is considered to describe the material attitude during a

machining process. Because of this definition, one can easily understand that the factors that can affect the machinability of a material are numerous. In the case of MMCs, apart from the mechanical and thermal properties of each component of an MMC, mainly characterized by the material composition and microstructure, which define a large portion of a machining process's parameters, several factors that develop during a machining process also seem to be dependent on the structural and chemical properties of the material components. Examples of such factors involve the developing cutting forces, chip formation, developing faults, and surface alterations. Furthermore, the chemical and mechanical relationship between the matrix material and the reinforcements of an MMC is one of the most affecting properties, regarding final machinability. Additionally, the machinability of an MMC can be heavily affected by the properties that are related to the contact between cutting tool and workpiece, such as the developing wear mechanisms, workpiece surface integrity, and power that is required to remove chip from the workpiece material. Finally, some properties that characterize the cutting tool and the machine performance raise some important to machining factors. Some such factors involve tool geometry, tool type, tool material, and stability of the machine during machining. A summary of the above-mentioned properties can be seen in Fig. 4.2.

Some of the above-mentioned factors tend to be more dominant during a machining process of a specific MMC. These factors can be summarized in the following list [14]:

- Cutting tool life and developing wear mechanisms
- Integrity of workpiece surface and subsurface
- Chip formation and attitude
- Cutting forces and required power
- BUE formation tendency

The combinations of the dominant factors, from the ones that are listed above, tend to differentiate in a large scale, depending on the actual setup and the MMC being machined. In order for a machining process to be considered effective, these factors have to be thoroughly evaluated and specified. The evaluation of these factors is fairly difficult and it is generally performed through a series of simulations and tests of the actual process. This procedure determines the machinability of the MMC for the current setup. However, caution should be practiced, as the specified values addressed to a particular setup may be utterly inappropriate for a similar but differentiated setup.

4.2.3.1 Turning of MMCs

Turning is one of the most common and widespread machining processes in industrial production, as through this process a large number of products and components can be manufactured. In the case of MMC turning, a lot of research regarding several aspects of this process has been performed. Although most of the

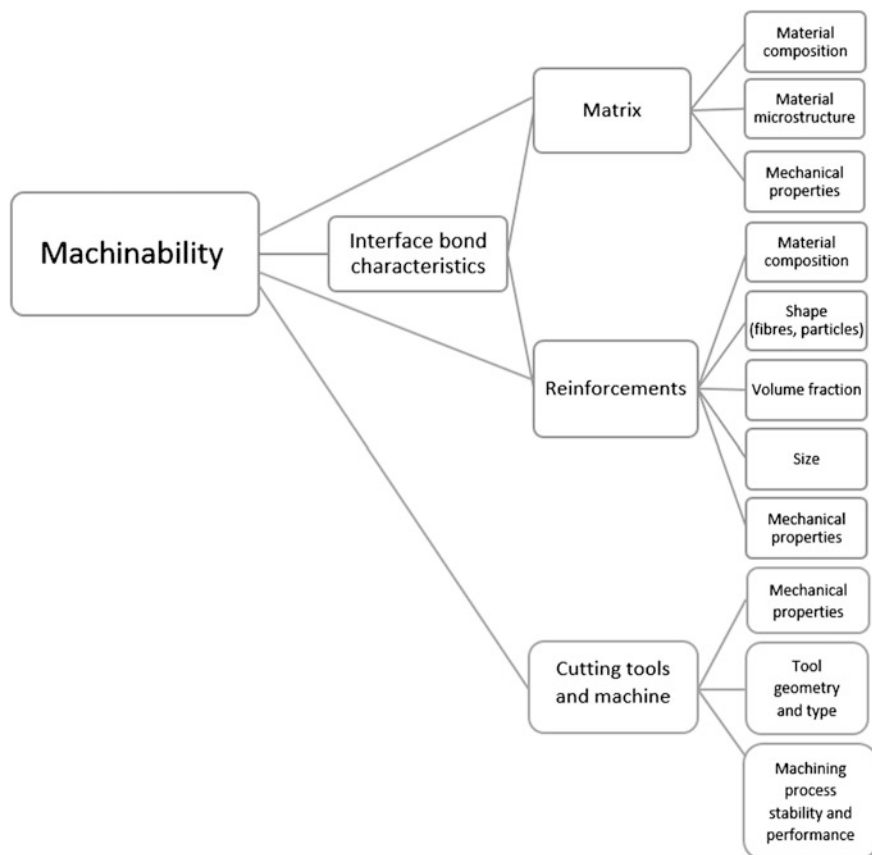


Fig. 4.2 Properties that affect the machinability of a material

factors that affect turning of MMCs are dependent on the actual material that is machined, some general guidelines can be drawn. In order to examine the effectiveness of each parameter to the turning result, means of measuring this factor has to be employed. In most cases the combination of tool wear and the final surface quality of the product after completion of the process are measured, in order to judge the results.

4.2.3.2 Parameters of Turning and Tool Wear

In most cases of turning, the whole process is performed in two steps. The first step contains a rough turning of the product, where the final dimensions are approached, while the second step contains a finish turning, where the final dimensions and the desired surface roughness are achieved. In various researches [14–17] it is often

implied that during the rough cutting step, certain turning parameters such as feed rate and depth of cut (DoC) should be chosen rather high, in order to have low tool wear, regardless of the tool material [17, 19, 20]. The exact values for these parameters vary in regard to the material combination of the item and the tool.

The way cutting speeds affect tool wear in turning of MMCs is a matter that raises contradictions. Researchers present results showing that cutting speed brings insignificant changes to tool wear [21], although Coelho et al. [22] propose an empirical method that relates the two. On the other hand, other researchers show high dependence between the cutting speed and tool wear [23–25]. Although this fact may seem problematic, whether the cutting speed affects tool wear or not, seems to also depend on the material of the tool used. Finally, the use of coolant is usually avoided when turning MMCs, as it brings no actual improvement in tool wear reduction [26]. In this way, the increased cost due to high tool wear can be controlled in large industrial productions, with the proper choice of feed rate and DoC; the BUE that forms on the tool can offer some protection [7]. The application of coolant, in the form of flood, should only be employed if the formation of BUE is to be avoided or chip clearing is poor.

4.2.3.3 Parameters of Turning and Surface Quality

Feed rate and DoC play a significant role on the finish surface of a turned MMC product. Studies have shown that increasing feed rate deteriorates the quality of the surface, as it leads to higher surface roughness [27]. Furthermore, application of DoC above a certain value increases the chance of rapid tool wear, which results in poor surface quality. Although both parameters can affect the surface finish, feed rate seems to be the predominant of the two [28]. Regarding cutting speed, results show that cutting speed values employed during finish turning do not seem to bring significant changes in the quality of the final surface. Should the value of cutting speed be limited in a value range that BUE is formed, then instabilities caused can affect the final surface quality [28]. Finally, surface quality is affected by the tool material used. This is mainly because the grains of the tool material can produce different roughness on the final surface, according to their size. Research shows that finer materials produce lower surface roughness, while coarser materials have the opposite effect [29]. Moreover, the friction coefficient that characterizes the tool and workpiece materials' contact can alter the final surface quality [30].

4.2.3.4 Proper Tool Selection

From all of the above, it seems that the proper tool choice for MMC turning is of great importance. Generally, tools that are employed for this process are cubic boron nitride (CBN), PCD, tungsten carbide (WC), high speed steel (HSS), diamond-coated carbide (DCC) tools [14], as well as tools coated with a hard layer, such as tools coated with diamond layers through chemical vapor deposition

(CVD) processes [8]. The material of the cutting tool has to be strong enough to perform the turning process through the hard reinforcements of the MMC, while its own hardness should be high enough to withstand the tool wear mechanisms that develop, thus increasing the overall tool life. This is why, a hard coated material is usually employed in turning, as the main tool wear mechanisms that develop during this process are considered to cause abrasion wear to the tool [26].

A lot of research has been conducted in order to verify the most appropriate tool for turning of MMCs. Most of this research seems to promote the use of PCD tools. The reason for this choice lies with the physical and chemical properties of PCD, as it is strong enough to perform the machining process, hard enough to provide an increased wear resistance, while it does not tend to form chemical bonds with any of the components of most MMCs [16]. Although PCD tools seem to be the obvious choice for turning of MMCs, the high tool wear rate of the process may increase the overall cost to prohibitive levels. Thus, many researchers have begun investigating the possibility of substituting PCD tools with others, for comparable properties, such as diamond-coated tools [30].

4.2.3.5 Hybrid Turning Processes

As mentioned above, the high tool wear resulting from the increased hardness of the particles of MMCs is the main factor that restricts MMC machining from being a widespread manufacturing and productive process. Although most of the conducted research concentrates in defining the optimal parameters and employing the appropriate tools for each type of MMC, some researchers proposed ways to differentiate traditional machining process, which would result in lower tool wear and better surface quality. Przystacki [31] performed MMC turning assisted via laser heating. The CO₂ laser used softened the material right before cutting it with the tool. In this way, the strength of the material was significantly reduced, while in some cases the material removal mechanism altered from fracturing to extensive plastic deformation. In regard to tool wear, tool life was increased for the same type of tool compared to tool life in conventional turning and for the same set of cutting parameters. The comparison between tools with different material, though, showed lower tool wear when turning conventionally with a harder tool, than laser-assisted turning with softer tools, thus the proper tool selection cannot be entirely eliminated. Finally, results seem to imply the existence of an optimal temperature, which provides the longest tool life in laser-assisted turning. With further research, this technique may prove capable of solving several of the problems that machining of MMCs exhibits. In the hybrid turning process proposed by Liu et al. [32], ultrasonic vibrations turning is employed. The mechanism of this process involves cutting tool vibration at a high frequency along a path with relatively small amplitude of vibrations. The results from this research show great reduction in the cutting forces that develop, in relatively low cutting speed and feed rate settings. These low forces seem to relate to the fact that BUE is not formed during this process, something that would otherwise take place for the reported settings.

4.2.4 Milling of MMCs

Following turning, another fairly common and widespread machining process that is usually performed for production of MMC products is milling. The analysis that follows is similar in structure to that performed for turning.

4.2.4.1 Parameters of Milling and Tool Wear

Same as turning, products manufactured through milling are often performed in two steps, roughing and finishing. In the case of most MMC milling processes, it is generally acceptable that during the roughing process, parameters should be chosen rather high, whereas the finishing step should be performed in a few cycles and a set of parameters with lower values. Although this general guideline can provide adequate results, it needs to be noted that it is not optimal.

Feed rate as a milling parameter is proven to be one of the most important parameters in MMC milling. Increasing feed rate above a critical value promotes the formation of BUE [18], which may insert instabilities in the machining process when sheared. The shearing of BUE is mainly related to the material of the tool used [22]. On the other hand, a relatively low feed rate leads to a high flank wear of the tool, thus drastically decreasing tool life. In order to maintain a balance in this specific parameter, a relatively high feed rate is often employed with the simultaneous use of coolant, which decreases the size of the formed BUE and enhances chip removal. It needs to be noted though that the use of coolant in high feed rates can decrease tool life for large productions, as the removal of BUE leaves the cutting edge exposed to the increased, from the higher feed rate abrasion [33]. In general, it has been proved that feed rate in MMC milling can heavily affect tool wear, regardless of the tools used [28, 34].

Regarding cutting speed, results show that it is related to the cutting tool wear. In most cases, research shows that an increase in cutting speed is usually accompanied by a simultaneous increase in the flank wear of the tool [18, 22]. This increase in flank wear is thought to have a comparatively lower effect than other parameters [34], although it should not be entirely ignored. Another research proposes that face-milling at a certain speed range can increase tool wear, whereas setting the cutting speed outside this range can increase tool life [35]. It needs to be noted that a correlation between the cutting speed and tool wear is only observed in milling, while in turning or drilling there is no such correlation [22]. The most severe effect in regard to tool wear seems to come from the hardness and volume fraction of the reinforcement particles inside the material [33]. It is generally shown that MMCs with harder particles than others, or with a greater volume fraction of these particles inside the material, drastically increase tool wear. In order to reduce this effect, MMCs that contain certain particles with auxiliary effects to the process are often

employed instead of others. One such example is the use of MMC with Ni-coated graphite particles, which are proven to function as lubricant factors when chipped. Finally, several other parameters can affect tool wear during MMC milling, such as DoC, although their effects on this factor are not mentioned sufficiently in the conducted research.

4.2.4.2 Parameters of Milling and Surface Quality

In regard to the final surface quality of the milled product, feed rate is reported to have a significant impact. Coelho et al. [22] show that an increased feed rate produces a fairly poor surface, as high feed rates favor the formation of unstable BUE. On the other hand, the influence of cutting speed in surface quality is considered negligible. The most important factors in the case of the produced surface, though, lie with the combination of tool and workpiece material. The effects of the tool material, similar to the case of turning, heavily affects the attributed surface, as tools with larger grain size produce poorer surface quality than the finer-grained tools. The material of the MMC can affect the surface outcome, as it affects tool wear, which can subsequently lead to poor surface quality. However, the material of the MMC can bring positive effects in the process as well, especially in the case where some of the chipped particles can function as solid lubricant [35].

4.2.4.3 Proper Tool Selection

Although the possible tools in turning can be chosen from a vast number of categories, effective milling tools are significantly less. In most cases in milling, HSS and carbide tools are not very effective, as they present low tool life, thus increasing the overall cost of the process [36]. Another research indicates that CVD-coated carbide tools are rather improper for milling, as they tend to fracture and fail during certain stages of the process [37]. Moreover, TiCN-coated carbide tools show poor attitude in milling, resulting from their low tool life [33]. Furthermore, PCD tools seem to perform well in various sets of parameters, while they provide adequate results in terms of tool wear and final surface quality. This is mainly attributed to the increased hardness that PCD tools possess, rendering them capable of withstanding abrasion wear, which is the main tool wear mechanism developed in milling [22, 34]. Finally, the greatest performance in terms of productivity during MMC milling is shown from DCC tools [28]. Although these tools may show wider flank wear zones than PCD tools, the flank wear that develops seems to stabilize at a certain point, thus making the whole process steadier. Furthermore, the cutting forces that develop during the process are higher and thus machining of some quite hard MMCs is possible.

4.2.5 Drilling of MMCs

Along with milling and turning, drilling is one of the most widely employed machining process. In the case of MMCs, a lot of research has been conducted regarding the parameters and tools used, as well as their results in the final product. The analysis that follows is similar to those of the previous sections.

4.2.5.1 Parameters of Drilling and Tool Wear

As with the previous machining processes, several factors seem to have a significant effect on tool wear, during the drilling of an MMC. From these parameters, cutting speed provides contradictory results. Coelho et al. [38] proved, while testing drilling of Al-based MMCs with a variety of different material tools and in a number of different cutting parameters, that cutting speed does not cause additional tool wear; similar results are also indicated in other works [36, 39]. On the other hand, increased tool wear while increasing the cutting speed, although the thrust force was decreasing, is reported by Jawaid et al. [40]. In most cases though, the cutting speed is considered to be of minimal importance in terms of the imposed tool wear [26].

In terms of thrust force, Ricci [41] investigated the effects of increasing the thrust force during drilling in tool life. The increase in thrust force was attained through the differentiation of tool material. The results showed no improvement on tool wear. Regarding feed rate, most research shows that it has some secondary effects on tool wear. Generally, feed rate brings a decrease in tool wear as a result of the reduction in the length that is cut [26]. In some cases, it has been proposed a general guideline of $1.5 \cdot d/75$ in mm/rev, where d represents the drill diameter, for feed rate, stands for a fairly good initial value, mainly for a range of drill diameters between 3 and 15 mm. Moreover, a higher feed rate is recommended, as a greater number of drillings can be performed with the same tool before a tool change is needed [36]. Furthermore, chip removal from the drilled hole is one of the main problems faced during drilling of MMCs. The reason for this lies with the increased hardness that chips possess, which can lead to a significantly increased tool wear [14]. A proper design of the tools and use of abundant coolant are auxiliary to this factor. It is recommended that after drilling up to three times the diameter of the tool in-depth, a drill retract should be performed in order to clear the remaining chips from the hole [7].

One of the most important factors that affect tool wear during drilling of MMCs is the MMC material composition. Apart from the determination of the prevailing tool wear mechanism, material composition also affects the type of chips formed [7, 14]. The hardness of the material reinforcements, as well as the ductility of the matrix material, can dictate the appropriate tool, as well as whether some types of faults will be formed during the process or not [11, 33]. Moreover, the volume fraction of reinforcements and their hardness promote one wear mechanism over others, thus thorough investigation of the optimal settings and the proper tool material are needed before every drilling process. Also, depending on the volume

fraction of the reinforcement particles, the formation of the chips may change drastically. If the volume fraction of the reinforcement particles is relatively small, the chips will be continuous and long, whereas if the volume fraction is higher the chip will break on its own [42]. Furthermore, in certain cases, the particles that are removed can function as a solid lubricant, leading to decrease in tool wear. Finally, tool wear is affected by the tool material itself.

4.2.5.2 Parameters of Drilling and Surface Quality

Surface and subsurface deformations that occur during drilling of MMCs can have significant results on the whole material. This is mainly because any damage or rips performed during drilling can lead to a general decrease of the material's properties, such as the causation of several micro-scale damages, increased plastic deformations and residual stresses, as well as changes in the surface hardness [8]. Carefully choosing the proper drilling parameters can minimize or prevent material deterioration.

The main factors that affect the final surface quality of a drilling process of MMCs are the materials of the tool and the MMC. The material composition of an MMC affects the attitude of the reinforcements in drilling. This is mainly due to the hardness that the reinforcements possess, as well as their volume fraction in the material. This factor in combination with the hardness of the material tool will dictate whether the reinforcement particles will be cleanly cut, or will be deformed, or pulled out [11, 43]. Finally, the quality of the final surface is affected by some of the drilling parameters. Both cutting speed and feed rate can significantly affect the roughness of the final surface. Basavarajappa et al. [44] concluded that an increase in cutting speed leads to a lower final roughness. The reverse effect occurred during the increase in feed rate.

4.2.5.3 Proper Tool Selection

In the case of drilling the choice of proper tool is of outmost significance. As mentioned above, both tool wear and final surface quality of the product are affected by the used tool. Furthermore, certain tools can prove rather inappropriate for this process, something which if not treated properly can significantly increase the overall drilling cost.

The most common tools used in MMC drilling are similar to those of the previous discussed processes, namely HSS drills, PCD tipped drills, carbide drills, as well as different types of coated drills, e.g., diamond-coated HSS drills, WC drills, and TiAlN coated drills [14]. Depending on the application needed, several types of tools may present increased tool wear, rendering them improper for use. One such example is WC drills, which present an increase in tool wear for higher values of drilling speed [18]. Weinert et al. [11] claim that certain coated drills present better behavior in drilling, in accordance with the predominant wear

mechanism during the process. This is mainly due to the fact that microcracking and fatigue are the predominant mechanisms during drilling of an Mg alloy, δ - Al_2O_3 reinforced MMC. In this case, TiAlN-coated drills decreased tool wear, compared to diamond-coated drills. On the other hand, when drilling an Mg alloy, SiCp reinforced MMC, diamond-coated drills presented better results, as the predominant wear mechanism in this case is microcutting, in which diamond-coated tools display higher durability than TiAlN-coated tools. Finally, although other tools can be a feasible solution for a specific set of drilling parameters, PCD drills remain, also in this process, the optimal choice. In [39], after comparison between different tools for a large number of parameter sets, PCD drills presented the optimal results compared to tools of different materials. This claim is supported by more research results [11], although many consider TiAlN or other coated drills to be a good alternative to high-cost PCD drills. However, for large-scale productions, PCD drills are preferred [14].

4.2.6 Other Machining Processes

Apart from the above discussed machining processes, several others are used on MMCs. The research conducted for these, though, is sparse and rather focused on certain types of MMCs. Below, some general guidelines concerning these processes are discussed.

4.2.6.1 Tapping

Tapping is usually considered as the most difficult process that can be performed on an MMC, mainly due to its physical restrictions. Research shows that the optimal results are acquired through form tapping, where HSS form taps are usually employed as cutting tools. On the other hand, HSS cutting taps show high wear rate and thus are considered inappropriate for tapping MMCs, as they break in an unpredictable way and fairly quickly. One of the most important factors that should always be considered is the utilization of adequate lubrication, which decreases tool wear and enhanced chip clearance. Finally, while tapping MMCs, a frequent inspection of the created thread, as well as the condition of the tool is considered necessary. It needs to be noted that tool wear is usually estimated by the leading teeth, as these teeth are expected to fail first.

4.2.6.2 Grinding

Grinding along with honing belongs to the so-called abrasive machining processes. The reason lies with the mechanism of material removal, which is abrasion of the surface material. Grinding is not usually performed in MMCs, due to their constant

differentiations in the hardness during a cutting cycle. The recommended tools for this process are usually electroplated diamond grinding wheels. This type of tool performs best in MMCs with high volume fraction, greater than 50 % of the total volume, as in such abrasive materials the bonding material of the grinding wheel can wear and thus the diamond particles are constantly renewed. The grinding parameters are usually determined specifically for each process, in accordance with the desired final surface. However, in the case of grit size of the wheel, it has been proposed that the coarsest grit size that is applicable according to the desired surface should be utilized when grinding MMCs [17].

4.2.6.3 Honing

Honing is similar to grinding; when honing MMCs, stones of metal-bonded diamond particles are usually utilized in the hones. The grit of the stones can vary according to the application, although it is limited to a value that will not overload the stones. Furthermore, the total width of the stones should be low, e.g. lower than 4 mm for honing Al-SiC MMCs, while the total width of all the stones should be lower than 20 % of the tool circumference. The use of guide shoes is often employed, although the guide shoes' material should present increased wear resistance and honing accuracy. Moreover, the use of lubricant is required, so as to effectively clear the removed MMC particles. A common honing process follows a drilling process, while it is usually performed in two steps, rough honing and finish honing. In the rough honing process, a low-grit tool is used for a few minutes, until a percentage of 90 % of the material that remains between the final diameter after the drilling and the desired diameter of the product has been removed. In the finish honing process, a high-grit tool is used for several seconds, until the desired dimensions have been reached. If the dimensions vary from the desired ones after finish honing, a brush-type hone can be utilized. It needs to be noted that, during all of the above steps stone loading should be carefully set through the applied pressure, while the stroking speed and tool rotation should be set according to the dimensions of the used tool.

4.2.6.4 Sawing

If a fairly big part of an MMC has to be cut, a sawing process is often employed. The tools generally used for this process are WC-tipped blades with 1 tooth/cm or more or plain HSS saw blade of similar structure, for most heavy applications. For lighter applications the use of low-grit industrial-diamond blades in high-range cutting speed provides the optimal results. The dimensions of the blade are recommended to be as high as the machine permits, as in this way the deflection of the blade caused during sawing is significantly reduced, thus improving the final quality of cutting. In order to have an effective chip clearance, the use of flood or forced jet type of coolant, as well as the employment of several chip-clearing tools,

such as in-line wire brushes combined with triple-chips, is of high importance. The cutting speed recommended in heavy applications is usually in mid-range, while the feed rate and the pressure should be gradually increased, in accordance with the blade wear. In cold-sawing a similar set of parameters can be employed with the exception of cutting speed, which should be kept in low-range. It is worth noting that when a new saw blade needs to be seasoned, a percentage of 50–75 % of the nominal cutting speed is recommended for the first few sawing processes.

4.2.7 Micro-machining of MMCs

Although micro-machining of MMCs is not widely researched, some first results have been reported. Micro-scaled manufacturing processes research has had a significant growth over the recent years, thus an increase in the research regarding the micro-machining of MMCs is expected in the near future.

Liu et al. [45] gathered a number of works relevant to the subject research and drew some conclusions. In this work, it was shown that the attitude of MMCs during micro-cutting differed significantly from the micro-cutting of multiphase engineering materials. However, the mechanisms that govern this kind of cutting are not yet fully understood. Material parameters, such as the particle shape and size, as well as their volume fraction in the material proved to be highly significant for the process. Several other aspects of micro-machining of MMCs, such as stress–strain distribution, chip formation mechanism, tool wear, and particle fracture mechanism need to be further researched. Venkatesh et al. [46] performed the drilling of Al–SiCp MMCs, using a new type of fine carbide grain micro-drill. The parameters used were high speed drilling conditions, with different feed rates and two different diameters for the micro-drill. After the process, it was shown that the lower feed rate resulted in better peripheral waviness. Furthermore, the tool wear in the microdrills increased with increase of the volume fraction of the particles in the material.

4.3 Nonconventional Machining Processes of MMCs

MMCs have been proven to be extremely difficult to machine using conventional manufacturing processes due to excessive tool wear caused by the presence of their reinforcement or hard reinforcing particles. Moreover, the worst surface finish due to tool–reinforcement–machined surface interactions in conventional machining significantly hinders the use of MMCs. As a result, nonconventional machining techniques, including electrical discharge, AWJ, laser beam, electrochemical, and USM, have also been applied to MMCs. The various nonconventional machining methods of MMCs have their own advantages and disadvantages although it is believed by many researchers that they are more suitable for MMC machining [47–50].

4.3.1 Electrical Discharge Machining

EDM is a machining process for processing geometrically complex or hard material parts that are extremely difficult to machine through ordinary machining processes. EDM has been continuously evolving from a mere tool and die making process to a microscale application machining appealing to many research interests [51]. The key feature of EDM is that the electrode does not make direct contact with the workpiece. As a result, the process eliminates mechanical stresses, chatter, and vibration problems during machining. The material erosion mechanism primarily uses electrical energy and turns it into thermal energy through a series of discrete electrical discharges occurring between the electrode and the workpiece immersed in a dielectric fluid. The thermal energy generates a channel of plasma between the cathode and anode where the temperature can be as high as 20,000 °C, initializing a substantial amount of heating and melting of material at the surface of each pole. When the pulsating direct current supply occurring at the rate of approximately 20,000–30,000 Hz is turned off, the plasma channel breaks down. This causes a sudden reduction in the temperature allowing the circulating dielectric fluid to implore the plasma channel and flush the molten material from the pole surfaces in the form of microscopic debris. EDM can be divided into two categories, namely die-sinking EDM and wire-cut EDM (WEDM). In the die-sinking EDM the shape of the die is machined into the workpiece by feeding the die into workpiece. On the other hand, WEDM uses a thin wire as tool electrode.

Ramulu and Taya [52] used EDM to machine SiCw/Al composites. The machined surfaces were examined by scanning electron microscopy (SEM) and profilometry in order to evaluate surface finish. The results showed that by controlling the cutting conditions, better surface characteristics can be obtained. Higher SiC volumes needed higher machining times. Furthermore, brass electrode had higher composite material removal rates (MRR) than copper electrode. EDM at higher cutting speeds caused severe micro-damage on the surface and subsurface areas. Microhardness tests on the MMC also revealed that EDM appears to cause surface softening at slower cutting speeds. Hocheng et al. [53] conducted a study of material removal in EDM of SiC/Al. They developed a correlation between the electrical current and on-time, and the crater size produced by a single spark for the representative material SiC/Al. The experimental results showed that the SiC particles can interfere with the discharges, despite the fact that the crater size of SiC/Al is larger than steel. They recommended large electrical current and short on-time, for obtaining minimal crater.

Rozenek et al. [54] analyzed the EDM characteristics of AlSi7 Mg with reinforcement of 20 % SiC and AlSi7 Mg with reinforcement of 20 % Al₂O₃. They studied the influence of discharge current, pulse-on time, pulse-off time, and voltage on the machining feed rate and surface roughness during WEDM. The results show that maximum cutting speed of both composites are found to be approximately 3 times and 6.5 times lower than the cutting speed of aluminum alloy, respectively. Yan et al. [48] presented an experimental study on WEDM of Al₂O₃p/6061Al

composites. In the experiments, machining parameters of pulse-on time were changed to explore their effects on machining performance, including the cutting speed, width of slit, and surface roughness. The results revealed that very low wire tension, high flushing rate, and high wire speed are required to avoid wire breakage in machining $\text{Al}_2\text{O}_3\text{p}/6061\text{Al}$ composites. Chicosz and Karokzak [55] studied the machinability of $\text{Al}/\text{Si}/\text{Mg}-\text{Al}_2\text{O}_3$ MMCs with EDM. They investigated the effect of current on the surface layer formation of machined surfaces and they found that the optimized pattern of current density and frequency of sparks is the main factor that improves machining performance.

4.3.2 Abrasive Water Jet Machining

In AWJ machining, materials are removed by impact of a continuous stream of high pressure and velocity water and abrasive slurry to cut the target material by means of erosion. The small abrasive particles act as cutting tools. During the cutting process the abrasive water jet exerts machining force on the workpiece causing the cut, while at the same time the water flushes away the machined chips. The attack angle is defined as the angle between the initial jet direction and the particle cutting direction at the point of attack. Though the abrasive water jet technology can be used for almost every material, it has received considerable attention in machining of difficult to machine and thermally sensitive materials [56].

Savrun and Taya [57] investigated the feasibility of machining of SiC whisker/2124 aluminum composites by AWJ. The results show that abrasive water jet machining is fast and yields relatively smooth surfaces with minimum sub-surface damage on MMCs. Machined surfaces do not show any microstructural changes and the microhardness tests on the MMCs have revealed that AWJ does not work-harden the surface. Also, AWJ does not cut MMCs SiC whiskers, and it either pulls or breaks them, but erodes the aluminum matrix. Impact of abrasive particles caused localized micromelting in the matrix and also abrasive particle embedment was observed. Hamatani and Ramulu [58] studied the AWJ machinability of particulate reinforced metal SiC/Al matrix composites. Machining performance was reported by both cut quality as measured by taper and machined surface characteristics. Based on these experiments, MMCs are easily machinable by abrasive water jet and good surface-finish can be produced. It was noted that kerf-taper ratio depends on cutting speed and abrasive size. With increase of cutting speed, the difference between top and bottom widths of the slot reduces. The accuracy of AWJ machining can be depicted by the degree of taper and precision machining would require a cut with little or no taper. Hashish [59] studied the machining capabilities of composites with abrasive water jet machining. The results show that by increasing the reinforcing particle volume, the AWJ cuts become more tapered, indicating greater resistance to jet penetration. Kerf taper correlates with surface waviness; bigger taper leads to wavy and striated surfaces. Also, drilling MMC with AWJ experiments resulted in rougher holes in comparison to typical

metals and higher surface waviness which was significantly affected by the transverse rate and DoC. In addition, the surface characteristics of the cut can be affected by the particles size of the reinforcing and abrasive particles effect. Larger reinforcing particles in MMCs than an abrasive particle impacting the metal matrix affects significantly the micro/macro characteristics of the penetration process.

4.3.3 Laser Beam Machining

Laser beam machining (LBM) is a widely used noncontact type, thermal energy-based advanced machining process. LBM can be applied for almost a whole range of materials and is not only limited to conductive materials. Laser beam is focused for melting and vaporizing the unwanted material from the parent material without the need for electrolyte, electrodes, high voltage, or electric spark. Various types of lasers have been developed for industrial machining with the CO₂ and Nd:YAG lasers being the most established. LBM can produce complex geometry cuttings and narrow width cut openings of 0.25 mm width. Therefore, materials with favorable thermal properties, such as low thermal diffusivity and conductivity, regardless of brittleness or hardness, are particularly well suited for laser machining. However, the surface quality of a laser made cut is usually relatively poor [60]. It is worth noticing that laser processing is also used for MMC welding [61].

Dahotre et al. [62] experimented on EBM of SiC/A356-Al alloy. The SiC/A356-Al MMCs were processed using several different laser-specific energies. The results showed that extent of reinforced material SiC-matrix A356-Al reaction is directly proportional to the laser energy input. By increasing the energy input, SiC particle dissolution becomes greater and aluminum carbide formation increases in both size and quantity. By controlling the amount and mode of energy input it is possible to control substantial physical and chemical change in reinforcing particles. Muller and Monaghan [63] studied the machinability of SiC particle reinforced aluminum matrix composites using LBM. The results showed that LBM presents many productivity advantages for rough cut-off applications. It is clear that laser machining is suitable for high feed rates of up to 3,000 mm/min. The reinforcing SiC ceramic particles allow reduction in the optical reflectivity of the material and as a result they improve the composite machinability. However, the quality of the laser cut surface is relatively poor and the kerf width is larger than that of the corresponding metal without the reinforcing particles. Striation patterns on the cut surface and burrs at the exit of the laser were also observed, though the striation surface obtained on the MMC was smoother than the corresponding results of metal without the reinforcing particles, which can be attributed to the more viscous melt that hinders striation formation. Also, the significant thermal input of the process induced microstructural changes within the MMC.

4.3.4 Electrochemical Machining

Electrochemical machining (ECM) has high potential on account of versatility of its applications and is expected that it will be a promising, successful, and commercially utilized machining process in the modern manufacturing industries. ECM is an economical process and applies in the machining of high strength and heat resistant materials into complex shapes which are difficult to machine by conventional techniques. During ECM the material is removed by controlled electrochemical dissolution process of a workpiece where workpiece and tool are anode and cathode, respectively, and are separated by an electrolyte. ECM starts when applying a voltage that induces a current between the workpiece and a counter electrode. At this stage, the anodic workpiece dissolves locally and the shape of the removed material in the workpiece is approximately a negative mirror image of that of the tool. The electrolyte is a concentrated salt solution which is pumped through the machining gap at high velocity to remove the reaction products and to reduce heat generation. ECM generates no burrs or stress and has a longer tool life, with damage-free machined surface, high MRR, and surface quality [64, 65].

Senthilkumar et al. [66] utilized effectively ECM on Al/10%SiC composites produced through stir casting. The results showed that various process parameters, namely electrolyte flow rate, electrolyte concentration, applied voltage, and tool feed rate greatly influence the surface roughness characteristics and the MRR. The MRR increases with increase in any of the machining parameters. However, at higher level of machining parameters, except applied voltage, high surface roughness is introduced. It is argued that this is attributed to the fact that increase in voltage causes excessive heating of electrolyte and a corresponding deterioration of the workpiece surface, which will increase the surface roughness. Sankar et al. [67] used ECM on aluminum/boron carbide/graphite composite using pre-shaped cylindrical copper tool electrodes. In order to increase the material removal rate and surface quality of the work, SiC abrasive particles of 50 μm size were used along with NaCl electrolyte. The results showed that abrasive assisted ECM imposes minor changes in the course of the anodic dissolution process. Also, due to the fact that the MMC reinforcing particles are poor conductors of electricity, increase in the volume of reinforced particles leads to decreased electrical conductivity of the composite, which decreases the MRR and hinders the anodic dissolution process. The negative impact on the anodic dissolution process was effectively resolved by incorporating SiC abrasive medium in the electrolyte flow path. During abrasives flow with electrolyte the reinforcement is removed effectively due to abrasion, which gives a smooth surface and improved machining performance. Abrasive assisted ECM exhibited higher MRR than ECM and resulted in lower surface roughness than the ECM process.

4.3.5 Ultrasonic Machining

USM is another nonconventional mechanical material removal process generally associated with low material removal rates. However, the main advantage of USM is that its application is not limited by the electrical or chemical characteristics of the workpiece materials. Typical ultrasonic machining converts high frequency electrical energy into mechanical vibrations via a transducer/booster combination, which are transmitted through a horn/tool assembly. This causes the tool to vibrate along its longitudinal axis at high frequency, usually ≥ 20 kHz, at amplitude 5–50 μm . A load is applied to the tool and abrasive slurry is pumped around the machining zone. The tool vibration causes abrasive particles held between the tool and workpiece to impact the workpiece surface resulting in material removal by microchipping. Variations on this basic configuration include non-machining ultrasonic applications such as cleaning, welding, and chemical processing and ultrasonic assisted conventional/unconventional machining such as turning. Piezoelectric actuators are widely used as transducers in ultrasonic machining applications, as well as in precision positioning applications [68].

Zhong and Lin [69] experimented on diamond turning with ultrasonic vibrations assistance of an aluminum-based MMC reinforced with SiC particles. The results showed that the roughness of the MMC surface turned with vibrations assistance was better than that turned without vibrations assistance. Though, turning with vibrations assistance created regular surface profiles along the cutting and vibration direction, resulting in a light dispersion phenomenon. Nath et al. [70] applied the ultrasonic elliptical vibration cutting (UEVC) method of sintered WC using PCD tools at different cutting conditions; additionally, conventional turning experiments were conducted with the same parameters. The cutting performance improved with decrease in both feed rate and cutting speed in the UEVC method like the conventional turning method. In addition, with UEVC better surface roughness was achieved. In the UEVC method, the PCD tools used in cutting sintered WC achieved better results at a specific DoC of 4 μm compared to both a lower DoC of 2 μm and higher depths of cut of 6 and 8 μm . Thus, the tests presented that UEVC method can be applied for precision manufacturing.

4.4 Machining Modelling of MMCs

The extensive experimental study of MMCs properties, of the MMCs machinability using various manufacturing processes, both conventional and nonconventional, and the consequent phenomena appearing in these processes cannot be sufficient for thorough understanding of MMC machining processes due to inherent disabilities in the experimental methods. Therefore, analytical and numerical models have been used in accordance with the experimental work with regard to a deeper investigation of MMC machining. The tremendous improvement in terms of available

computational power facilitated the use of well-established numerical methods such as the finite element method (FEM) in various studies concerning the behavior of MMCs and the simulation of MMC manufacturing processes. Furthermore, an increasing trend exists in MMC machining processes simulation using soft computing methods such as, the artificial neural networks (ANN), often combined with an optimization study as an alternative to traditional numerical simulation techniques.

Accordingly, in this section a review of the developed analytic methods, numerical simulation techniques, atomistic simulation techniques, and soft computing methods is attempted with a view to provide an essential and practical guide for researchers who want to investigate MMC machining processes.

4.4.1 Analytic Models for MMC Machining Processes

Several analytic models concerning machining processes of MMCs have been developed. Although these models were primarily in use before the tremendous increase in application of numerical simulation methods, they can still provide a fundamental understanding of various subjects such as cutting tool wear, machinability, cutting forces, stresses, material strength, damage, failure, and fatigue in MMC machining. The analytic models can be divided into three main categories based on their derivation: the models derived from (i) the theory of elasticity and the theory of plasticity, in the case of material strength, damage, failure and fatigue investigations, (ii) the Taylor formula, especially in the case of tool wear and machinability studies, and (iii) the Ernst-Merchant orthogonal cutting theory, in the case of cutting forces investigation. The theoretical models related to each of these three categories are presented in this section.

An ideal wear model would help to reduce the cost of machining experiments [71]. Tool flank wear progression can be modeled as a function of tool/workpiece properties and cutting parameters. Wear volume models considering the so-called two-body (Archard's relation) and three-body (using Rabinowicz relation or its modified version) abrasion models are employed for different mechanisms of wear. Thus, volume loss is related to cutting speed, load, hardness, particle size, volume fraction, and spaces between particles. The volume loss calculated from each model is combined in a formula, along with the necessary modifications considering the geometric characteristics of the cutting tool, to calculate the total volume loss [72]. Tool wear acceleration, caused by the interference between the reinforcement particles, is modeled using relationships based on geometric characteristics of reinforcement particles and their movement. In order to study tool wear acceleration, the critical reinforcement weight ratio is calculated as a function of the density of the matrix and the reinforcement and a dimensionless ratio related to the cutting tool edge geometry and the size of reinforcement particles. The proposed model helps the development of MMC machinability maps [73]. Prediction of tool life is attempted using cumulative damage models derived from Taylor equation that

relate tool life to the cutting speed [74]. Models based on the modified Taylor equation can be used to optimize machining conditions and study tool performance and related subsurface damage [75]. By incorporating the workpiece volume removal in the Taylor equation, by using experimental data and regression models, a generalized model of tool wear rate can be derived [76]. Subsurface damage types on machined MMCs could be identified in [77] using a previously developed model by verifying it with MMC machining data.

An energy-based analytic model for prediction of cutting forces in orthogonal cutting conditions was proposed in [78]. The total specific energy and the debonding energy were estimated as function of volume fraction and material properties using analytic expressions in the primary and secondary deformation zones. The calculation of the resultant cutting force is proposed as the sum of chip cutting forces, plowing forces, and forces caused from debonding and fracture of the reinforcing particles. Cutting forces are calculated from the Merchant model using the Johnson–Cook model for the shear strength, two factors, after the Colwell model, for the incorporation of the influence of the cutting edge geometry and a separate methodology to determine the friction angle taking into account abrasive and interface phenomena [12]. The plowing force is calculated by the slip line field model and the particle fracture force was related to the debonding energy; a similar model for calculation of cutting forces is proposed in [79]. The chip–tool interface friction is used to predict the cutting force in an oblique cutting method [80]. Quantitative analysis of chip forms can be conducted by measuring the thickness and estimating the effective shear angle from an analytical formula. Statistic analysis was conducted to investigate the important parameters affecting the effective shear angle [81]. Furthermore, the relationship between shear angle and friction angle for an MMC was investigated to estimate cutting forces and contact stresses at the chip–tool interfaces more accurately [82].

The degree of load sharing, which plays an important role in fiber breakage during tensile straining and consequently to composite strength and variability, and is governed mainly by the interfacial shear strength, is investigated using the fiber bundle strength formula [83, 84]. The predictions are compared to experimental results which are rationalized using Weibull statistics for the fiber strength and Gaussian distribution for fiber volume fraction. Shear-lag model (SLM), which considers the micro-damage phenomena of interfacial debonding and interfacial yielding, can be employed to study the mechanical behavior of MMCs [85]. By conducting Monte Carlo simulations, the ultimate tensile stress can be obtained. An alternative method is the Green's function method, used for simulation of fiber damage evolution and tensile strength [86]. It was found that this method can be employed in many cases where the SLM model cannot be easily employed and reduces the computational cost significantly. Composite strength and its size dependence was investigated using a Monte Carlo simulation model based on the 3D Lattice Green's function technique; the algorithm is described in [87]. Furthermore, the elastoplastic field on a machined MMC was calculated using an integral approach and a convergence criterion for ellipsoidal particles under thermal and mechanical loads in an iterative process [88]. A similar technique is applied to

elongated particles or prolate ellipsoids [89]. A modified Eshelby model was employed in elastoplastic calculation for oblate, prolate, and spherical inclusions using an iterative method [90]. Another modified Eshelby model, considering the reinforcement orientation distribution was found to be in accordance with experimental data [91]. Furthermore, a model for the fatigue crack growth life prediction is proposed in [92]. Finally, the Buriansky–Fleck model is used to simulate plastic kinking, which is considered as a significant failure mechanism [93].

4.4.2 Numerical Macro and Microscale Models

Macro and microscale simulations of MMC machining processes constitute nowadays the most important nonexperimental part of MMC machining investigations. The increasing capabilities of modern computer systems allow more demanding and detailed simulations to be conducted using specialized software. The majority of modelling concepts in the numerical simulation of MMC machining processes is common with the modeling of metal cutting processes but several specific details, characteristic to the particularities of MMCs, are introduced so as to increase the accuracy of simulations. The use of FEM is dominant but several studies using the boundary elements method (BEM) exist due to its capability of dealing with interfaces, which is a fundamental subject in MMC machining simulations. The results of FEM simulations are often used as input for soft computing methods, such as ANN and response surface methodology among others, in order to develop specialized and inexpensive simulation tools. In Fig. 4.3, the initial mesh in FEM simulation of an MMC is shown, where the reinforcement particles are modeled as separate areas within the matrix material.

All categories of MMCs, namely fiber reinforced metal matrix composites (FRMMC), particle reinforced metal matrix composites (PRMMC), and whisker

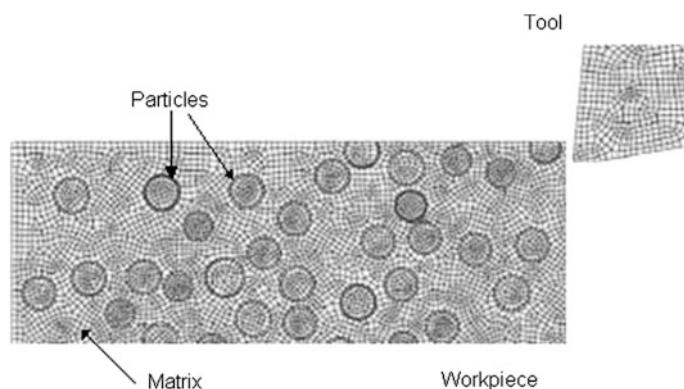


Fig. 4.3 2D FEM model initial mesh for simulation of MMC machining

reinforced metal matrix composites (WRMMC) [94–96] have been investigated through use of numerical methods. In the majority of cases, FRMMC and PRMMC are considered. A special category of MMCs, the metal matrix nanocomposites (MMNC) is referred in the relative literature and will be considered separately. Furthermore, a brief description of multi-scale methods, which combine the macro and microscale simulations, primarily with FEM, with nanoscale simulations, primarily with the molecular dynamics method, will be also presented.

Numerical simulation methods are employed for various subjects concerning MMC machining processes such as: the prediction of yield and collapse of an MMC by calculating the residual stresses and the influence of the interface [97], the simulation of ultraprecision machining of MMCs with diamond tools and the study of surface roughness [98, 99], the study of deformation behavior of MMCs [96, 100], damage and fracture of MMCs [101–104], creep [105, 106], surface integrity and tool wear [107–109], modeling of grinding [107], edge defects and their formation [110], subsurface damage [111], residual stresses in the machined workpiece [112], and the effect of volume fraction and fiber characteristic in the interfacial stress [113]. Although some of these subjects are not directly associated to machining process simulation, it is fundamental for the engineer who desires to machine MMCs to have a deep knowledge of the behavior of these materials.

4.4.2.1 General Modelling Methods

The nature of MMCs, which are composed of a macroscale metal matrix with microscale reinforcements and the fact that the principal phenomena concerning their machining appear in the microscale dictates the use of a combined macro and microscale simulation method in every case. In general, three categories of simulation methods exist in the literature: macro models, micro models and unified micro–macro models [114, 115].

In the macro models approach [114], the composite is considered as a single continuum or equivalent orthotropic homogeneous material (EOHM), something that can be regarded as a very rough estimation suitable for the prediction of global quantities such as the cutting forces. On the contrary, micro models treat the reinforcement, particles, fibers, or whiskers as distinct from the matrix and so, the effect of various parameters concerning these reinforcements can be investigated. However, some approximations need to be used in the micro models and a detailed modeling of the fiber-matrix interface needs to be performed [115]. Another solution is to employ unified micro–macro models in order to simulate effectively the MMCs [111, 116, 117]. Usually the microscale model is embedded in the macroscale model in the case of micro–macro unified models. The length of the macroscale model is often hundreds of times larger than the scale of the microscale models in order to reduce undesirable influences on the deformation behavior of the microscale models [117]. Adaptive mesh techniques or a special mesh for each zone can be employed. In [111] a multi-step model using also a cohesive zone model (CZM) is employed. A suggested reference for further reading on the micro–macro

models is the work presented by Kouznetsova et al. [48]. Nowadays, the popularity of the unified micro–macro approach is significantly greater and many future studies are expected to be conducted using this approach.

Although the FEM method is the most common simulation method employed, several studies exist where alternative analysis methods, such as the method of cells, are extended to full simulation methods like the generalized method of cells (GMC) [119–121] and the high fidelity generalized methods of cells (HFGMC) [103, 122]. The GMC is a full micromechanics model, adequate for multi-phased materials with arbitrary periodic microstructures. It can provide constitutive equations for MMCs using viscoplastic deformation, failure, and damage models for each phase [121]. The HFGMC method can be used for a refined nonlinear analysis of multi-phase composite materials. Its main difference from the GMC is the use of a higher-order displacement expansion and various reformulations exist [122].

4.4.2.2 Geometric Modelling Aspects

The modeling of the geometry of metal matrix composite is an intriguing subject. The main difficulty is the accuracy of description of the reinforcements geometry. The cell concept is the most extensively used to simulate MMCs where a representative volume element (RVE) of the actual material is studied. Some of the geometric modelling methods account not only for the geometric representation of the composite but also for its behavior and consist of fully self-consistent methods for simulation of MMCs or can be combined with FEM models in order to perform more realistic simulations.

RVE is a fundamental concept in MMC simulations. The RVE dimensions should satisfy both the requirements of being statistically and microstructurally relevant and being not exceedingly large, in order to be computationally efficient. The critical size of an RVE is determined by quantitative criteria so that the geometry of the RVE stays barely influenced by size effects. More specifically, deterministic size effects are induced due to incorrect choice of the ratio between the macroscopic scale and the microscopic fracture zone and the influence of boundary conditions, while statistical size effects arise due to poor spatial distribution and orientation of fibers [123]. Using the RVE concept, the composite is replaced by an array, regularly or unevenly spaced, of inclusions embedded in a matrix.

The smallest, fully informative segment of the array is called a unit cell. The unit cell approach with periodic boundary conditions was one of the earliest methods to represent the MMCs. A rectangular array of cells was assumed and the reinforcements were positioned inside the composite using a certain packing arrangement, e.g., square or hexagonal [97, 124–126]. In cases when symmetry can be assumed for reinforcement, the RVE can be reduced to one-quarter of the original cell, thus simplifying the simulation [97, 113]. Later, due to necessity of conducting simulations with random fiber arrangements in the MMC, the unit cell method was further extended. The simplified unit cell model [6] assumes an RVE consisting of a

number of unit subcells surrounded randomly by matrix cells [127]. The self-consistent embedded cell method (ECM) was proposed in order to remove the unrealistic constraints imposed in the cell methods [104, 124, 125]. Using the ECM, a fiber of a circular cross-section or a spherical-shaped particle is surrounded by the metal matrix which is embedded in the composite. The inclusions can be nonperiodic, thus closely simulating the actual geometry and also complicated cell geometries like elliptic can be studied. An orientation distribution function (ODF) can be employed for the study of nonspherical and nonaligned inclusions [128, 129]. Additionally, the combined cell method (CCM) [25] was used to study the mechanical behavior of short fiber reinforced MMC combining results from different 2D and 3D cell models [130]. In the case of discontinuous fiber architectures, the generation of the inclusions inside the RVE is usually performed using a random adsorption model, the random sequential adsorption (RSA), the Monte Carlo (MC) method or the simulated annealing (SA) method. The RSA model generates the reinforcement at random positions and then checks for intersected or overlapped inclusions [104] while the MC method and the SA method produce an initial arrangement for the reinforcements and then adjust this arrangement in order to achieve the required statistics in the RVE [126].

4.4.2.3 Modelling Parameters

The choice of adequate modeling parameters for a numerical study is crucial. Parameters such as the dimensionality of the problem, i.e., 2D or 3D and the relevant assumptions, finite element type for FEM studies, boundary conditions, and type of analysis, i.e., thermal, mechanical, or their combination, are the most important modeling parameters. Although the basic aspects of the choice of modeling parameters that are valid for every FEM machining study are also valid in MMC machining studies, it is considered helpful to summarize some of these aspects here.

Both 2D [97, 99, 110, 114] and 3D [101, 109, 124] models can be used for MMC machining studies. However, the more accurate representation of the process is performed by 3D models rather than 2D models with plain strain assumptions, when adequate computational power is available. Several types of finite elements can be used in the finite element studies such as 4 or 8-noded elements for 2D models [99, 110] or tetrahedral elements for 3D models [109]. Symmetric boundary conditions allow for a 3D model to become more manageable in terms of computational cost. The workpiece is usually displacement-constrained in order to prevent undesired rigid-body motion and the cutting tool can be considered a rigid body if the tool deformation and wear progression is not to be studied. Thermal effects and various heat sources can be employed in a coupled thermo-structural analysis. The analysis can be either coupled or a two-step procedure, where the mechanical analysis follows the thermal analysis [108, 112]. Finally, in some cases the cutting forces can be applied also as boundary conditions instead of being calculated through the contact interaction between the tool and the workpiece [108, 112].

4.4.2.4 Material Models and Properties

Various material models can be employed for the metal matrix and the reinforcement materials, depending on each case and on the level of accuracy required in the modelling of the machining process. The metal matrix material can be modeled using: isotropic homogeneous material model [98], temperature-independent bilinear kinematic hardening material model [100], temperature-dependent material model [112], Johnson–Cook model [109, 110], either elastic or plastic deformation depending on the local effective stress level [113], elastoplastic material [97, 126], exponential hardening law elastoplastic [117] model. For the failure, the Zhang failure criterion [98, 99] can be employed. The reinforcement material can be modeled using a linear elastic material model [97, 100, 102, 110, 114, 124–126], i.e., using the generalized Hooke's law, or a temperature-dependent model [112]. In case of failure, a normal stress failure criterion was proposed in [99]. Furthermore, in MMC simulations the Ramberg–Osgood equation power law for plastic, isotropic hardened materials, combined with a von Mises yield criterion can be used as a material model, too [101, 124, 125]. In other cases, a rule of mixture for the averaging of metal matrix and reinforcement materials' properties can be employed and global properties for an equivalent homogeneous material can be obtained [114, 127]. In cutting simulations, the cutting tool can be modeled using a tool wear model such as the abrasion tool wear model of Rabinowicz [108]. Finally, the Tsai–Hill [114] or alternative criteria [110] can be employed for modelling of chip separation.

Modelling of the interface between the metal matrix and the reinforcement is a fundamental subject in MMC machining simulations. Although in several studies a very strong interface with perfectly bonded reinforcements and no occurring debonding is often assumed [110, 113, 124–127], a cohesive zone model can be assumed in order to model the interface more realistically. Several phenomena related to the interface between the metal matrix and its ceramic reinforcements such as: interfacial debonding, trans-granular and inter-granular fracture, frictional sliding and thermal residual stresses can be modeled using a cohesive zone law. Empirical data from experiments are usually employed to properly formulate a law for the traction-separation behavior of the MMC interfaces [106, 111]. In a following subsection, a reference to molecular dynamics calculations for establishment of cohesive zone laws is made.

4.4.2.5 Boundary Element Method Simulations

The boundary element method (BEM) is considered capable of simulating more accurate models of MMC with less computational cost than FEM [131]. Using the BEM only a boundary solution needs to be obtained in order to determine the required solution in the computational domain. Thus, BEM reduces the dimension of the problem by one [132, 133], as only boundaries between different regions are discretized and not the whole computational domain. Furthermore, BEM allows the

interface between the metal matrix and the reinforcement to be modeled efficiently and accurately [134–136]. Thus, this method is especially useful in MMC simulations in which the accuracy of geometric modeling of the reinforcement and the interface between the two phases is essential. BEM is observed to have a relatively rapid convergence of the solution [132], it has a potential for complex composite architectures [137] and also a higher order of accuracy of the solution can be achieved. However, difficulties such as evaluation of singular and nearly singular integral in several cases exist [135]. BEM has been successfully employed in problems with both fiber [133–135, 137, 138] and particle reinforcements [131, 132], 2D or 3D models for the computational domain, for structural [131, 132, 134–139], thermal [132, 133, 137], interfacial [134–136] problems, i.e., effect of microstructure, cracks, and stochastic defects.

Special features of BEM or several modeling concepts can be employed with a view to use BEM for efficient simulation of MMCs. Circular shaped-unctions can be used to convert 2D integrations on fiber reinforcement into 1D integrations [137]. Cylindrical-shaped fibers in a 3D matrix can be represented by multiple curvilinear line elements [133, 139]. A trigonometric shape function can be used to model the variations in the temperature and flux field in the circumferential direction along with a linear or quadratic variation in the longitudinal direction [133].

Several approaches discussed in previous subsections can be combined with BEM as well. The unit cell approach can be used to model discontinuously reinforced MMCs [132], mainly with plane strain or axisymmetric models. The model of an entire cell allows an arbitrary shape and orientation of the reinforcement particle [132]. In [133] where the reinforcing fibers have a prescribed radius, the arrangement of fibers can be easily varied without remodeling by changing the fiber radius. A parallel implementation of BEM is presented in [135] to replace the traditional unit-cell models by analyzing large RVEs with over 100 individual fiber cross-section in the domain. The embedded cell approach with periodic, uniformly spaced fiber arrangement in square and hexagonal embedded cells is employed with fully bonded interfaces in [138].

4.4.3 MD Models

Simulations conducted using the molecular dynamics (MD) method concerning MMCs are considered both as a tool to model microstructure-related topics in macro and microscale simulations and as a tool to investigate the behavior of a special category of composite materials, the MMNC. These are composite materials with nanometerscale reinforcements, usually less than 100 nm in size. An alternative definition includes also the composites comprised of a nanoscale matrix. A further improvement of material properties is noted but it is difficult to achieve a clearly homogeneous structure [140]. These composites are proven to exhibit important penetration resistance and thus, they are particularly useful in military applications [141].

The MD method can provide the required atomic level information on the high-strain rates deformation mechanisms and may be helpful in interpretation of experimental observations. The accuracy of the MD simulation results depends heavily on the accuracy and adequacy of the selected potential function. For systems with metal-covalent bonds, existing in metals and ceramic materials, such as the MMC, an alternative version of the well-known embedded atom model (EAM) potential, the A-EAM potential was proposed in order to facilitate studies on the design of new alloys [141, 142]. This potential combines already existing potentials, i.e., the EAM potential for the metal matrix and the Stillinger-Weber potential for the reinforcement, and involves reformulation of the electron density function employed in the EAM potential. Another modification of the EAM potential is the MEAM potential, which includes angular dependencies to describe the electronic orbitals [143]. The EAM, Buckingham, and Tershoff potentials [144, 145] are used to model the matrix and reinforcement materials as well as special formulas [144] or simpler potentials such as the Morse potential, parameterized from ab initio data [145] for the matrix-reinforcement interface.

The MD method can account for the interface effects and interface mechanical parameters more accurately so as to improve material performance with minimal cost compared to expensive and rare experimental methods. Using the MD method, several aspects concerning the metal matrix-reinforcement interface such as the impact of matrix texture configuration or volume fraction on composites properties [144], fracture phenomena [146], interface failure due to porosity [143], or failure initiation [142] can be studied. Conclusions on the strengthening effect and the dislocations in the matrix-reinforcement interface can also be drawn [144].

Modelling of the interface between metal matrix and reinforcement in macro-microscale simulations is often attempted using cohesive zone models [145, 147]. The cohesive zone is used to transfer the traction loads between the two phases until a separation criterion is reached and the interface is no longer able to carry loads [145]. As the macro-micro models cannot properly account for the atomistic phenomena present in the matrix-reinforcement interface, a combination of these methods and MD method is often more desirable in order to obtain more accurate traction-separation laws [111]. In the first MD studies, only relatively small in size single phase materials were used. Later, MD simulations for a more realistic approach to the interphase mechanics were conducted [145]. The empirical traction-separation laws for the cohesive zone were validated and the results showed good agreement with experimental investigations. These multiscale methods are more preferable due to the fact that it is still considered infeasible to conduct multibillion atomistic simulations [2]. Two method types are primarily employed for the combined continuum-atomistic or multiscale simulations: the quasi-continuum method [148–150], proposed by several researchers, and the hierarchical model [148, 151, 152]. In the quasi-continuum method, a small representative subset of atoms is examined in order to reduce the cost of the hybrid study [148], while in the hierarchical model an MD model is run at first, to determine the traction-separation law and these data are then introduced in a continuum simulation model.

4.4.4 *Soft Computing Models*

A variety of soft computing methods, namely ANN [153–158], Taguchi method [154, 159, 160], regression models [153, 160–162], response surface method (RSM) [161–169], data-dependent systems (DDS) approach [159, 170–173], genetic-fuzzy and gray-fuzzy methods [174–176] have been employed in several studies concerning the simulation of manufacturing processes of MMCs as a rather inexpensive way to obtain realistic results. These methods can utilize data both from experimental studies and numerical simulations and model various MMCs machining processes.

Among the aforementioned methods, ANN is the most extensively used soft computing method in MMC machining simulations. ANN is a computational technique capable to simulate systems that cannot be described easily using an analytic model, by employing a system of interconnected neurons which process input values to produce the desired outputs after a sufficient training period. Further details for the characteristics of the ANN can be found in [155, 156, 177]. Specifically, using ANN, various structural characteristics and material properties of the composite, as well as various machining process outputs such as surface roughness, cutting force/torque/speed or quality measures such as cylindricity and circularity have been already studied. A wide range of input parameters are employed in the simulations such as operating characteristics, geometry of reinforcements, and inherent parameters of machining process, i.e., DoC, cutting tool geometry and speed, cutting forces.

All researchers who have employed the ANN in MMC machining simulations conclude that the results obtained by ANN present very good agreement with the experimental or numerical results and can be considered a highly reliable method. Some crucial issues for successful application of the ANN are primarily the determination of the number of hidden layers and the number of neurons in each hidden layer as well as the more suitable training algorithm. The choice of the proper training algorithm is case sensitive and often an extensive search for the optimal learning parameters such as learning rate and momentum factor is required; long training sessions are performed before the ANN can be used effectively as an analytical tool. However, once the best set of parameters is determined, the ANN is proven to be a very cost and time-saving tool which can be employed especially when the relationship between the various machining parameters is nonlinear, not only to predict the system response when experimental or numerical data cannot be obtained, due to cost or experimental constraints, but also to improve the accuracy of predictions achieved by other techniques or even to replace partially the need of experimental measurements and thus reduce testing time and cost.

The Taguchi method is a statistical method, often employed before a run of experiments or even numerical simulations, so as to determine the plan of experiments by choosing the exact values of every parameter involved in each experiment. The purpose of employing the Taguchi method is to conduct the desired experiments in an organized and controlled way so as to find the minimum set of

experiments for a given number of variable parameters, called factors, and a given number of values, called levels, for each parameter. The Taguchi method uses an orthogonal array and produces a set of proposed experiments by defining their characteristics in a random way. Then, after the execution of experiments or numerical simulations is completed, the set of results are often treated using the analysis of variance (ANOVA) in order to determine the effect of each factor to the final result as well as the effect of the interaction between different factors. At a later stage, correlation between the factors is also obtained by ANOVA analysis. Apart from ANOVA analysis, the Taguchi method can be combined with a gray relational analysis [160].

An alternative method for establishing analytical relationships between experimental data is regression models. Regression models constitute one of the fundamental prediction methods and are related to the least-squares method. Various forms of data fit can be employed such as linear, quadratic or power law. The determination coefficient R^2 is primarily used as a measure of accuracy for the model. As in many cases of machining processes more than one parameter is studied, the multiple regression method is readily employed [153]. Usually, a confidence level of 95 %, equivalent to a significance level of 5 %, is desirable [160, 178] but also the establishing of a ± 10 % zone for the error of the approximation is considered acceptable. While prediction using ANN is shown to be more accurate [153], regression models are still widely employed especially as a means of a first investigation of the relationship between experimentally obtained data.

In accordance with the other soft computing methods described, ANOVA can also be conducted with a view to determine the insignificant factors before the regression model is created [166, 178]. The RSM is the second more employed soft computing method in modelling of MMC machining processes and exhibits a close relationship with the regression models. The RSM method is a collection of experimental strategies, mathematical, and statistical techniques that are useful for the modeling and analysis of problems in which a response of interest is influenced by several variables and the objective is to optimize this response. Furthermore, it enables an experiment to make efficient empirical exploration of the system of interest. Thus, it helps to quantify the relationships between one or more measured responses and the vital input factors. Before the RSM method is applied, a statistical analysis of experimental data is often required. The independent variables are presumed to be continuous while the response variable is considered to be a random variable. A suitable functional relationship of the independent variables and the response variable is assumed. This function is usually a second order polynomial in terms of the independent variables and essentially describes the behavior of the system within the experimental region, when the exact mathematic form of the relationship between the system inputs and output is not known. An error term, called noise, is used, which measures the experimental error. ANOVA is used to summarize the required tests for the validation of the model: test for significance of the regression model, test for significance of individual model coefficients, and test of lack of fit. The value of the determination coefficient R^2 is used, as in the case of regression models, to measure the wellness of the fit.

Like the ANN method, the RSM method is also suitable to be used in both linear and nonlinear problems. The RSM method is more able to ignore the contribution of the insignificant factors in the calculation of the output and the contribution of each factor to the result is more visible than in ANN but requires a well-defined value range for each factor involved and is not able to determine efficiently the response of the system outside the experimental region. ANN is also proved to be more accurate in certain cases, especially in cases where a highly nonlinear behavior is exhibited [163, 165]. However, the use of the RSM method requires significantly less calculations than ANN. The RSM method is often used in optimization problems [161, 163, 167], as well as the ANN because they constitute two reliable and inexpensive techniques to obtain the response of a system, given a set of design variables.

The following operations are generally followed during modelling of experimental results using RS methodology: (i) construction of a statistical response surface model for experimental observations, (ii) determination of the unknown coefficients of the model using a statistical estimation method, the regression coefficients can be estimated using a number of available experimental design techniques [163], and (iii) calculation of the stationary point of the RS model. A more detailed explanation of the RSM method, including the steps and formulation of the equations, can be found in [163, 164, 168].

DDS analysis can be employed as an alternative soft computing method. Its applicability was first investigated to modal analysis, single-grit scratching, before it was applied to MMCs. This method was introduced in MMC machining processes modelling due to the fact that the spectrum analysis method could not account for the contribution of individual factors upon the desired output [159]. The DDS analysis method makes wavelength decomposition of a measured profile and determines the contribution of several factors to this measured output through “FFT-like” methods. Its application to the prediction of factors affecting the surface roughness of an MMC was successful [159] and it facilitated also the determination of various mechanisms that are present during the MMC machining processes.

Several methods based on the fuzzy set theory, namely a fuzzy expert system, a combination of a fuzzy system and a genetic algorithm, and the gray-fuzzy analysis methods can be used as a prediction tool for the machining processes of MMC. Fuzzy logic is considered as a powerful tool for the construction of a successful rule-based expert system [174]. On the other hand, the gray-fuzzy theory is recognized as important for manipulation of uncertainty and discrete data. Thus, a combination of the two methods can provide an improved reasoning grade for the prediction system and the minimization of uncertain output [176]. Furthermore, the use of genetic algorithm can improve the performance of a fuzzy logic system considerably [174]. A more detailed description of the implementation of the gray-fuzzy analysis method can be found in [175]. This method has been successfully employed for the optimization of MMC machining parameters and also for the prediction of surface roughness in machined MMCs.

4.5 Conclusions

Although MMCs exhibit exceptional properties that place them in the first position as candidate materials for numerous high-end applications in many contemporary industrial sectors, their machining is proven to be rather difficult. Considering the fact that machining is the most suitable manufacturing processes category for providing the required accuracy in the final products, the investigation of the possibilities and capabilities of machining in manufacturing MMC products is quite interesting and important.

In the previous paragraphs an overall account of machining performance on MMCs was presented. First, conventional machining processes and specifically the influence of machining parameters on tool wear and workpiece surface quality were considered. Tool wear mechanisms were identified and material removal mechanisms of composite materials comprising of a metal matrix and a reinforcement material were discussed. Cutting tool materials and optimal cutting conditions were suggested based on the relevant literature. Second, as an alternative approach to MMCs machining, nonconventional processes were investigated. Since there is no physical contact between a tool and the workpiece in these processes, machining exhibits certain advantages. In the last part, machining modeling techniques were considered. Chip formation, tool wear, matrix-reinforcement coherence, and other basic aspects of MMC machining cannot be fully investigated through experimental work. Micro and macroscale modeling techniques are employed for prediction of several important aspects of the processes and for their optimisation as well.

The bibliography on MMC machining, though not complete in this chapter, is quite vast; this serves as an indication of the importance of the subject. In the near future, more work is expected to be performed as these materials are expected to be introduced in many more applications and products.

References

1. Wilk W, Staniewicz-Brudnik B (2008) Abrasive machining of metal matrix composites. In: Proceedings of the 8th international conference advanced manufacturing operations, pp 373–379
2. Dandekar CR, Shin YC (2012) Modeling of machining of composite materials: a review. *Int J Mach Tools Manuf* 57:102–121
3. Shin YC, Dandekar C (2012) Mechanics and modeling of chip formation in machining of MMC. In: Davim JP (ed) *Machining of metal matrix composites*. Springer, London
4. Muthukrishnan N, Davim JP (2009) Optimization of machining parameters of Al/SiC-MMC with ANOVA and ANN analysis. *J Mater Process Technol* 209:225–232
5. Santha Kumar S, Thenappan V, Srinath G (2012) PCD cutting insert behavior on turning (Al-SiC15p) MMC. In: *International conference on thermal, material and mechanical engineering*, Singapore, pp 133–137
6. Durante S, Rutelli G, Rabezana F (1997) Aluminum-based MMC machining with diamond-coated cutting tools. *Surf Coat Technol* 94–95(1):632–640

7. Persson H (2001) Machining guidelines of Al/SiC particulate MMC. MMC-assess-thematic network, vol 6, MMC-Assess Consortium
8. Teti R (2002) Machining of composite materials. *CIRP Ann Manuf Technol* 51(2):611–634
9. Thamizhmanii S, Hasan S (2008) Investigating flank wear and cutting force on hard steels by CBN cutting tool by turning. In: *Proceedings of the world congress on engineering WCE 2008*, London, UK
10. Weinert K, König W (1993) A consideration of tool wear mechanism when machining metal matrix composites (MMC). *CIRP Ann Manuf Technol* 42(1):95–98
11. Weinert K, Lange M, Schroer M (2000) Machining of light-metal matrix composites. In: Kainer KU (ed) *Magnesium alloys and their applications*. Wiley-VCH Verlag, Weinheim
12. Sikder S, Kishawy HA (2012) Analytical model for force prediction when machining metal matrix composite. *Int J Mech Sci* 59(1):95–103
13. Ciftci I, Turker M, Seker U (2004) CBN cutting tool wear during machining of particulate reinforced MMCs. *Wear* 257:1041–1046
14. Di Ilio A, Paoletti A (2012) Machinability aspects of metal matrix composites. In: Davim JP (ed) *Machining of metal matrix composites*. Springer, London
15. Biermann D (1995) Untersuchungen zum Drehen von Aluminiummatrix-Verbundwerkstoffen. *Fortschrittberichte, Reihe 2, Nr 338*, VDI Verlag Düsseldorf
16. Jani DV (2014) Machining of Sic—metal matrix composite (MMC) by polycrystalline diamond (PCD) tools and effect on quality of surface by changing machining parameters. *Int J Sci Res Dev* 2(7):106–108
17. Cook MW (1998) Machining MMC engineering components with polycrystalline diamond and diamond grinding. *Mater Sci Technol* 14:892–895
18. Cronjäger L, Meister D (1992) Machining of fibre and particle-reinforced aluminium. *CIRP Ann Manuf Technol* 41(1):63–66
19. El-Gallab M, Sklad M (1998) Machining of Al/SiC particulate metal-matrix composites: Part I: Tool performance. *J Mater Process Technol* 83(1–3):151–158
20. Iuliano L, Settineri L, Gatto A (1998) High-speed turning experiments on metal matrix composites. *Compos A* 29A:1501–1509
21. Chen P, Hoshi T (1992) High-performance machining of SiC whisker-reinforced aluminium composite by self-propelled rotary tool. *CIRP Ann Manuf Technol* 41(1):59–62
22. Coelho RT, Yamada S, LeRoux T, Aspinwall DK, Wis MLH (1993) Conventional machining of an aluminium based Sic reinforced metal matrix composite (MMC) alloy. In: *Proceedings of the 30th MATADOR*, Manchester, UK, pp 125–133
23. Looney LA, Monaghan JM, O'Reilly P, Taplin DMR (1992) The turning of an Al/SiC metal-matrix composite. *J Mater Process Technol* 33(4):453–468
24. Sahin Y (2004) Preparation and some properties of SiC particle reinforced aluminium alloy composites. *Mater Des* 24(8):671–679
25. Lin JT, Bhattacharyya D, Lane C (1995) Machinability of a silicon carbide reinforced aluminium metal matrix composite. *Wear* 181–183(Part2):883–888
26. Narutaki N (1996) Machining of MMC's. *VDI Berichte* 1276:359–370
27. Tomac N, Tannessen K, Rasch FO (1992) Machinability of particulate aluminium matrix composites. *CIRP Ann Manuf Technol* 41(1):55–58
28. Songmene V, Balazinski M (2001) Machining of a graphitic SiC-reinforced aluminium metal matrix composites with diamond tools. In: *CIRP international seminar on progress in innovative manufacturing engineering—PRIME 2001*, Sestri Levante, pp 73–76
29. Tönshoff HK, Karpuschewski B, Winkler J, Podolsky C (1999) Manufacturing of magnesium by turning and burnishing operations. *Advanced technology of plasticity*, vol 1, *Ecological manufacturing*. In: *Proceedings of the of the 6th ICTP*, Nürnberg, pp 607–612
30. Weinert K, Buschka M, Niehues J, Schoberth A (2001) Spanende Bearbeitung von Al-Matrix-Verbundwerkstoffen. *Materialwiss Werkstofftech* 32(5):447–461
31. Przystacki D (2014) Conventional and laser assisted machining of composite A359/20SiCp. *Procedia CIRP* 14:229–233

32. Liu CS, Zhao B, Gao GF, Jiao F (2002) Research on the characteristics of the cutting force in the vibration cutting of a particle-reinforced metal matrix composites SiCp/Al. *J Mater Process Technol* 129(1–3):196–199
33. Songmene V, Balazinski M (1999) Machinability of graphitic metal matrix composites as a function of reinforcing particles. *CIRP Ann Manuf Technol* 48(1):77–80
34. Chandrasekaran H, Johansson J (1996) On the behaviour of fibre/particle reinforced aluminium alloy matrix composites in milling and grinding. *VDI Berichte* 1276:463–478
35. Lane C (1992) The effect of different reinforcement on PCD tool life for aluminium Composites. Machining of composites materials. In: *Proceedings of the ASM/TMS materials week symposium*, Chicago, Illinois, pp 17–27
36. Lane C (1990) Machining characteristics of particulate-reinforced aluminum. In: *Fabrication of particle reinforced metal composites*, ASM, pp 195–201
37. Lane C, Finn M (1992) Observations on using CVD diamond in milling MMCs. In: *Materials issues in machining and the physics of machining processes*. TMS, pp 39–51
38. Coelho RT, Yamada S, Aspinwall DK, Wise MLH (1995) The application of polycrystalline diamond (PCD) tool materials when drilling and reaming aluminium based alloys including MMC. *Int J Mach Tools Manuf* 35(5):761–774
39. Coelho RT, Aspinwall DK, Wise MLH (1994) Drilling and reaming aluminium-based metal matrix composites (MMC) using PCD tooling. In: *Transactions of NAMRI/SME*
40. Jawaid A, Barnes S, Ghadimzadeh SR (1992) Drilling of particulate aluminum silicon carbide metal matrix composites. In: *Proceeding of the ASM materials workshop*, Chicago, IL
41. Ricci WC (1987) Machining metal matrix composites. *SME*, MR87-827
42. Songmene V, Stephenson TF, Waner AEM (1997) Machinability of graphitic silicon carbide aluminum metal matrix composite GrA-Ni®. In: *ASME international mechanical engineering congress and exposition*, Dallas, Texas
43. Tosun G, Muratoglu M (2004) The drilling of an Al/SiCp metal-matrix composites. Part I: Microstructure. *Compos Sci Technol* 64(2):299–308
44. Basavarajappa S, Chandramohan G, Prabu M, Mukund K, Ashwin M (2007) Drilling of hybrid metal matrix composites-workpiece surface integrity. *Int J Mach Tools Manuf* 47:92–96
45. Liu J, Li J, Xu C (2014) Interaction of the cutting tools and the ceramic-reinforced metal matrix composites during micro-machining: a review. *CIRP J Manufact Sci Technol* 7(2):55–70
46. Venkatesh VC, Norizah R, Murugan VS, Mehrota PK, Ourdjini A, Hamidon M (2001) Microdrilling of composites. In: *International conference on materials for advanced technology, symposium on advances on polymers and composites*, Sun Tech City, Singapore
47. Monaghan J, O'Reilly P (1992) The drilling of an Al/SiC metal-matrix composite. *J Mater Process Technol* 33(4):469–480
48. Yan BH, Tsai HC, Huang FY, Lee LC (2005) Examination of wire electrical discharge machining of Al₂O₃p/6061Al composites. *Int J Mach Tools Manuf* 45(3):251–259
49. Pramanik A, Zhang LC, Arsecularatne JA (2007) An FEM investigation into the behavior of metal matrix composites: tool–particle interaction during orthogonal cutting. *Int J Mach Tools Manuf* 47:1497–1506
50. Pramanik A (2014) Developments in the non-traditional machining of particle reinforced metal matrix composites. *Int J Mach Tools Manuf* 86:44–61
51. Ho KH, Newman ST (2003) State of the art electrical discharge machining (EDM). *Int J Mach Tools Manuf* 43(13):1287–1300
52. Ramulu M, Taya M (1989) EDM machinability of SiCw/Al composites. *J Mater Sci* 24(3):1103–1108
53. Hocheng H, Lei WT, Hsu HS (1997) Preliminary study of material removal in electrical-discharge machining of SiC/Al. *J Mater Process Technol* 63:813–818
54. Rozenek M, Kozak J, Dąbrowski L, Łubkowski K (2001) Electrical discharge machining characteristics of metal matrix composites. *J Mater Process Technol* 109:367–370

55. Chicosz P, Karokzak P (2008) Sinking EDM of aluminum matrix composites. *Mater Sci Poland* 26(3):547–554
56. Shanmugam DK, Chen FL, Siores E, Brandt M (2002) Comparative study of jetting machining technologies over laser machining technology for cutting composite materials. *Compos Struct* 57(1–4):289–296
57. Savrun E, Taya M (1988) Surface characterization of SiC whisker/2124 aluminium and Al_2O_3 composites machined by abrasive water jet. *J Mater Sci* 23(4):1453–1458
58. Hamatani G, Ramulu M (1990) Machinability of high temperature composites by abrasive waterjet. *J Eng Mater Technol* 112(4):381–386
59. Hashish M (1995) Water jet machining of advanced composites. *Mater Manuf Processes* 10 (6):1129–1152
60. Dubey AK, Yadava V (2008) Laser beam machining—a review. *Int J Mach Tools Manuf* 48 (6):609–628
61. Wang AH, Xu HG, Yang P, Zhang XL, Xie CS (2007) Nd:YAG laser butt welding of a 12 vol.% SiC particulate-reinforced magnesium alloy composite. *Mater Lett* 61(19–20):4023–4026
62. Dahotre NB, McCay TD, McCay MH (1989) Laser processing of a SiC/Al-alloy metal matrix composite. *J Appl Phys* 65:5072–5077
63. Müller F, Monaghan J (2000) Non-conventional machining of particle reinforced metal matrix composite. *Int J Mach Tools Manuf* 40(9):1351–1366
64. Kozak J (1998) Mathematical models for computer simulation of electrochemical machining process. *J Mater Process Technol* 76(1–3):170–175
65. Bhattacharyya B, Munda J, Malapati M (2004) Advancement in electrochemical micro-machining. *Int J Mach Tools Manuf* 44(15):1577–1589
66. Senthilkumar C, Ganesan G, Karthikeyan R (2009) Study of electrochemical machining characteristics of Al/SiC_p composites. *Int J Adv Manuf Technol* 43(3–4):256–263
67. Sankar M, Gnanavelbabu A, Rajkumar K (2014) Effect of reinforcement particles on the abrasive assisted electrochemical machining of aluminium-boron carbide-graphite composite. *Procedia Engineering* 97:381–389
68. Thoe TB, Aspinwall DK, Wise MLH (1998) Review on ultrasonic machining. *Int J Mach Tools Manuf* 38(4):239–255
69. Zhong ZW, Lin G (2006) Ultrasonic assisted turning of an aluminium-based metal matrix composite reinforced with SiC particles. *Int J Adv Manuf Technol* 27(11–12):1077–1081
70. Nath C, Rahman M, Neo KS (2009) A study on ultrasonic elliptical vibration cutting of tungsten carbide. *J Mater Process Technol* 209(9):4459–4464
71. Hung NP, Loh NL, Xu ZM (1996) Cumulative tool wear in machining metal matrix composites Part II: Machinability. *J Mater Process Technol* 58(1):114–120
72. Kishawy HA, Kannan S, Balazinski M (2005) Analytical modeling of tool wear progression during turning particulate reinforced metal matrix composites. *CIRP Ann Manuf Technol* 54 (1):55–58
73. Li X, Seah WKH (2001) Tool wear acceleration in relation to workpiece reinforcement percentage in cutting of metal matrix composites. *Wear* 247(2):161–171
74. Hung NP, Zhong CH (1996) Cumulative tool wear in machining metal matrix composites Part I: Modelling. *J Mater Process Technol* 58(1):109–113
75. Hung NP, Boey FYC, Khor KA, Phua YS, Lee HF (1996) Machinability of aluminium alloys reinforced with silicon carbide particulates. *J Mater Process Technol* 56(1–4):966–977
76. Lin JT, Bhattacharyya D, Lane C (1995) Machinability of a silicon reinforced aluminium metal matrix composites. *Wear* 181–183(2):883–888
77. Hung NP, Boey FYC, Khor KA, Oh CA, Lee HF (1995) Machinability of cast and powder formed aluminium alloys reinforced with SiC particles. *J Mater Process Technol* 48(1–4):291–297
78. Kishawy HA, Kannan S, Balazinski M (2004) An Energy based analytic force model for orthogonal cutting of metal matrix composites. *CIRP Ann Manuf Technol* 53(1):91–94

79. Pramanik A, Zhang LC, Arsecularatne JA (2006) Prediction of cutting forces in machining of metal matrix composites. *Int J Mach Tools Manuf* 46(14):1795–1803
80. Dabade UA, Dapkekar D, Joshi SS (2009) Modeling of chip-tool interface friction to predict cutting forces in machining of Al/SiCp particles. *Int J Mach Tools Manuf* 49(9):690–700
81. Dabade UA, Joshi SS (2009) Analysis of chip formation mechanism in machining of Al/SiCp metal matrix composites. *J Mater Process Technol* 209(10):4704–4710
82. Pramanik A, Zhang LC, Arsecularatne JA (2008) Machining of metal matrix composites: effect of ceramic particles on residual stress, surface roughness and chip formation. *Int J Mach Tools Manuf* 48(15):1613–1625
83. Ramamurty U, Zok FW, Leckie FA, Deve HE (1997) Strength variability in alumina fiber-reinforced aluminium matrix composites. *Acta Mater* 45(11):4603–4613
84. Ramamurty U (2005) Assessment of load transfer characteristics of a fiber-reinforced titanium-matrix composite. *Compos Sci Technol* 65(11–12):1815–1825
85. Okabe T, Takeda N, Kamoshida Y, Shimizu M, Curtin WA (2001) A 3D shear-lag model considering micro-damage and statistical strength prediction of unidirectional fiber-reinforced composites. *Compos Sci Technol* 61:1773–1787
86. Xia Z, Curtin WA, Okabe T (2002) Green's function vs shear lag models of damage and failure in fiber composites. *Compos Sci Technol* 62(10–11):1279–1288
87. Ibnabdeljalil M, Curtin WA (1997) Strength and reliability of fiber-reinforced composites: localised load-sharing and associated size effects. *Int J Solids Struct* 34(21):2649–2688
88. Roatta A, Bolmaro RE (1997) An Eshelby inclusion based model for the study of stresses and plastic strain localization in metal matrix composites I: general formulation and its application to round particles. *Mater Sci Eng A* 229(1–2):182–191
89. Roatta A, Bolmaro RE (1997) An Eshelby inclusion based model for the study of stresses and plastic strain localization in MMC II: Fiber reinforcement and lamellar inclusions. *Mater Sci Eng A* 229(1–2):192–202
90. Roatta A, Turner PA, Bertinetti MA, Bolmaro RE (1997) An iterative approach to mechanical properties of MMCs at the onset of plastic deformation. *Mater Sci Eng A* 229(1–2):203–218
91. Bruno G, Fernandez R (2007) The dependence of the Eshelby model predictions on the microstructure of MMC. *Acta Mater* 55(4):1267–1274
92. Tevatia A, Srivastava SK (2015) Modified shear lag theory based fatigue crack growth life prediction model for short-fiber reinforced metal matrix composites. *Int J Fatigue* 70:123–129
93. Deve HE (1997) Compressive strength of continuous fiber reinforced aluminium matrix composites. *Acta Mater* 45(12):5041–5046
94. Zhang H, Daehn GS, Wagoner RH (1991) Simulation of the plastic response of whisker reinforced metal matrix composites under thermal cycling conditions. *Scr Metall Mater* 25(10):2285–2290
95. Dutta I, Sims JD, Seigenthaler DM (1993) An analytical study of residual stress effects on uniaxial deformation of whisker reinforced metal-matrix composites. *Acta Metall Mater* 41(3):885–908
96. Lee WJ, Son JH, Kang NH, Park IM, Park YH (2009) Finite-element analysis of deformation behaviors in random whisker reinforced composite. *Scripta Mater* 61(6):580–583
97. Aghdam MM, Smith DJ, Pavier MJ (2000) Finite element micromechanical modelling of yield and collapse behavior of metal matrix composites. *J Mech Phys Solids* 48(3):499–528
98. Chan KC, Cheung CF, Ramesh MV, Lee WB, To S (2001) A theoretical and experimental investigation of surface generation in diamond turning of an Al6061/ SiC_p metal matrix composite. *Int J Mech Sci* 43:2047–2068
99. Ramesh MV, Chan KC, Lee WB, Cheung CF (2001) Finite-element analysis of diamond turning of aluminium matrix composites. *Compos Sci Technol* 61(10):1449–1456
100. Pramanik A, Zhang LC, Arsecularatne JA (2008) Deformation mechanisms of MMCs under indentation. *Compos Sci Technol* 68:1304–1312

101. Miserez A, Rossoll A, Mortensen A (2004) Investigation of crack-tip plasticity in high volume fraction particulate metal matrix composites. *Eng Fract Mech* 71:2385–2406
102. Mishnaevsky L Jr, Brondsted P (2009) Micromechanical modeling of damage and fracture of unidirectional fiber reinforced composites: a review. *Comput Mater Sci* 44(4):1351–1359
103. Haj-Ali R, Aboudi J (2010) Formulation of the high-fidelity generalized method of cells with arbitrary cell geometry for refined micromechanics and damage in composites. *Int J Solids Struct* 47(25–26):3447–3461
104. Harper LT, Qian C, Turner TA, Li S, Warrior NA (2012) Representative volume elements for discontinuous carbon fiber composites-Part I: Boundary conditions. *Compos Sci Technol* 72 (2):225–234
105. Dlouhy A, Eggeler G, Merk N (1995) A micromechanical model for creep in short fibre reinforced aluminium alloys. *Acta Metall Mater* 43(2):535–550
106. Xu Q, Tao W, Qu S, Yang Q (2015) A cohesive zone model for the elevated temperature interfacial debonding and frictional sliding behavior. *Compos Sci Technol* 110:45–52
107. Di Ilio A, Paoletti A, D'Addona D (2009) Characterization and modelling of the grinding process of metal matrix composites. *CIRP Ann Manuf Technol* 58:291–294
108. El-Gallab M, Sklad M (2000) Machining of Al/SiC particulate metal matrix composites Part III: Comprehensive tool wear models. *J Mater Process Technol* 101:10–20
109. Rao B, Dandekar CR, Shin YC (2011) An experimental and numerical study on the face milling of Ti–6Al–4 V alloy: tool performance and surface integrity. *J Mater Process Technol* 211(2):294–304
110. Zhou L, Wang Y, Ma ZY, Yu XL (2014) Finite element and experimental studies of the formation mechanism of edge defects during machining of SiCp/Al composites. *Int J Mach Tools Manuf* 84:9–16
111. Dandekar CR, Shin YC (2013) Multi-scale modeling to predict sub-surface damage applied to laser-assisted machining of a particulate reinforced metal matrix composite. *J Mater Process Technol* 213(2):153–160
112. El- Gallab MS, Sklad MP (2004) Machining of aluminium/silicon carbide particulate metal matrix composites Part. IV Residual stresses in the machined workpiece. *J Mater Process Technol* 152:23–34
113. Prabu SB, Karunamoorthy L, Kandasami GS (2004) A finite element analysis study of micromechanical interfacial characteristics of metal matrix composites. *J Mater Process Technol* 153–154:992–997
114. Mahdi M, Zhang L (2001) A finite element model for the orthogonal cutting of fiber-reinforced composite materials. *J Mater Process Technol* 113:373–377
115. Rao GVG, Mahajan P, Bhatnagar N (2007) Micro-mechanical modeling of machining of FRP composites-cutting force analysis. *Compos Sci Technol* 67(3–4):579–593
116. Mkaddem A, Demirci I, El Mansori M (2008) A micro-macro combined approach using FEM for modelling of machining of FRP composites: cutting force analysis. *Compos Sci Technol* 68(15–16):3123–3127
117. Peng Z, Fuguo L (2010) Micro-macro unified analysis of flow behavior of particle-reinforced metal matrix composites. *Chin J Aeronaut* 23:252–259
118. Kouznetsova V, Brekelmans WAM, Baaijens FPT (2001) An approach to micro-macro modelling of heterogeneous materials. *Comput Mech* 27:37–48
119. Orozco CE (1997) Computational aspect of modeling complex microstructure composites using GMC. *Compos B Eng* 28(1–2):167–175
120. Pindera M-J, Bednarczyk BA (1997) An efficient implementation of the GMC for unidirectional, multi-phased composites with complex microstructures. NASA Contract, Report 202350
121. Pahr DH, Arnold SM (2002) The applicability of the generalized method of cells for analysing discontinuously reinforced composites. *Compos B Eng* 33(2):153–170
122. Haj-Ali R, Aboudi J (2009) Nonlinear micromechanical formulation of the high fidelity generalized method of cells. *Int J Solids Struct* 46(13):2577–2592

123. Harper LT, Qian C, Turner TA, Li S, Warrior NA (2012) Representative Volume Elements for discontinuous carbon fiber composites-Part II: Determining the critical size. *Compos Sci Technol* 72(2):204–210
124. Dong M, Schmauder S (1996) Modelling of metal matrix composites by a self-consistent embedded cell model. *Acta Mater* 44(6):2465–2478
125. Dong M, Schmauder S (1996) Transverse mechanical behavior of fiber reinforced composites-FE modelling with embedded cell models. *Comput Mater Sci* 5:53–66
126. Bohm HJ, Eckschlagner A, Han W (2002) Multi-inclusion unit cell models for metal matrix composites with randomly oriented discontinuous reinforcements. *Comput Mater Sci* 25(1–2):42–53
127. Aghdam MM, Dezhsetan A (2005) Micromechanics based analysis of randomly distributed fiber reinforced metal matrix composite using simplified unit cell method. *Compos Struct* 71(3–4):327–332
128. Doghri I, Tinel L (2005) Micromechanical modeling and computation of elasto-plastic material reinforced with distributed-orientation fibers. *Int J Plast* 21(10):1919–1940
129. Doghri I, Tinel L (2006) Micromechanics of inelastic composites with misaligned inclusions: numerical treatment of orientation. *Comput Methods Appl Mech Eng* 195(13–16):1387–1406
130. Dong M, Schmauder S, Bidlingmaier T, Wanner A (1997) Prediction of the mechanical behavior of short fiber reinforced MMCs by combined cell models. *Comput Mater Sci* 9(1–2):121–133
131. Mammoli AA, Bush MB (1993) A boundary element analysis of metal matrix composite materials. *Int J Numer Meth Eng* 36(14):2415–2433
132. Mammoli AA, Bush MB (1995) Effects of reinforcement geometry on the elastic and plastic behavior of metal matrix composites. *Acta Metall Mater* 43(10):3743–3754
133. Chatterjee J, Henry DP, Ma F, Banerjee PK (2008) An efficient BEM formulation for three-dimensional steady-state heat conduction analysis of composites. *Int J Heat Mass Transf* 51(5–6):1439–1452
134. Liu YJ, Xu N (2000) Modeling of interface cracks in fiber-reinforced composites with the presence of interphases using the boundary element method. *Mech Mater* 32:769–783
135. Chen X, Papathanasiou TD (2004) Interface stress distributions in transversely loaded continuous fiber composite: parallel computation in multi-fiber RVEs using the BEM. *Compos Sci Technol* 64(9):1101–1114
136. Kaminski M (2012) Stochastic boundary element method analysis of the interface defects in composite materials. *Compos Struct* 94(2):394–402
137. Goldberg RK, Hopkins DA (1995) Application of the boundary elements method to the micromechanical analysis of composite materials. *Comput Struct* 56(5):721–731
138. Knight MG, Wrobel LC, Henshall JL (2003) Micromechanical response of fibre-reinforced materials using the boundary element technique. *Compos Struct* 62(3–4):341–352
139. Banerjee PK, Henry DP (1992) Elastic analysis of three-dimensional solids with fiber inclusions by BEM. *Int J Solids Struct* 29(20):2423–2440
140. Saheb N, Iqbal Z, Khalil A, Hakeem AS, Al Aqeeli N, Laoui T, Al-Qutub A, Kirchner R (2012) Spark plasma sintering of metals and metal matrix nanocomposites: a review. *J Nanomater* 2012, Article ID 983470
141. Dongare AM, Zhigilei LV, Rajendran AM, LaMattina B (2009) Interatomic potentials for atomic scale modelling of metal-matrix ceramic particle reinforced nanocomposites. *Compos B Eng* 40(6):461–467
142. Dongare AM, LaMattina B (2011) Atomic scale study of deformation and failure mechanisms in ceramic-reinforced metal-matrix composites. In: Hashim A (ed) *Advances in nanocomposite technology*. InTech
143. Dandekar CR, Shin YC (2011) Effect of porosity on the interface behavior of an Al_2O_3 —aluminum composite: a molecular dynamics study. *Compos Sci Technol* 71(3):350–356

144. Mei H, Liu LS, Lai X, Zhai PC (2013) Analysis of mechanical properties of nanocrystalline Al + α -Al₂O₃ composites using molecular dynamics simulation. *J Phys Conf Ser* 419 012049 FGM 2012
145. Dandekar CR, Shin YC (2011) Molecular dynamics based cohesive zone law for describing Al-SiC interface mechanics. *Compos A Appl Sci Manuf* 42(4):355–363
146. Tomar V, Zhou M (2007) Analyses of tensile deformation of nanocrystalline α -Fe₂O₃ + fcc-Al composites using molecular dynamics simulations. *J Mech Phys Solids* 55:1053–1085
147. Berner A, Mundim KC, Ellis DE, Dorfman S, Fuks D, Evenhaim R (1999) Microstructure of Cu-C interface in Cu-based metal matrix composite. *Sens Actuators A* 74(1–3):86–90
148. Lidorikis E, Bachlechner ME, Kalia RK, Nakano A, Voyiadjis GZ, Vashishta P (2000) Coupling of length scales: hybrid molecular dynamics and finite element approach for multiscale nanodevice simulations. In: *MRS Proceedings*, vol 653, pp Z9.3.1–Z9.3.6
149. Nakano A, Bachlechner ME, Kalia RK, Lidorikis E, Vashishta P, Voyiadjis GZ, Campbell TJ, Ogata S, Shimojo F (2001) Multiscale simulation of nanosystems. *Comput Sci Eng* 56–66
150. Ogata S, Lidorikis E, Shimojo F, Nakano A, Vashishta P, Kalia RK (2001) Hybrid finite-element/molecular-dynamics/electron-density-functional approach to materials simulation on parallel computers. *Comput Phys Commun* 138:143–154
151. Aly MF, Ng E, Veldhuis SC, Elbestawi MA (2006) Prediction of cutting forces in the micro-machining of silicon using a “hybrid molecular dynamic-finite element analysis” force model. *Int J Mach Tools Manuf* 46:1727–1739
152. Tian Y, Shin YC (2007) Multiscale finite element modeling of silicon nitride ceramics undergoing laser-assisted machining. *Trans ASME J Manuf Sci Eng* 129(2):287–295
153. Lin JT, Bhattacharyya D, Kecman V (2003) Multiple regression and neural networks analyses in composites machining. *Compos Sci Technol* 63(3–4):539–548
154. Davim JP (2003) Design of optimization of cutting parameters for turning metal matrix composites based on the orthogonal arrays. *J Mater Process Technol* 132(1–3):340–344
155. Koker R, Altinkok N, Demir A (2007) Neural network based prediction of mechanical properties of particulate reinforced metal matrix composites using various training algorithms. *Mater Des* 28(2):616–627
156. Shabani MO, Mazahery A (2012) Artificial intelligence in numerical modeling of nano sized ceramic particulates reinforced metal matrix composites. *Appl Math Model* 36(11):5455–5465
157. Shabani MO, Mazahery A, Rahimpour MR, Razavi M (2012) FEM and ANN investigation of A356 composites reinforced with B4C particulates. *J King Saud Univ Eng Sci* 24(2):107–113
158. Ozyurek D, Kalyon A, Yildirim M, Tuncay T, Ciftci I (2014) Experimental investigation and prediction of wear properties of Al/SiC metal matrix composites produced by thixomoulding method using artificial neural networks. *Mater Des* 63:270–277
159. Cheung CF, Chan KC, Lee WB (2003) Surface characterization in ultra-precision machining of Al/SiC metal matrix composites using data dependent systems analysis. *J Mater Process Technol* 140(1–3):141–146
160. Sahoo AK, Pradhan S, Rout AK (2013) Development and machinability assessment in turning Al/SiCp-metal matrix composites with multilayer coated carbide inset using Taguchi and statistical techniques. *Arch Civil Mech Eng* 13(1):27–35
161. Gopalakannan S, Senthilvelan T, Ranganathan S (2012) Modeling and optimization of EDM process parameters on machining of Al7075-B4C MMC using RSM. *Proc Eng* 38:685–690
162. Gopalakannan S, Senthilvelan T (2013) Application of response surface method on machining of Al-SiC nano-composites. *Measurement* 46(8):2705–2715
163. Lakshminarayanan AK, Balasubramanian V (2009) Comparison of RSM with ANN in predicting tensile strength of friction stir welded AA7039 aluminium alloy joints. *Trans Nonferr Met Soc China* 19(1):9–18

164. Bayhan M, Önel K (2010) Optimization of reinforcement content and sliding distance for AlSi7 Mg/SiC_p composites using response surface methodology. *Mater Des* 31(6):3015–3022
165. Shandilya P, Jain PK, Jain NK (2013) RSM and ANN modelling approaches for predicting average cutting speed during WEDM of SiC_p/6061 Al MMC. *Proc Eng* 64:767–774
166. Kiran TS, Kumar MP, Basavarajappa S, Viswanatha BM (2014) Dry sliding wear behavior of heat treated hybrid metal matrix composites using Taguchi techniques. *Mater Des* 63:294–304
167. Chaudhary G, Kumar M, Verma S, Srivastav A (2014) Optimization of drilling parameters of hybrid metal matrix composites using response surface methodology. *Proc Mater Sci* 6:229–237
168. Joardar H, Das NS, Sutradhar G, Singh S (2014) Application of response surface methodology for determining cutting force model in turning of LM6/SiC_p metal matrix composites. *Measurement* 47:452–464
169. Kumar R, Chauhan S (2015) Study on surface roughness measurement for turning of Al 7075/ 10/ SiC_p and Al 7075 hybrid composites by using response surface methodology (RSM) and artificial neural networking (ANN). *Measurement* 65:166–180
170. Pandit SM (1977) Stochastic linearization by data dependent systems. *J Dyn Syst Meas Contr* 99(4):221–226
171. Pandit SM, Mehta NP (1988) Data dependent systems approach to modal analysis Part I: Theory. *J Sound Vib* 122(3):413–422
172. Pandit SM, Jacobson EN (1988) Data dependent systems approach to modal analysis, Part II: Application to structural modification of a disc-brake rotor. *J Sound Vib* 122(3):423–432
173. Subhash G, Loukus JE, Pandit SM (2002) Application of data dependent systems approach for evaluation of fracture modes during a single-grit scratching. *Mech Mater* 34(1):25–42
174. Roy SS (2006) Design of genetic-fuzzy expert system for predicting surface finish in ultra-precision diamond turning of metal matrix composites. *J Mater Process Technol* 173(3):337–344
175. Rajmohan T, Palanikumar K, Prakash S (2013) Grey-fuzzy algorithm to optimize machining parameters in drilling of hybrid metal matrix composites. *Compos B Eng* 50:297–308
176. Suresh P, Marimuthu K, Ranganathan S, Rajmohan T (2014) Optimization of machining parameters in turning of Al-SiC-Gr hybrid metal matrix composites using grey-fuzzy algorithm. *Trans Nonferr Met Soc China* 24(9):2805–2814
177. Muthukrishnan N, Davim JP (2009) Optimization of machining parameters of Al/SiC MMC with ANOVA and ANN analysis. *J Mater Process Technol* 209(1):225–232
178. Kumar A, Mahapatra MM, Jha PK (2013) Modeling the abrasive wear characteristics of *in-situ* synthesized Al–4.5 %Cu/TiC composites. *Wear* 306(1–2):170–178

Chapter 5

Intelligent CNC Tool Path Optimization for Sculptured Surface Machining Through a Virus-Evolutionary Genetic Algorithm

Nikolaos A. Fountas, Nikolaos M. Vaxevanidis,
Constantinos I. Stergiou and Redha Benhadj-Djilali

Abstract Priorities for manufacturers worldwide include their attempt towards optimizing modern manufacturing systems to satisfy the needs of their customers. Major goal of the proposed study is to present a novel optimization methodology based on Artificial Intelligence using the Virus Theory of Evolution. The methodology implements a Virus-Evolutionary Genetic Algorithm to undertake sculptured surface tool path optimization in terms of geometrical machining error to reflect part quality and machining time to reflect productivity for both 3- and 5-axis sculptured surface machining. The algorithm implements its virus operators to create efficient solution representations, to rapidly reproduce enhanced schemata during the evaluations' loops, and finally come up with the optimum machining parameters based on the available resources and constraints ought to be imposed. Through a fully automated environment, time-consuming activities and repetitive tasks are no more of the CNC programmers' concern since the algorithm handles the CAM system's

N.A. Fountas

School of Pedagogical and Technological Education (ASPETE),
Faculty of Mechanical Engineering-Laboratory of Manufacturing Processes
and Machine Tools (LMPProMaT), N. Heraklion, 141 21 Athens, Greece
e-mail: n.fountas@webmail.aspete.gr

N.M. Vaxevanidis (✉) · C.I. Stergiou

Technological Institute (TEI) of Piraeus, Mechanical Engineering
Department-Laboratory of Advanced Computer-Aided Design
and Applications, Aigaleo, 12244 Athens, Greece
e-mail: vaxev@aspete.gr

C.I. Stergiou

e-mail: csterg@teipir.gr

N.A. Fountas · R. Benhadj-Djilali

Faculty of Science, Engineering and Computing (SEC), School of Mechanical
and Automotive Engineering, Kingston University, Roehampton Vale Campus,
SW15 3DW London, UK
e-mail: R.Benhadj-Djilali@kingston.ac.uk

© Springer International Publishing Switzerland 2015

J.P. Davim (ed.), *Modern Manufacturing Engineering*, Materials Forming,
Machining and Tribology, DOI 10.1007/978-3-319-20152-8_5

143

routines to handle them for its own benefit. The proposed methodology is deemed capable of providing uniform tool paths with low geometric machining error distribution as well as high productivity rates to the best possible extent.

Keywords Virus-evolutionary genetic algorithm • Tool path generation • Sculptured surface machining • CAM software • CNC programming

5.1 Introduction

With the increasing globalization trend and strict production demands, modern manufacturing industries are experiencing much higher pressure on achieving high product quality at low production cost. To respond to such challenges, enabling technologies and soft computing have actively deployed to introduce novel approaches for collaborative engineering, systems automation and intelligent manufacturing. Collaborative engineering, systems automation and intelligent manufacturing are some of the modern philosophies implemented to recapture traditional product life cycle management processes to shorten lead time, enhance product quality and suggest more competitive cost. Towards this concept, a full-scale employment of the aforementioned trends to formulate a novel integrated manufacturing environment suggests two major aspects: (1). The development and deployment of robust automation modules able to handle new or already existing engineering software tools and (2). The formulation and usage of intelligent algorithms that will integrate engineering software and address decision-making through loops of evaluations until arriving to optimum solutions.

The aspects of systems automation and intelligence ought to support modern manufacturing engineering towards the design and production of aesthetic, functional parts. A well-known material removal manufacturing process for such parts is Sculptured Surface Machining (SSM) (Choi and Gerard [4]). Research works concerning tool path planning for complex surfaces deal with precision machining modelling via already existing cutting strategies [3]; the development of new tool paths considering technological aspects and mechanics of processes [2], tool path generation considering machinability parameters based on software [31] and the generation of tool paths by taking into account proper tool positioning given the geometry and features of 3D CAD models [9]. Artificial intelligence and its capabilities are now implemented to optimize tool path planning activity using objectives that either directly or indirectly reflect productivity and quality under balance [8, 21].

Tool paths employed to machine sculptured surfaces consist of a group of tool positions. The CNC system that controls the machine tool sequentially interpolates between these positions as the cutting tool moves from point to point. Tool paths are usually modelled to make several passes across a surface, whereas pass interval and feed direction affect the size of the scallops which are formulated during the machining process (Lin et al. [16]). In addition, the interpolation between individual tool positions on a single cutting pass may force the tool to deviate from the ideal

surface. An optimum tool path would result to a machined surface having small-sized scallops, uniformly distributed across the surface. Thereby, interpolation strategies ought to be investigated during tool path generation so as to produce successful cutter contact trajectories given a sculptured surface. Such interpolation schemes already applied in industry are linear interpolation, circular interpolation and non-uniform rational B-spline (NURBS) interpolation. Tool path computation for sculptured surfaces in either 3- or 5-axis CNC machining technology involves also the specification of the feed direction and the two discretization steps; the longitudinal step that is actually the step along the cutter path and the transversal step also known as radial tool engagement or stepover. Given that most CNC programming units are yet to be integrated with advanced interpolation functions like NURBS except for some being considered as state of the art [11], generated tool paths should be linearized from CAM software through the determination of the two aforementioned surface discretization steps. Consecutively, specifying the space between successive tool positions along tool trajectories becomes of major importance. As the CNC control unit sequentially joins the tool positions trying this way to formulate the actual path, a chordal deviation is yielded with reference to the predetermined values for the steps. Hence, it is the job of the NC programmer to ensure that the designed tool path will hold the tolerance by choosing a relatively low value for the space among tool positions. On the other hand, should the value is low enough just to generate tightly spaced positions, too large NC files will have to be stored, whereas the time needed to compute and simulate the tool path might be excessive.

Several research efforts have studied the problem of computing optimum curve discretization steps for both 3- and 5-axis sculptured surface machining [15]. As a key objective to reflect geometrical error in machining, chordal deviation is adopted by many researchers for characterizing it as an optimization objective. Yang [29] presented a biarc curve-fitting approach to efficiently interpolate complex surfaces. The distances computed from the tessellation of the surface through biarcs are further investigated to obtain the maximum one which is finally set as the deviation to reflect the machining error. Lai et al. [14] proposed a methodology to investigate the geometrical error for large sculptured parts by employing 5-axis machining. In their work a mathematical expression is used as a function to be solved where the step formulated by two successive tool positions is controlled via the calculated chordal deviation. Towards the same philosophy, Yen and Hsu [30] developed an interpolation scheme based on adaptive feedrate to machine sculptured surfaces. Their work utilizes the chordal deviation when parametric curves are tessellated to small segments and employ it as the objective criterion. Towards the same concept, Del Prette et al. [5] established a framework of utilizing in advance measured surface points with a CMM in order to build an intelligent approach of minimizing chordal deviation. The discretization step length is defined by setting the limit on the maximum chord length which is used as the objective function in their algorithm. Drysdale et al. [6] computed the minimum number of circular arcs/biarcs needed to approximate curves by setting three discrete criteria that should be simultaneously satisfied. The first criterion is the positions (start and end) of the arcs; the second is the correct side that arc segments should be placed and the third

is the non-intersection between the arcs and the tolerance boundary with the latter being described by chordal deviation. Vijayaraghavan et al. [25] advocate that NURBS interpolation scheme is highly limited owing to the computational complexity when applied to real-time motion control systems and presented a method of subdividing curves via the application of “Catmull-Clark” subdivision scheme [19] in two dimensions to represent machine tool trajectories. Their goal was to find a set of points separated by the required chord length which lies on the curve.

Geometrical error is also affected by scallop height and several contributions have targeted on proposing methods to control or optimize its magnitude when it comes to sculptured surface machining. Shukun et al. [24] presented a method to produce constant scallop height tool trajectories by taking advantage of the highest scallop pick so as to discretize the surface boundary regarding the maximum machining tolerance. They managed to control machining precision via the connection among adjacent surface patches using the diagonal to achieve continuous cutting trajectories. Zhang et al. [32] studied the influence of scallop heights distribution on four types of well-known tool path strategies, namely equal-interval; parallel; parallel-tangency and free-form. They verified through experiments that scallop height distribution can be employed to display surface texture and may constitute a trustworthy research objective. Duroobi et al. [7] estimated scallop height magnitude by taking into account the types of existing end mills, the types of surfaces (concave, convex and flat), and the modes available for precision surface machining (3- and 5-axis). An extensive mathematical development for modelling scallop height is presented by the authors and important research results have been obtained concerning the effect of cutting tools’ geometrical shape, cutting direction angle and tool inclination in the case of 5-axis surface machining. Ponomarev [22] forwarded an analysis experiment for the implementation of a particular machining strategy fully dedicated to finish-machine sculptured surfaces. Results from this work have shown that micro-irregularities concerning scallop heights impose substantial impact when using different machining strategies for complex parts and a method is presented capable of tracking the principal surface curvature for different sculptured parts under the scope of producing effective tool trajectories to sustain low geometrical error. Zou et al. [33] proposed a framework capable of globally optimizing tool path planning by considering multiple objectives through a combinatorial scalar function. Their approach implements a mechanism to select iso-level curves with respect to certain scallop height tolerance.

5.2 Problem Statement and Research Objectives

The field of SSM is such that CAD/CAM technology implementation is considered vital. In its narrow sense, the manufacturing modelling environment that commercial CAM systems provide has the major goal of generating efficient tool paths that will produce a part within specifications, given its geometry prepared in CAD. The task of producing parts comprising sculptured surfaces turns out to be

more challenging should requirements for high quality and productivity are set. Despite the extensive research on developing strategies and methods to ease human efforts on machining modelling and NC programming, CAM systems are still user-intensive and engineers are responsible for harnessing the advantages offered by existing tools for tool path planning in CAM environment.

As far as CNC control systems are concerned, their ongoing evolution has led to the implementation of advanced interpolations to machine sculptured surfaces such as non-uniform rational B-splines (NURBS) as it has been mentioned. NURBS can be employed when retrieving the high-precision contour control mode. The NURBS interpolation function can be then programmed according to ISO 6983 NC code (G-code programming principles) and the specific NC control unit configurations. The function is actually a modal code of G-code group 01 and operates with the curve order (P), the control points (X, Y, Z), the weights (R), the knots (K) and the feedrate in mm/min. Despite the availability of such technology when it comes to NC sculptured surface machining, its implementation seems to lag behind and is still in its infancy [17]. Very few top CNC units apply NURBS interpolation and it is questionable whether NURBS interpolation indeed provides higher surface finish. Practically speaking, “segmented” interpolations (linear or circular) under a specified chord error may hold tolerances just precise as NURBS interpolations do with the difference that huge NC files need to be stored in NC control units against NURBS format which is by far more efficient. From a practical viewpoint, there is no accuracy level that NURBS interpolation can achieve whilst chordal interpolations cannot. On the other hand, numerous NC blocks might cause NC programme length as well as the file size to swell yet; this is not of major concern given the current state of advances in machine tools and CNC programming units. Fortunately, high-tech NC systems have become more adept while coping with large NC files under fast processing rates. Moreover, high-frequency servo loop functions integrated to CNC systems allow smoother machining operations whilst maintaining good transition from one move to the next, mainly in terms of feedrate. Thereby, it comes as a conclusion that simple interpolators can still be implemented for high-precision machining applications not only for industry but also to current academic research [28].

Should common interpolators are to be implemented one has to ensure that a tighter chordal tolerance in CAM environment is specified to capture more precise illustration of the ideally designed part geometry to be machined. Given the machining tolerance, that determines the cutting envelope zone in which a cutting pattern should be embedded and the rest of tool path planning parameters involved, several scenarios for tool path modelling may be formulated; some of them may be strict enough to lead to high quality but increased machining time, whereas some others might be productive but of low surface quality. Moreover, not all of the resulting tool paths will properly orient the cutting tool for a given surface. Particularly, values specified for discretization step and stepover may not allow end mills to be always in absolute contact with the ideal surface, yielding deviations between the ideal and the machined part. The magnitude of the resulting faceted surface regions can dramatically vary, forcing the tool to produce variable chords on sequential sidestep intervals; maximizing this way the geometrical error.

5.3 Sculptured Surface Machining–SSM

The term “Sculptured Surface Machining” (SSM) refers to the technology employing advanced computer numerical control machine tools and controllers coupled with cutting-edge manufacturing software to cover the need of high-precision machining. Such machining is performed to manufacture aerodynamic components, optics, structural parts and last but not in the least, moulds and dies. The increased need for developing a variety of products that will meet both aesthetics and functionality as fast as possible has led to the research efforts of numerous academics and industrials worldwide.

Owing to its high complexity in terms of process planning, SSM is by default time-consuming and error-prone process. However, rapid advances in manufacturing technology and surface representation, SSM technology is nowadays deemed more robust, efficient and trustworthy enough to meet the requirements of productivity and surface quality. The application of high-order curves and surfaces in CAD environment constitutes a very important aspect to quickly produce accurate 3D models that will reflect actual products whilst sophisticated machining strategies and advanced surface tool paths integrate today’s CAM systems to model machining operations, simulate their process and finally come up with NC codes that will drive 3- or 5-axis CNC machine tools via their control units. The aforementioned applications formulate the modern framework of SSM technology currently implemented in industry to some extent.

5.3.1 Technologies Employed

Information processing, machine tool technology (3- and 5-axis or multi-axis surface machining), Tool path planning for CNC programming (CNC-CAM) and parametric computer-aided design (CAD), are the key features that give SSM its edge. Such features are fully dedicated to advanced manufacturing and it comes as an evident that their usage is capable of achieving low programming/machining (P/M) ratio, cutting efficiency and improved quality. The features are presented in the following sub-sections.

5.3.2 3-Axis Milling

Despite its low efficiency when compared to multi-axis SSM, 3-axis surface machining is still employed by many shop floors worldwide. Milling machines that follow 3-axis coordinate system are actually machining centres integrated with servo motors and hydraulic actuators. The Z-axis is vertical to both X and Y axes and rotates the cutting tool, whereas X and Y formulate the working plane on which

the workpiece is properly attached. With the relatively low cost of a 3-axis machine tool investment being as an advantage, the rotating axis (Z-axis) is restricted to all freedom degrees, thus the tip of the cutter contacts the part's surface and deteriorates it since cutting velocity (V_c —m/min) in the tool's centre is zero.

5.3.3 5-Axis Milling

In five-axis milling, two additional orientation axes allow the machining of very complex parts that cannot be machined employing 3-axis machining technology. Several cases of components comprising polyhedral planes or ruled surfaces impose the application of 5-axis surface machining so as to take advantage of fixturing in a single set-up and achieve geometric tolerance demands in precision cutting. In addition, tool overhang may be reduced when employing 5-axis machining which in turn sustains tool stiffness; provides rigid cutting and avoids primary tool wear. While the implementation of 5-axis surface machining reduces cycle time and improves part quality, two major shortcomings occur: The first involves the complexity of programming using a CAM system to generate tool paths, whereas the second deals with imminent collisions between the cutting tool and the workpiece or fixtures, or even the machine tool peripherals.

5.3.3.1 Parametric Computer-Aided Design -CAD

Computer-aided design via parametric modelling is widely applied owing to its accurate representation mainly when it comes to complex surfaces. With new tools being already provided by CAD software vendors, surfaces can be modelled utilizing several patches which can be continuously controlled through their joints existed in each patch. Parametric technology on the other hand allows rapid adaptations of new products according to old reference models through dynamic dimensioning via relations that can change the whole model should new design concepts are to be tested until arriving to the most convenient solution. Furthermore, approaches for creating surfaces from physical products are already available via 3D scanning technology and surface reconstruction. Polyhedral models, tessellated surfaces, faceted or triangular surface patterns can be processed accordingly in order to come up with new complex products and machine them by taking advantage of their shape information. Representations like the aforementioned are usually created either by point clouds or parametric surfaces, especially when it comes to the manufacturing of surfaces that created from a prototype in an intermediate phase using soft materials like clay to be later converted into CAD data employing either contact or non-contact digitizers. Owing to its geometric computation and data exchange engines, computer-aided design constitutes an interface of paramount importance since 3D representations of this level are entirely used for process planning and precision machining.

5.3.3.2 Tool Path Planning for CNC Programming—CNC/CAM

Tool path planning is a critical task in SSMSSM. Operations need to be carried out in different machining modelling stages like roughing, semi-finishing, finishing, etc. In roughing, most of the material is removed from the stock to generate an approximate shape of the final part's surface. In finishing stage, the roughed surface is formulated to the desired shape which has to meet its engineering drawing requirements in terms of geometrical and dimensional tolerancing—GD and T and surface quality usually expressed via roughness indicators. Technological constraints are determined in tool path planning planning for the different machining stages so as to achieve optimum productivity and quality.

Tool path planning currently involves two fundamental steps; specifying path topology and setting its process parameters. The former is defined by the trajectories that the cutting tool should follow to produce the surface, whereas the latter requires the definitions for feeds and speeds, axial and radial cutting depths, machining tolerance and discretization step; all found under a selected cutting strategy in a CAM environment. Several groups of tool paths together with their cutting styles are available and are applied according to the machining phase the planner wants to model, i.e. rough machining tool paths, semi-finishing; pencil cutting; engraving, etc. The main purpose of rough-machining is to efficiently remove large volumes of material and leave only a small proportion of raw stock to be removed by finishing operation. A number of semi-finish cuts may be applied to leave a more uniform surface for finishing. Tool paths dedicated for finishing are in general “surface-dependent”, that is they utilize surface shape in order to produce tool path trajectories by offsetting it, by copying it or by just following it, considering the known types of surface interpolation; iso-parametric; iso-planar and iso-scallop. Special algorithms recognize the surface's unique entities like curvature, convex and concave regions and then collision-free trajectories are then ought to be produced for further processing by the post-processor engine embedded to commercial CAM software packages. Owing to the high level of sculptured surface complexity, tool paths for finishing may be applied to the entire part's surface or by sequentially selecting limiting contours. Thus; an NC manufacturing programme for SSM can either involve a single machining operation for the whole surface by applying a specific tool path, or a list of machining operations constituted by several neighbouring trajectories grouped according the number of subdivided contours of the surface.

The philosophy of selecting tool paths is tough and tedious task especially when it comes to the selection of 5-axis machining operations for sculptured parts owing to perplex kinematical issues that 5-axis machining involves. Kinematics of 5-axis machine tools can be completely different should the type of 5-axis establishment of machine tools available in the market is taken into account. A 5-axis machine tool with its two rotary axes in the table differs from a “wrist-type” machine tool having its two rotary axes in the spindle. Information concerning the types of 5-axis machine tools can be found in Warkentin et al. [26, 27]. As an outcome, the selection of inclination angles for simultaneous 5-axis surface machining with

respect to the surface and longitudinal–transversal steps according to the feed direction are parameters that should carefully be determined by the CAM programmer. Commercially available CAM packages prompt NC programmers to specify these parameters by offering cutting-edge properties and tools yet; no recommendation is forwarded concerning proper implementation tactics.

The product of machining modelling for SSM using CAM software is a list of motion commands and tool positioning coordinates with respect to the parametric space that the part's surface determines. These coordinates are known as cutter contact (CC) data and vary according to the cutting tool geometry. Most often employed cutting tools for surface machining are flat-end mills, ball-end mills and torus (bull) end mills. The tool tip for each of these tools is located in different regions of their geometry, resulting in differences in computed CC data for surface tool paths. Post-processor engine is then executed to transform calculated CC data to an adapted file format for the CNC unit; the CNC file. The file includes the set of tool positions and tool axis orientations along with the corresponding feeds and speeds. Information concerning tool positions is produced here with reference to the machining axis system by solving Inverse Kinematical Transformation (IKT) algorithms that are capable of giving direct axis commands to the machine tool. The new data is called cutter location (CL) data referring to the position of the tool tip when a given cutter has a contact with the surface in the CC point. Mathematical relations about computing CL data with reference to CC data as a result of tool path computation and the given tool geometry can be found in Warkentin et al. [26, 27].

5.3.3.3 NC Verification

Having extracted the NC file from the above described operations, virtual simulations for material removal are performed to have an initial sense of cutting procedure and assess the tool path for its efficiency and quality. Dedicated software is currently available capable of verifying 3- and 5-axis NC programs for sculptured surface. Their functionality lies mainly on algorithms capable of comparing solid entities in terms of their predetermined nature distinguishing from tools, fixtures, stock, design part and machine tool. Their output is a list of interferences, collision detections, gouges and overcuts. With reference to the design requirements, the NC programme is sent to the CNC unit for production or new machining scenarios are developed after changing the process parameters leading thus to a new CNC programme free of errors. However, the result is far from optimum solutions, since NC verification packages can only enhance tool paths with respect to initial values set by the CAM programmer by locally controlling machining attributes. This leads to the conclusion that the process is enhanced without taking into account economical–technological criteria and constraints as well. Nevertheless, NC verification process is a trustworthy tool for ensuring error-free tool paths for complex machining, especially under the 5-axis SSM mode. Current trends suggest the integration of CAM systems with special NC verification modules for virtual simulation and process enhancement.

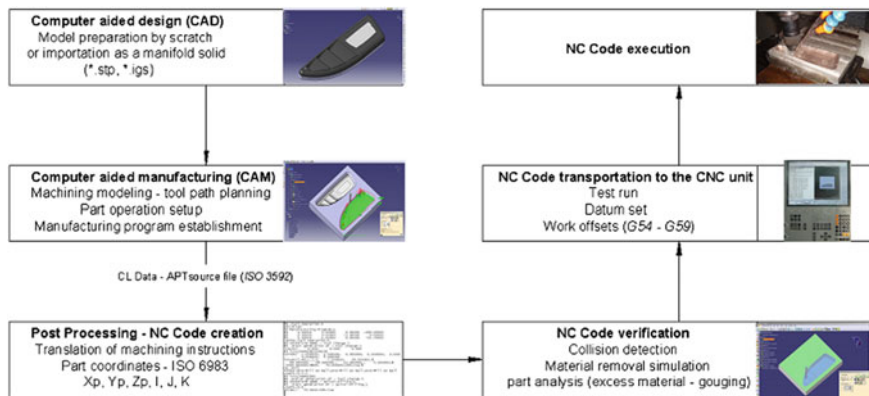


Fig. 5.1 Workflow of current tool path planning operation

The above features can be graphically summarized by giving the workflow representing the current approach adopted for tool path planning for sculptured surface CNC machining in existing CAM systems. Figure 5.1 illustrates this workflow.

5.3.4 Sculptured Surface Machining Error Representation

SSM formulates complex engineering problems introducing a large number of process parameters that need to be controlled in order to reach the required result. Machining errors during machining operation involve process-related inconsistencies owing to the low stiffness of the cutting tool when compared to the rest of the components, i.e. machine tool, fixture and clamped workpiece. Errors fall in this category deal with variations of cutting forces exerted on the tool during machining as well as tool deflections mainly in the horizontal directions (X - Y plane). Such errors violate machining process and deteriorate final surface quality eliminating to a large extent any opportunity of reaching the design requirements in terms of tolerance, dimensioning and geometry.

Our research efforts refer to the geometrical surface error occurrence when the whole process is modelled and prepared using CAM systems and/or relative manufacturing engineering software. Besides, process parameters which finally integrate an NC programme as well as tool path style along with feeds/speeds are set offline within CAM software. Moreover, CAM systems constitute a safe and more or less an easy-to-use interface to model machining operations, whilst the cost of exploiting computer modules is by far reduced rather than utilizing actual resources and materials.

Based on such an assumption one starts to wonder whether such cutting-edge and flexible systems can be further integrated to be “intelligent” and fully

automated not only on the basis of tool path computation, but also on their entire usage. Such an approach can be easily achieved if we take under consideration the openness of the architecture of most commercially available CAD/CAM systems and the current state of artificial intelligent systems that have already seen successful service in engineering problems with their benefits to be mentioned by numerous noticeable research contributions. As a matter of fact an SSM problem can be solved via automation and intelligence yet; the accurate process simulation and correct problem-solving will come by defining suitable quality criteria worthy of assessment and capable of representing physical objectives as good as possible under the basis of manufacturing software involvement.

5.3.4.1 Machining Error Modelling

It is easy to understand that since tool path points (CL and/or CC data) are responsible for locating the tool in discrete coordinates towards its interpolation of a given surface, it comes as an outcome that these instances are also responsible for the success of the machining operation in terms of quality and tolerance of the desired profile. CC and consecutively CL points topology determines the pattern of tool trajectory lines, whereas the parameters such as longitudinal and transversal step specify the distances between these points in a computed tool path. It is mentioned that CL points are generated via the translation of each CC point along the surface normal direction regarding the tool's position on the surface.

In general, a minimum density is required in order to machine a sculptured surface under a predetermined cutting tolerance. The density of the CL/CC point pattern is dependent on the surface profile and the parameter values and especially on stepover and discretization step. Machining surface is then interpolated by adopting one of the widely known interpolation strategies, linear, circular or spline (NURBS) interpolation to remove the uncut material between points in the tool path trajectory. The error caused by the interpolation is actually the deviation existed between the theoretical and actual tool path; known in academic literature as chordal deviation. Chordal deviation represents the deviation existed between the design trajectory of a surface and the actual interpolation trajectory followed by the cutting tool and determines the spacing among tool positions in surface machining, either using 3- or multi-axis machining mode (Fig. 5.2).

With NURBS function (G06.2 command) yet to be embedded to most of hi-tech CNC controllers, still linear and circular interpolations are of great value in terms of their current usage. Besides, new processors integrating these units allow the fast processing of the numerous NC code strings which are inevitably produced when operating with linear (G01) and circular (G02) interpolators to illustrate tool positions with small spacing and thus low chord error average. Having industrials to currently produce complex parts by linearly or circularly approximating sculptured surfaces, leads us to consider the attribute of chordal deviation as an important

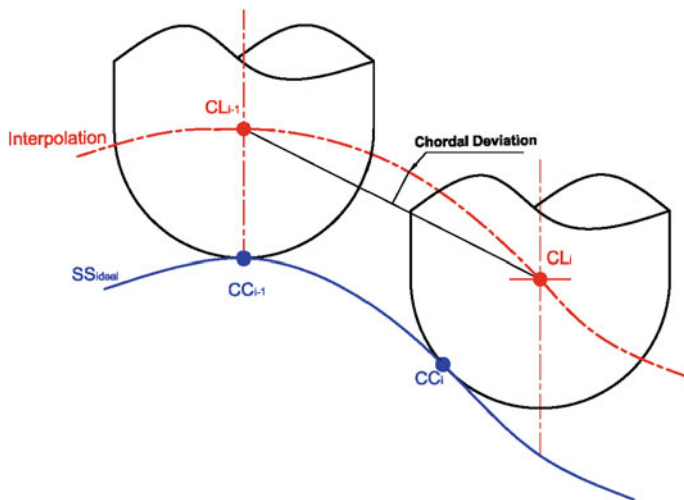


Fig. 5.2 Representation of chordal deviation between theoretical and actual tool path

quality objective to represent the machining error. Under this assumption, fine quality will be reached should very tight separations between tool positions are to be determined to maintain the required tolerance referring to the tool and the surface. On the contrary, requirements for high productivity restrict such decision-making introducing this way a trade-off between the maximum discretization step parameter that is responsible for the chordal deviation and machining time.

Scallop height is directly related to the tool geometry, size and stepover value selected for a given machining strategy. Larger tools in diameter will normally produce smaller scallops in magnitude, hence it is wise to apply large tools to machine sculptured surfaces unless gouges or interferences occur. Smaller tools produce larger scallops for the same stepover value since the latter is a function of the tool diameter's radial movement yet; they manage to reach tight areas of freeform contours such as small fillets, small sculptured slots, etc. Yet again a trade-off is introduced between productivity and scallop height determination owing to the fact that reducing tool pass interval will result to reduce scallops yet at the expense of increased machining time. Nevertheless, research efforts have shown that only improved or optimized tool positioning approaches can balance the above trade-offs and maintain both quality and productivity.

It is within the objectives of the current study to properly model criteria to express the attributes of chordal deviation and scallop height in order to optimize the overall machining error through the novel intelligent algorithm which is about to be presented. The machining error (represented via discretization step and scallop) antagonizes productivity referring to machining time to a series of

evaluations by the algorithm embedded to CAM software suggesting an integrated, easy-to-operate tool path optimization framework for SSM. Criteria modelling operation has been conducted for both 3- and 5-axis SSM modes.

5.3.4.2 Discretization Step Control via CL Point Projections

A novel approach based on projecting computed CL points onto sculptured surfaces is presented here for controlling maximum discretization step parameter. Through this technique, maximum discretization step control offers an “indirect”, yet effective way to generate optimized spacing among CL points since the magnitudes of their projection heights are demanded to be as equidistant as possible. We verify this by sequentially measuring their differences, whilst simultaneously taking into account machining time. The result is uniform patterns of CL points meaning effective tool trajectories, hence regular tool paths. The approach is applicable to both 3- and 5-axis SSM with slight modifications to the latter machining technology (5-axis) for even better control.

5.3.4.3 3-Axis SSM

In 3-axis surface machining the tool orientation (Z-axis) is always vertical to X-Y plane, regardless of the shape to be machined. For this reason, ball-end mills are employed to finish-machine free-form shapes owing to their spherical geometry that ensures tool contact in any curvature. Indeed, a sculptured surface can be generalized as having one or more of any three contours at any given point, convex, concave or flat surface contours. Owing to the restricted freedom degrees in 3-axis machining the ideal contour cannot be always reached leading thus a spherical cutter to produce large facets as CAM software generates non-uniform steps within the specified range.

The requirement of computing new CL points in each iteration based on the minimum difference of projected heights onto the surface, whilst simultaneously considering productivity through machining time criterion prompts our intelligent algorithm to repetitively evaluate these differences, yielding the deviations of all CL points produced by CAM under the applied machining strategy and stochastically arrive at a tool path whose CC points (and consecutively CL points) are uniformly distributed along the curvature with low machining error. Since discretization step is stochastically adjusted to produce small CL point projection height differences, its control minimizes faceting and produces more accurate tool paths under a specified machining tolerance zone. It is mentioned that the same concept may be adopted by investigating CL points coordinates instead of their projections yet; the machining error generated by their corresponding CC points may not be the true one since some of them may not lie on the ideal surface [27]. Projection process ensures that all CL instances will meet a sculptured region of any curvature and the value can be easily retrieved by the application program interface (API).

Let the proposed optimization criterion to be indicated as $h_{CLi_Pj}^{Dif}$, stemming from the requirement of minimum incremental differences for all CL points that constituting the computed tool path. Hence,

$$h_{CLi_Pj}^{Dif} = |h_{CL_Pj}(i-1) - h_{CL_Pj}(i)| = \min, \forall CC_i \in SS \quad (5.1)$$

with

$$\sum_{CC_i=1}^k h_{CLi_Pj} = \min \quad (5.2)$$

where

$h_{CLi_Pj}^{Dif}$: The mean average of the differences computed when projecting CL points onto a part's sculptured surface to control discretization step and thus chordal deviation in (mm);

$h_{CL_Pj}(i-1)$: The projection height distance from the CL(i-1) point to surface;

$h_{CL_Pj}(i)$: The projection height distance from the CL(i) point to surface.

Figure 5.3 depicts the proposed method of controlling the maximum discretization step parameter via the assessment of projection height magnitudes of CL data for sequential tool positions.

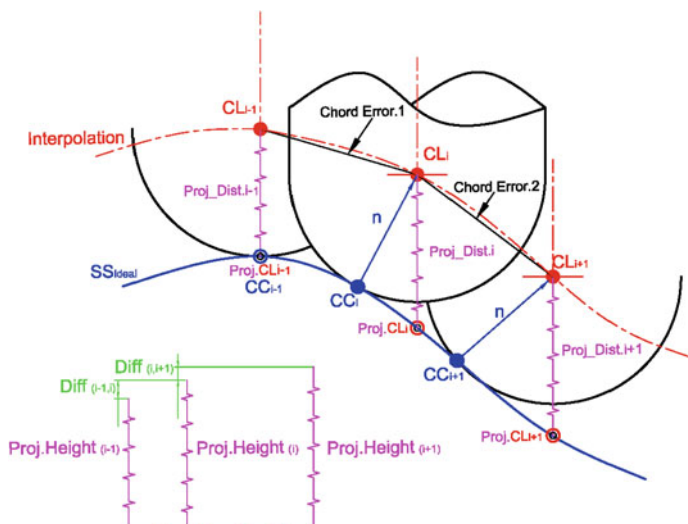


Fig. 5.3 Optimum control of maximum discretization step parameter through CL data projections

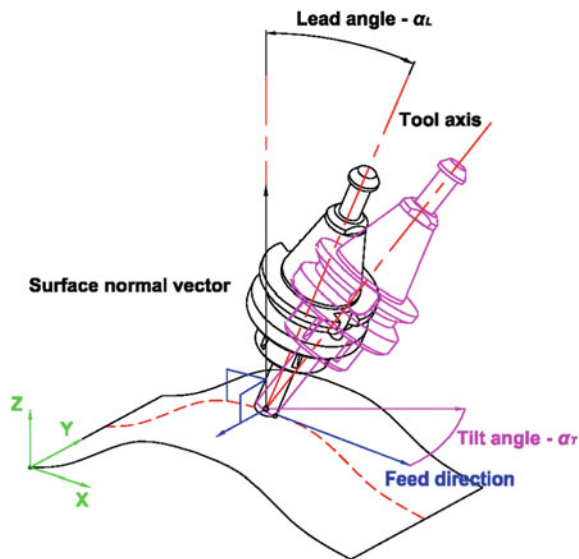
5.3.4.4 5-Axis SSM

In 5-axis machining mode the tool axis orientation is controlled through lead and tilt inclination angles. Lead angle (a_L) controls the tool axis orientation which is normal to the part's surface in the feed direction, whilst tilt angle (a_T) inclines the tool axis in the perpendicular direction of feed (Fig. 5.4). A common problem in 5-axis surface machining is how to restrict variations in terms of tool inclination so that collisions are avoided [18]. As a result the philosophy of implementing the proposed machining error approach should definitely involve tool inclination and cope with the variable tool orientations to estimate accurate discretization step towards the feed direction given the tool type and the surface curvature as well. Kinematics of 5-axis surface machining suggest that each cutter location (CL) point is computed according to each of the corresponded cutter contact (CC) points, and a vector n that is always normal to surface curvature.

Owing to the ability of the cutting tool to change its vertical axis orientation via inclination, projected CL points may produce low distances in advance, yet discretization step towards the path may not generate the required chord error, but a larger one. To cope with this problem in the 5-axis surface machining mode, the objective of attaining minimum incremental differences $h_{CL_Pj}^{Dif}$ for all CL points formulating the tool path is replaced here by a criterion aiming at controlling the ratio of normal vector magnitude when inclining the tool, to the projection distance of its given CL point on the surface. The proposed criterion is expressed as follows:

$$R_{h_{CL_Pj}}^{n_{CCi}} = \frac{\|\vec{n}\|_{CCi}}{h_{CL_Pj}} \forall CCi \in SS, h_{CL_Pj} \neq 0, \|\vec{n}\| > h_{CL_Pj} \quad (5.3)$$

Fig. 5.4 Representation of lead and tilt angles in 5-axis surface machining



where,

$R_{h_{CLi}Pj}^{n_{CCI}}$: The ratio of normal vector magnitude to the distance of a projected CL point to control discretization step parameter and thus control chordal deviation (mm);

$||\vec{n}||_{CCI}$: The normal vector magnitude at the i th CC point;

$h_{CLi}Pj$: The projection height distance from the i th CL point's origin to sculptured surface.

This property controlled by our intelligent algorithm, forces CAM software to stochastically produce CC points for the tool path such that tool axis orientation variability range is restricted as the tool is guided by the surface curve. On the other hand the normal vector should always be vertical to surface curvature. These two instances constraint the solutions range for tool path generation and converge it to those that will satisfy the criterion being set. The constraint of $h_{CLi}Pj \neq 0$ in the above formula ensures that tool tip contact where cutting velocity is zero, is avoided, and normal vector is controlled to sustain low tool inclinations to avoid collisions between the tool and the workpiece or the tool and fixture. The concept is valid for both flat and corner radii (torus) end mills since mathematical principles in terms of the relation between normal vector and projection distance of a CL point are common. When machining using ball-end tools in 5-axis, the normal vector is always equal to tool radius owing to its spherical geometry. Hence, it is the CL point's projection distance that forces tight curve discretization as it occurs in the case of 3-axis surface machining. To initialize the environment and give a good seeding for the algorithm, additional constraints are determined in terms of tool axis orientation when a specific 5-axis surface machining strategy is to be applied. The range of -25° , $+25^\circ$ for lead and tilt angle values has been set for the intelligent algorithm to select from, on its pursuit to generate successful CC points through the evaluations of the objective function that contains the criterion presented. Tilt angle a_T is finally controlled via both the constraints of taking values within the range of $(-25^\circ, +25^\circ)$ and the respective adjustment according to the given CC point's local coordinate system and the surface normal vector for the surface region on which the CC point lies.

5.3.4.5 Scallop Height Control via Effective Radii for Cutting Tools

Moving towards the proposal of a methodology to satisfy both academia and industry, scallop height modelling was conducted by utilizing both simplified mathematical relations and geometrical properties. Thereby, a formula common to most of industrial applications referring to scallop computing was used for 3-axis scallop height objective assessment, whilst a special attribute was adopted for representing scallop height objective evaluation for 5-axis surface machining since the latter is far more of added value to SSM than 3-axis machining technology.

5.3.4.6 3-Axis SSM

The formula employed to estimate the scallop in the case of 3-axis surface machining is given in Eq. 5.4 [23].

$$h_s^{3x} = R(1 - (\sqrt{1 - (\frac{a_e}{D})^2}) \quad (5.4)$$

where,

h_s^{3x} : The scallop height by machining using 3-axis (mm);

R : The radius of the ball-end tool (either in mm or in % D);

a_e : The tool's stepover in the transversal direction (mm);

D : The tool diameter (mm).

5.3.4.7 5-Axis SSM

By adopting the same mathematical relation to assess scallop height magnitude when using ball-end mills, focus is given when machining in 5-axis using flat-end and/or toroidal (bull) end mills being inclined relative to the surface normal vector as illustrated in Fig. 5.5.

It is clearly observed that the shape of a flat-end mill engaging the surface is an elliptical silhouette when projected onto a plane perpendicular to the feed direction involving the surface normal. At the corresponding CC point, the elliptical contour can be interpolated by a circle whose radius is known as the effective radius, R_{ef} .

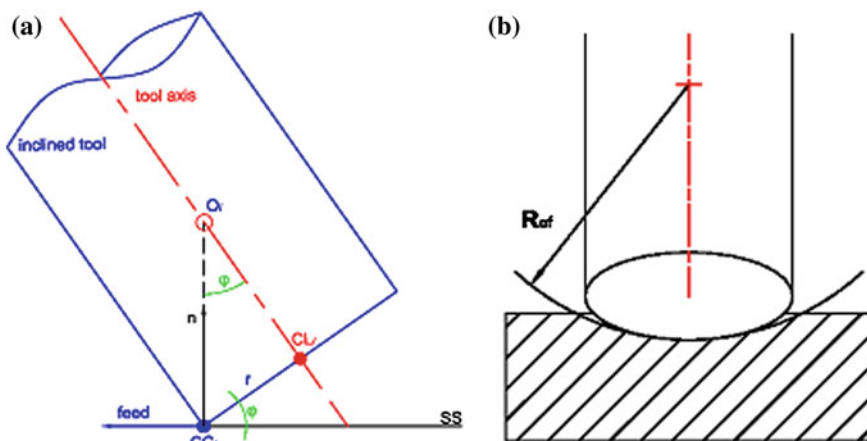


Fig. 5.5 a Inclined flat-end mill; b corresponding effective radius

The effective radius is a function of both the tool's lead angle a_L and its radius R , related as follows:

$$R_{ef} = \left\{ \frac{\frac{R_{tool}}{\sin(a_L)}}{\frac{(R-r)\cos^2(a_L)}{\sin(a_T)[1-\sin^2(a_T)\times\sin^2(a_T)]}} + r \right\} \quad (5.5)$$

Obviously, by varying lead angle a_L and tilt angle a_T through a series of evaluations which our proposed algorithm initializes, a range of effective radii will be obtained and thus different scallops will be assessed. Note that depending on the stochastic tool selection between an end mill and a toroidal mill by our algorithm, the objective function for assessing the scallop will automatically alter its properties concerning the R_{ef} computation formula (either Eq. 5.5). Thus;

R_{ef} : The effective radius of the inclined tool when machining in 5-axis (mm);

R_{tool} : The radius of the tool (either in mm or in %D);

r : The corner radius for a filleted-end (toroidal) mill (mm);

a_L : The tool's lead angle towards its path on the feed direction (°);

a_T : The tool's tilt angle (°).

5.4 Sculptured Surface Tool Path Optimization

An optimization problem related to machining modelling for sculptured surfaces should be designed considering a number of fundamental aspects involving the formulation of the objective function to be assessed, the representation of the solution region (either "Pareto" multi-objective depiction or "weighted" multi-objective transformation to a single-objective one), the removal of bias owing to the differences in measuring units of criteria and the introduction of constraints to better adopt to actual conditions, hence penalizing results considered nonapplicable or infeasible during the convergence procedure.

5.4.1 Objective Function Formulation

Objective functions represent key elements to assess quality objectives in optimization problems, especially when it comes to artificial intelligence and genetic algorithms. Several kinds of objective functions are formulated with the most often used type to be a simplified linear expression among the objectives involved and their weights. Simplifications are made to this stage so as to maintain low computational cost against complex mathematical relations. The weights are utilized to express the importance of influence on corresponding objectives, whilst their sum should be equal to 1 or 100 % depending on the scale to be adopted. We have formulated two objective functions for our algorithm to employ them as assessment

features; one for 3-axis surface machining and one for 5-axis surface machining. The objectives that control chordal deviation and scallop height are the ones that are previously introduced for these two machining technologies. For 3-axis SSM, the objective function is formulated as follows:

$$f(L_{\text{step}}^{3x}, a_e) = \min(h_{\text{CL}_{-}Pj}^{\text{Dif}}, h_S^{3x}, t_m^{3x}) = \min \sum_{w=1}^i w_i f(L_{\text{step}}^{3x}, a_e) \quad (5.6)$$

where,

L_{step}^{3x} : The discretization (longitudinal) step in the feed direction (mm);

a_e : The tool's stepover value in the transversal direction (mm);

$h_{\text{CL}_{-}Pj}^{\text{Dif}}$: The mean average of the differences computed when projecting CL points onto a part's sculptured surface to control chord tolerance in (mm); with

$$h_{\text{CL}_{-}Pj}^{\text{Dif}} = \min, \forall \text{CC}_i \in \text{SS} \text{ thus, } \sum_{\text{CC}_i=1}^n h_{\text{CL}_{-}Pj} = \min$$

h_S^{3x} : The scallop height (mm) produced;

t_m^{3x} : The machining time for 3-axis machining in (min);

w_1, w_2 and w_3 : The weights of $h_{\text{CL}_{-}Pj}^{\text{Dif}}, h_S^{3x}$ and t_m^{3x} , respectively, to identify their influence to the total cost ($w_1, w_2, w_3 \geq 0$ with $\sum w_i = 1$).

For 5-axis SSM, the objective function is formulated as follows:

$$f(L_{\text{step}}^{5x}, a_e) = \min(R_{h_{\text{CL}_{-}Pj}}^{n_{\text{CC}_i}}, h_S^{5x}, t_m^{5x}) = \min \sum_{w=1}^i w_i f(L_{\text{step}}^{5x}, a_e) \quad (5.7)$$

where,

L_{step}^{5x} : The discretization (longitudinal) step in the feed direction (mm);

a_e : The tool's stepover value in the transversal direction (mm);

$R_{h_{\text{CL}_{-}Pj}}^{n_{\text{CC}_i}}$: The ratio of normal vector magnitude to the distance of a projected CL point in (mm); with $R_{h_{\text{CL}_{-}Pj}}^{n_{\text{CC}_i}} = \frac{\|\vec{n}\|_{\text{CC}_i}}{h_{\text{CL}_{-}Pj}} \forall \text{CC}_i \in \text{SS}, h_{\text{CL}_{-}Pj} \neq 0, \|\vec{n}\| > h_{\text{CL}_{-}Pj}$;

h_S^{5x} : The scallop height (mm);

t_m^{5x} : The machining time for 5-axis surface machining in (min);

w_1, w_2 and w_3 : The weights of $R_{h_{\text{CL}_{-}Pj}}^{n_{\text{CC}_i}}, h_S^{5x}$ and t_m^{5x} , respectively, to identify their influence to the total cost ($w_1, w_2, w_3 \geq 0$ with $\sum w_i = 1$).

5.4.2 Normalization

The values of the two objective functions introduced above are meaningful if only their objectives' magnitudes will be taken into account omitting thus their measuring units via proper transformations. Proceeding on a normalization process to

conduct such a task, maximum values for the objectives are used and obtained either by the upper (maximum) working range value given in the initialization process, or by taking the constrained values for the objectives which by default reflect maximum ones. Thus, for 3-axis surface machining mode the following relations are finally utilized.

$$h_{CL_Pj}^{Dif} Norm = \frac{h_{CL_Pj}^{Dif}}{h_{CL_Pj}^{Dif} max} \quad (5.8)$$

$$h_S^{3x} Norm = \frac{h_S^{3x}}{0.01} \quad (5.9)$$

$$t_m^{3x} Norm = \frac{t_m^{3x}}{480} \quad (5.10)$$

where, $h_{CL_Pj}^{Dif} max$ is set to 0.02 as the maximum allowable value for the scallop height and the maximum allowable machining time is 8 h (typically one shift in industry) which corresponds to 480 min. Similar settings were also followed to normalize the objectives of 5-axis surface machining mode.

5.4.3 Constraints

Constraints applied to the current research study involve the constrained properties, their expression and the affected parameters. For a complex machining optimization problem such as this, properties may involve machining parameters from tool path strategies and their workable ranges so as to ensure that obtained optima may be employed to actual industrial operations. Table 5.1 summons the constraints implemented.

5.4.4 Biological Aspects of Virus-Evolution Theory

Genetic and evolutionary algorithms (GAs-EAs) are the most representative attributes of Artificial Intelligence yet; they are prone to premature convergence problem [20]. The cause of this problem is the fact that only a few outstanding solutions take over the population, affecting this way diversity and finally trapping to a local region suggested as the one having the optimum solution. To overcome premature convergence problem without modifying the algorithm is impossible since its intelligent architecture is the instance that forces the algorithm to finally converge towards some regions during the search. One possible solution to the problem is storing patterns as the algorithm changes candidate solution schemes

Table 5.1 Constraints determined for 3- and 5-axis sculptured surface machining

Constraints for 3-axis surface machining mode			
No:	Constrained property	Expression	Affected attributes
1	Tool selection restriction to ball-end mills	“SelectCase – ToolID”	Vf (mm/min), Vc (m/min) according to the tools, scallop height and discretization step according to ball-end mills’ configurations
Constraints for 5-axis surface machining mode			
No:	Constrained property	Expression	Affected attributes
1	a_L (°)	$-25^\circ < a_{L \text{ selected}} < 25^\circ$	$ \vec{n} , R_{h_{CLi_pj}}^{n_{CCI}}, L_{step}^{5x}, h_s^{5x}$
2	a_T (°)	$-25^\circ < a_{T \text{ selected}} < 25^\circ$	$ \vec{n} , R_{h_{CLi_pj}}^{n_{CCI}}, L_{step}^{5x}, h_s^{5x}$
3	$h_{CLi}Pj$ (mm)	1. Flat-end mill: $h_{CLi}Pj \neq 0$ 2. Torus-end mill: $h_{CLi}Pj \neq r$ 3. Ball-end mill: $a_L \neq a_T$, if: $h_{CL_pj} = r$	$R_{h_{CLi_pj}}^{n_{CCI}}, L_{step}^{5x}$
4	$ \vec{n} $ (mm)	$ \vec{n} > h_{CLi}Pj$	$a_L, a_T R_{h_{CLi_pj}}^{n_{CCI}}, L_{step}^{5x}$
General constraints for machining parameters			
No:	Constrained property	Expression	Affected attributes
1	Vc (m/min)	$V_{c_{max}} \text{ tool} > V_{c_{selected}} > V_{c_{min}}$	n (rpm)
2	fz (mm/tooth)	$fz_{max \text{ tool}} > fz_{selected} > fz_{min}$	$V_{f_{selected}}$ (mm/min), t_m^{5x} (min)
3	α_e (% Ø, mm)	$5 \% \text{ Ø} < \alpha_{e \text{ selected}} < 45 \% \text{ Ø}$	h_s^{5x}, t_m^{5x}
4	$L_{step}^{3x}, L_{step}^{5x}$	$0.001 < L_{step}^{3x}, L_{step}^{5x} < 0.1$	h_s^{5x}, t_m^{5x}
General constraints for quality objectives			
No:	Constrained property	Expression	Affected attributes
1	$h_{CL_pj}^{Dif}$ (mm) and $R_{h_{CLi_pj}}^{n_{CCI}}$ (mm)	$0.001 < h_{CL_pj}^{Dif}, < 0.2$ $R_{h_{CLi_pj}}^{n_{CCI}} < 5000$	Overall geometrical machining error and t_m^{3x}, t_m^{5x}
2	Scallop height— h_s^{3x} and h_s^{5x} (mm)	$0.0001 < h_s^{3x}, h_s^{5x} < 0.02$	
3	Machining time, t_m^{3x} and t_m^{5x} (min)	$t_m^{3x}, t_m^{5x} < 8 \text{ h}$	

during its search for global optimum. Thus; efficient patterns are not to be eliminated from the search region when the algorithm converges, hence diversity will be sustained.

The algorithm proposed to address the optimization problem formulated for SSM mimics infection procedures performed by existing viruses. In biology, the viruses’ process of infecting individuals existed to a population is based on two fundamental mechanisms. The mechanism of viruses to utilize their enzyme and

reverse-transcribe (copy backwards) their RNA genomes into DNA, thus integrating it to that of the hosts, is called reverse transcription. Viruses found in nature are also capable of modifying their genetic material or even multiply it to produce new virus individuals. This process is known as transduction. The incorporation of a host's DNA segments into effective viruses and subsequent transfer to other cells is widely known. Besides, entire virus genomes can be incorporated into germ cells and transmitted from generation to generation as vertical inheritance. [1]. The natural mechanism of "vertical inheritance" among genomes was successfully simulated by Kubota et al. [13] through reverse transcription operator. The proposed algorithm's special features and operators involve functions presenting host and virus populations, reverse transcription and transduction operators. The rest of the functions for selection, crossover and mutation operators are as in conventional GAs-EAs. Evidences assembled by other researchers employing Virus-evolutionary genetic algorithm to solve problems out of the field of manufacturing engineering science [12] have encouraged the authors of the proposed work to support that key mechanisms of such an intelligent module can lead to trustworthy results when it comes to machining modelling for sculptured surface tool path planning. Besides, since GAs-EAs are capable of operating without needing derivative information and do not rely on problems' characteristics but only an objective function [10], it is expected by the module to solely follow its optimization concept to this problem as well.

5.4.5 Virus-Evolutionary Genetic Algorithm Architecture

Virus-evolutionary genetic algorithm operates with two populations. The first population is that of hosts (candidate solutions) and plays just the same role as that of a typical host population found in a conventional GA structure, whereas the second population is that of virus individuals. The virus population is needed for storing effective candidate solution patterns during a search. When a new generation of the host population is created, these effective patterns offer information to make the new hosts even better than their parents.

A modified framework for the operational workflow of the virus-evolutionary genetic algorithm was established against the one already proposed by other researchers. On the way to develop a new algorithm of this kind completely by scratch, several improvements were made to the already existed virus-evolutionary genetic algorithm. The already existed one randomly creates the virus population as a substring of a host and as a consequence viruses produced cannot carry more efficient schemata than the ones already captured by the hosts. On the other hand should only the elite of hosts be kept to create the virus population a bias is yielded favouring only the fitted hosts withdrawing in this way the possibility of extracting good data from the rest of the population. To improve this shortcoming in the proposed virus algorithm, virus individuals are generated after determining their number as a fraction of the number of host individuals. The algorithm performs

transduction operation to some of the best-fitted individuals after evaluating their fitness function, whereas the rest of the viruses are created by randomly selecting from the rest of the hosts. Thus, the seed for producing candidate solutions will hold no bias favouring only outstanding individuals who produce high-fitted offspring.

Initialization process involves the random generation of host population. As a parameter representation scheme, binary encoding is selected since it facilitates the pattern formulation process. Initialization is achieved by creating the individuals' chromosomes according to the parameter value range and accuracy (number of binary digits to describe the phenotypic values for variables). Due to GAs stochastic nature, determining convergence criteria is usually an arbitrary process. A common ground in many studies is that the algorithm terminates after a predetermined number of generations or when no further improvement is indicated to the solutions for a given number of generations. Thereby, virus-evolutionary genetic algorithm is adjusted to terminate its evaluation process after specifying a constant number of generations.

5.4.6 Virus Operators

Once the two populations have been created by applying the transduction operator, the population of viruses infects host individuals by applying reverse transcription operator. Reverse transcription operator manages to overwrite a virus' binary string to a host's binary string. Programmatically, this is achieved by sequentially typing each binary digit or the virus' string to the host's string according to the determined locus for replacement. To do so, the indices of both the virus and the host together with their replacement loci for the strings are declared. As a result, a new host (infected host) is generated. Reverse transcription and transduction operators are dynamically collaborated under the major goal of increasing more effective individual representation schemata that will rapidly lead to the global optimum solution for a given problem. Figure 5.6 depicts the operational sequence for reverse transcription and transduction operators towards their virus infection result.

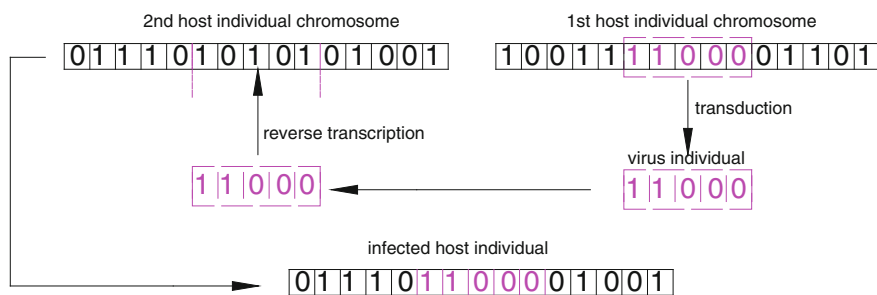


Fig. 5.6 Function of reverse transcription and transduction operators

In addition to common parameter settings that conventional GAs–EAs suggest (crossover probability, mutation probability and rate, etc.), virus-evolutionary genetic algorithm involves parameters to determine virus fitness, infection rate, the “life” of viruses, etc. A virus individual (*virus “i”*) has a fitness value (*fitvirus (i)*) which is calculated to indicate its efficiency. The fitness of each virus is determined as the sum of the fitness of each infection caused by the current virus to the host population (Eq. 5.11). Moreover, the fitness of each infection is computed which is determined as the difference between the fitness value of the original host and the one calculated after its infection (Eq. 5.12).

$$fitvirus(i) = \sum_{j \in S} fitvirus(i,j) \quad (5.11)$$

$$fitvirus(i,j) = fithost(j') - fithost(j) \quad (5.12)$$

Thereby, each virus has a measuring parameter for its infection strength; that is *fitvirus (i)*. *Fithost (j)* and *fithost (j')* are the fitness values of a host “j” before and after its infection, respectively. The indicator *fitvirus (i,j)* denotes the difference between the fitness values, *fithost (j)* and *fithost (j')*, which is equal to the improvement value obtained through the infection process. To the equations presented above, “i” denotes the virus number and “S” represents the sum of host individuals infected by the virus “i”. The number of infections caused by each virus is controlled through infection rate (*infrate (i)*). If a virus has a positive fitness, the infection rate is increased according to a constant parameter “α”. In contrast, if the virus has a negative value the infection rate is reduced. Kubota et al. [13] suggested that maximum infection rate to be 0.1 and initial infection rate to be 0.05. The infection rate of each virus should satisfy the criterion $0 \leq infrate(i) \leq 1.0$ so as to perform a reverse transcription operation to a given host population. Equation 5.13 represents the formulation of these settings for the determination of infection rate by Kubota et al. and is depicted below:

$$inf\ rate_{i,t+1} = \begin{cases} (1 + \alpha) \times inf\ rate_{i,t}, & fitvirus(i) \geq 0 \\ (1 - \alpha) \times inf\ rate_{i,t}, & fitvirus(i) \leq 0 \end{cases} \quad (5.13)$$

Consecutively, the higher the infection rate of a virus “i” is, the higher its infection capability becomes and the virus infection rate is equal to the frequency increasing a schema in a population. The operational duration for virus individuals is controlled by virus life. The virus life indicates the contribution and positive impact of virus infection to the evolution process. The virus life is programmatically computed as follows:

$$life_{i,t+1} = r \times life_{i,t} + fitvirus_i \quad (5.14)$$

where “r” is a life reduction rate and “t” represents the generation being evaluated. If life is negative then the virus individual transduces a new substrating from a random host to change its scheme and become efficient. If life is positive the virus

individual transduces a partially new substring from one of the infected host individuals to manipulate it for its benefit (further increase its efficiency). The positive calculus of a virus' life implies that its fitness is quite high and the schema of the successfully infected host by this virus is strong. Hence partial transduction is applied to this host to generate another good sub-string pattern which is another virus and that virus proceeds to further infections. In general efficient schemata in virus-evolutionary genetic algorithm are increased exponentially through this mechanism and local regions of a given solution space are rapidly searched.

5.5 Manufacturing Software Integration

Customized engineering environments play key role in today's pressing needs for high quality and low costs. One way for industries to ensure and improve their competitiveness is to examine which of the tasks warrant automation towards the adaptation of an integrated product manufacturing framework. Should a number of preparation phases involve routine and repetitive activities, one may apply automation techniques to shorten lead time of product machining modelling, NC part programming and process optimization.

To keep up with the above philosophy on rapidly delivering results referring to the stage of CNC tool path generation with the aid of CAM systems, the API of a cutting-edge CAD/CAM/CAE package was utilized to develop automated functions capable of handling the system's tools and execute sequential operations according to the evaluation phase processed by the virus-evolutionary genetic algorithm.

5.5.1 Automated Framework

The values for computing the objective function are provided by an external infrastructure which automates CAM software utilities, hence coupling the virus-evolutionary GA to CAM interface. Cooperation between the algorithm and the CAM system was achieved by additional code developed to customize the collaborative environment. The code embedded to the environment as stand-alone automation routines and was written in Visual Basic for Applications (VBA) utilizing the hosted programming development platform (API) of *Dassault systèmes*® CATIA® V5-R18. The code developed undertakes to automatically:

- Scan the machining modelling history tree, retrieve the machining operations with their related process parameters and pass the values proposed by the genetic algorithm as candidate solutions;
- Compute the tool path according to the specified settings and run the machining simulation;
- Extract information and statistics corresponding to quality objectives.

By utilizing the structure of automation objects existed in a SSM set-up document, the parametric tree structure is accessed so as to retrieve the machining operations containing the strategies and their related parameters for automation. Common functions of visual basic are then applied to declare the parameters according to their role (integer, double, string, Boolean, etc.) whereas special programming is needed for proper argument passing and data exchange. In general, input–output files employed for such applications are represented either in *.txt or *.dat format containing the data. By sequentially accessing the files, associated objects to the commands retrieve the corresponded values of inputs–outputs and current properties are updated towards new simulations.

When the framework is activated by the user, a selection in terms of the manufacturing programme type according to the machining set-up document (3- or 5-axis) is done. Through this selection the programming functions corresponded to each of the two machining modes are retrieved. Further on, the user is prompted to specify the importance of quality objectives through the determination of weights. The values for the weights are based on industrial demands and special needs, thus they ought to vary depending on the case. Optimization settings involve the specification for process parameter values which are loaded as initial inputs to the system (initial seeding for the genetic algorithm). The document's parametric tree is scanned to summon data as explained above. The procedure is initially executed for roughing operation (which is not a concern on this part of our research), whilst one of the finishing operations follows next in the sequence. If a previous run with the same variable values is detected, the automation infrastructure developed will directly expose results for that run to avoid unnecessary computations. To do so, Visual Basic's flag states were programmed in the code reducing this way overall performance time of the algorithm. The phenotype values for process parameters are loaded as soon as the machining operation is retrieved and a check whether they satisfy technological constraints is performed. Should the values violate the constraints, the system returns a penalized value for the corresponding objective function.

5.6 High-Precision Cutting Experiments on Sculptured Surfaces

To test our proposed optimization methodology, two SSM experiments were modelled and conducted; one adopting 3-axis CNC surface machining and one adopting 5-axis CNC surface machining. Two test parts were modelled to plan their machining operations utilizing three approaches.

Validation of the simulated entities via our approach was achieved by comparing the results with two different approaches. The first approach was that of a manual tool path “optimization” by considering current industrial practices to enhance CNC programming through trial-and-error, whilst the second was a tool path

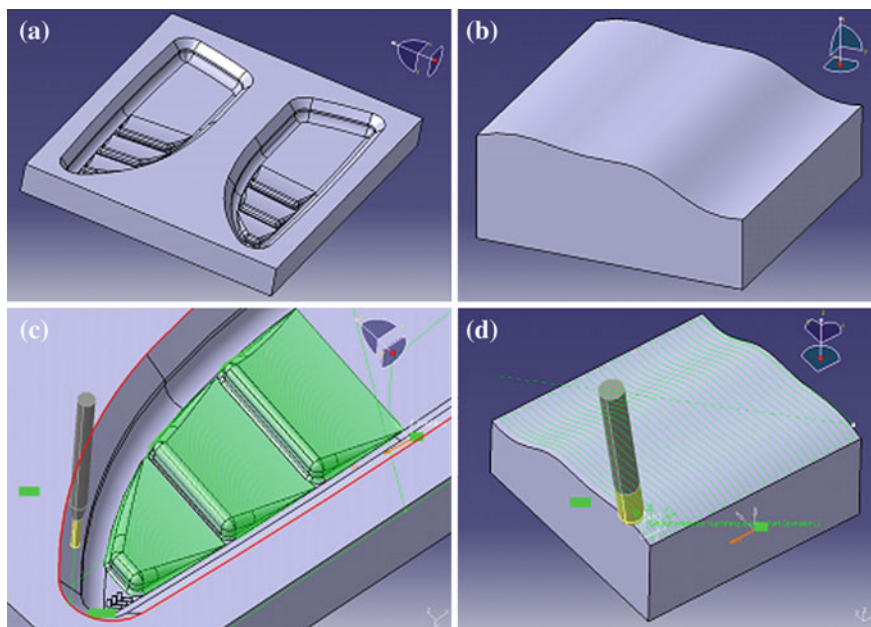


Fig. 5.7 **a** Test part for 3-axis SSM; **b** test part for 5-axis SSM; **c** 3-axis surface machining tool path; **d** 5-axis surface machining tool path

optimization via our intelligent algorithm without activating the Virus operators, hence using a conventional genetic algorithm. In the third approach the virus operators were activated in the genetic algorithm and the operation was optimized with our proposals in this study. The two test parts are depicted in Fig. 5.7a (3-axis) and Fig. 5.7b (5-axis), whereas the tool paths applied to machine their free-form contours are depicted in Fig. 5.7c, d for 3-axis and 5-axis, respectively.

In all three alternatives, the quality objectives introduced in Sect. 4.1 were utilized. For the manual NC tool path planning only the part of the automation module that projects the CL data was used so as to measure the distances from their origins to the surface and consecutively to compute their incremental differences to assess chordal deviation. Scallop height formulas were in this module as well. The rest of the alternatives that involve the genetic algorithms, were run in full automation performing the iterative evaluations.

5.7 3-Axis SSM Case

The results obtained in terms of the tool path CL data patterns for the 3-axis part, and for the three alternatives, are depicted in Fig. 5.8a, b, c for the manual, the conventional GA and the Virus-evolutionary GA, respectively. It is observed that

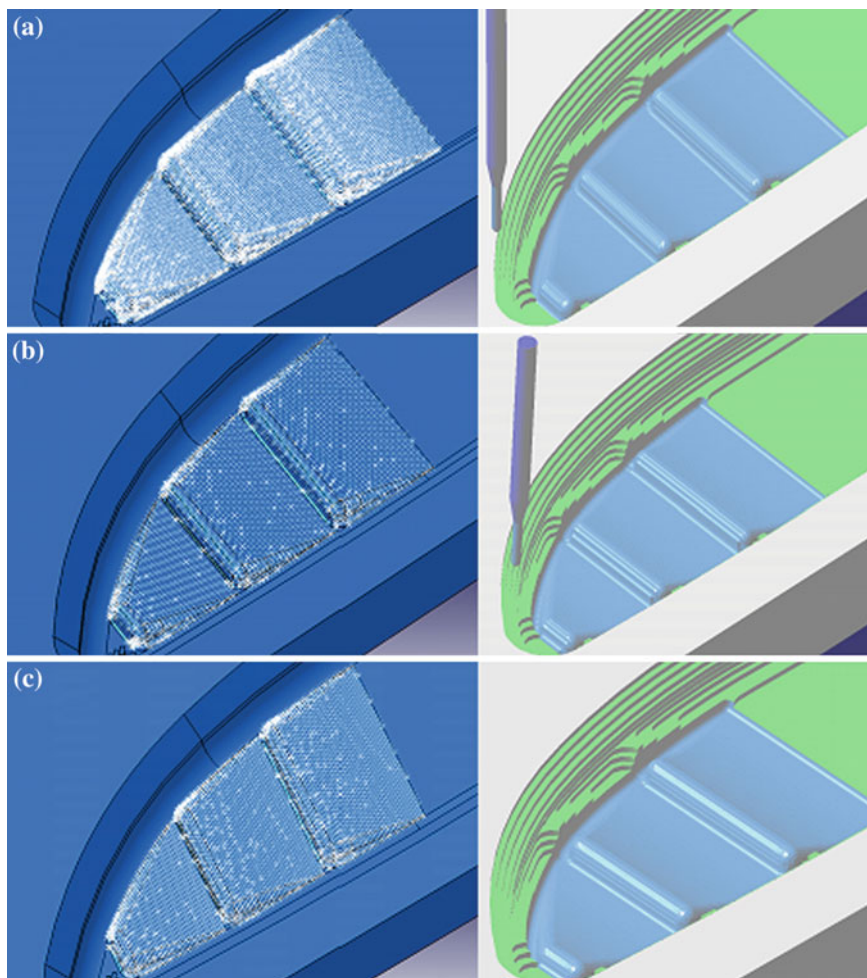


Fig. 5.8 Projected CL point grids to assess 3-axis sculptured surface machining error: **a** manual CNC programming; **b** CNC programming using conventional GA; **c** CNC programming using virus-evolutionary genetic algorithm

the last approach produced the most uniform CL point pattern meaning both regular surface approximation and a uniformly distributed error that is actually low, considering the simulated solid shown in the right-hand side of Fig. 5.8c.

For this machining mode, the outputs from the two “intelligent” approaches (machining via GA and machining via Virus-evolutionary GA) were also used to conduct an actual machining operation for the 3-axis SSM part in a 3-axis CNC vertical machining centre *BRIDGEPORT*[®] VMC 460₁₂ equipped with a *Heidenhain TNC-320* CNC control system. As the 3-axis test part is a mirrored mould, one-half machined via GA optimization and the other half via the virus algorithm. Despite

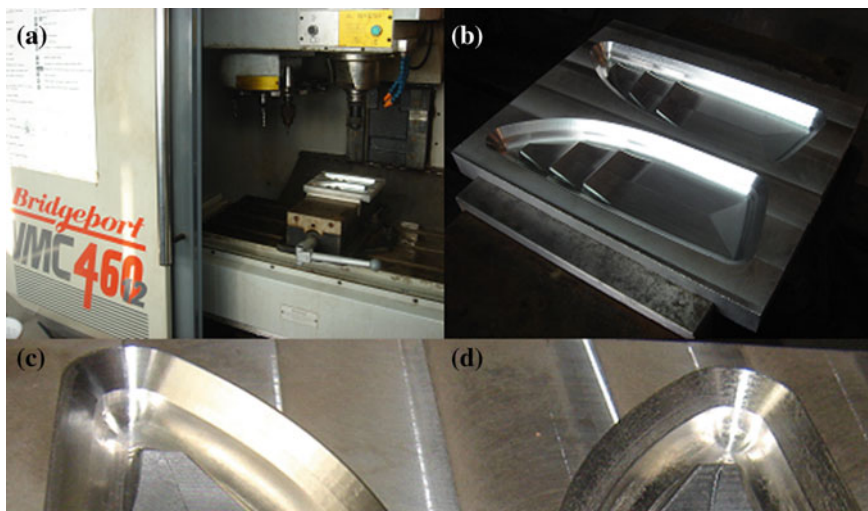


Fig. 5.9 Actual machining of the 3-axis test part: **a** machining set-up; **b** finished part; **c** detailed surface result obtained via virus-evolutionary algorithm; **d** detailed surface result obtained via conventional GA

the fact that process parameters, i.e. feed and speed are also involved for optimization process, they kept constant to limit the interest only to the attributes that formulate the geometric machining error, stepover and maximum discretization step. The material was a $20 \times 170 \times 200$ mm Al-1050 plate. To select feeds and speeds according the tools used, a tool catalogue was built considering the data taken by www.Garant-tools.com. Figure 5.9a shows the machining set-up, Fig. 5.9b the finished part, Fig. 5.9c a limited region in detail achieved via the application of virus-evolutionary genetic algorithm and Fig. 5.9d a limited region in detail achieved via the application of the genetic algorithm without activating the virus operators.

Feeds and speeds for the tools as well as the results for quality objectives for the 3-axis SSM optimization are given in Table 5.2.

5.8 5-Axis SSM Case

Virtual machining experiments were conducted to validate the proposed modelling and optimization approach in the case of 5-axis sculptured surface tool path generation. Sweeping strategy was determined to variable lead/tilt angles for the tool orientation in the case of 5-axis machining part which was simulated and verified using *CG-Tech® Vericut 7.3* NC tool path verification system. The range for the 5-axis tool orientations was $-25^\circ/+25^\circ$ for both inclination angles to avoid imminent interferences among the tool and the workpiece or the fixture. Resulting

Table 5.2 Results for machining parameters and target objectives for 3-axis SSM

Operation	3-axis sculptured surface machining
Manual	
Parameters	
n (rpm) 5200	Tool: Ball-end Ø2
V_f (mm/min) 900	
a_e (% Ø) 5 % (0.12 mm)	
L_{step}^{3x} (mm) 0.001	
Quality objectives	
No. CL points	3025
$h_{CL_Pj}^{Dif}$ (average)	0.1722
h_S^{3x} (mm)—computed	0.002
t_m^{3x} (min)	27.68
Conventional GA	
Parameters	
n (rpm) 5200	Tool: Ball-end Ø2
V_f (mm/min) 900	
a_e (%Ø) 17.85 % (0.357 mm)	
L_{step}^{3x} (mm) 0.078	
Quality objectives	
No. CL points	1934
$h_{CL_Pj}^{Dif}$ (average)	0.1509
h_S^{3x} (mm)—computed	0.016
t_m^{3x} (min)	7.83
Virus-evolutionary GA	
Parameters	
n (rpm) 5200	Tool: Ball-end Ø2
V_f (mm/min) 900	
a_e (%Ø) 14.8 % (0.296 mm)	
L_{step}^{3x} (mm) 0.014	
Quality objectives	
No. CL points	2017
$h_{CL_Pj}^{Dif}$ (average)	0.1120
h_S^{3x} (mm)—computed	0.011
t_m^{3x} (min)	9.46

outputs are of similar interpretation concerning the CL point patterns produced. Figure 5.10a illustrates the CL data pattern and the corresponded simulated part by adopting a manual tool path generation. Figure 5.10b, c shows the same results by applying the conventional GA and the Virus-evolutionary Genetic Algorithm,

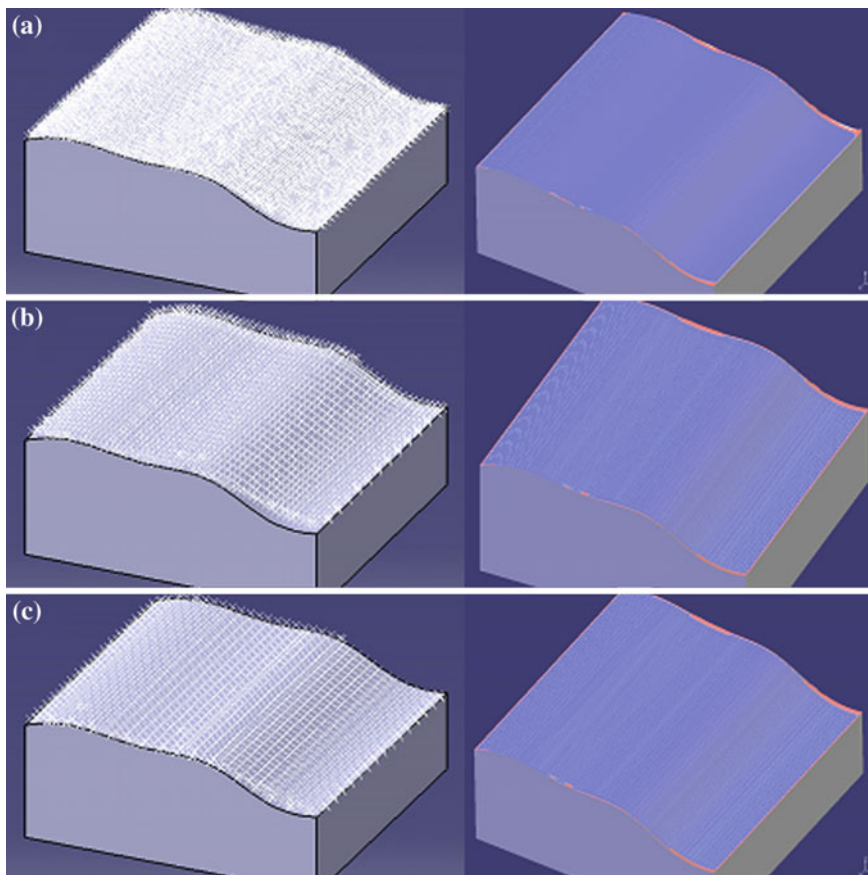


Fig. 5.10 Projected CL point grids to assess 5-axis sculptured surface machining error: **a** manual CNC programming; **b** CNC programming using conventional GA; **c** CNC programming using virus-evolutionary genetic algorithm

respectively. Yet again a more uniform CL data pattern is obtained with the proposed optimization algorithm and machining time results lower than the conventional GA's employment to the problem's multi-objective response. The surface obtained is very close to manual mode where maximum discretization step value was set to 0.001 to ensure low error surcharging machining time on the other hand.

For this machining mode, the outputs from all three approaches were used to conduct virtual machining experiments for the 5-axis SSM part in *CG-Tech® Vericut 7.3* NC tool path verification system. Yet, again we limited the interest only to the attributes responsible for yielding the geometric machining error, stepover and maximum discretization step. The material was considered the same to that being used in 3-axis SSM, whilst the same tool catalogue adopted also for this case. Figure 5.11a shows the virtual machining setup, Fig. 5.11b the virtual machine employed, Fig. 5.11c the part surface obtained in terms of the machining error by

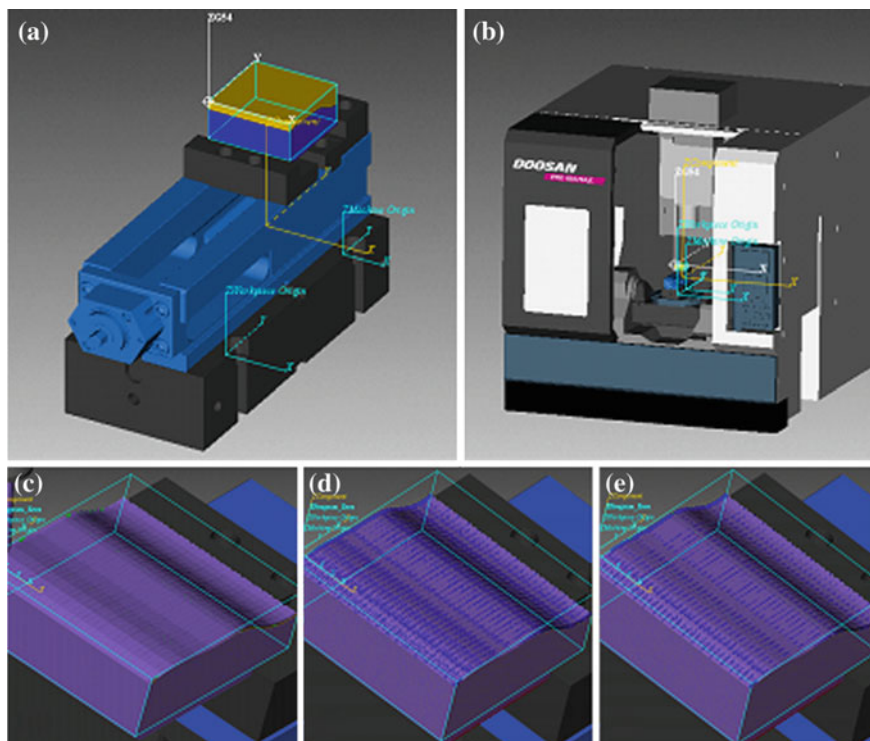


Fig. 5.11 Virtual machining of the 5-axis test part: **a** machining set-up; **b** virtual CNC machine tool used; **c** resulting part surface error via manual CNC programming; **d** resulting part surface error via the application of conventional GA; **e** resulting parts surface error via the application of virus-evolutionary genetic algorithm

adopting manual programming, Fig. 5.11d the part surface obtained in terms of the machining error by implementing the conventional genetic algorithm and Fig. 5.11e the resulting surface obtained by applying the virus-evolutionary genetic algorithm. Feeds and speeds for the tools as well as the results for quality objectives for the 3-axis SSM optimization are given in Table 5.3.

5.9 Discussion of Results

The current study proposes an intelligent methodology for sculptured surface tool path optimization. Intelligence is introduced by developing a non-standard genetic algorithm based on the virus theory of evolution, whilst it is embedded to a cutting-edge CAD/CAM system as the main environment to plan tool paths for complex surfaces. By suggesting a user-friendly interface NC programmers may give the inputs for machining parameters responsible to formulate the cutting path style

Table 5.3 Results for machining parameters and target objectives for 5-axis SSM

Operation	5-axis sculptured surface machining
<i>Manual</i>	
Parameters	
$a_L(^{\circ})$ 10	Tool: Flat-end Ø16
$a_T (^{\circ})$ 5	
a_e (% Ø) 10 % (1.6 mm)	
L_{step}^{5x} (mm) 0.001	
<i>Quality objectives</i>	
<i>No. CL points</i>	4826
$R_{h_{CLi_pj}}^{n_{CCi}}$ (average)	499.78
h_S^{5x} (mm)—computed	0.0016 n_{CCi} = 45.98, h_{CLi_pj} = 0.092
t_m^{5x} (min)	25.56
<i>Conventional GA</i>	
Parameters	
$a_L(^{\circ})$ 21.65	Tool: Flat-end Ø16
$a_T (^{\circ})$ 3.27	
a_e (%Ø) 5.94 % (0.951 mm)	
L_{step}^{5x} (mm) 0.0173	
<i>Quality objectives</i>	
<i>No. CL points</i>	3402
$R_{h_{CLi_pj}}^{n_{CCi}}$ (average)	285.26
h_S^{5x} (mm)—computed	0.00054 n_{CCi} = 21.68, h_{CLi_pj} = 0.076
t_m^{5x}	16.02
<i>Virus-evolutionary GA</i>	
Parameters	
$a_L(^{\circ})$ 1.537	Tool: Bull-end Ø16-Rc4
$a_T (^{\circ})$ 3.39	
a_e (% Ø) 5.6375 % (0.902 mm)	
L_{step}^{5x} (mm) 0.0152	
<i>Quality objectives</i>	
<i>No. CL points</i>	3112
$R_{h_{CLi_pj}}^{n_{CCi}}$ (average)	4003.92
h_S^{5x} (mm)—computed	0.00049 n_{CCi} = 296.29, h_{CLi_pj} = 0.074
t_m^{5x}	13.5

and influence the geometrical machining error at the same time. Since trial-and-error approaches and tool catalogue-based selections for machining parameter values might introduce inconsistencies, global outputs become far from optimum.

The methodology suggests to take advantage of the CL data computed during the post-processing phase of tool path planning, since they represent the only instances which CNC programming units take into account in actual machining operations and thus are responsible for the final outcome in terms of part quality and machining time. The study uses CL data to project their origins to the sculptured surface in order to sequentially measure their distances and hence compute the incremental step which in turn controls chordal deviation. Moreover, the scallop is introduced as the second objective to be optimized since it strongly affects machining error as well. Results summoned via experiments for 3- and 5-axis SSM reveal that proposed objective modelling is deemed rather efficient considering the resulting tool path patterns. The tool paths computed minimize machining time to the best possible extent, whilst they are adopted to the minimum geometric machining error in terms of maximum discretization step parameter and scallop height.

Time-intensive operations were successfully automated towards the conjugation of the virus-evolutionary genetic algorithm and the rest of the environment. The special mechanism of virus operators reveals that this kind of algorithm is capable of representing more effective schemata during the evaluations performed in a loop of generation. A proof of our assumptions is the uniformity of the projected CL point grids meaning that viruses suggest efficient information carriers covering broader solution regions belong to the overall study space. This did not occur when the same algorithm run without the activation of its virus operators representing this way a conventional genetic algorithm coming up with its known drawbacks referred in the literature.

References

1. Anderson N (1970) Evolutionary significance of virus infection. *Nature* 227:1346–1347
2. Budak E, Tunç LT, Alan S, Özgüven HN (2012) Prediction of workpiece dynamics and its effects on chatter stability in milling. *CIRP Ann-Manuf Technol* 61(1):339–342
3. Can A, Ünüvar A (2010) A novel iso-scallop tool-path generation for efficient five-axis machining of free-form surfaces. *Int J Adv Manuf Technol* 51(9–12):1083–1098
4. Choi BK, Jerard RB (1998) *Sculptured surface machining: theory and applications*. Kluwer Academic Publishers, Dordrecht
5. Del Prete A, Mazzotta D, Anglani A (2007) Control and optimization of toolpath in metal cutting applications through the usage of computer aided instruments. 8th AITeM Conf Montecatini Terme, p 10–12
6. Drysdale SRL, Rote G, Sturm A (2008) Approximation of an open polygonal curve with a minimum number of circular arcs and biarcs. *Comput Geom* 41:31–47
7. Duroobi AA, Mohamed JH, Kazem BI, Wenlaing C (2013) Pick-interval scallop height estimation using three types of geometrical end mill cutters on cnc milling machine. *Int J Eng Technol* 31(8):1580–1591
8. Fountas NA, Vaxevanidis NM, Stergiou CI, Benhadj-Djilali R (2014) Development of a software-automated intelligent sculptured surface machining optimization environment. *Int Adv Manuf Technol* 75(5–8):909–931

9. Gilles P, Cohen G, Monies F, Rubio W (2013) Torus cutter positioning in five-axis milling using balance of the transversal cutting force. *Int J Adv Manuf Technol* 66(5–8):965–973
10. Goldberg DE (1989) Genetic algorithms in search, optimization, and machine learning. Reading, Massachusetts, Addison-Wesley
11. Hacene A, Assas M (2011) NURBS interpolation strategies of complex surfaces in high speed machining. *Int J CAD/CAM* 11(1):1–6
12. Jian C, Li F (2013) An improved virus evolutionary genetic algorithm for workflow mining. *J Theor Appl Inform Technol* 47(1):406–411
13. Kubota N, Fukuda T, Shimojima K (1996) Virus-evolutionary algorithm for a self-organising manufacturing system. *Comp Ind Eng* 30(4):1015–1026
14. Lai XD, Zhou YF, Zhou J, Peng FY, Yan SJ (2003) Geometrical error analysis and control for 5-axis machining of large sculptured surfaces. *Int J Adv Manuf Technol* 21:110–118
15. Li H, Remus TF, Feng HY (2007) An improved tool path discretization method for five-axis sculptured surface machining. *Int J Adv Manuf Technol* 33(9–10):994–1000
16. Lin Z, Fu J, Shen H, Gan W (2014) A generic uniform scallop tool path generation method for five-axis machining of freeform surface. *Comput Aided Des* 56:120–132
17. Liu M, Huang Y, Yin L, Guo J, Shao X, Zhang G (2014) Development and implementation of a NURBS interpolator with smooth feedrate scheduling for CNC machine tools. *Int J Mach Tools Manuf* 87:1–15
18. López de Lacalle LN, Lamikiz A (2008) Sculptured Surface Machining. In: Davim JP (ed) *Machining*. Springer, New York
19. Ma W, He P (1998) B-spline surface local updating with unorganised points. *Comput Aided Des* 30(11):165–172
20. Malik S, Wadhwa S (2014) Preventing premature convergence in genetic algorithm using DGCA and elitist technique. *Int J Adv Res Comp Sci Soft Eng* 4(6):410–418
21. Manav C, Bank HS, Lazoglu I (2013) Intelligent tool path selection via multi-criteria optimization in complex sculptured surface milling. *J Intell Manuf* 24:349–355
22. Ponomarev B (2014) Selecting optimal machining strategy parameters when milling complex surfaces by spherical milling cutters. *Int J Mech Mechatr Eng* 14(1):1–5
23. Quinsat Y, Sabourin L, Lartigue C (2008) Surface topography in ball end milling process: description of a 3D surface roughness parameter. *J Mater Proces Technol* 195(1–3):135–143
24. Shukun C, Li S, Ke D, Kaifeng S, Zhiming A (2012) Research on path optimization technology for free-form surface five-axis NC machining. *Adv Mater Res* 443–444:202–208
25. Vijayaraghavan A, Sodemann A, Hoover A, Mayor JR, Dornfeld D (2010) Trajectory generation in high-speed, high-precision micromilling using subdivision curves. *Int J Mach Tools Manuf* 50(4):394–403
26. Warkentin A, Ismail F, Bedi S (2000) Comparison between multi-point and other 5-axis tool positioning strategies. *Int J Mach Tools Manuf* 40(2):185–208
27. Warkentin A, Ismail F, Bedi S (2000) Multi-point tool positioning strategy for 5-axis machining of sculptured surfaces. *Comput Aided Geomc Des* 17(1):83–100
28. Yang J, Altintas Y (2015) A generalized on-line estimation and control of five-axis contouring errors of CNC machine tools. *Int J Mach Tools Manuf* 88:9–23
29. Yang X (2002) Efficient circular arc interpolation based on active tolerance control. *Comput Aided Des* 34:1037–1046
30. Yen SS, Hsu PL (2002) Adaptive feedrate interpolation for parametric curves with confined chord error. *Comput Aided Des* 34:229–237
31. Zeroudi N, Fontaine M, Necib K (2012) Prediction of cutting forces in 3-axes milling of sculptured surfaces directly from CAM tool path. *J Intell Manuf* 23(5):1573–1587
32. Zhang XF, Xie J, Xie HF, Li LH (2012) Experimental investigation on various tool path strategies influencing surface quality and form accuracy of CNC milled complex freeform surface. *Int J Adv Manuf Technol* 59:647–654
33. Zou Q, Zhang J, Deng B, Zhao J (2014) Iso-level tool path planning for free-form surfaces. *Comput Aided Des* 53:117–125

Chapter 6

Friction Stir Welding: Scope and Recent Development

**Rahul Jain, Kanchan Kumari, Ram Kumar Kesharwani,
Sachin Kumar, Surjya K. Pal, Shiv B. Singh,
Sushanta K. Panda and Arun K. Samantaray**

Abstract Friction Stir Welding (FSW) is a new solid-state welding technique which finds application in various industries. This chapter introduces the process, basic mechanism, application, and recent research developments. Research work in this book chapter is broadly divided in two parts: experimental-based, and finite element modeling (FEM)-based approaches of the FSW process. In the experimental studies, three recent developments are presented in this chapter: first, a unique twin-tool concept to modify the FSW process and provide alternative to multi-pass FSW; second, feasibility of using ultrasonic coupled with FSW is studied to reduce the amount of force generated during the process and improve the process efficiency; and finally, formability study of friction stir welded blank is presented. Formability of welded blank plays a vital factor for different industrial application, especially in automobile industry. In the second part, FEM method is implemented to simulate the process. Different modeling techniques are also discussed. A case study in each case is presented with sample results, to have a better understanding on the process and development.

6.1 Background on Development of FSW

For the last two decades, aspiration of human kind to curb fuel consumption has emerged out as utmost priority. Fuel efficiency can be achieved by technological upgradation, or by weight reduction. Technological revamp means replacing the old

R. Jain · K. Kumari · R. Kesharwani · S. Kumar · S.K. Pal (✉)
S.K. Panda · A.K. Samantaray
Mechanical Engineering Department, Indian Institute of Technology,
Kharagpur 721302, India
e-mail: skpal@mech.iitkgp.ernet.in

S.B. Singh
Metallurgical and Materials Engineering Department,
Indian Institute of Technology, Kharagpur 721302, India

© Springer International Publishing Switzerland 2015
J.P. Davim (ed.), *Modern Manufacturing Engineering*, Materials Forming,
Machining and Tribology, DOI 10.1007/978-3-319-20152-8_6

179

technology with a newer and better one, for example in automobile sector, two wheelers which were launched in late 1990s gave an average mileage of 35–45 km/l; whereas two wheelers of 2015 give an average mileage of 60–70 km/l, even more. This was possible with refurbishing of engine from two stroke to four stroke to electronically controlled four stroke engines, but technological revamp is a time consuming process, and also there is limitation. On the other hand, use of lower density material instead of higher one without compromising quality and functionality of product can improve fuel efficiency, e.g., Honda replaced a part of a steel subframe of chassis with aluminum–steel lap welding to reduce 25 % of weight of the subframe as compared to conventional steel sub frame [1]. Two wheelers' mudguards and some other parts are made up of polymer instead of metals to reduce weight.

Various light-weight materials like aluminum, magnesium etc. are alternative to high density material, out of which aluminum is the best suited candidate because of high strength-to-weight ratio. None of the low-density material can replace steel in a permanent way, since they cannot provide the required stiffness for the functionality; therefore, use of higher and lower density material must go hand in hand, which makes joining of material a vital factor. Aluminum is known as a difficult to weld material because of following reasons.

Solubility of hydrogen is higher in liquid state than that in a solid state. This leads to formation of defects like porosity, blow holes etc. due to hydrogen entrapment during conventional fusion welding processes.

Aluminum has got a strong affinity toward oxygen, which leads to formation of hard and brittle aluminum oxide layer, having melting point three times higher than that of pure aluminum.

High thermal conductivity of aluminum causes higher heat dissipation.

High thermal expansion (almost twice that of steel) and high shrinkage volume (approx 6 % of volume) increase distortion and weld crater size [2].

Various fusion welding techniques like TIG and MIG are used to weld aluminum, but the maximum joint efficiency achieved is in the range of 50–60 % of the base metal strength [3–5]. This may not be sufficient for high-strength applications like aerospace and marine sectors. To overcome these difficulties, researchers in TWI Cambridge developed a new solid-state joining process, called FSW [6]. This process was initially intended to weld aluminum alloys only. Since, the potential of the process is so high, presently it is used to weld all kinds of materials, starting from aluminum to titanium alloys, and even to plastics.

6.2 Introduction to FSW

Friction stir welding (FSW) is a welding technique, which joins the material in the solid state. The complete process can be divided into three stages. The sequence of the FSW process is schematically shown in Fig. 6.1. The *first stage* is known as

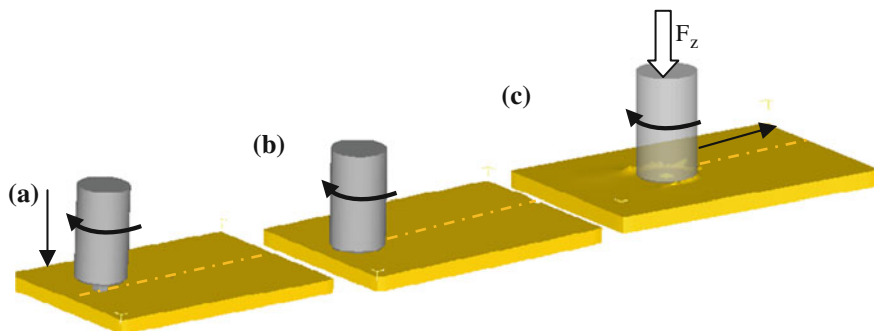


Fig. 6.1 Schematic representation of sequence of the FSW process. **a** First stage: plunging, **b** second stage: dwelling, **c** third stage: welding. *Note: Dashed line and arrow shows abutting edges and tool movement in respective directions*

plunging, which is analogous to a drilling operation. Here, the *pin* of a specially designed nonconsumable rotating tool plunges on the abutting edges of the clamped workpiece, as shown in Fig. 6.1a. This produces heat because of friction at the *shoulder* face (at the interface of the tool and the work piece) of the tool, and plastic deformation of the work piece. Generated heat raises the temperature and softens the workpiece. Plunging is followed by the dwelling operation, which is the *second stage*. Here, the tool stirs at a constant rotational speed at the same plunging position to increase the temperature further up to a desired level, and this brings the material to a viscous state. In the *third stage*, the rotating tool travels along the welding line, and mixing of viscous material takes place under the influence of an axial force, as shown in Fig. 6.1c. Nonconsumable tool primarily performs two major functions; heat generation through friction, and plastic deformation and mixing of materials to perform welding. Apart from the above stated functions, tool also contains the viscous material beneath its shoulder face. FSW, being a solid-state joining process, eliminates complexities and defects (like porosity, blow holes etc.) related to the solubility of gases and solidification of molten material during welding. Temperature required in FSW is in the range of 0.6–0.8 times of T_m (T_m is the melting point of work piece, in $^{\circ}\text{C}$). The temperature in this process never goes beyond the stated value, because frictional and mechanical (plastic deformation) works only get converted to the heat energy, which in turn raises the work piece temperature. With the increase in temperature, workpiece strength reduces as both are inversely proportional to each other. Since, working temperature in FSW is above the recrystallization temperature, new grains form in the weld zone. In addition to the high temperature rise, work material is also under the compressive loading. Therefore, new grains, formed in the weld zone, are smaller in size and almost identical in shape. This improves weld strength.

Temperature and plastic strain have different effects on grain size and micro-structure of the material. A transverse cross-section of FSWed sample can be classified into four different zones viz. nugget zone (NZ), thermomechanical affected

zone (TMAZ), heat-affected zone (HAZ), and base material (BM). A material at the nugget zone is subjected to high strain and heat due to stirring actions of tool pin and shoulder. Grain size of the nugget zone is finer as compared to that of the base metal because of dynamic recrystallization. TMAZ is majorly subjected to heat, and a small deformation of material, which slightly changes the grain orientation; and HAZ is subjected to heat only. Since heat input in FSW is less as compared to fusion welding, softening of material in HAZ is negligible, and even in some cases HAZ does not exist [3, 7].

6.2.1 Pros and Cons of FSW Process

Being a solid-state joining process, FSW offers a lot of advantages over fusion welding techniques. Following are the advantages of FSW over other fusion welding techniques:

Defects related to solidification of material like blow holes, porosity are eliminated as it is a solid-state joining process.

Low distortion of the work piece occurs due to lesser heat input. This improves the surface integrity and dimensional accuracy.

Fine equiaxed grains form in the nugget zone due to dynamic recrystallization, which improves weld efficiency.

FSW can effectively weld dissimilar materials like aluminum and steel, aluminum and magnesium etc., which are used in automobile, aerospace, and marine industries to reduce weight of the product.

No filler material is used and hence no extra material is added during welding which keeps base material composition intact.

It is a green technology as no fume is generated during the process and also shielding gas is not required.

Energy-efficient process as compared to laser welding, electron beam welding.

On the opposite side, FSW has some disadvantages as mentioned below.

At the end of the welding, an exit hole occurs which leads to loss of material. Thinning of material at the weld zone takes place, if flash formation is not controlled.

High reactive force is generated during the process.

6.2.2 Application of FSW Process

FSW finds tremendous applications in the wide range of industrial sectors like automobile, aerospace, marine, electronics etc. Some of the renowned industries which use FSW process are Honda, Boeing, and Apple etc. Honda Accord used

FSW, to perform lap welding of steel with aluminum for one of its subcomponent in the chassis [1]. Apple, in one of its products called iMac, used FSW to weld the front panel with the back panel which has a thickness of 5 mm [8]. Similarly, various industries have already used the process in either joining of aluminum or for different materials. Welding of dissimilar materials majorly finds applications in many industries, as aluminum or any lighter material alone cannot cater the strength and stiffness requirement. Like, a combination of aluminum–steel is used in aerospace and automobile sectors to manufacture chassis, pillars, bumpers etc. [9, 10]. Various researchers have successfully welded Al–steel combination using FSW [11–15]. Researchers have obtained a weld efficiency of 80–85 % of the strength of aluminum. They have successfully welded aluminum alloys with different grades of steel like low-carbon steel, mild steel, and stainless steel etc. On the similar line, aluminum and magnesium alloys are also used in different industries like marine and automobile. In automobile, Al–Mg welded plates are used in clutch, transmission exhaust décor etc. [9]. Several researchers have achieved a weld efficiency of 70–80 % while welding aluminum alloy with AZ31 magnesium alloy [16, 17]. FSW is used for successful welding of hybrid combination Al–Cu which is used to manufacture household utensils and industrial power protection. Welding efficiency of 70–80 % is achieved [18–21]. Other dissimilar combinations which are used in aerospace and automobile sectors are Mg–Cu and Al–Ti and these are efficiently welded by FSW [22, 23]. FSW is used for high weld strength applications like aerospace, automobile and marine industries, and it also finds its application in electronic industry, where only aesthetics of the product is important, for e.g., iMac computer of Apple etc. This versatility in application tells about the potentiality and capability of the process.

6.2.3 Terminology in FSW and Its Significance

Various terminologies that are used in FSW technique are shown in Fig. 6.2. Definitions of different nomenclatures used in FSW are as follows:

Advancing side: It is the side of the plate where direction of tool rotation is same as that of the tool travel.

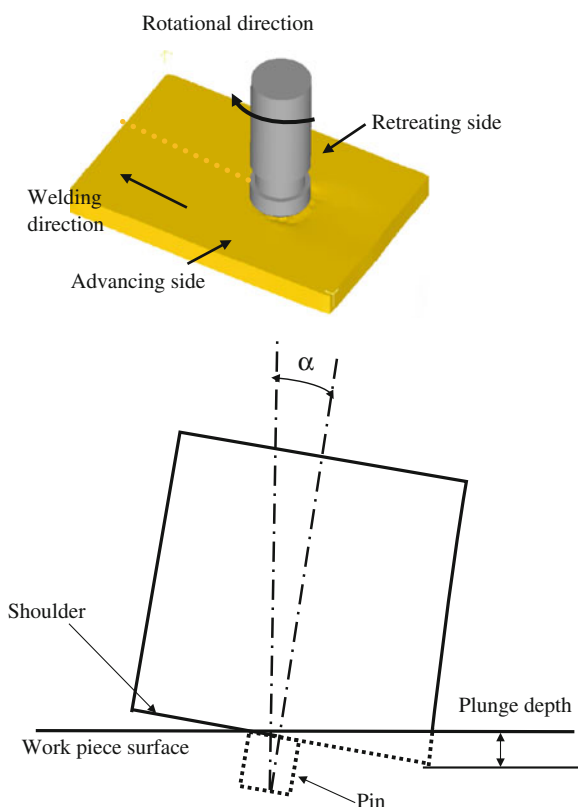
Retreating side: It is the side of the plate where direction of tool rotation is opposite to that of the tool travel.

Tool shoulder: It is the part of the tool, which comes in contact with the top surface of the workpiece. It is mainly responsible for the maximum amount of heat generation, and also mixing of material on the top surface.

Tool pin: It is the part of the tool the plate along the weld line, and is responsible for the mixing of material inside the work piece.

Spindle tilt angle (α): It is the angle between the normal to workpiece top surface and the axis of the tool. Flash formation is reduced by providing a tilt to the tool. It generally ranges from 1° to 4° .

Fig. 6.2 Terminologies used in FSW process



Plunge depth: It is the distance by which tool shoulder impinges the work piece top surface. Plunge depth is specified when higher contact area is required for heat generation.

6.2.4 Process Variables and Their Effects

Process variables play important roles in producing a good weld. Therefore, it is important to understand the process variables, and their effects on the process. Process variables can be classified into three different categories, as mentioned in Table 6.1.

Process variables: Selection of proper combination of process parameters is crucial, as they have varied influence on the output variables like temperature and material flow behavior. Heat generation is directly proportional to the rotational speed of the tool. With the increase in rotational speed, relative velocity between tool and work piece increases, and thus frictional heat input increases. On the other hand, welding velocity has an inverse effect on heat generation. This is because of the fact

Table 6.1 Process variables in FSW process

Process variables	Design variables	Material parameters
Tool rotational speed	Pin geometry and its dimension	Tool material
Welding speed	Shoulder geometry and its dimension	Work piece material
Tool tilt angle	Joint configuration	Back up material
Plunge depth		

that with the increase in welding velocity, contact time between the work piece and tool reduces, and hence heat generation reduces; and at the same time lower welding speed hampers the productivity of the process. Tilt angle helps in reducing the flash formation. Tilt angle should be given toward trailing edge of the tool.

Design parameters: Dimension and geometry of tool shoulder and pin play a vital role in the defect-free FSW process. Optimum shoulder diameter is important because higher heat generation can lead to loss in traction between work piece and tool, leading to improper mixing of material due to slippage. On the opposite side, lower heat generation may not soften the work piece properly. Shoulder geometry can be flat, concave, or convex depending upon the welding requirement. Concave shoulder leads to less ribbon formation as it contains viscous material better than other two due to its geometry, but at the same time contact area is reduced. Normally concavity of 5° – 20° is considered [3, 7, 24]. Flat shoulder is the most commonly used as it gives larger contact area, but tendency of ribbon flash formation is higher in this case. However, this can be reduced by using proper tilt angle toward trailing edge of the tool. Tool pin height should be properly chosen such that mixing of the material takes place in through thickness direction, but higher pin height dimension can lead to sticking of material on the backing plate. Though there is no empirical relation to calculate pin height, experience suggests that difference between work piece thickness and pin height should not be more than 0.5 mm, and the ratio between the diameter of shoulder to that of pin should lie between 3 to 5 [3, 7, 24–26]. These parameters largely depend upon the work piece material and cross-section of the pin. Cross-section of the pin is important for proper mixing of material. Various cross-sections of pin like cylindrical, conical, threaded cylindrical, square etc. have been used in the research work out of which square-shaped pin geometry performs better than the rest [25].

Material parameters: Loss of heat takes place from tool and work piece; this largely dictates the quality of the weld. Anvil material (backing plate) should be rigid enough to provide sufficient reaction force; and work piece material should not stick to the anvil material; otherwise, it will deteriorate the quality of the weld.

As, discussed, different process parameter have varied effects on output variables. Few process parameters complement each other for, e.g., larger shoulder diameter can successfully weld by using lower rpm, and vice versa. Therefore, in order to achieve a sound weld, it is mandatory to select the combination of process parameters appropriately, and thus independent choice of parameter by neglecting the influence of other will not serve the purpose.

6.2.5 Mechanism of Material Flow

The overall joining technique in FSW is a simple one, but material flow behavior during welding is reasonably complex, as it largely depends on the pin geometry. Material flow pattern changes as cross-section of pin geometry changes. For example, no material flow is observed along the thickness direction with cylindrical pin because direction of resultant tangential velocity lies in horizontal plane only, whereas in tapered cylindrical pin, resultant tangential velocity of tool has two components (due to tapered shaped), one in horizontal plane and other in vertical plane and this vertical velocity component is responsible for vertical material flow. Similarly, dynamic mixing of material takes place with square- or triangular-shaped pin because, difference in static and dynamic swept volume, pulsating effect is generated and results in better mixing of material, while it does not occur with either cylindrical- or conical [25]-shaped pin geometry. Material flow pattern in a plane varies across the thickness of material. Tracer material is used to study material flow pattern during a FSW process. Tracer material such as steel, or copper, or tungsten carbide is embedded on the faying surface in different directions before the start of the weld, and it flows along with the material during welding. Once, welding is finished, distribution of tracer material on the weld zone helps in understanding the material flow pattern [27, 28]. Most of the researchers agree with the fact that, material from the front of the weld (both from advancing and retreating side), flows to retreating side and then get deposited toward advancing side of the weld in a scattered fashion, while vertical movement of the material largely depends upon the pin profile as discussed above [27].

6.2.6 Defects in FSW

A good understanding on the effect of combination of process parameters and physics of the process is required to get a defect-free weld. As discussed earlier, each process parameter is vital and optimum combinations of those parameters lead to formation of the sound weld. Thorough understanding on various defects and their mechanisms of formation can also help in eliminating them.

Different types are defects are categorized based on the physics of their formation in Table 6.2.

Table 6.2 Classification of various FSW defects

Improper heating	Excessive heating	Defects due to faulty design
Kissing bond	Nugget collapse	Oxide entrapment
Tunnel defect	Ribbon flash	Lack of penetration
Lack of fill	Root flaw	Excessive indentation
	Surface galling	

Kissing bond: It is a type of defect that occurs in the solid-state joining processes. Joining between two sides occurs at a small portion. Insufficient softening of material leads to improper mixing or fusion of material. Static load bearing capacity of the kissing bonded materials is less. Higher heat input by increasing tool rotational speed or proper selection of pin geometry can be a remedy of this defect.

Tunnel defect: Formation of cavity due to insufficient material flow near the advancing side, or due to too high welding speed. It occurs due to lack of plunge force or proper welding speed.

Lack of fill: It is a surface void formed due to insufficient plunge force or plunge depth. Proper plunge force or tilt angle can eliminate this defect.

Nugget collapse: It occurs due to excessive softening of material due to high heat generation. It can be avoided by controlling the tool rotational speed or by reducing the shoulder diameter.

Ribbon flash: It occurs because shoulder is unable to contain the viscous material beneath it. Tilt angle and concave tool shoulder can eliminate this defect.

Root flaws: Excessive heat generation softens work piece to a high extent; and under compressive load, material tends to stick with the backing plate. This can be controlled by selection of proper process parameters and proper choice of pin height.

Surface galling: It is a series of void visible on advancing side of material due to excessive softening of work piece. This occurs due to excessive heat generation and can be controlled by proper selection of process parameters.

Oxide entrapment: Aluminum has a strong affinity toward oxygen, and thus forms a layer of a hard and brittle layer of aluminum oxide. This oxide layer, especially on the abutting edges, mixes with material during welding. Surface preparation before welding can be a remedy of this problem.

Lack of penetration: It occurs due to smaller pin length compared to the desired one.

Excessive indentation: It occurs because of a very high plunge force resulting in excessive flash formation (also called excessive indentation).

6.3 Recent Experimental Advancement in FSW

Various research activities are being carried out across the globe into various aspects of FSW to improve the process capabilities. The biggest challenges in FSW process are to get a defect-free weld; to reduce the force generation during the process, and to come up with a better surface finish; and to plastically deform the welded sample having dissimilar components.

Keeping above challenges in mind, in this section three different experimental research works are discussed, addressing the solution to the above stated issues.

First, a twin-tool concept is discussed which helps in eliminating different FSW defects; second, an ultrasonic-coupled FSW process is explained. This research work focuses to improve the weld surface quality and to reduce the force generation during the process; and the other research work focuses on formability of friction

stir welded blank. The formability study of tailor-welded blanks is a thrust area in various industries.

FSW is a complex phenomenon in terms of choice of optimized process parameters. As discussed in earlier section, a lot of associated variables influence the process; and a proper combination of those variables only can lead to a defect-free weld. Few researchers have suggested multi-pass FSW as an alternative approach to achieve a defect-free weld, but multi-pass FSW reduces productivity, and it is difficult to choose the time gap in between two passes. In this section, a twin-tool concept in FSW is discussed. This setup is developed indigenously, replacing multi-pass FSW, to have improved productivity and to eliminate various defects arising due to insufficient heat generation in a conventional single-pass FSW process.

6.3.1 Multi-Pass Friction Stir Welding/Processing

Since FSW is not a fusion welding technique, melting of the mating materials does not occur. Hence, problems such as porosity, solidification cracking, or heat-affected liquation cracking do not appear as a defect in FSW. As discussed earlier about the complexity of this process, formation of defects like lack of fill, tunnel defect, nugget collapse, and kissing bond are some of the major problems generated due to imbalance in material flow, or due to other factors such as welding and process parameters [29]. Though temperature does not go beyond the melting temperature of the parent material, the heat generation, because of friction and plastic deformation, affects the microstructural behavior such as grain coarsening, dynamic recrystallization, dissolution of precipitates, and grain orientation with growth. The improper process parameters in FSW process give rise to either a too hot or a too cold weld condition. One of the major drawbacks in conventional single tool FSW technique is the insufficient heat generation. This cold weld condition is due to wrong selection of process parameters or insufficient material flow which gives rise to defects like void formation and nonbonding. Work hardening is one of the problems arises during cold weld conditions. As a result, dry slip situation comes between the tool pin and the work piece material [30]. The lack of surface fill or void, and channel formation are the main defects arising due to insufficient heat generation. The insufficient heat generation causes improper material mixing, and thus responsible for nonbonding. This was analyzed by Kim et al. [30]. They found that at a higher welding speed with lower tool rotational speed, heat generation is insufficient, which causes improper bonding resulting defects like cavity or groove formation. Apart from this, one more defect is analyzed which is termed as abnormal stirring. This type of defect mainly occurs when both the welding and rotational speeds are very high. They found that due to unequal temperature generation between upper and lower parts, there is an abnormal stirring, which also results in discontinuous flow of material in the stir zone.

Therefore, getting a good weld in FSW process is also a challenging task till date. Optimization of a proper combination with hit and trial technique on process

parameters is still a part of research work in the area of FSW. In order to overcome those defects, extensive research is being carried out in the area of multi-pass FSW technique. In this field, repair of a defective part is done instead of throwing or rejecting the welded sample as a scrap. This is also termed as a rewelding process, where the same tool passes over the processed area with the parametric condition. Some of the published research works are narrated here in this section.

Brown et al. [31] performed five overlapping passes and found that there is no need of any adjustment for multi-pass welding. Further there is a significant reduction in feed force when welding is done over the previous weld. However, grain size, hardness, and temperature during welding are unaffected with the number of passes. Again, there is a gradual reduction of residual stress with the increase in pass number.

Compared to the as-cast base metal, an improvement in both hardness and tensile properties were observed by Nataka et al. [32] using multi-pass FSP. Elimination of cold flake and distribution of Si particles over the aluminum matrix were the main reasons of improvement in mechanical properties. He et al. [33] showed a comparative study between single and two-pass FSW, tested on skin-stringer (an equilateral right angled structure used in air craft) structure to get a defect-free welding. Results showed that the strengths of single and two-pass welded samples are more or less same, but the average peel strength of two-pass weld is twice as that of the single-pass weld. Leal and Louriero [34] investigated the effect of overlapping FSW passes using two variants of Al alloys (AA5083-O and AA 6063-T6). In their observation, they conclude that the quality as well as strength of the weld not only depends on the process parameters but also on the material type and treatment used during welding. Barhami et al. [35] examined the effect of two-pass with SiC reinforced particles by switching the pin geometry from tapered to square one. They found the ductile fracture mode with superior hardness on SiC reinforced joint for both the passes. On the other hand, Ma et al. [36] reported that there is no effect of overlapping passes on size, aspect ratio or distribution of the Si particle while performing five-pass FSP with 50 % overlap on cast A365. As FSP is one of the most promising techniques for grain refinement and flaw removal, many researchers used multi-pass FSP to improve the properties of as-cast material. To achieve super plastic deformation, grain boundary sliding is one of the crucial mechanisms which are used by Johannes and Mishra [37]. They used this to demonstrate the effectiveness of multiple passes to create larger area of super plastic materials. Similarly, Ma et al. [38] used two-pass FSP to enhance the elongation rate with a rise in temperature, both in the middle as well as in the transitional area, after two passes. Multi-pass FSP, compared to the base metal, improved corrosion resistances as experimentally reported by Surekha et al. [39]. Multiple passes can also be able to overcome the difficulty related to abnormal grain growth, where high value of rotational speed was found to be the most influential parameter [40].

To avoid the use of multi-pass FSW/FSP, two-tool-FSW concept has been developed at TWI in several variants and is referred to as a Twin-Stir [41–44] group. One of those techniques is the Tandem twin-stir technique. It uses two FSW tools (with or without counter rotation) positioned one in front of the other.

6.3.2 Advantages of Contra-Rotating FSW Tools

Homogeneous mixing of materials occurs between the advancing and the retreating sides because of opposite rotations of two tools.

In this new variant of FSW/FSP tool, setup the opposite rotations of the two tools counteract each other. As a result, low securing force is required to clamp both the parts to be welded.

Weld integrity improves by this tandem twin-stir technique because of fragmentation of residual oxide layer remained in the first pass by the follower tool. There is no change in mechanical properties as such.

Further the motion produced by the counter rotating tandem twin-stir is similar to Re-stir tool, but the twin-stir produces faster travel speed, and in addition efficiency of the FSW process can be improved [45].

6.3.3 Case Study on Twin-Tool

6.3.3.1 Twin-Tool Setup

The indigenously designed twin-tool setup fabricated for FSP/FSW is shown in Fig. 6.3a, b with pictorial representation as well as actual photograph, which was mounted on the vertical milling machine [45]. The twin-tool system is composed of two counter rotating tools. In this case, the rotor plate of the attachment (shown in Fig. 6.3a) is directly mounted on the spindle rod of the vertical milling machine. There is no height difference between the two tools of the setup. The primary tool is mounted on the main spindle shaft. Therefore, the main tool rotates at the same rotational speed and in the same direction as the spindle during the welding process. The secondary tool is connected to the primary one with the help of a gear assembly. The power transmission from the primary to secondary tool is similar to the transmission of power from the driver to the driven gear. So the rotation of the secondary tool is just the opposite of the primary tool. Distance between the two tools is 36.8 mm.

6.3.3.2 Experimental Plan

The principle and functioning of twin-tool (TT) is investigated initially using friction stir processing. Commercially pure AA1100 plate of thickness 2.5 mm with 200 mm length, and 80 mm breadth were used for FSP. Two similar cylindrical tools made up of SS316 steel were used as primary and secondary tools for the twin-tool attachment. Spur gear assembly having 18 teeth with 2.1 mm module is used in both the shafts which help to rotate the tools opposite to each other. As per the design, the distance between two tools is kept as 36.8 mm. The gear material used here is EN 24 grade of steel with 56 HRC having higher machinability with

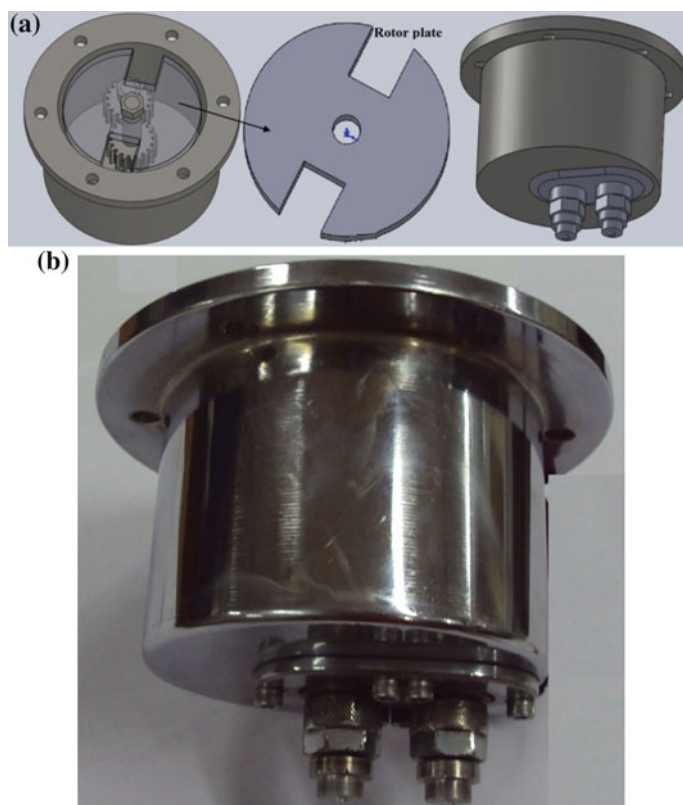


Fig. 6.3 **a** Pictorial representation of twin tool (both *front* and *top* view), **b** actual photograph of twin-tool

strength. 6202ZZ SKF bearings were used for minimizing the friction between the moving elements.

To avoid the sticking of welded material over the bed, specially designed fixture having mica sheet in the middle was used for friction stir processing. In this case, three welding speeds of 16, 20, and 25 mm/min with four different rotational speed of 900, 1120, 1400, and 1800 rpm were taken to perform the experiment using vertical milling machine. Hence total twelve set of experiments were conducted with different combinations of tool rotational and welding speeds for twin-tool (TT) as well as single-tool (SP) systems. To reveal the different zones, sample were cleaned and polished by using different rates of emery paper over variable speed grinder machine. The photograph of friction stir processed plate is shown in Fig. 6.4.

By using Vickers microhardness test (Micromet 5103, Buehler Company), hardness values at different locations were measured and are plotted with distance across the cross section of the processed zone. The hardness was measured on the polished cross-section with a spacing of 200 μm between two adjacent indentations with a testing load of 200 gmf, and a dwell time of 15 s. The microhardness profiles

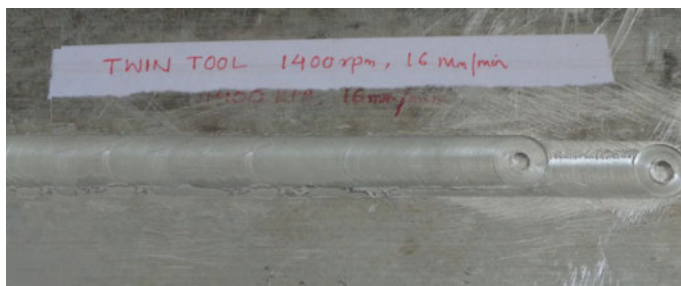


Fig. 6.4 Welded surface appearance using twin tool set up

across FSWed joint is shown in Fig. 6.5. FSP using twin-tool shows higher values of hardness compared to the single-pass for the different combinations of weld parameters. This is due to the hardening effect caused by intense plastic deformation in the processed zone. As materials in the nugget zone are subject to two stirring actions, materials undergo severe plastic deformations compared to a single-pass material.

This twin-tool concept not only reduces various defects but also improves the weld quality. With this twin-tool concept, productivity of the process will be improved and even welding at higher speed can be performed.

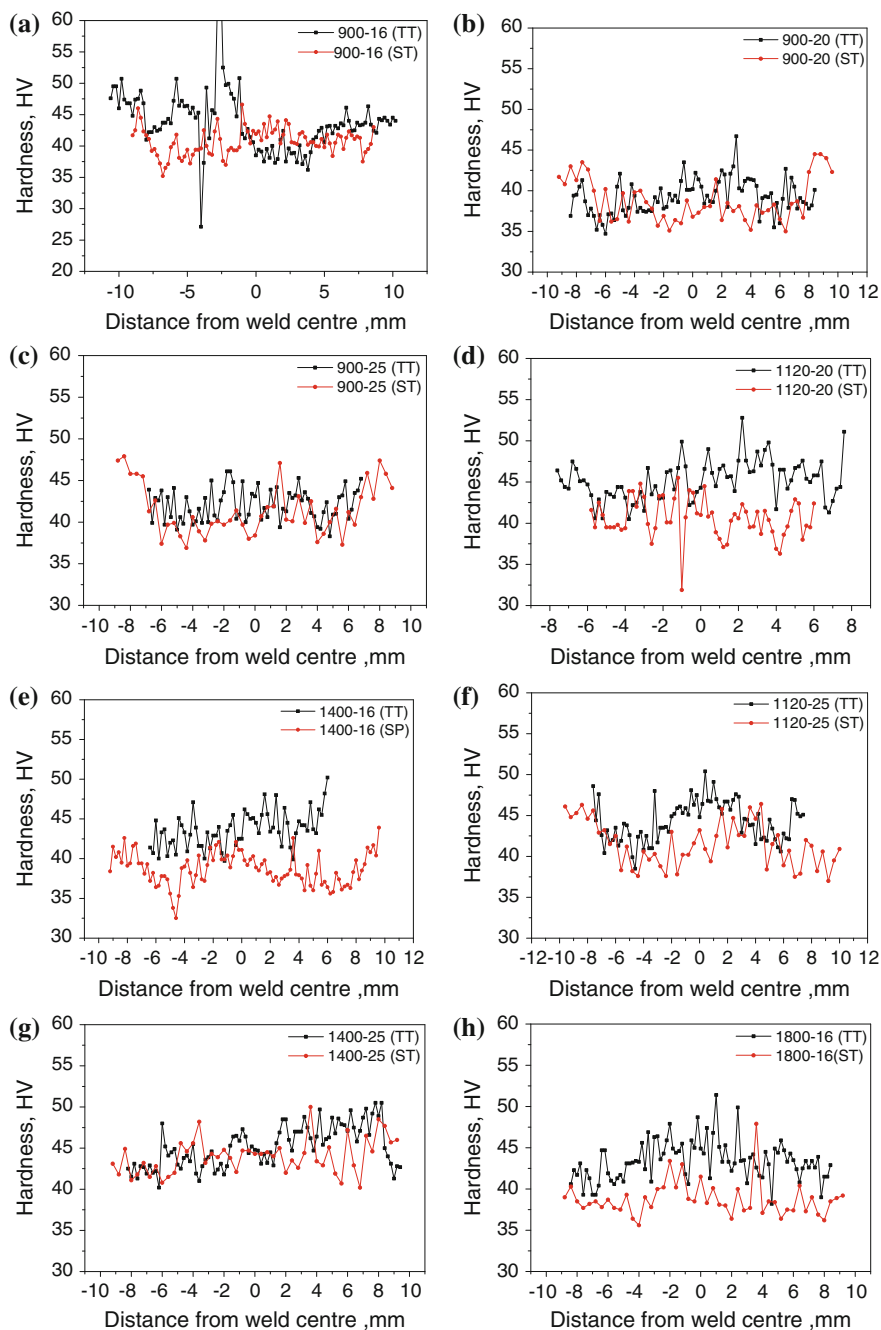
Reactive forces generated during FSW process are very high, which in turn raises the need of a rigid backing plate, proper tool design and clamping fixtures. This adds to the initial cost of the process. In the past, ultrasonic vibration is successfully coupled with some of the manufacturing processes like machining, welding etc. Here, a feasibility study of ultrasonic-coupled FSW is discussed along with the design of ultrasonic setup. Initial results suggest that force generation is reduced with ultrasonic.

6.4 Ultrasonic Assisted FSW

In this section, use of ultrasonic energy in manufacturing is mentioned, and also a detailed description on ultrasonic-assisted FSW is given.

6.4.1 Introduction

Ultrasonic vibrations refer to the sound waves that have a frequency above the human hearing range, i.e., more than about 20 kHz. The vibrations themselves are the physical vibrations of the molecules in the medium through which the sound travels. Frequency range between 20–60 kHz is usually termed as the ultrasonic range.



◀ **Fig. 6.5 a–j** Hardness plot with different combination of welding speed with rotational speed. **a** For 900 rpm rotational and 16 mm/min welding speed, **b** for 900 rpm rotational and 20 mm/min welding speed, **c** for 900 rpm rotational and 25 mm/min welding speed, **d** for 1120 rpm rotational and 20 mm/min welding speed, **e** for 1400 rpm rotational and 16 mm/min welding speed, **f** for 1120 rpm rotational and 25 mm/min welding speed, **g** for 1400 rpm rotational and 25 mm/min welding speed, **h** for 1800 rpm rotational and 16 mm/min welding speed, **i** for 1800 rpm rotational and 20 mm/min welding speed, **j** for 1800 rpm rotational and 25 mm/min welding speed

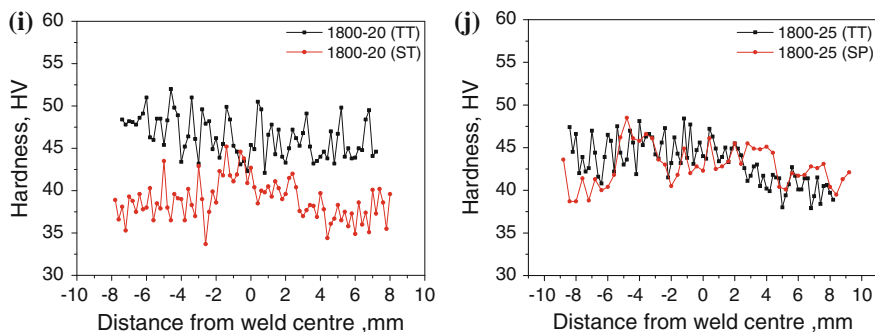


Fig. 6.5 (continued)

Ultrasonic vibrations are employed in manufacturing purposes involving mainly metals and alloys. The usefulness of ultrasonic integration in metal working is well-detailed in the literature [46–50]. Many researchers are working on inventing processes to facilitate acoustic softening during material processing. In the modern time, ultrasonic vibrations are widely used method for metal working. Ultrasonic metal working has some advantages over others as follows:

It does not require preheating of the metal, hence eliminating the extra cost and time.

Ultrasonic device requires a very little amount of energy as compared to the other processes [51].

Once properly fitted in the fixture, it is easy to use.

If properly handled, the ultrasonic components have long-lasting life.

Based on the area of interest, ultrasonic-assisted manufacturing is grouped under three categories as detailed in subsequent sections.

6.4.2 Ultrasonic Machining

In ultrasonic machining (USM), the metallic tool is made to vibrate at ultrasonic frequencies to aid metal removal process. Abrasive slurry flowing freely between the work piece and the tool is integrated with this process. USM is employed for machining conductive as well as nonmetallic materials; preferably, materials with low ductility [52, 53] and a hardness value above 40 HRC such as inorganic

glasses, silicon nitride, nickel/titanium alloys, etc. [51, 54]. Very little heat is produced during USM. The tool does not make physical contact with the work piece. Thus, very small force is required for such machining. Therefore, this operation is easy and effective for machining extremely hard and brittle materials, for example glass, diamond, and ceramics.

Chang and Bone [55] investigated the outcome of ultrasonic integration on chip formation and thrust forces. Usually, large burrs affect part quality and impede assembly. They observed that burr height and width were reduced with ultrasonic assistance. They also observed a reduction in thrust force during the process. However, the ultrasonic assisted drilling introduced some disadvantages in terms of tool strength and life. Ishikawa et al. [56] reported the effect of combined vibration drilling by using ultrasonic vibration at the core drill while vibrations of low frequency are used in work piece. Their research was focused on establishing a relationship in drilling force with respect to accuracy of drilled hole. They observed that drilling force decreased with the integration of ultrasonic vibrations. It further decreased when ultrasonic vibration amplitude was increased.

6.4.3 Ultrasonic Welding

Ultrasonic metal welding was invented in Germany during the Second World War. It is a solid-state process in which two parts are welded by the application of ultrasonic vibrations under moderate pressure. Little or no heat is applied and the material reaches near to 50 % of its melting temperature. This process permits welding of thin to thick sections of materials with lower pressures than used in fused deposition or static press welding. Figure 6.6 shows the line diagram of essential components of a typical ultrasonic welding machine.

Tsujino et al. [57] proposed a new method to weld metals and plastic materials by using the property of ultrasonic waves for different size metal specimen and

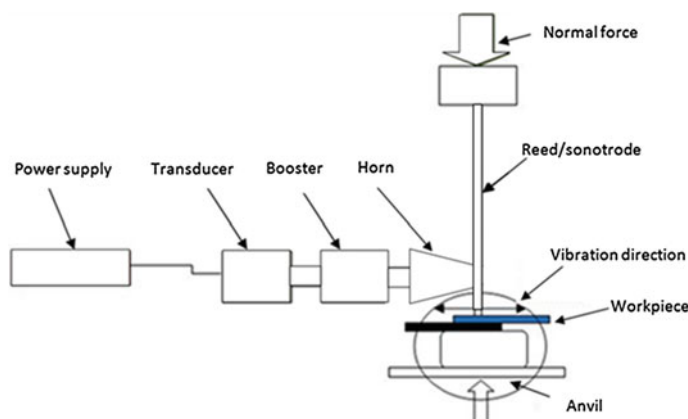


Fig. 6.6 Principle of ultrasonic welding set up

plastic. They proposed butt welding to effectively utilize the vibrations at two mutually perpendicular directions. It was proved to be much better if plates are joined in butt fashion.

For plastic welding, frequency above 20 kHz and two vibration systems showed successful results. Further, Tsujino et al. [58] used the concept of complex vibration ultrasonic welding for 0.3–1.0 mm thickness Al sheet by using 27 and 40 kHz frequencies. The complex vibrations have their locus in some forms like elliptical, circular, square, and rectangular. They are usually meant for packaging of electronic devices without soldering. The thin sheet of Al was welded successfully. The final welded Al sheet is found to be of same strength as that of parent metal.

Matsuoka et al. [59] studied ultrasonic welding of dissimilar metal like Al–Cu in air and in water. They concluded that welding pressure and welding time are more for underwater welding as compared to atmospheric welding. However, no difference in strength of weld metal was found for both the cases.

De Vries et al. [60] focused on in-depth study of physical mechanism involved in ultrasonic metal welding. An infrared camera was used to measure temperature during Al welding under variable welding parameters. Experimentally, it was seen that the temperature at the interface was in the range of 40–80 % of the melting point temperature. Jeng and Horng [61] used a pull tester and an ultrasonic machine to analyze the effect of applied pressure, surface roughness, and input power on ultrasonic bonding. Experimentally, it was observed that lower value of applied load or input power facilitates to join wires and pads under wide range of parameters. The bonding strength of welded part is linearly dependent on the contact temperature; and surface roughness is a vital measure in final specimen.

6.4.4 Ultrasonic Assisted FSW

The conventional FSW suffers from some limitations which are: inability to weld high temperature material, large axial force requirement, and less travel speed, etc. To overcome these limitations, conventional FSW is integrated with the ultrasonic system. The new process is named as ultrasonic-assisted friction stir welding (UaFSW). UaFSW is a hybrid process that utilizes the ultrasonic energy coupled with the FSW. In this process, high frequency vibration (20–40 kHz) is superimposed on a rotating tool by means of roller bearings. This offers some advantages over conventional FSW in terms of force reduction, less defects, smooth weld, improved elongation and yield strength, and the ability to weld high melting temperature materials [62].

6.4.4.1 Literature Review

A very little study is available on the effect of ultrasonic vibrations in FSW for joining of metals. This has attracted many researchers to work in this area more

intensively. Park [62] has reported a considerable amount of axial force reduction (up to 25 %) in UaFSW as compared to conventional FSW. He further found that as the amplitude of ultrasonic vibration increases, the axial force decreases correspondingly. During UaFSW process, the elongation of the weldment is found to be 15 % higher than conventional FSW process. Ruilin et al. [63] studied the temperature fields during UaFSW process. They explained that UaFSW imparts extra heat to weld zone, thereby producing better material flow in UaFSW as compared to conventional FSW. Also, the temperature gradient in UaFSW is more than that obtained in conventional FSW. Amini et al. [64] studied the effect of ultrasonic vibrations on process parameters in FSW process. They confirmed the axial force reduction up to 25 % as reported in [62]. It was observed that ultrasonic vibrations do not have significant effect on force along the welding direction. The temperature in the vicinity of weldment was found to be higher in UaFSW as compared to conventional FSW process. They further confirmed the enhanced weld strength and elongation by up to 10 %. During UaFSW, the hardness in advancing path is found to be 15 % higher.

Ahmadnia et al. [65] studied the role of UaFSW welding parameters on the tribological properties of AA6061 metal joints. They found out that ultrasonic vibrations increase the tensile strength, as well as Erichsen number, and reduce the surface roughness and wear rate. They established a set of optimized parameters with which maximum tensile strength and Erichsen number, as well as minimum surface roughness and wear rate could be obtained. Ma et al. [66] also studied the effect of ultrasonic vibrations on mechanical properties of AA 6061 welded joints. They found that the tensile strength and also hardness of welded part are more with UaFSW as compared to that obtained with conventional FSW. The difference in strength and hardness can increase up to 50 % with increase in ultrasonic energy input. Rostamiyan et al. [67] experimentally studied the ultrasonically assisted friction stir spot welding of AA6061. They concluded that with the integration of ultrasonic energy, the lap shear force as well as hardness of the welded part is increased. They further claimed the optimum rotational speed as 1200 rpm where highest lap shear force as well as highest hardness is achieved.

6.4.4.2 Components of Ultrasonic System

In this section, the integration of an ultrasonic vibration set up with the FSW machine is explained. A detailed and comprehensive design is required to meet the requirement of integration of ultrasonic vibrations with the existing FSW machine. The design is evolved to allow setting up the required process parameters for UaFSW. An ultrasonic system used for this work consists of a horn/sonotrode, booster, converter, and a generator.

Horn/sonotrode: It is an acoustic tool which is designed to augment the oscillation displacement amplitude received from booster. Design of horn is a crucial task as it is a part that contacts the rotating tool; hence in addition to



Fig. 6.7 Ultrasonic assembly for FSW integration

boosting the amplitude, the horn should have enough strength to sustain the shock and stresses produced during the operation.

Booster: A booster is also known as an amplifier. It is used to amplify the amplitude of vibrations coming from the transducer. It is mounted between the converter and the horn. Different diameters are given to booster to have different gains, originating from its nodal point.

Converter: The converter receives electrical energy from the power supply and converts it into mechanical vibrations. When alternating voltage at a frequency of 20 kHz is applied to the converter, it physically vibrates at that same frequency.

Generator: It is the most important and complex part of ultrasonic system. It receives AC input of 220 V at 50 Hz and gives an output within 800–1000 V at a range in between 20 to 40 kHz. It consists of a set of wired logical programmes, microprocessors, and other necessary power-electronic components. Power rating of the generator is based on the application and varies for plastic welding to metal welding.

The integration of these parts into the conventional FSW is a difficult task. A detailed design analysis is required to ensure efficient transfer of ultrasonic vibrations to the weld metal parts. This requires the design of horn, selection of an optimum combination of booster, transducer, and generator. A proper selection of these components ensures optimum delivery of power at horn tip. A horn is designed in such a way that it could be connected to the FSW rotating tool. Stationary horn is required to be connected with the rotating tool. To make it feasible, roller bearings are designed, fabricated, and attached at horn face such that these parts can make proper contact without much rubbing (see Fig. 6.7).

6.4.5 Design and Fabrication of Ultrasonic System

6.4.5.1 Design of Horn

The detailed design of ultrasonic horn is a complex task. However, following design handbook guidelines, a thumb rule approach is employed here to design ultrasonic horn meant for integration into the FSW process. The shape and size of the ultrasonic horn depends on the application. For this work, a circular horn with

rectangular face is selected due to its high bearing strength and ergonomic design. The horn used for this experiment consists of two roller bearings which are designed separately. The gain ratio of the horn depends on its end diameters. The horn material is titanium alloy. The wavelength of longitudinal vibration of a thin rod can be written as

$$\lambda = \frac{1}{f} \sqrt{\frac{E}{\rho}} \quad (6.1)$$

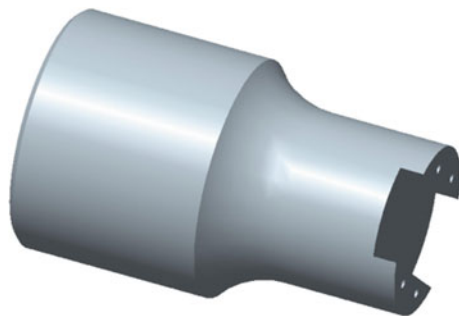
where, λ is wavelength, f is resonant frequency, E is modulus of elasticity, and ρ is density of the horn material. On putting the values corresponding to material properties of the titanium alloy, and the resonant frequency of 20 kHz, λ of 247.5 mm is achieved. Thus, the length of horn is chosen as $\lambda/2 = 123.7$ mm. A groove is cut at the face of horn to accommodate the bearings. Figure 6.8 shows the ultrasonic horn designed for this study.

6.4.5.2 Roller Bearing

Roller bearing is an extra attachment made with ultrasonic system to transfer ultrasonic vibrations to a rotating tool. It is made to facilitate contact between stationary part (horn) and a rotating part (FSW tool). Two roller bearings are used side by side and are screw mounted within the groove cut in the horn.

Design of roller bearing is a crucial task which depends on several factors like load bearing capacity, torque applied, shear stress and bending stresses, and deflection. A careful bearing design is essential for efficient and safe transfer of ultrasonic vibration to the rotating tool. Figure 6.9 shows the CAD model of the roller bearing and the fabricated part. The cylindrical part of bearing is hollow and rotates relative to the part with square section or shaft. Thus, a part of the shaft is shaped to a solid cylindrical part and a needle bearing is inserted between the solid and hollow cylinders. The holes at two ends of the square section of the shaft are for mounting the roller bearing to the horn. The diameter of the roller bearing is restricted by the depth and width of the groove cut in the horn (see Fig. 6.8).

Fig. 6.8 Horn with groove cut



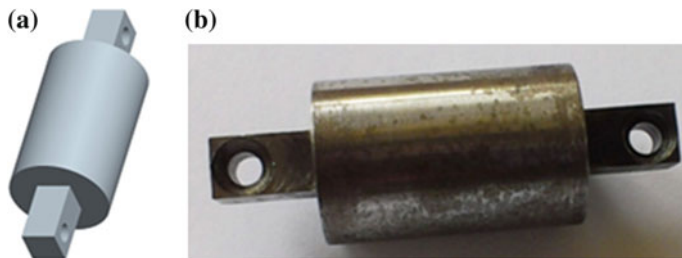


Fig. 6.9 **a** CAD model of roller bearing, **b** fabricated roller bearing

Finite element analysis (FEA) is used to design the roller bearing and its attachments. Commercial FEA tool ABAQUS was used for this purpose. The actual solid model of the roller pin designed in Pro/Engineer software is imported into ABAQUS software and then the analysis is done under 3 kN point load acting at the center of the roller bearing. An eight-noded linear brick and Hex-type meshing was selected in ABAQUS for FE modeling. The results are shown in Figs. 6.10 and 6.11. This analysis aids in selecting bearing material and its dimensions. It is seen that von Mises stress coming maximum at the center of the bearing that is equals to 217.7 MPa. Hence, the tensile strength of roller bearing material should be more than 217.7 MPa. Considering the safe side and availability, AISI D2 steel as a roller bearing material is selected which do have tensile strength between 640 and 2000 MPa.

In addition to the roller itself, the screw needed to mount it on the horn needs to be designed properly. The screw strength depends on its material and diameter. It predominantly fails due to bending stresses and shear. The small needle bearing at the core needs to be lubricated in order to avoid heating up the roller and thereby preventing its rotation.

6.4.5.3 Ultrasonic Assembly Mounting

A fixture is used to mount the horn assembly on the FSW machine base. Booster end ring is inserted in the recess provided in fixture and is fixed by using screws. The arrangement allows vertical adjustment of horn assembly. This configuration simplifies the integration procedure since the ultrasonic transmitter can be independently designed and fabricated without changing any part of the existing FSW machine. Fixture is made of mild steel material. Figure 6.12 shows the fixture used for holding the ultrasonic assembly.

Forming of FSW blanks are widely being used in automobile sector since most of its parts are complex in shape. This demands understanding of deformation of friction stir welded blank necessary. In the following section, formability of tailor friction stir welded blanks (TFSWBs) is discussed.

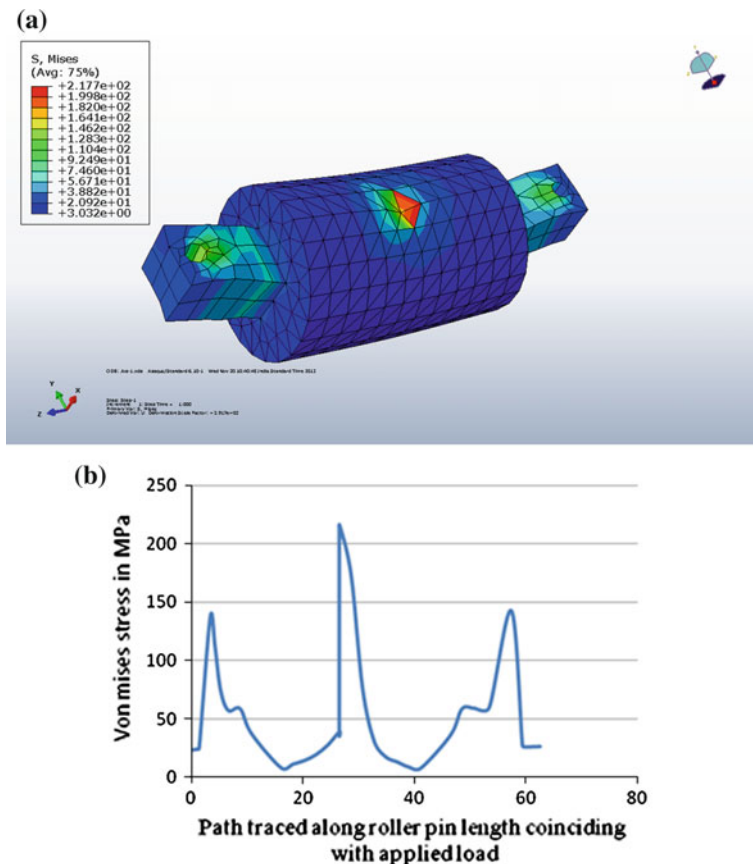


Fig. 6.10 **a** von Mises stresses in roller pin, **b** von Mises stress variation along roller pin with point load at center

6.5 Forming of Friction Stir Welded Blanks

In metal forming processes, the work piece gets desired shape through plastic deformation where the volume is conserved without removal of materials. Most of the components, which we generally use in our day-to-day life, do not have simple shapes, such as blades of a fan, household utensils, automotive body panels etc. In sheet metal forming processes, length and breadth of the work piece remain much larger than its thickness. Aircraft wings, space craft front panels, automotive body panels, and fuel tanks etc. are a few good examples of sheet metal formed products. There are a number of sheet forming processes, namely: bending, stretch forming, deep drawing, ironing, coining, embossing etc. Ability of a material to be deformed into a complex shape without getting fractured is called formability. Measure of formability varies according to the forming method.

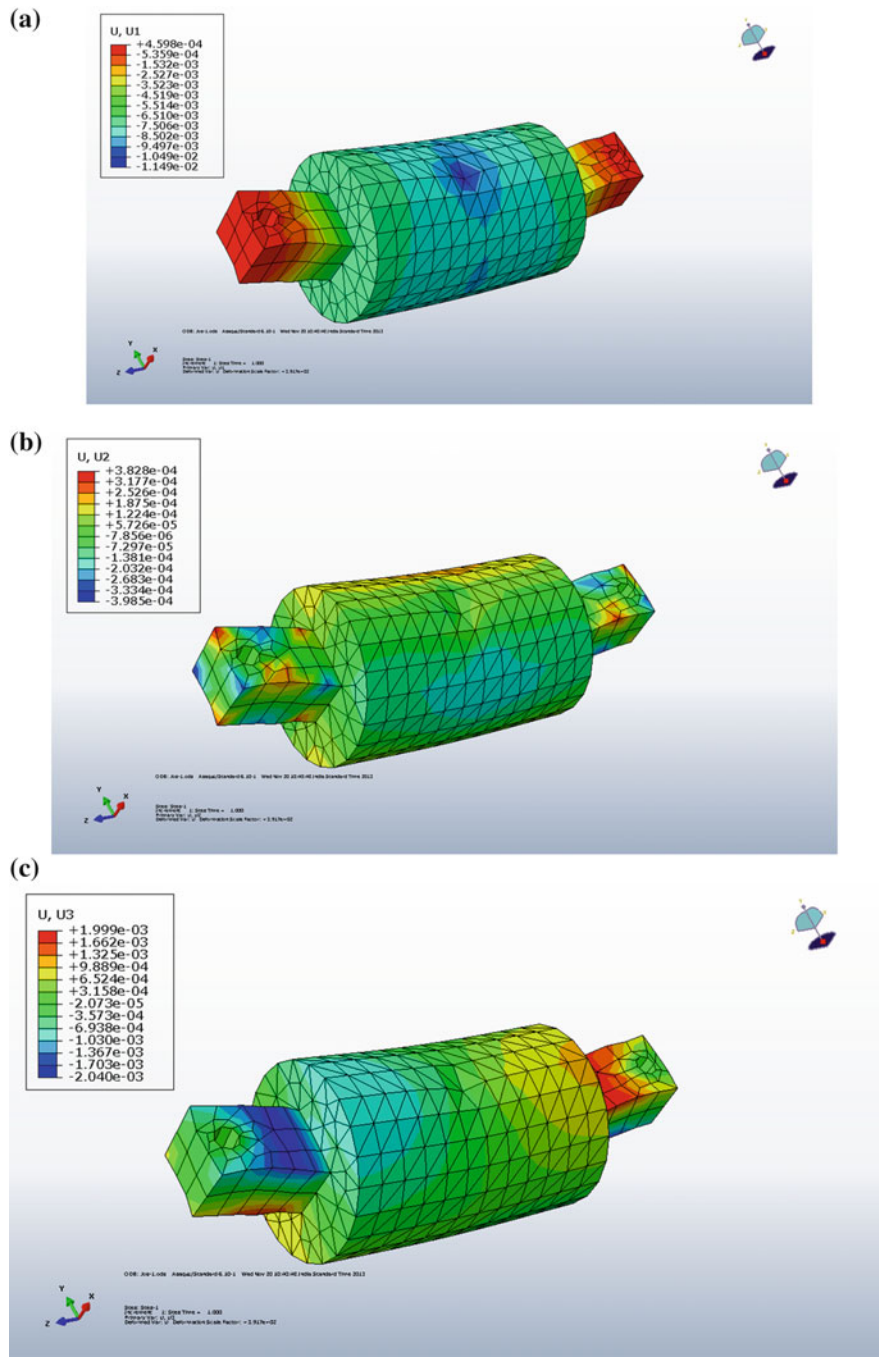
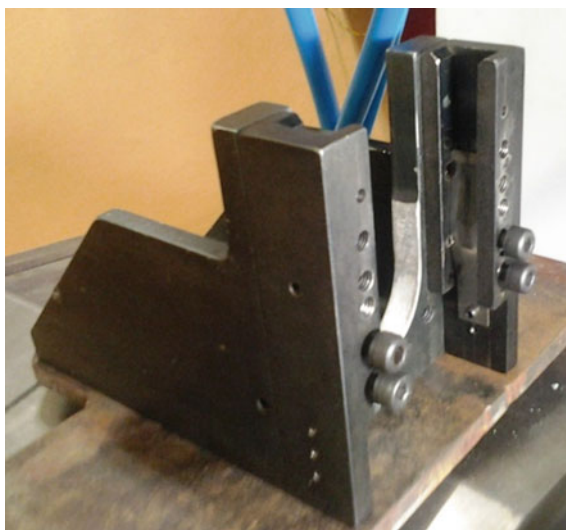


Fig. 6.11 FE results for deflection of roller pin along. a x, b y, and c z directions

Fig. 6.12 Fixture for ultrasonic assembly



Previously most of the parts of an automotive body were made up of steel. Since, steel has a higher density, its continuous use in automotive bodies increases the weight of the vehicle, and as a result fuel consumption increases. The automotive body panels were made in several separate smaller components. These were initially stamped and later on were welded with each other. These cause dimensional inaccuracies, consume more time and also incur high cost. Keyby solved these problems by proposing the concept of tailor welded blanks (TWBs) in 1964 [68]. In fabrication of TWBs, materials having different thicknesses, properties, and coatings are initially welded to each other, and subsequently stamped in a single stage. This minimized dimensional inaccuracies, and also increases the productivity without affecting the strength and safety. Initially, steels were mostly used as the base materials for TWBs, but now-a-days medium strength aluminum alloys (such as 5XXX and 6XXX series) provide their candidature for the base materials of TWBs. This is due to the fact that they do have reasonably good specific strength and high resistance to corrosion as compared to the steel. Aluminum quickly reacts with atmospheric oxygen and forms aluminum oxide, which itself acts as a coating. Resistance mash seam welding and laser welding were initially used to fabricate TWBs of materials other than aluminum. In laser welding, significant softening takes place at the HAZ; and also the weld pool quickly solidifies and forms vary hard structures. Because of that, high difference in hardness across the weld remains; which creates difficulties in post-weld forming. In FSW, less difference in hardness occurs across the weld. The major advantages of FSW for fabricating TFSWBs are discussed below:

In FSW, at the NZ fine equiaxed grains are formed, which cause improvement in material properties of the local region. Achieving this phenomenon, Mishra and Mahoney [69] proposed the concept of FSP. They used FSP to enhance the mechanical properties of as-received sheet metals and few cast materials which

yield to super plasticity. Similarly, Miles et al. [70], Vaze et al. [71], Mahoney et al. [72], and Fuller et al. [73] also used FSP to enhance the material properties prior to forming. Sato et al. [74] tried to find a relationship between the microstructures of FS-welded NZ and formability of the welded sheets. They found that the grain size of the stir zone increased with the increase in heat input. As a result, formability (fracture limit strain) also increased. However, this increase in fracture limit strain was with the grain variation up to 10 μm , beyond which it decreased. Similarly, Hirata et al. [75] also reported decrease in grain size in stir zone with the decrease in frictional heat flow during FSW.

Apart from that, less softening takes place in the HAZ of TFSWBs as compared to other TWBs. Miles et al. [76] fabricated similar TFSWBs of 5XXX series aluminum alloys by using tungsten inert gas (TIG) welding and FSW. They conducted uniaxial tensile test, limiting dome height test and Ohio state university test to determine formability, and compared the results. They observed that FSWed sheets exhibit better formability than those joined using TIG. It is due to less softening at the HAZ in case of FSWed sheets.

However, there are few challenges in stamping of aluminum TFSWBs. These are as follows:

Removal of thin layer of materials, at the retreating side, as flash causes strain localization in post-weld forming of the blanks, (reported by Kumar et al. [77]). Effect of thickness ratio also plays a major role in affecting the formability in TFSWBs. Similar results were observed by Zadpoor et al. [78].

Wide weld bead causes more region of mismatch in material properties; which also creates difficulties during post-weld forming (reported by Rodrigues et al. [79]).

In FSW, there remain TMAZ at both sides of the NZ, where grains are oriented differently than the orientations of grains in the base metals and NZ. These different orientations of grains sometimes cause stress corrosion cracking during post-weld forming, and reduce the formability (reported by Franke and Xia [80] and Srinivasan et al. [81]).

Movement of the weld line toward higher strength materials while forming dissimilar materials TFSWBs; as observed by many researchers in forming of various TWBs.

Below is the brief discussion on formability evaluation of aluminum TFSWBs specific to the basic sheet forming operations, namely: bending, stretch forming, and deep drawing. Here, only formability evaluation of aluminum TFSWBs by using afore said three basic sheet forming processes are discussed. Detailed discussions on post-weld forming of other TWBs are beyond the scope of this chapter.

Sheet bending: It is the most common operation which knowingly or unknowingly occurs in every sheet metal forming practices. Mostly, bending test is used to determine spring back of materials. There are three subclassifications of sheet bending, namely: corner, U and V bending; out of which V bending is the most common used method. Okada et al. [82] used this test to determine bendability of TFSWBs of aluminum alloys. Similarly, Lee et al. [83] investigated formability

and spring back of FSWed aluminum and steel sheets of same and different gauges, both by experimentation and numerical modeling. The formability and magnitude of spring back were found largely dependent on the ratio of yield strength to young modulus, and thickness of sheet metals.

Stretch forming: This operation is used to achieve dome type of structure. In this operation, blank holding pressure remains too large to allow the flange materials to deform in radial direction. Mostly, the punch used in this case is of hemispherical shape. Limiting dome height (LDH) is the measure of formability in this test. The region of sheet metal, which faces the punch, undergoes higher strain path. A number of researchers [76, 84–90] have used this method to evaluate formability of TFSWBs. Ramulu et al. [91] also used this method to analyze the influence of tool shoulder diameter and plunge depth on the formability of aluminum TFSWBs. They measured limiting dome height, thickness distribution, and strain hardening exponent of the welded region. They also studied forming limit curve. The forming limit was found improving with the increase in shoulder diameter and plunge depth.

Deep drawing: Here, flange materials are allowed to deform in radial direction. The region of the sheet metal, which faces punch, undergoes less strain path. However, this method is used to produce complex shaped objects, which are difficult to get otherwise by using other sheet forming operations. Most of the regions of a stamped automotive body panel are deep drawn. Rodrigues et al. [79] used the method to evaluate formability of fabricated similar and dissimilar TWBs of aluminum and steel alloys. They observed formation of wrinkles due to mismatch in mechanical properties in the weld beads during the test. However, Determination of limiting drawing ratio (LDR), which is a measure of formability in deep drawing experiment, was not carried out. Kesharwani et al. [92] determined the LDR in a cylindrical deep drawing test of dissimilar materials TFSWBs of 5XXX series aluminum alloys.

6.5.1 Techniques to Improve Formability of TFSWBs

6.5.1.1 Post-weld Heat Treatment

TFSWBs can undergo different heat treatment procedures to improve formability. Bhanodaya et al. [93] carried out solution heat treatment on the fabricated dissimilar material TFSWBs of 2XXX and 6XXX series aluminum alloys, and observed significant improvement in formability.

6.5.1.2 Hydroforming

In hydroforming, high viscous fluid is used to deform the metal against the complex shaped die. Since no punch is used in this method, hence, thinning of the sheet metal at the punch corner does not occur. Hydroforming is of two types; sheet

forming and tube forming. Till date, there is no published research work available on sheet hydroforming of TFSWBs. However, Yuan et al. [94] performed hydroforming of tubes, which were fabricated from the flat sheets by FSW and further undergone post-weld heat treatment. Nowadays, this method is used to manufacture aircrafts' tubular components.

6.5.1.3 Incremental Forming

It is the most significant invention in the last decade. In this method, a small rotating forming tool is used to incrementally deform the sheet metal into the desired shape. In this method, backing plate is used in place of dies. Though, the method is very slow, it is a very effective way to form the extremely deep products. Silva et al. [95] tried this method to deform FSWBs made up of pure aluminum sheets. They confirmed that the method can also be applied to TFSWBs to manufacture a complex sheet metal parts with higher accuracy.

6.5.1.4 Use of Conical and Tractrix Dies in Deep Drawing

In a conventional cylindrical deep drawing die, a blank holder is essentially required to avoid wrinkle formation. Also, at the die corner sudden bending of the sheet metal takes place, which further get deformed as it comes in contact with the punch corner. This causes work hardening of the metal and reduces the ductility. In order to avoid this, a number of researchers have proposed the concept of conical and tractrix dies. In these dies, no blank holder is used; and also the sheet metal does not undergo sudden bending at the die corner. The complete bending required for the fully drawn condition is achieved gradually. This reduces the loss of ductility by reducing the work hardening, and improves drawability of the material. The actual tractrix shape is difficult to manufacture, as compared to manufacturing conical shapes. Therefore, a modified conical tractrix die was developed, and used by Kesharwani et al. [92] to improve the drawability of TFSWBs. They found 27 % improvement in LDR by using modified conical tractrix die as compared to the LDR while using a conventional cylindrical die.

6.5.2 *Forming of Dissimilar Materials TFSWBs: A Case Study*

In this study, two aluminum alloys (AA5754-H22 and AA5052-H32 of thickness 2.0 mm each) were used to fabricate TFSWBs from dissimilar materials. Both the materials find their applications in automotive, marine and ship building sectors, and in kitchen utensils, because of their good formability and strong corrosion

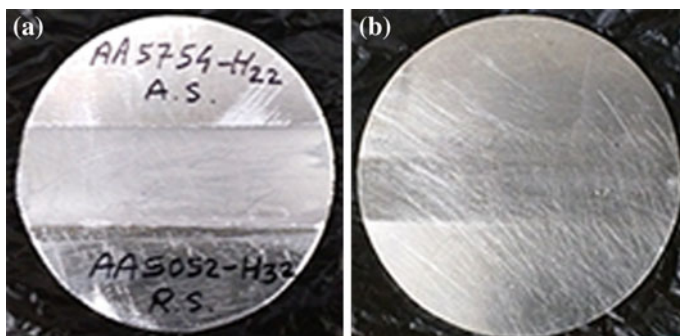
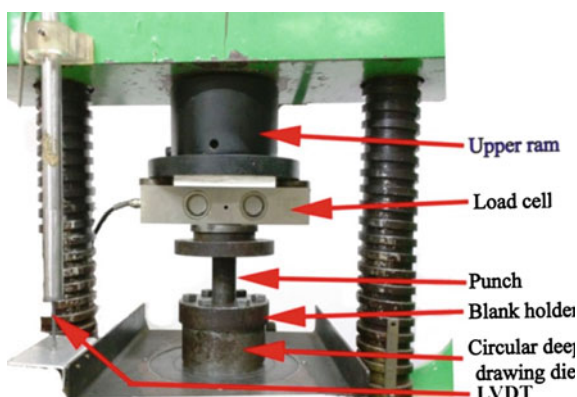


Fig. 6.13 Fabricated TFSWBs from dissimilar materials with parameters corresponding to good weld. **a** Weld top surface, **b** weld root surface

resisting properties. TFSWBs from dissimilar materials were fabricated exhibiting good, as well as defective, welds by using corresponding parameter settings. Subsequently, circular blanks were prepared and deep drawn with a cylindrical die in a hydraulic press for formability evaluation. The weld bead was at the center and weld root surface was kept facing punch. During drawing, punch load and ram travel were also recorded for analyzing the load displacement curve. Figure 6.13 shows a flat circular blank (both from top and bottom) before drawing operation. Figure 6.14 shows the apparatus used for the drawing process. Figure 6.15a shows a successfully drawn cup, and Fig. 6.15b shows a partially fractured cup in deep drawing. Figure 6.16 shows the load displacement curve recorded during deep drawing. It is clear from the figure that initially there remains a small increment in punch load for each unit of ram displacement; whereas, it increases by a big amount later on. It occurs due to work hardening of the blank material. Formability was

Fig. 6.14 Machine tool and deep drawing set up used in the present case study



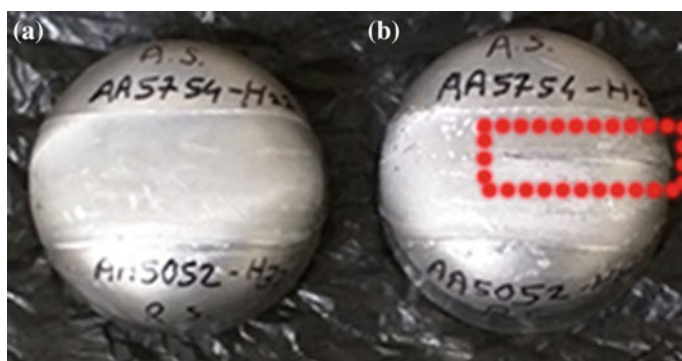
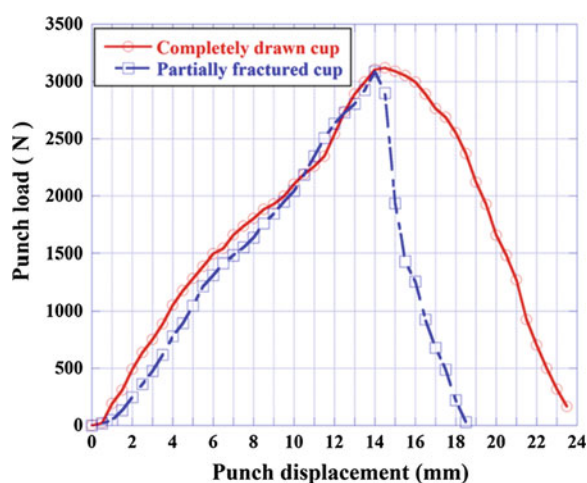


Fig. 6.15 Drawn cups of TFSWBs. **a** Successfully drawn, **b** partially fractured near to the weld center

Fig. 6.16 Punch load–displacement curve for the drawn cups



measured in terms of drawing ratio, and it was found 1.552; whereas, cup height of the successful drawn cup was 22.5 mm. The successfully drawn cup was further sectioned across the weld bead to observe thickness variations along the cup wall (as shown in Fig. 6.17). Small reduction in thickness corresponding to punch corner region was observed.

Computational methods have become important tools for analysis in the last few decades, and with the evolution of high-speed computer the analysis has become faster. In the next section, basic information on FEM is provided along with the methods to simulate FSW. A case study is also shown with sample results of temperature and plastic strain distributions.



Fig. 6.17 Thickness variations along the wall of a successfully drawn cup

6.6 Computational Methods Applied to FSW

Experimental methods are both time consuming and resource dependent. With the evolution of computers, numerical methods have become important tools for investigation of engineering problems. Some of the responses such as stress, strain etc. which are very difficult to be measured in FSW can also be predicted by the advent of the computers. Broadly, computational method can be classified into two sections, analytical and numerical models.

6.6.1 Analytical Model

Analytical model or mathematical model is the representation of a physical problem in the form of mathematical equations or expressions. Physical problem is simplified and is written in the form of equations, which correlate input and output variables. This method is very accurate for simple problems like structural analysis or thermal analysis, but it is very difficult to capture every detail once the problem becomes complex, like in the case of FSW process. FSW is a coupled thermo-mechanical process, i.e., displacement and temperature are interdependent, and also contact interaction between tool and the work piece is non linear. Due to this, it is very difficult to develop a model for FSW to predict heat flux or material flow pattern. Quite a few researchers have developed various mathematical models with certain assumptions.

Schmidt et al. [96] have developed an analytical model based on heat generation for different contact conditions, i.e., sticking, sliding, and sticking-sliding at the tool and work piece contact surface. This model includes frictional heat only, neglecting heat generation because of plastic deformation. For certain tool dimension, they estimated that 86 % of total frictional heat is generated due to shoulder and remaining by the pin. They have used both cylindrical and conical pins for analysis with a flat shoulder. Heurtier et al. [97] have derived material flow pattern by using fluid velocity concept of fluid mechanics. For material flow, three different velocity fields are considered viz. circumventing velocity field, vortex velocity field and a

torsion velocity field. Along with the velocity field, thermal modeling is also done to calculate strain and temperature produced during the process. Heat generation is considered due to friction, as well as deformation. Here, all analyses are done under steady-state condition, and effect of plunging is not considered.

Song and Kovacevic [98, 99] have developed a coupled analytical model for heat generation at the interface of tool and work piece, and heat is distributed within work piece and tool. They have used a moving coordinate system to model FSW and weld line is considered as the line of symmetry. Finite difference technique is used to solve the problem and convective heat transfer condition is used for heat dissipation to the atmosphere from all the surfaces of work piece and the tool. They have considered plunging and welding stages of FSW only. Khandkar et al. [100] have proposed a model, where heat input is calculated based on experimentally measured torque by considering shear stress at the interface. Arora et al. [101] have modeled torque and power requirement in FSW of AA2524 aluminum alloy by solving the conservation of mass, momentum, and energy equations. They have considered a threaded pin. Torque and power requirement have shown good agreement with the experimental data.

Different analytical equations have been developed for heat generation and material flow by considering different contact conditions and velocity fields, respectively.

6.6.2 Numerical Analysis

Though analytical method is highly accurate, but most of the engineering problems, such as FSW process, GMAW process etc., are nonlinear in nature and highly complex, which make analytical solution difficult to be obtained. Sometimes some assumptions are required to simplify the problem nature, which make solutions incorrect. In order to overcome these difficulties, numerical methods are used in FSW, which provide approximate solution of the problems by solving governing differential equations using numerical integration techniques. A lot of numerical techniques are used. Some of those are finite element method (FEM), finite difference method (FDM), and finite volume method (FVM), and so on. Out of these, FEM has become a powerful tool for numerical analysis with the evolution of high-speed computers. FE simulation of the high deformation processes like FSW is very complex due nonlinear contact condition between tool and work piece, high mesh distortion, variable heat dissipation from the bottom surface of work piece etc. Still, since its inception in TWI Cambridge 1991 [6], a lot of researchers have attempted FE simulation of FSW process. Numerous FEM software packages like DEFORM 3D, ABAQUS/Explicit, ANSYS, FLUENT have been used for numerical modeling of FSW process. FEM can be used to predict different aspects of the FSW process, like temperature distribution, force generation, material flow behavior, and grain size refinement in nugget zone etc.

6.6.2.1 Basic Steps in FEM

Accuracy of a FEM solution needs to be balanced with the computational cost, and also error can be minimized with proper selection of input variables and boundary conditions. All the physical problems are boundary value problems, which have one or more primary variables. For example, displacement and temperature are primary variables in structural and heat transfer problems, respectively. Secondary variables like stress, heat flux are dependent on primary variables. Primary variables must satisfy the governing equations at all points within the domain of interest. Primary variables defined at the boundary of the domain are called boundary condition, and this is the initial solution to the problem and is used for the next step of iteration. During the formulation of FEM, fundamental steps remain unchanged irrespective of the nature of the problem. General steps of FEM are stated below, and can be found in any FEM text books [102–104].

Discretization: In FEM, whole domain is subdivided into smaller subdomains to simplify the problem and these subdomains are called as finite elements, and process is known as discretization [102]. Discretization of geometry into subdomains is vital because of two major reasons. First, most of the engineering system by design are complicated and/or materially different, and solution for these are represented by different functional that are continuous within the subdomains. Hence, to minimize the error, approximation of solution should be made within the subdomains. Second, approximation of solution over the single element is easier as compared to the entire domain. Depending upon the nature of the problem, element type of one-dimensional (beams or bar), two-dimensional (triangular, rectangular etc.), or three-dimensional (tetrahedron, brick etc.) can be chosen. Choice and size of element largely affect the accuracy of the problem. Smaller the element size, higher is the accuracy of the solution, but it increases computational cost. Therefore, element size should be chosen such that neither the accuracy of the solution is compromised too much, nor computational cost is too high.

Derivation of element equation: The governing equations must be satisfied for the entire domain of the problem. Along with the governing equations, material constitutive equations need to be solved which characterize the material behavior under different loading conditions. The generation of finite element equations is done in three steps:

(i) A weak form is a weighted integral statement of governing equations in which differentiation is transferred to weight function from dependent variables, such that all natural boundary conditions of the problem are included in the integral. The weighted residual method and the variational approach are the two widely used methods to obtain weak forms of differential equations. Some of the commonly used weighted residual methods are Galerkin's method, Petrov–Galerkin method, least square method, and Collocation method [103]. On the other hand, variational principle is based on either principle of virtual work, principle of minimum potential energy, or Castigliano's theorem to derive elemental equations [104].

(ii) Interpolation function or shape function is assumed in the form of a complete polynomial over each finite element. To achieve a continuous solution over the

entire domain, solution must be same at points common to elements. To do this, end point of each line element is identified as elemental nodes, which act as an interpolation point. Interpolation function is put into the weak form integral equation. Exact evaluation of the integrals that is obtained from element stiffness matrix is sometime not possible due to algebraic complexity, and this is avoided by using numerical integration scheme. Gaussian quadrature integration scheme is most commonly used in practice.

(iii) The weak form obtained after putting interpolation function over the element also contains natural boundary conditions, and this gives necessary algebraic equations among the nodal values for the element in matrix form, which is mentioned in Eq. 6.2.

$$[K^e]\{u^e\} = \{f^e\} + \{Q^e\} \quad (6.2)$$

where, K^e is the elemental stiffness matrix, f^e is the source vector matrix and is evaluated based on the choice of element, u^e is the unknown variable matrix also called as primary nodal degrees of freedom, and Q^e is called as secondary nodal degrees of freedom, some of this is obtained through boundary conditions.

Element connectivity and assembly of elements: To derive elemental equation, a single element was isolated from the mesh and is used to develop finite element model. But this single elemental equation cannot be solved individually as they are interconnected with each other and has impact on each other. These individual elemental equations are combined together using the method of superposition to form a global stiffness matrix.

Boundary conditions: Once the global equations are ready, boundary conditions are imposed to give a final set of simultaneous equations.

Solution of equations: A set of simultaneous equations is solved by using different iterative methods, like direct iteration scheme, Newton–Raphson method etc.

6.6.3 Modeling Techniques

There is a remarkable development in commercially available FEM packages. This has made FEM as an important tool for simulation. But at the same time, it is the researcher's responsibility to give proper and correct input to the FEM software; otherwise, the output will be inappropriate and incorrect. In the FEM software, choice of solver, type of element, solution method, and approach are some of the important aspects on which one must take judicious and tactful decision. Therefore, a better understating of the above-mentioned points is needed and some of those with reference to simulation of FSW are discussed here.

6.6.3.1 Type of Approach

Selection of appropriate formulation method is very important especially for large deformation problems like FSW. There are three different methods to formulate the problem.

Lagrangian approach

Eulerian approach

Arbitrary Lagrangian and Eulerian (ALE) approach

Each method shares its own pros and cons. These methods are mainly distinguished based on mesh movement, kinetic, and kinematic description [105].

Lagrangian approach: In Lagrangian approach, the material is attached to the nodes and it moves as the material deforms; and by tracking the node, different properties like temperature, displacement etc. are estimated. Here, material derivative or total derivative of the property is calculated. Imposing boundary conditions is easier in case of Lagrangian approach as interface between two objects can be defined accurately. As, material point is attached with nodes, mesh distortion remains a issue in this approach, and due to this fact it is majorly used in structural problems where deformations are very small. Mesh distortion becomes a critical issue when large deformation problems like FSW are solved with this method; but this can be avoided by using a remeshing technique, though it increases computational time. Also, selections of appropriate solver and iterative method are also important for non linear problems, otherwise it may lead to non convergence of the solution. Conjugate gradient, Sparse etc. are some of the solvers which can be used along with direct iteration, Newton–Raphson iterative methods.

Many researchers [24, 26, 106–115] have opted Lagrangian approach to simulate FSW. With this approach, FSW can be simulated from inception to steady-state which is not possible with Eulerian approach. The interface between tool and work piece can be appropriately defined.

Eulerian approach: In Eulerian approach, a control volume is defined in space and the change in material property is estimated as material flows to and from the control volume. As nodes are fixed in space, complexity related to mesh distortion is eliminated. Major disadvantages of Eulerian approach are its inability to define interface and boundary accurately. Plunging stage of the FSW process cannot be modeled by this approach, and also imposing frictional heat at the interface is a tedious task. This approach is widely used by researchers to simulate material flow in FSW [116–121]. Computational time in Eulerian approach is less as compared to that in Lagrangian approach.

Arbitrary Lagrangian Eulerian approach: ALE approach combines advantages of Lagrangian and Eulerian approaches to perform better. ALE allows both a flexible grid and a grid that allows material to flow through it. It allows grid to track the material, but when grid deforms excessively and distorts beyond the acceptable points it adjusts the grid and measures the flux of the material during adjustment. Difficulty faced in using ALE is to decide the amount by which grid will extend and how much flux will flow. This is generally taken care of by defining a critical

distortion limit. Once grid deforms above the critical limit then that part is adaptively meshed. In FSW, material flows as a viscous fluid. ALE has to be combined with the remeshing technique to avoid high mesh distortion. Due to this reason, ALE technique is very rarely used to simulate FSW.

6.6.3.2 Literature on FE Simulation of FSW

For FE simulation, either Lagrangian or Eulerian approach is chosen. It depends upon the objectives of the research. Lagrangian approach is justified when simulation covers the zone from plunging to welding to predict temperature, forces, strain etc. On the other hand, Eulerian approach is best suited to simulate the welding portion of the FSW process only to predict material flow behavior and temperature distribution.

Lagrangian and ALE Approaches

Buffa et al. [26, 106] have proposed a 3D coupled thermomechanical analysis to simulate FSW by using DEFORM-3D package. Work piece is considered as a rigid viscoplastic material, and Lagrangian incremental technique is used. They have simulated FSW process in two stages, i.e., plunging and welding. Material model, used to define flow stress, is a function of temperature, strain, and strain rate. Two sheets of work pieces are considered as a single block to avoid contact instabilities between abutting edges. Strain plot is nonsymmetric with higher strain in advancing side, whereas temperature distribution is found to be almost symmetric. Using particle tracking method in simulation, they have also predicted the material flow to be nonsymmetric. Fratini et al. [107] have simulated material flow pattern in FSW using the same model explained before. They have performed experiments to investigate material flow in AA7075-T6 inserting 0.1 mm thick copper sheets in longitudinal, transverse, and horizontal directions, respectively. Different combinations of rotational and welding speeds are used to study material flow by using flat cylindrical and conical pins. Higher material flow in vertical direction is observed while using the conical pin as compared to that by using the cylindrical pin.

Zhang and Zhang [108, 109] have used Arbitrary Eulerian and Lagrangian (ALE) formulation to simulate FSW. The proposed coupled thermomechanical model is capable in predicting temperature, stress, plastic strain, and material deformation. They have used coulomb's law of friction to define the interface between tool and the work piece. Mandal et al. [110] has simulated plunging stage during FSW by using a coupled thermomechanical model in ABAQUS/Explicit. Johnson Cook material and Johnson Cook shear models are used to define flow stress and element deletion, respectively. Temperature and axial force are predicted through the model, and the same is compared with the experimental data. Alfaro et al. [111] have used a meshless technique (natural element method in this case) in

Lagrangian setting. Use of meshless technique avoids high mesh distortion, and can save computational time. Assidi et al. [112] have simulated FSW process by using two different methods, i.e., ALE approach and Eulerian approach. For ALE approach, authors have used adaptive remeshing technique to avoid mesh distortion. Researchers found that the computational time of ALE is almost twice than that in Eulerian approach due to mesh distortion problem. They have used a 3D thermomechanically coupled model to simulate plunging, dwelling and welding stages; however, dwelling is simulated for 1 s only. Trimble et al. [24] have simulated tool forces (vertical, axial and torque) generated during FSW, and the same are validated with experimental values. FE simulation of plunging, dwelling, and welding stages is done by using cylindrical and threaded cylindrical pin. Dwelling is simulated for about 8 s. Johnson Cook material model is used to define the flow stress. A rotating type piezoelectric Kistler dynamometer is used to measure force, and thermocouples are used for temperature measurement. Various researchers [113–115] have also used Lagrangian technique to simulate FSW for different materials like copper, magnesium alloys etc. They have predicted temperature and strain field and also gave an insight on the material flow using point tracking method.

Lagrangian and ALE method can be used for the simulation of FSW, but re-meshing is required to tackle the mesh distortion.

Eulerian Approach

Colegrove and Shercliff [116] have used computational fluid dynamics (CFD) to model FSW. A 3D FSW is modeled in a commercial FEM package, FLUENT. Material model of Sellars and Tegards is used to define flow stress of AA5083 and AA7075 aluminum alloys. FSW is simulated under steady-state condition with sticking boundary condition. Weld force is poorly predicted, and temperature predicted in the model is much higher than that observed experimentally. This is attributed because of noninclusion of thermal softening phenomenon in the model.

Chen et al. [117] have done CFD analysis to simulate FSW of AA 6060 alloy. Tool is considered as a rigid body and already inserted inside the work piece. Frictional heat generation is neglected and only heat generation due to viscous dissipation is considered. Flow stress is defined as a function of strain rate and temperature by using a hyperbolic inverse sine function. They have estimated temperature field and material flow. Temperature field is asymmetric in nature with higher value in advancing side and lower on retreating side; but heat flux is reported to be axisymmetric in nature. Other researchers [118–121] have used FVM or CFD method, which is based on Eulerian approach to simulate FSW. In CFD, steady-state condition is assumed. CFD is the best suited for simulating material flow behavior. Commercial packages like ANSYS Fluent, Star CCM etc. are used for CFD analysis. Kuykendall et al. [122] have analyzed the parameters (temperature, strain, strain rate etc.) to compare eight different material models. They have performed a 2D FSW simulation and compared the results obtained by using three

different material models viz. Johnson Cook (JC), Sellars and Tegart, and Kocks and Mecking material models.

CFD is suited for simulation of material flow. Work piece is considered as a non-Newtonian fluid and different material models are used to define flow stress. CFD method eliminates mesh distortion problem.

6.6.4 Methodology to Simulate FSW

In this section, a step-by-step methodology is explained on the simulation of the FSW process. This methodology focuses on a 3D thermomechanical analysis performed in DEFORM 3D software using Lagrangian implicit code. Adaptive remeshing is considered to counter mesh distortion problem.

6.6.4.1 Geometric Modeling and Boundary Conditions of FSW

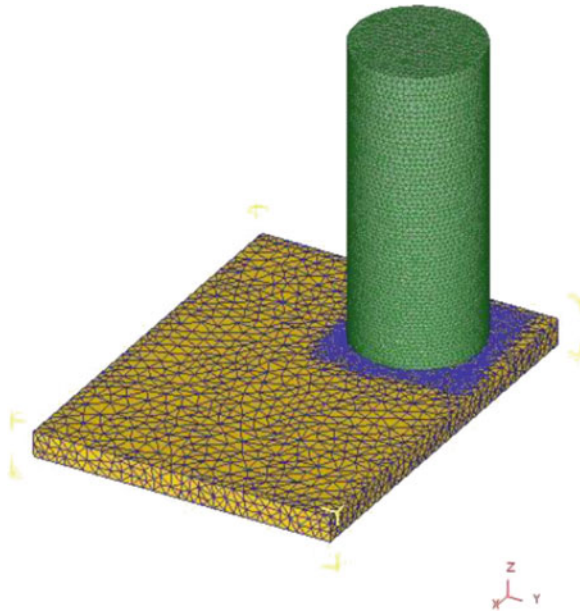
Geometric modeling of work piece and tool is an important aspect in FE simulation as it should closely replicate the actual shape and size of the work piece with desired accuracy. Work piece is considered as a rigid viscoplastic material, i.e., elastic deformation is neglected, and is a valid assumption since plastic deformation is much higher than elastic deformation. This assumption also takes care of non-convergence of the solution when deformation is changing from elastic zone to plastic zone. Work piece is modeled as a 3D rectangular cuboid with a dimension of 80 mm × 60 mm × 5 mm, with AA2024 as the material. To avoid contact instability during simulation, work piece is assumed as a single continuum body. 44,730 coupled tetrahedral elements are used to mesh work piece. Finer mesh is considered at the contact region and remaining portion of the work piece is meshed with a coarser mesh with minimum element size of 1 mm. To tackle large deformation, remeshing is incorporated. Figure 6.18 shows the meshed tool and the work piece. Tool is defined as a rigid body, as yield stress of tool material (H13 tool steel) is much higher than that of the work piece material. Therefore, stress, strain are not calculated on tool, but heat transfer to the tool is considered to calculate temperature rise inside the tool. Diameter of the shoulder is considered as 24 mm. The included angle of the conical pin is assumed as 40° with the larger diameter of 7 mm, pin height and plunge depth are 4.6 and 0.1 mm, respectively. Following are the boundary conditions applied in the model:

In the bottom surface of the work piece, velocity of all nodes is assigned to zero to arrest all degrees of freedom of the work piece.

Rotational speed and welding speed are defined on the tool.

Convective heat transfer coefficient of 20 W/m² °C is used between work piece and environment and in between work piece and tool.

Fig. 6.18 Geometric model of FSW in DEFORM 3D



In FSW, a backing plate is used beneath the work piece to provide support to the work piece and conductive heat transfer takes place between them. To simplify the FE simulation, backing plate can be neglected to improve computational efficiency as use of a backing plate will increase total number of elements and will increase the computational time. Equation 6.3 is used to define heat transfer loss from the bottom face of the work piece. The convective heat transfer coefficient of $200 \text{ W/m}^2 \text{ } ^\circ\text{C}$ is defined.

Radiation between work piece surface and environment is also defined.

Thermal boundary condition defined on the faces other than bottom face of the work piece is given by Eqs. 6.4 and 6.5.

$$k \frac{\partial T}{\partial n} = h(T_w - T_a) \quad (6.3)$$

$$Q_{\text{conv}} = h(T_w - T_a) \quad (6.4)$$

$$Q_{\text{rad}} = \sigma(T_w^4 - T_a^4) \quad (6.5)$$

where, k is conductive heat transfer coefficient in $\text{W/m}^\circ\text{C}$, h is convective heat transfer coefficient in $\text{W/m}^2^\circ\text{C}$, Q_{conv} is convective heat transfer in W/m^2 , Q_{rad} is radiational heat loss in W/m^2 , σ is the Stephan–Boltzmann constant with a value of $5.6703 \times 10^{-8} \text{ W/m}^2 \text{ } ^\circ\text{C}^4$. T_w and T_a are work piece and ambient temperatures, respectively.

Table 6.3 Physical properties of work piece and tool [123]

Properties	AA2024	Tool steel H13
Young's modulus (N/mm ²)	68,900	210,000
Thermal conductivity (N/s °C)	181	149
Heat capacity (N/mm ² °C)	2.43	2.78
Thermal expansion (μmm/mm °C)	22	11.7
Poisson's ratio	0.33	0.3

Following assumptions are made to simplify the simulation of the FSW process:

Thermal and elastic properties are taken as constant to improve computational efficiency.

Backing plate is neglected

Plunging and dwelling are neglected, i.e., at the start of simulation, workpiece has the impression of the tool

No spindle tilt angle is considered.

Physical properties of the work piece and the tool materials are mentioned in Table 6.3.

6.6.4.2 Material Constitutive Relation

Constitutive relation describes the thermo-mechanical behavior of work piece under loading condition. Depending upon the nature of the problem, there will be one or more than one constitutive relation to relate flow stress with deformation or deformation rate. Constitutive relation of plasticity includes yield criteria, flow rule and hardening rule. Yield criteria describe stress state during yielding. Flow rule describes variation in flow stress with incremental change in primary variables like temperature, strain, and strain rate. Hardening rule defines the hardening of material under plastic strain. In the present work, von Mises yield criterion, and isotropic hardening law is used.

Use of appropriate flow rule to define flow stress is a critical aspect of FSW simulation. Since material is under viscous state during FSW, it is important to define flow stress at different temperature, strain, and strain rate to capture the mechanism of FSW, as given in Eq. 6.6. Here, flow stress is considered as a function of temperature, strain, and strain rate. Stress-strain curve of AA2024 material is defined for temperature range of 20–550 °C, and for strain rate of 0.3–100 s⁻¹ [123].

$$\bar{\sigma} = \bar{\sigma}(\bar{\epsilon}, \dot{\bar{\epsilon}}, T) \quad (6.6)$$

where, $\bar{\sigma}$ is the flow stress in MPa, $\bar{\epsilon}$ is strain, $\dot{\bar{\epsilon}}$ is strain rate in s⁻¹, and T is the temperature in °C.

6.6.4.3 Friction Model

Interfacial interaction between the tool and the work piece in FSW is very complex and critical in terms of accuracy of the solution. Due to lack of experimental data and evidence of the actual conditions, researchers have assumed different contact conditions. As discussed in the literature review, some researchers have assumed coulomb's law of friction [108, 112] or some have assumed sticking condition [26, 106]. A few researchers [101, 121] have used a friction model, which is the function of the pressure and the slip rate. In the present work, sticking boundary condition, as given in Eq. 6.7, is used.

$$\bar{\tau} = m\tau_{\max} \quad (6.7)$$

where, $\bar{\tau}$ is the contact stress at the interface of tool and the work piece in MPa, m is the shear factor whose value is 1, τ_{\max} is the yield strength of the material which is 0.577 times of the ultimate strength of the material according to von Mises yield criterion.

6.6.4.4 Thermal Model

In FSW, heat is generated due to friction and plastic deformation of the material. In DEFORM 3D, inelastic heat fraction is defined to incorporate heat generated due to plastic deformation, as expressed in Eq. 6.8.

$$\dot{q} = \dot{q}_f + \dot{q}_p \quad (6.8)$$

where, \dot{q} is the total heat generation during welding, \dot{q}_f is the frictional heat generation, and \dot{q}_p is the heat generation due to plastic deformation of the material and is calculated by Eq. 6.9.

$$\dot{q}_p = \eta \bar{\sigma} \dot{\epsilon} \quad (6.9)$$

where, η is amount of mechanical work converted to heat and is assumed as 0.9 in this work. Temperature distribution is dictated by Fourier law of heat conduction equation, as stated in Eq. 6.10.

$$k\nabla^2 T + \dot{q} = \rho c_p \frac{\partial T}{\partial t} \quad (6.10)$$

where, k is thermal conductivity of the material, T is temperature in °C, ρ is density of the material, and c_p is the heat capacity of the material per unit mass. Transient heat transfer analysis is considered in this work.

6.6.4.5 FEM Formulation and Governing Equations

FEM of rigid viscoplastic material use variational approach, where admissible velocities u_i should satisfy the compatibility and incompressibility condition, and also the velocity boundary conditions, which gives the following functional (function of a function) a stationary value.

$$\pi = \int_V E(\dot{\epsilon}_{ij}) dV - \int_{S_v} F_i u_i dS \quad (6.11)$$

where, $E(\dot{\epsilon}_{ij})$ is a work function and F_i is the surface traction. A penalized form of the incompressibility is added to remove the incompressibility constraint on admissible velocity fields. The actual velocity field is determined from the stationary value of the variation equation, which is stated as

$$\delta\pi = \int_V \bar{\sigma} \delta\dot{\bar{\epsilon}} dV + K \int_V \dot{\epsilon}_v \delta\dot{\epsilon}_v dV - \int_{S_F} F_i \delta u_i dS = 0 \quad (6.12)$$

where, $\bar{\sigma} = \bar{\sigma}(\dot{\bar{\epsilon}}, \bar{\epsilon})$ and $\dot{\epsilon}_v = \dot{\epsilon}_{ii}$ is the volumetric strain rate. δu_i is arbitrary variation; $\delta\dot{\epsilon}_v$ and $\delta\dot{\bar{\epsilon}}$ are the variations in the strain rate derived from δu_i . The penalty constant, K has a very large positive value [124]. Lagrangian formulation satisfies conservation of mass, momentum, and energy equations as given in Eqs. 6.13, 6.14, and 6.15, respectively.

$$\frac{d\rho}{dt} + \rho \nabla \cdot v = 0 \quad (6.13)$$

$$\rho \frac{dv}{dt} = \nabla \cdot \sigma + \rho b \quad (6.14)$$

$$\rho \frac{dE}{dt} = \nabla \cdot \sigma \cdot v + v \cdot \rho b \quad (6.15)$$

where, ρ , v , σ , E , t , and b are mass density, material velocity vector, Cauchy stress vector, specific energy, time, and specific body force, respectively [124].

6.6.5 Simulation Results

This section shows the capability of DEFORM 3D to simulate FSW process. Temperature and strain distribution of AA2024 material are shown and a quantitative assessment on accuracy of result is also discussed.

6.6.5.1 Complexity in Simulation of FSW

Finite element simulation of FSW is a complex problem due to large deformation, high strain rates and strain near the pin and beneath the shoulder. The problem is highly nonlinear in nature. Accuracy of FSW simulation depends on large number of parameters like flow stress definition, type of contact, step size, mesh size etc. Biggest challenge in simulating FSW is to eliminate the groove behind the tool. This groove formation is due to lack of material flow during simulation, which is mostly due to incorrect definition of material model and contact condition. Step size and mesh size also play a vital role to avoid the problem.

In actual experiment also, this kind of behavior is noticed due to insufficient temperature, when too high welding velocity is chosen.

6.6.5.2 Temperature Distribution

In FSW, temperature is a critical parameter to achieve a sound weld. It is a known fact that with the increase in temperature, yield strength of material reduces, and thus material flows easily under loading condition. Heat is generated due to friction and plastic deformation of material, where former depends upon the shear factor and later on the amount of deformation. Figure 6.19a shows the temperature distribution in longitudinal and transverse directions for a tool rotation of 1000 rpm and a welding speed of 80 mm/min.

In transverse and longitudinal directions, temperature distribution is forming a V shaped structure which indicates higher heat generation at the top due to larger shoulder dimension as compared to the pin.

Figure 6.20 shows the temperature distribution on FSW tool. The maximum temperature is observed at the tool pin and at the shoulder, as both of them remain in contact with the work piece.

6.6.5.3 Strain Distribution

Plastic deformation along with temperature is crucial for microstructural evolution as well as grain refinement in FSW. Experimentally, it is difficult to predict the plastic deformation during FSW. Only qualitative prediction of deformation is possible based on grain refinement and microstructure. Finite element simulation is an important tool to predict plastic deformation. Figure 6.21 shows the effective strain distribution on work piece top surface, and in transverse direction during FSW for a tool rotation of 1000 rpm and a welding speed of 80 mm/min. Effective strain distribution forms an inverted trapezoidal structure, which is also seen in experimental result due to higher deformation on the top surface as compared to the bottom surface.

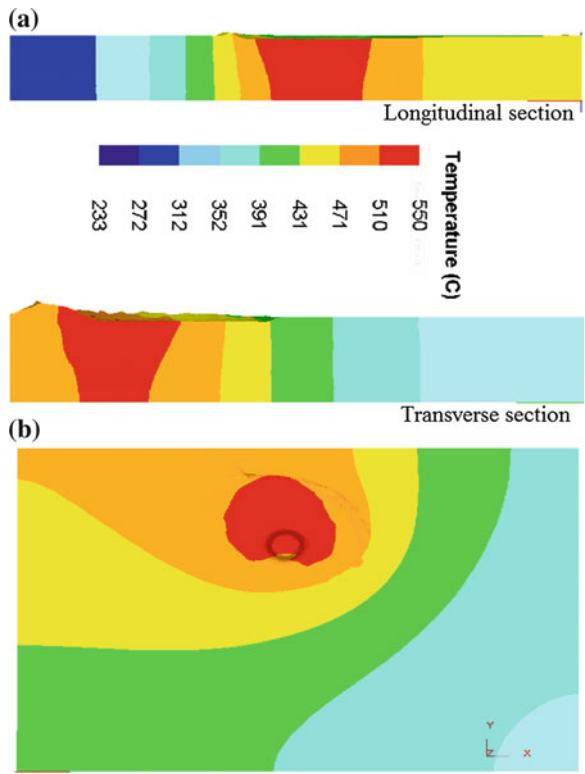


Fig. 6.19 Temperature distribution. **a** A long longitudinal and transverse direction, **b** top surface of work piece for the simulation of 1000 rpm and 80 mm/min

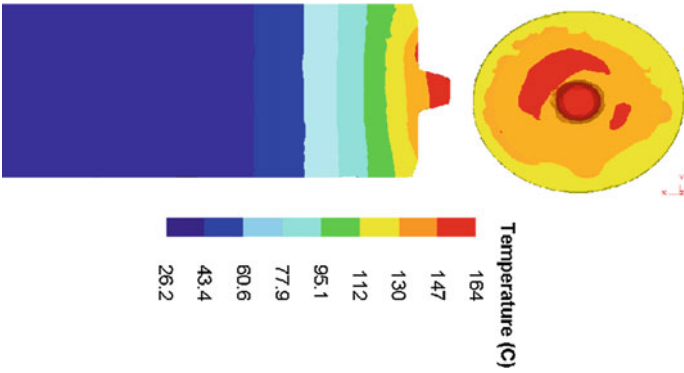
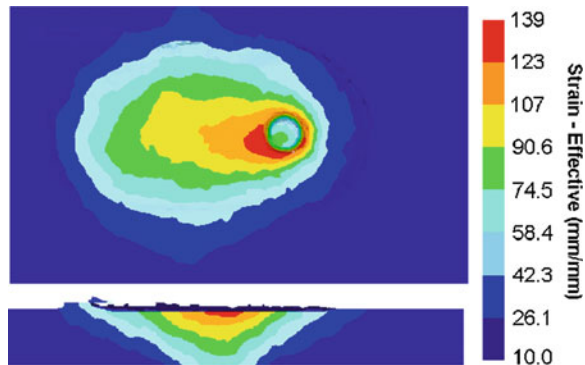


Fig. 6.20 Temperature distribution on FSW tool

Fig. 6.21 Effective strain distributions for 1000 rpm and 80 mm/min



6.7 Conclusion

This chapter has introduced FSW as a joining process along with various aspects of the process like basic mechanism, advantages, disadvantages, application, and different types of defects are discussed in detail. Application of the process hints that the process has got tremendous capability and can cater to a varied range of industries. The process solves a lot of issues related to welding of aluminum alloys and dissimilar material, which is the need of hour.

Recent research works on FSW process are also discussed in experimental and computational method sections. Twin-tool is a novel concept which improves the FSW process and can be an alternative to multi-pass welding. This will also improve the productivity of the process as welding is done in a single step by using two tools having a specially designed fixture. A case study on twin-tool concept is explained which suggests improved hardness of welded plates as compared to single-pass welding.

Coupling ultrasonic with FSW is another way to improve the process. Detailed review on feasibility of ultrasonic assisted FSW is done. Horn design is also discussed which is responsible for ultrasonic vibration along with generator and other components.

Formability of tailor-welded blanks, which is very vital for application of sample, is discussed.

Finite element modeling is an important tool for to analyze the complex engineering problems. Significance of FEM over experimental process is discussed and different modeling methods like Lagrangian and Eulerian are also discussed in details. A brief review on research works using FEM in FSW is also discussed. A case study on simulation of 3D thermomechanically coupled model using Lagrangian method is discussed. This model is capable of predicting temperature, strain, and has got the potential to predict forces and material flow during the process.

References

1. Yoshihiro K (2013) Honda develops robotized FSW technology to weld steel and aluminum and applied it to a mass production vehicle. *Ind Robot Int J* 40(3):208–212
2. <http://aluminium.matter.org.uk/content/html/eng/default.asp?catid=217&pageid=2144417175>. Accessed 19 Mar 2015 at 7:38 AM
3. Mishra RS, Mahoney MW (2007) Friction stir welding and processing. ASM international
4. Cabello MA, Ruckert G, Huneau B, Sauvage X, Marya S (2008) Comparison of TIG welded and friction stir welded Al-4.5 Mg-0.26Sc alloy. *J Mater Process Technol* 197:337–343
5. Ericsson M, Sandstorm R (2003) Influence of welding speed on fatigue of friction stir weld and comparison with MIG and TIG. *Int J Fatigue* 25:1379–1387
6. Thomas WM, Nicholas ED, Needham JC, Murch MG, Templesmith P, Dawes CJ (1991) G.B. Patent 9125978.8
7. Nandan R, Debroy T, Bhadeshia HKDH (2008) Recent advances in friction stir welding: process, weldment and properties. *Progr Mater Sci* 53:980–1023
8. <https://www.apple.com/in/imac/design/>. Accessed 19 Mar 2015 at 8:19 AM
9. Toros S, Ozturk F, Kacar I (2008) Review of warm forming of aluminum–magnesium alloys. *J Mater Process Technol* 207(1–3):1–12
10. <http://www.aluminiumleader.com/en/around/transport/cars>. Accessed 19 Mar 2015 at 8:33 AM
11. Liu X, Lan S, Ni J (2014) Analysis of process parameters effects on friction stir welding of dissimilar aluminum alloy to advanced high strength steel. *J Mater Des* 59:50–62
12. Uzun H, Dalle C, Argagnotto A, Ghidini T, Gambaro C (2005) Friction stir welding of dissimilar Al 6013-T4 To X5CrNi18-10 stainless steel. *Mater Des* 26:41–46
13. Coelho RS, Kostka A, Santos JF, Kaysser-pyzalla A (2012) Friction-stir dissimilar welding of aluminium alloy to high strength steels: mechanical properties and their relation to microstructure. *Mater Sci Eng, A* 556:175–183
14. Lee W, Schmuecker M, Mercardo A, Biallas G, Jung S (2006) Interfacial reaction in steel–aluminum joints made by friction stir welding. *Scripta Mater* 55:355–358
15. Chen C, Kovacevic R (2004) Joining of Al 6061 alloy to AISI 1018 steel by combined effects of fusion and solid state welding. *Int J Mach Tools Manuf* 44(11):1205–1214
16. Sato YS, Park SHC, Michiuchi M, Kokawa H (2004) Constitutional liquation during dissimilar friction stir welding of Al and Mg alloys. *Scripta Mater* 50(9):1233–1236
17. Fu B, Qin G, Li F, Meng X, Zhang J, Wu C (2015) Friction stir welding process of dissimilar metals of 6061-T6 aluminum alloy to AZ31B magnesium alloy. *J Mater Process Technol* 218:38–47
18. Galvão I, Verdera D, Gesto D, Loureiro A, Rodrigues DM (2013) Influence of aluminium alloy type on dissimilar friction stir lap welding of aluminium to copper. *J Mater Process Technol* 213(11):1920–1928
19. Wei Xia, Datong Z, Cheng QIU, Wen Z (2012) Microstructure and mechanical properties of dissimilar pure copper/1350 aluminum alloy butt joints by friction stir welding. *Trans Nonferrous Met Soc China* 22:1298–1306
20. Tan CW, Jiang ZG, Li LQ, Chen YB, Chen XY (2013) Microstructural evolution and mechanical properties of dissimilar Al–Cu joints produced by friction stir welding. *Mater Des* 51:466–473
21. <http://materion.com/~media/Files/PDFs/TechnicalMaterials/Bond%20Integrity%20in%20Aluminum-Copper%20Clad%20Metals.pdf>. Accessed 19 Mar 2015 at 4:00 PM
22. Bo L, Zhang Z, Shen Y, Hu W, Luo L (2014) Dissimilar friction stir welding of Ti6Al4V alloy and aluminum alloy employing a modified butt joint configuration: influence of process variables on the weld interfaces and tensile properties. *Mater Des* 53:838–848
23. Hassan SF, Gupta M (2003) Development of high strength magnesium copper based hybrid composites with enhanced tensile properties. *Mater Sci Technol* 19–2:253–259

24. Trimble D, Monaghan J, O'Donnell GE, Donnell GEO (2012) Force generation during friction stir welding of AA2024-T3. *CIRP Ann Manuf Technol* 61(1):9–12
25. Elangovan K, Balasubramanian V, (2007) Influences of pin profile and rotational speed of the tool on the formation of friction stir processing zone in AA2219 aluminium alloy. *Mater Sci Eng A* 459:7–18
26. Buffa G, Hua J, Shivpuri R, Fratini L (2006) Design of the friction stir welding tool using the continuum based FEM model. *Mater Sci Eng A* 419(1–2):381–388
27. Colligan K (1991) Material flow behavior during friction stir welding of aluminum. *Adv Weld Res* 229–237
28. Dickerson T, Shercliff HR, Schmidt H (2003) A weld marker technique for flow visualization in friction stir welding. In: 4th international symposium on friction stir welding, USA, pp 14–16
29. Qian J, Li J, Sun F, Xiong J, Zhang F, Lin X (2013) An analytical model to optimize rotation speed and travel speed of friction stir welding for defect-free joints. *Scripta Materiala* 68:175–178
30. Kim YG, Fujii H, Tsumura T, Komazaki T, Nataka K (2006) Three defects types in friction stir welding of aluminium die casting alloy. *Mater Sci Eng A* 415:250–254
31. Brown R, Tang W, Reynolds AP (2009) Multi-pass friction stir welding in alloy 7050-T7451: effects on weld response variables and on weld properties. *Mater Sci Eng A* 513:115–121
32. Nataka K, Kim YG, Fujii H, Tsumura T, Komazaki T (2006) Improvement of mechanical properties of aluminium die casting alloy by multi-pass friction stir processing. *Mater Sci Eng A* 437:274–280
33. He D, Yang K, Li M, Guo H, Li N, Lai R, Ye S (2013) Comparison of single and double pass friction stir welding of skin-stringer aviation aluminium alloy. *Sci Technol Weld Join* 8: 610–615
34. Leal RM, Loureiro A (2008) Effect of overlapping friction stir welding passes in the quality of welds of aluminium alloys. *Mater Des* 29:982–991
35. Barhami M, Nikoo MF, Givi MKB (2015) Microstructural and mechanical behaviors of nano-SiC-reinforced AA7075-O FSW joints prepared through two passes. *Mater Sci Eng A* 626:220–228
36. Ma ZY, Sharma SR, Mishra RS (2006) Effects of multiple-pass friction stir processing on microstructure and tensile properties of a cast aluminium-silicon alloy. *Scripta Mater* 54: 623–1626
37. Johannes LB, Mishra RS (2007) Multiple passes of friction stir processing for the creation of super plastic 7075 aluminium. *Mater Sci Eng A* 464:255–260
38. Ma ZY, Mishra RS, Liu FC (2009) Superplastic behaviour of micro-regions in two-pass friction stir processed 7075Al alloy. *Mater Sci Eng A* 505:70–78
39. Surekha K, Murty BS, Rao KP (2008) Microstructural characterization and corrosion behaviour of multipass friction stir processed AA2219 aluminium alloy. *Surf Coat Technol* 202:4057–4068
40. Jana S, Mishra RS, Baumann JA, Grant G (2010) Effect of process parameters on abnormal grain growth during friction stir processing of a cast Al alloy. *Mater Sci Eng A* 528:189–199
41. Thomas WM, Staines DJ, Watts ER, Norris IM (2005) The simultaneous use of two or more friction stir welding tools. TWI Ltd. Report, Cambridge
42. Thomas WM, (1999) Friction stir welding of ferrous materials: a feasibility study. In: proceedings of the first international conference on friction stir welding. Thousand Oaks, TWI, paper on CD
43. Mitsuo H (2000) Friction agitation joining method and friction agitation joining device. Japan Patent Application 2000-094156
44. Atsuo K, Yoshinora O, Mutsumi Y (2003) Friction stir welding method, Japan. Patent Application 2003-112271 and 2003-112272
45. Kumari K, Pal SK, Singh SB (2015) Friction stir welding by using counter-rotating twin tool. *J Mater Process Technol* 215:132–141
46. Blaha F, Langenecker B (1955) Tensile deformation of zinc crystal under ultrasonic vibration. *Naturwissenschaften* 42:556

47. Lucas M, Huang ZH, Daud Y (2005) Ultrasonic compression tests on aluminium. *Appl Mech Mater* 3:99–104
48. Daud Y, Lucas M, Huang Z (2007) Modelling the effects of superimposed ultrasonic vibrations on tension and compression tests of aluminium. *J Mater Process Technol* 186 (1):179–190
49. Inoue M (1984) Studies on ultrasonic metal tube drawing. *Memoira of Sagami Institute of Technology*, vol 19, pp 1–7
50. Kumar V (2011) Understanding ultrasonic plastic assembly. Nevik Ultrasonics Publishers, Nashik
51. Brook RJ (ed) (1991) Concise encyclopedia of advanced ceramic materials. Pergamon Press, Oxford, pp 1–2 and p 488
52. Moreland MA, Moore DO (1988) Versatile performance of ultrasonic machining. *Am Ceram Soc Bull* 67(6):1045–1047
53. Gilmore R (1990) Ultrasonic machining and orbital abrasion techniques. Society of Manufacturing Engineers, Transactions: AIR, NM89-419, pp 1–20
54. Kennedy DC, Grieve RJ (1975) Ultrasonic machining—a review. *Produc Eng* 54(9):481–486
55. Chang SS, Bone GM (2005) Burr size reduction in drilling by ultrasonic assistance. *Robot Comput Integr Manuf* 21(4–5):442–450
56. Ishikawa KI, Suwabe H, Nishide T, Uneda M (1998) A study on combined vibration drilling by ultrasonic and low-frequency vibrations for hard and brittle material. *Precis Eng* 22 (4):196–205
57. Tsujino J, Ueoka T, Hasegawa K, Fujita Y, Shiraki T, Okada T, Tamura T (1996) New methods of ultrasonic welding of metal and plastic materials. *Ultrasonics* 34(2):177–185
58. Tsujino J, Sano T, Ogata H, Tanaka S, Harada Y (2002) Complex vibration ultrasonic welding systems with large area welding tips. *Ultrasonics* 40(1):361–364
59. Matsuoka SI, Imai H (2009) Direct welding of different metals used ultrasonic vibration. *J Mater Process Technol* 209(2):954–960
60. De edga, De Vries E (2004) Mechanics and mechanisms of ultrasonic metal welding. The Ohio State University. PhD Thesis
61. Jeng YR, Horng JH (2001) A microcontact approach for ultrasonic wire bonding in microelectronics. *Trans Am Soc Mech Eng J Tribol* 123(4):725–731
62. Park K (2009) Development and analysis of ultrasonic assisted friction stir welding process. Doctoral dissertation, The University of Michigan
63. Ruilin L, Diqiu H, Luo Cheng L, Shaoyong Y, Kunyu Y (2014) A study of the temperature field during ultrasonic-assisted friction-stir welding. *Int J Adv Manuf Technol* 73(1–4): 321–327
64. Amini S, Amiri MR (2014) Study of ultrasonic vibrations' effect on friction stir welding. *Int J Adv Manuf Technol* 73(1–4):127–135
65. Ahmadnia M, Seidanloo A, Teimouri R, Rostamiyan Y, Titrashi KG (2015) Determining influence of ultrasonic-assisted friction stir welding parameters on mechanical and tribological properties of AA6061 joints. *Int J Adv Manuf Technol* 1–16
66. Ma HK, He DQ, Liu JS (2015) Ultrasonically assisted friction stir welding of aluminium alloy 6061. *Sci Technol Weld Join* 20:216–221
67. Rostamiyan Y, Seidanloo A, Sohrabpoor H, Teimouri R (2014) Experimental studies on ultrasonically assisted friction stir spot welding of AA6061. *Archives of Civil and Mechanical Engineering*
68. Kinsey BL, Wu X (2011) Tailor welded blanks for advanced manufacturing. Woodhead Publishing Limited, First Edit. UK
69. Mishra RS, Mahoney MW (2001) Friction stir processing: a new grain refinement technique to achieve high strain rate superplasticity in commercial alloys. *Mater Sci Forum* 357–359:507–514
70. Miles MP, Mahoney M, Nelson W, Mishra RS (2003) Finite element simulation of plane-strain thick plate bending of friction-stir processed 2519 aluminum. In: TMS annual meeting, pp 253–258

71. Vaze SP, Xu J, Ritter R, Colligan K, Fisher JJ (2003) Friction stir processing of aluminum alloy 5083 plate for cold bending. *Mater Sci Forum* 426–432(4):2979–2986
72. Mahoney M, Barnes AJ, Bingel WH, Fuller C (2004) Superplastic forming of 7475 Al sheet after friction stir processing (FSP). *Mater Sci Forum* 447–448:505–512
73. Fuller CB, Miles MP, Bingel W (2005) Thick plate bending of friction stir processed aluminum alloys. In: *Friction stir welding and processing III—proceedings of a symposium sponsored by the shaping and forming committee of (MPMD) of the minerals, metals and materials society, TMS*, pp 131–137
74. Sato YS, Sugiura Y, Shoji Y, Park SHC, Kokawa H, Ikeda K (2005) Effect of microstructure on postweld formability in friction stir welded Al alloy 5052. In: *ASM proceedings of the international conference: trends in welding research*, vol 2005, pp 387–391
75. Hirata T, Oguri T, Hagino H, Tanaka T, Chung SW, Takigawa Y, Higashi K (2007) Influence of friction stir welding parameters on grain size and formability in 5083 aluminum alloy. *Mater Sci Eng A* 456(1–2):344–349
76. Miles MP, Decker BJ, Nelson TW (2004) Formability and strength of friction-stir-welded aluminum sheets. *Metall Mater Trans A Phys Metall Mater Sci* 35A(11):3461–3468
77. Kumar M, Kailas SV, Narayanan RG (2013) Influence of external weld flash on the in-plane plane-strain formability of friction stir welded sheets. *J Strain Anal Eng Des* 48(6):376–385
78. Zadpoor AA, Sinke J, Benedictus R (2008) The effects of friction stir welding on the mechanical properties and microstructure of 7000 series aluminium tailor-welded blanks. *Int J Mater Form* 1(Suppl 1):1311–1314
79. Rodrigues DM, Chaparro BM, Leitão C, Baptista AJ, Loureiro A, Vilaça P (2007) Formability of steel and aluminium tailor welded blanks. *Weld. World* vol 51, no. SPEC. ISS., pp 667–676
80. Frankel GS, Xia Z (1999) Localized corrosion and stress corrosion cracking resistance of friction stir welded aluminum alloy 5454. *Corrosion* 55(2):139–150
81. Srinivasan PB, Dietzel W, Zettler R, dos Santos JF, Sivan V (2005) Stress corrosion cracking susceptibility of friction stir welded AA7075–AA6056 dissimilar joint. *Mater Sci Eng A* 392 (1–2):292–300
82. Okada T, Hashimoto HH, Tanikawa T, Iwaki H, Takeda S, Miyamichi J, Eguchi N, Tanaka S Oiwa, Namba K (2005) Studies on characteristics of friction stir welded joints in structural thin aluminium alloys part 2: metallurgical features and mechanical properties of friction stir welded joints. *Weld World* 49(3–4):83–92
83. Lee W, Kim D, Kim J, Kim C, Wenner M, Okamoto K, Wagoner H, Chung K (2007) Formability and springback evaluation of friction stir welded automotive sheets. In: *TMS annual meeting*, pp 155–164
84. Sato YS, Sugiura Y, Shoji Y, Park SHC, Kokawa H, Ikeda K (2004) Post-weld formability of friction stir welded Al alloy 5052. *Mater Sci Eng A* 369(1–2):138–143
85. Miles MP, Pew J, Nelson TW, Li M (2005) Formability of friction stir welded dual phase steel sheets. In: *Friction stir welding and processing III—proceedings of a symposium sponsored by the shaping and forming committee of (MPMD) of the minerals, metals and materials society, TMS*, pp 91–96
86. Miles MP, Melton DW, Nelson TW (2005) “Formability of friction-stir-welded dissimilar-aluminum-alloy sheets. *Metall Mater Trans A Phys Metall Mater Sci* 36(12):3335–3342
87. Buffa G, Fratini L, Hua J, Shivpuri R (2006) Friction stir welding of tailored blanks: investigation on process feasibility. *CIRP Ann Manuf Technol* 55(1):279–282
88. Miles M, Pew J, Nelson TW, Li M (2006) Comparison of formability of friction stir welded and laser welded dual phase 590 steel sheets. *Sci Technol Weld Join* 11(4):384–388
89. Sato YS, Sugiura Y, Shoji Y, Park SHC, Kokawa H, Ikeda K (2006) Effect of microstructure on fracture limit strain of pseudo-plane strain deformation in friction stir welded Al alloy 5052. *Keikinzoku Yosetsu/Journal Light Met Weld Constr* 44(5):15–22
90. Buffa G, Fratini L, Merklein M, Staud D (2007) Investigations on the mechanical properties and formability of friction stir welded tailored blanks. *Key Eng Mater* 344:143–150

91. Ramulu PJ, Narayanan RG, Kailas SV (2013) Forming limit investigation of friction stir welded sheets: influence of shoulder diameter and plunge depth. *Int J Adv Manuf Technol* 69 (9–12):2757–2772
92. Kesharwani RK, Panda SK, Pal SK (2014) Experimental investigations on formability of aluminum tailor friction stir welded blanks in deep drawing process. *J Mater Eng Perform* 24 (18):1038–1049
93. Bhanodaya Kiran Babu N, Davidson MJ, Neelakanteswara Rao A, Balasubramanian K, Govindaraju M (2014) Effect of differential heat treatment on the formability of aluminium tailor welded blanks. *Mater Des* 55:35–42
94. Yuan SJ, Hu ZL, Wang XS (2012) Evaluation of formability and material characteristics of aluminum alloy friction stir welded tube produced by a novel process. *Mater Sci Eng A* 543:210–216
95. Silva MB, Skjoedt M, Vilaça P, Bay N, Martins PAF (2009) Single point incremental forming of tailored blanks produced by friction stir welding. *J Mater Process Technol* 209 (2):811–820
96. Schmidt H, Hattel J, Wert J (2004) An analytical model for the heat generation in friction stir welding. *Modell Simul Mater Sci Eng* 12(1):143–157
97. Heurtier P, Jones MJ, Desrayaud C, Driver JH, Montheillet F, Allehaux D (2006) Mechanical and thermal modelling of friction stir welding. *J Mater Process Technol* 171(3):348–357
98. Song M, Kovacevic R (2003) Thermal modeling of friction stir welding in a moving coordinate system and its validation. *Int J Mach Tools Manuf* 43(6):605–615
99. Song M, Kovacevic R (2004) Heat transfer modelling for both workpiece and tool in the friction stir welding process: a coupled model. *Proc Inst Mech Eng Part B J Eng Manuf* 218 (1):17–33
100. Khandkar MZH, Khan J, Reynolds AP (2003) Prediction of temperature distribution and thermal history during friction stir welding: input torque based model. *Sci Technol Weld Join* 8(3):165–174
101. Arora A, Nandan R, Reynolds AP, DebRoy T (2009) Torque, power requirement and stir zone geometry in friction stir welding through modeling and experiments. *Scripta Mater* 60 (1):13–16
102. Reddy JN (1993) An introduction to the finite element method, 2nd edn. McGraw-Hill Inc., New York
103. Bathe KJ (1996) Finite element procedures. Prentice Hall, Englewood Cliffs
104. Zienkiewicz OC, Taylor RL (2000) The finite element method, 5th edn. Butterworth-Heinemann, Oxford
105. Belytschko T, Liu WK, Moran B (2000) Nonlinear finite elements for continua and structures. Wiley, New York
106. Buffa G, Hua J, Shivpuri R, Fratini L (2006) A continuum based fem model for friction stir welding—model development. *Mater Sci Eng A* 419(1–2):389–396
107. Fratini L, Buffa G, Palmeri D, Hua J, Shivpuri R (2006) Material flow in FSW of AA7075–T6 butt joints: numerical simulations and experimental verifications. *Sci Technol Weld Join* 11(4):412–421
108. Zhang Z, Zhang HW (2008) A fully coupled thermo-mechanical model of friction stir welding. *Int J Adv Manuf Technol* 37(3–4):279–293
109. Zhang Z, Zhang HW (2009) Numerical studies on controlling of process parameters in friction stir welding. *J Mater Process Technol* 209(1):241–270
110. Mandal S, Rice J, Elmustafa AA (2008) Experimental and numerical investigation of the plunge stage in friction stir welding. *J Mater Process Technol* 203(1–3):411–419
111. Alfaro I, Racineux G, Poitou A, Cueto E, Chinesta F (2009) Numerical simulation of friction stir welding by natural element methods. *Int J Mater Form* 2(4):225–234
112. Assidi M, Fourment L, Guerdoux S, Nelson T (2010) Friction model for friction stir welding process simulation: calibrations from welding experiments. *Int J Mach Tools Manuf* 50 (2):143–155

113. Ammouri AH, Hamade RF (2014) Correlating process parameters to thrust forces and torque in the friction stir processing of AZ31B. In: Proceedings of NAMRI/SME, 42
114. Pashazadeh H, Masoumi A, Teimournezhad J (2013) A study on material flow pattern in friction stir welding using finite element method. *Proc Inst Mech Eng Part B J Eng Manuf* 227(10):1453–1466
115. Uyyuru RK, Kailas SV (2006) Numerical analysis of friction stir welding process. *J Mater Eng Perform* 15(5):505–518
116. Colegrove PA, Shercliff HR (2005) 3-Dimensional CFD modelling of flow round a threaded friction stir welding tool profile. *J Mater Process Technol* 169(2):320–327
117. Chen G, Shi Q, Li Y, Sun Y, Dai Q, Jia J, Wu J (2013) Computational fluid dynamics studies on heat generation during friction stir welding of aluminum alloy. *Comput Mater Sci* 79: 540–546
118. Chen GQ, Shi QY, Fujiya Y, Horie T (2014) Simulation of metal flow during friction stir welding based on the model of interactive force between tool and material. *J Mater Eng Perform* 23(4):1321–1328
119. Ji SD, Shi QY, Zhang LG, Zou AL, Gao SS, Zan LV (2012) Numerical simulation of material flow behavior of friction stir welding influenced by rotational tool geometry. *Comput Mater Sci* 63:218–226
120. Kim D, Badarinarayan H, Kim JH, Kim C, Okamoto K, Wagoner RH, Chung K (2010) Numerical simulation of friction stir butt welding process for AA5083-H18 sheets. *Eur J Mech, A/Solids* 29(2):204–215
121. Nandan R, Roy GG, Lienert TJ, Debroy T (2007) Three-dimensional heat and material flow during friction stir welding of mild steel. *Acta Mater* 55(3):883–895
122. Kuykendall K, Nelson T, Sorensen C (2013) On the selection of constitutive laws used in modeling friction stir welding. *Int J Mach Tools Manuf* 74:74–85
123. Deform manual, SFTC, version 10.2
124. Kobayashi S, Altan T (1989) Metal forming and finite element method. Oxford University Press, New York

Chapter 7

Innovative Joining Technologies Based on Tube Forming

L.M. Alves, C.M.A. Silva and P.A.F. Martins

Abstract This chapter is focused on innovative and environmental friendly joining technologies for connecting tubes and fixing tubes to sheets in situations where the axis of the branch tube or sheet is perpendicular or inclined to the axis of the main body tube. In case of connecting tubes, the chapter will also cover the challenge of joining two tubes by their ends. The proposed joining technologies are based on the utilization of plastic instability waves in thin-walled tubes subjected to axial compression and may be seen as an alternative to conventional joining based on mechanical fixing with fasteners, welding and structural adhesive bonding. Besides allowing connecting dissimilar materials (e.g. metals and polymers) and being successfully employed in fixture conditions that are difficult and costly to achieve by means of conventional joining the new proposed technologies also cope with the growing concerns on the demand, lifecycle and recycling of materials.

7.1 Introduction

Conventional technologies for connecting tubes are widely utilized in lightweight structures made from tubular trusses, plumbing, air conditioner, refrigeration, supply lines and pipelines to convey fluids from one location to another. The most well-known technologies are based on commercially available tee fittings, saddle adapters and weld-o-lets for standard geometries and materials, such as carbon steel, stainless steel and copper (Fig. 7.1a–c). A standard tee fitting (Fig. 7.1a) has three welds; two in the main tube and one in the branch tube. Saddle adapters or

L.M. Alves · C.M.A. Silva · P.A.F. Martins (✉)
Instituto Superior Técnico, Universidade de Lisboa, Av. Rovisco Pais,
1049-001 Lisbon, Portugal
e-mail: pmartins@tecnico.ulisboa.pt

L.M. Alves
e-mail: luisalves@tecnico.ulisboa.pt

C.M.A. Silva
e-mail: alves.silva@tecnico.ulisboa.pt

© Springer International Publishing Switzerland 2015
J.P. Davim (ed.), *Modern Manufacturing Engineering*, Materials Forming,
Machining and Tribology, DOI 10.1007/978-3-319-20152-8_7

231

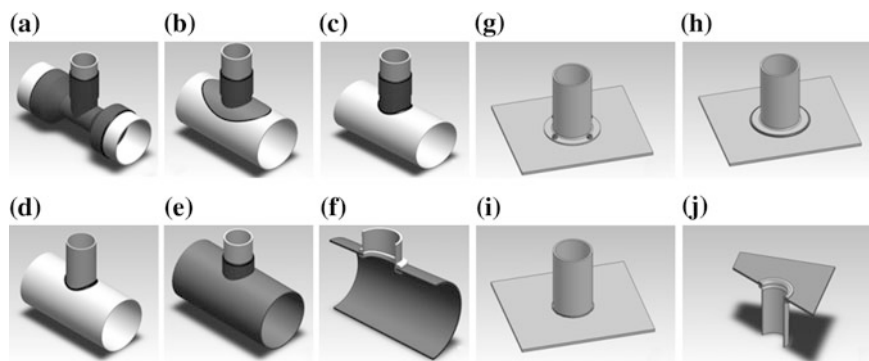


Fig. 7.1 Conventional and new technologies for connecting tubes and fixing tubes to sheets

weld-o-lets (Fig. 7.1b, c) also need to be brazed or welded to the main tube over a pre-cut hole and the attachment to the branch tube is made through a weld or a threaded connection.

Custom-based solutions are mainly based on nozzle-weld and spin-forming (Fig. 7.1d, e). Nozzle-weld connections (Fig. 7.1d) require cutting a hole in the main tube, shaping a contoured end in the branch tube to match the diameter of the main tube and welding along the contour. Spin-forming (Fig. 7.1e) also requires cutting a hole in the main tube but the difference is that material around the hole is subsequently shaped into a tee fitting where the branch tube will be brazed or welded.

In case of fixing tubes to sheets, the most widespread technologies are based on the utilization of mechanical fixing with fasteners (nuts and bolts or rivets), welding and structural adhesive bonding (Fig. 7.1g–i).

No matter the application and the differences between the technologies that are currently available for connecting tubes and fixing tubes to sheets, their universe of applicability is always limited by aesthetic, physical, chemical and mechanical requirements.

The utilization of mechanical fasteners usually suffers from unwanted aesthetic features, corrosion problems, or functional difficulties related to the maximum effort that nuts, bolts and rivets can support safely. Welding has similar problems to those mentioned for mechanical fasteners plus specific difficulties in dimensional accuracy and quality related to the heat-cooling cycles, in the weldability of dissimilar materials (e.g. joining steel or aluminium tubes to aluminium or copper sheets), in the production of undesirable fumes and smokes in fabrication, and also in expensive and time-consuming issues related to quality inspection of the welds. Structural adhesive bonding offers engineers the possibility of joining different types of materials while improving aesthetics by avoiding rivets and bolt heads. However, adhesives require careful preparation of the surfaces where they are to be applied and may experience significant decrease in performance over time and in the presence of hostile environmental conditions (e.g. prolonged expose in moist environments).

Table 7.1 Summary of the main features of joining by forming and by welding

	Joining by forming	Joining by welding
Mechanism	Plastic deformation	Melting with addition of filler materials
Shape of the connections	Arbitrary geometries	Limited to butt, lap, corner and edge joints
Operating temperature	Ambient	Melting point
Heat-affected zones	No	Yes
Shielding gases	No	Yes
Materials	Metals and polymers	Metals (similar)
Coated materials	Possible	Very difficult or impossible
Energy consumption	Less	More
Productivity	More	Less
Cost	Less	More
Environmental friendliness	More	Less

Recent developments in joining by forming that are comprehensively systematized in state-of-the-art reviews by Mori et al. [1] and Groche et al. [2] allow concluding the plastic deformation offers great potential to connect tubes and fix tubes to sheets while combining the growing demands for high productivity, low fabrication costs and environmental friendliness with high performance and material versatility. Table 7.1 summarizes the main differences between joining by forming and by welding.

This chapter presents new cost competitive and environmental friendly joining technologies that make use of axisymmetric or asymmetric plastic instability waves in thin-walled tubes subjected to axial compression for connecting tubes and fixing tubes to sheet panels at room temperature. Figure 7.1f, j presents glimpses of the new proposed technologies in case the axis of the branch tube or sheet is perpendicular to the axis of the main body tube.

The presentation draws from previous developments by Gonçalves et al. [3] in tube branching, by Silva et al. [4] in tube joining by their ends and by Gonçalves et al. [5] in fixing tubes to sheets, to new developments in extreme inclined, in-plane, instability waves that are produced by elastomer-assisted axial compression of tubes. Finite element modelling using an in-house computer program gives support to the presentation and several experimental parts are included to show the overall feasibility of the new proposed joining technologies.

7.2 Materials and Methods

This section of the chapter summarizes the mechanical characterization of the tube material, presents the new joining technologies for connecting tubes and fixing tubes to sheets and provides a summary of the experimental work plan that was utilized in the investigation.

7.2.1 Mechanical Characterization

The technological developments were performed on commercial S460MC (carbon steel) welded tubes with an outer radius $r_0 = 16$ mm and a wall thickness $t_0 = 1.5$ mm in the ‘as-received’ condition.

The stress–strain curve of the tube material was determined by means of tensile and stack compression tests carried out at room temperature. The tensile test specimens were machined from the supplied tube stock and the stack compression test specimens were assembled by piling up circular discs cut from the tube stock by a hole-saw.

The tests were performed at room temperature on a hydraulic testing machine (Instron SATEC 1200 kN) with a cross-head speed equal to 100 mm/min (1.7 mm/s) and the resulting stress–strain curve was approximated by the following Ludwik–Hollomon’s equation,

$$\sigma = 616 \varepsilon^{0.06} (\text{MPa}) \quad (7.1)$$

The effects of temperature, strain rate and anisotropy were neglected.

The onset of local plastic instability was characterized by compressing tubular specimens with 77.5 and 100 mm initial length between flat parallel compression platens. The experimental value of the critical load P_{cr} that is needed for triggering plastic instability waves (or wrinkles) along the tubes was determined experimentally as $P_{cr} = 93.5$ kN to compare with later finite element and experimental modelling of the new proposed joining technologies.

Further information on the methods and procedures that were utilized to obtain the stress–strain curve and the critical instability load at the onset of plastic instability are available elsewhere [6].

7.2.2 The Experimental Workplan

The new proposed technologies for connecting tubes and fixing tubes to sheets are schematically shown in Fig. 7.2. In case of tube branching (Fig. 7.2a) the left and middle schematic drawings show the upper and lower dies that are needed to develop and propagate inclined, out-of-plane, instability waves between contoured dies at the open and closed positions. The rightmost schematic drawing shows an application of this concept for producing inclined tube joints. The sectional views show the active tool components consisting of upper and lower contoured dies and internal mandrels (if present). The internal diameter of the dies is dedicated to a specific outer radius r_0 of the main body tube. The radius R_d of the parting out-of-plane surface of the dies together with its inclination α to the axis of the main body tube are dedicated to a specific instability wave or, in case of tube joining, to a specific radius of the branch tube. The difference between the radius R_{d+2t_0} and R_d of the upper and lower parting surfaces is crucial to accommodate the plastic

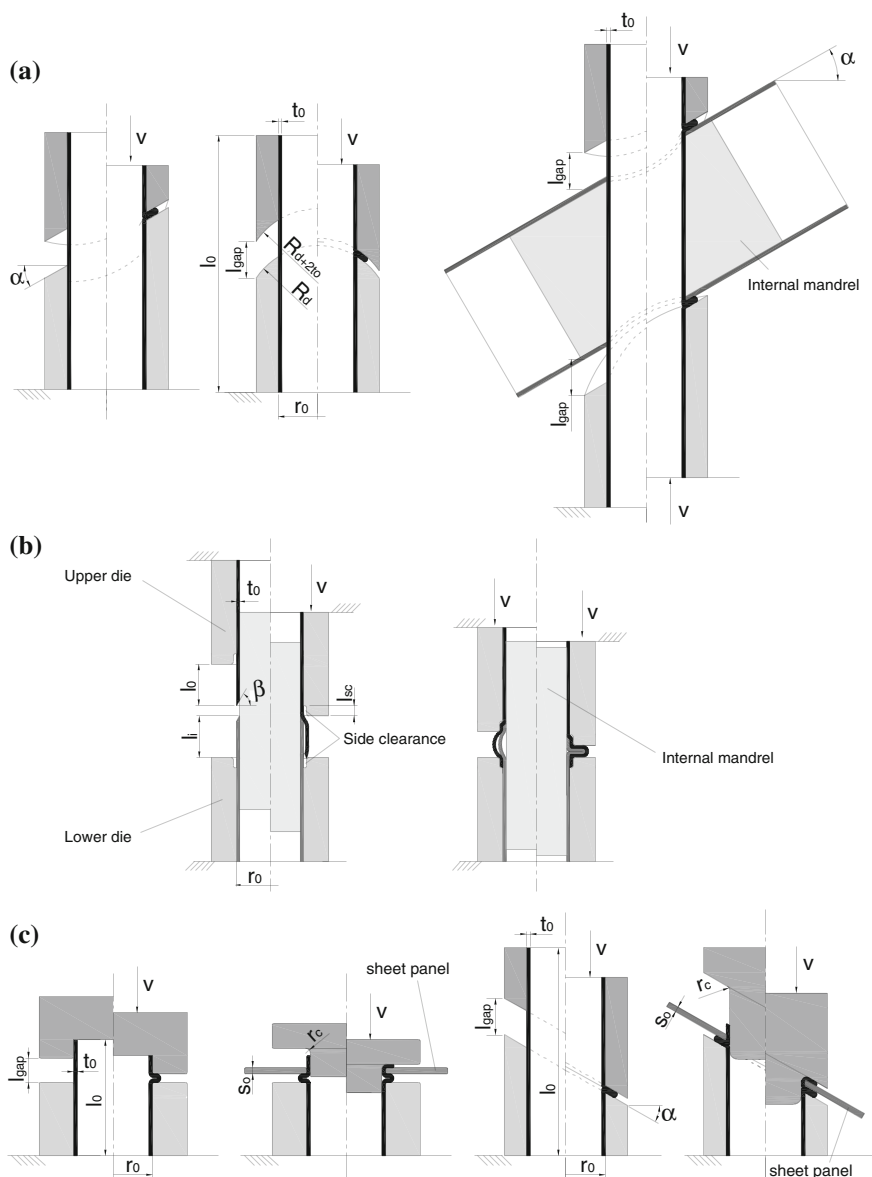


Fig. 7.2 **a** Sectional schematic views of the tool setup to develop and propagate inclined, out-of-plane, instability waves in tubes and to produce inclined tube joints. **b** Sectional schematic views of the tool setup to develop and propagate simultaneous, in-plane, instability waves in tubes to produce end-to-end joints. **c** Sectional schematic views of the tool setup to develop and propagate inclined, in-plane, instability waves to fix tubes to sheets

compression bead at the end of stroke. The initial gap opening l_{gap} between the upper and the lower contoured dies controls triggering and propagation of the plastic instability waves namely, the number and the width of the compression beads along the axis of the main tube.

In case of joining tubes by their ends (Fig. 7.2b), the left and right schematic drawings show the upper and lower dies that are needed to develop and propagate simultaneous, in-plane, instability waves between contoured dies at the initial, intermediate and final clamped positions. The upper tube starts being forced against the chamfered end of the lower tube in order to expand and produce a significant overlap between the adjacent counterfacing surfaces of the two tubes to be joined. During this stage, the chamfered end of the lower tube acts like a tapered punch and the depth of insertion is controlled by the side clearance available in the lower die. Later, the simultaneous development and propagation of in-plane plastic instability waves in both tubes will lead to a compression bead that will lock the adjacent counterfacing surfaces of the mating tubes. The internal mandrel ensures compression beads to be formed exclusively outward and guarantees design specifications of the inner diameter of the tube joint to be met.

Figure 7.2c shows two different setups utilized for fixing tubes to sheets that make use of axisymmetric (leftmost setup) or asymmetric (rightmost setup), in-plane, plastic instability waves to produce compression beads and axisymmetric or asymmetric tube end flarings. The plastic instability waves are produced by means of appropriate flat or contoured dies, whereas flaring is accomplished by compressing the upper tube end with an appropriate radiused punch in order to expand material outwards and form a single-lap inclined flange.

In view of the overall investigation carried out by the authors, the main operating parameters that were considered relevant to the new proposed joining technologies are: (i) the slenderness ratio l_{gap}/r_0 between the initial gap opening and the outer radius of the tube (please notice that $l_{\text{gap}} \cong l_0 + l_i + 2l_{\text{sc}}$ in case of joining tubes by their ends), (ii) the ratio t_0/r_0 between the wall thickness and the outer radius of the tube, (iii) the mandrel (if present) and (iv) the tribological conditions. Other relevant operating parameters that are technology dependent (e.g. they may not exist in all cases) are: (i) the inclination angle α of the contoured dies, (ii) the radius r_c of the flaring punch, (iii) the angle β of the tube end chamfers and (iii) the depth of the side clearance l_{sc} that controls the insertion of the tubes in the lower and upper dies.

The experimental apparatuses corresponding to the different joining technologies shown in Fig. 7.2 were installed in the hydraulic testing machine (Instron SATEC 1200 kN) where the mechanical characterization of the tubes had previously been performed. The experiments were carried out at room temperature with a cross-head speed equal to that utilized in the mechanical characterization of the tube material with the purpose of identifying the modes of deformation and setting up the process feasibility window of the new joining technologies as a function of a selected number of operating parameters. By keeping the remaining parameters at a constant value, it was possible to reduce the total number of variables that influence the process window and, therefore, to avoid a large number of possible combinations.

7.3 Finite Element Modelling

Because the development of the new joining technologies for connecting tubes and fixing tubes to sheets was performed under a quasi-static constant displacement rate of the upper-table of the hydraulic testing machine, no inertial effects on plastic deformation are likely to occur and therefore no dynamic effects in the joining process are needed to be considered. These operating conditions allowed numerical modelling to be performed with the finite element flow formulation and enabled the authors to utilize the in-house computer program I-form that has been extensively validated against experimental measurements of metal forming processes since the end of the 1980s [7].

The finite element flow formulation giving support to I-form is built upon the following extended variational statement that accounts contact and friction between different rigid and deformable objects:

$$\begin{aligned} \Pi = & \int_V \bar{\sigma} \dot{\varepsilon} dV + \frac{1}{2} K \int_V \dot{\varepsilon}_V^2 dV - \int_{S_T} T_i u_i dS + \int_{S_f} \left(\int_0^{|u_r|} \tau_f du_r \right) dS \\ & + \frac{1}{2} P \sum_{c=1}^{N_c} (g_n^c)^2 + \frac{1}{2} \mu P \sum_{c=1}^{N_c} (g_t^c)^2 \end{aligned} \quad (7.2)$$

where $\bar{\sigma}$ denotes the effective stress, $\dot{\varepsilon}$ is the effective strain rate, $\dot{\varepsilon}_V$ is the volumetric strain rate, K is a large positive constant imposing the incompressibility of volume V , T_i and u_i are the surface tractions and velocities on surface S_T , τ_f and u_r are the friction shear stress and the relative velocity on the contact interface S_f between workpiece and tooling.

The last two terms in Eq. (7.2) account for a node-to-segment-based contact algorithm between the counterfacing surfaces of the workpieces to be joint by penalizing normal gap velocity g_n^c , when otherwise leading to penetration, and by constraining tangential gap velocity g_t^c to account for frictional effects. Gap velocities in each of the N_c contact pairs are defined as,

$$\begin{aligned} g_n^c &= \mathbf{v}_p \cdot \mathbf{n} - \beta \mathbf{v}_1 \cdot \mathbf{n} - (1 - \beta) \mathbf{v}_2 \cdot \mathbf{n} \\ g_t^c &= \mathbf{v}_p \cdot \mathbf{t} - \beta \mathbf{v}_1 \cdot \mathbf{t} - (1 - \beta) \mathbf{v}_2 \cdot \mathbf{t} \end{aligned} \quad (7.3)$$

where nodal velocities \mathbf{v}_p , \mathbf{v}_1 and \mathbf{v}_2 are illustrated in Fig. 7.3, which schematically shows a contact pair consisting of a contacting nodal point N_p and the nodal points of the opposing line segment N_1 and N_2 of an element of the counterfacing tube or sheet surfaces.

Figure 7.3 also identifies the normal and tangential versors \mathbf{n} and \mathbf{t} . The projection point of the contacting node on the opposing line segment, which is calculated based on the relative nodal velocities, is identified by the dimensionless parameter β (Fig. 7.3a). Natural symmetry is obtained because nodes of the counterfacing element face can be contacting nodes in other contact pairs. The penalization of the normal gap velocity is ensured through a large positive number

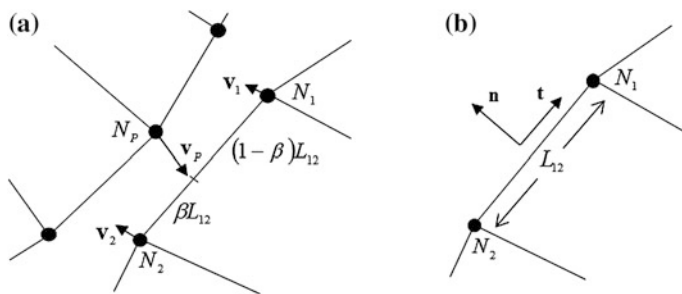


Fig. 7.3 Sectional representation of the contact between two adjacent surfaces and associated notation. **a** Boundary node N_P contacting line segment $N_1 - N_2$ due to nodal velocities \mathbf{v}_P , \mathbf{v}_1 and \mathbf{v}_2 (The dimensionless parameter β defines the projection point of the contacting node on the line segment). **b** Identification of line segment length L_{12} and versors \mathbf{t} and \mathbf{n} defining tangential and normal directions in the contact pair

P while the constraining of the tangential gap velocity takes place through penalization by μP . By doing this, the ratio of the tangential and the normal penalties is equal to μ , which is used for calibration of the frictional effects between the tubes in analogy to Amonton–Coulomb friction. Further information on the finite element flow formulation, on the node-to-segment contact algorithm and on the computer program I-form, can be found elsewhere [8].

The numerical simulation of the new proposed joining technologies was carried out in both two- and three-dimensional modelling conditions in order to replicate the axisymmetric or the asymmetric material flow conditions of each specific joint.

Figure 7.4, for example, shows the numerically predicted development and propagation of an inclined, out-of-plane instability wave in a tube, which may be used to produce inclined tube joints. The model of the tube consists of roughly 7500 eight-node hexahedral elements and 10,500 nodal points, whereas the models of the dies and of the internal mandrel were built upon discretization by means of contact-friction spatial linear triangular elements. No anisotropy effects due to material or welding seam were taken into account.

The overall numerical model requires less than 1 h of CPU time to be successfully solved in a standard laptop computer equipped with an Intel i7 CPU (2.7 GHz) processor and making use of two cores. The photograph of the real test specimen included in the figure allows concluding on the overall quality of the finite element predicted geometry.

7.4 Results and Discussion

This section of the chapter discusses the application of the new proposed joining technologies for connecting tubes in situations where the axis of the branch tube or sheet is inclined (perpendicular position is considered a special case) to the axis of the main body and for connecting two tubes by their ends.

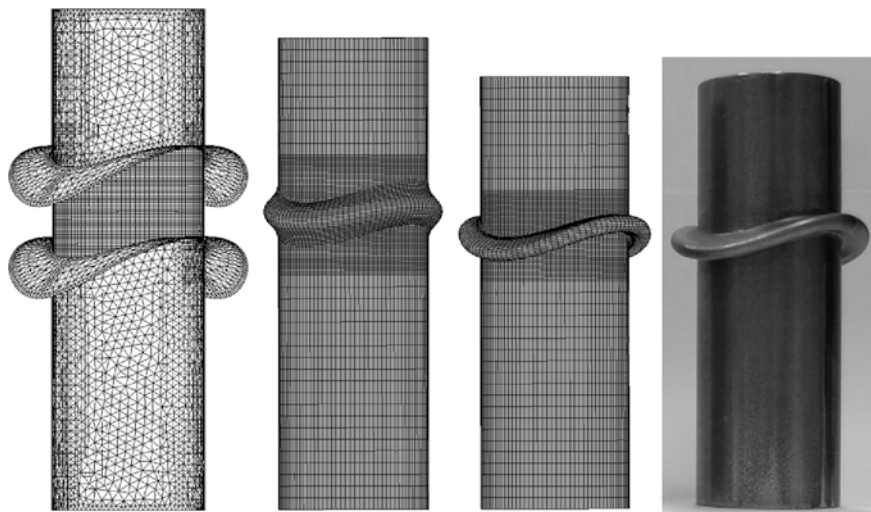


Fig. 7.4 Finite element model utilized in the numerical simulation of the development and propagation of inclined, out-of-plane instability waves in tubes with a photograph of a test sample corresponding to the *rightmost* numerically predicted geometry

7.4.1 Inclined Connections of Tubes

The tube forming technology to produce inclined tube attachments is based upon the development and propagation of sound plastic instability waves in tubes subjected to axial compression between out-of-plane contoured die surfaces. The numerical and experimental investigation that were carried out for different testing conditions revealed the existence of three different modes of deformation, which are dependent upon the combined influence of the slenderness ratio l_{gap}/r_0 and the inclination angle α of the contoured dies (refer to Fig. 7.5 and afterwards to Table 7.2).

The modes of deformation are easily understood through analysis of the finite element predicted geometries that are included in Fig. 7.5. As seen in Fig. 7.5b, there exists a threshold of the slenderness ratio (say, $l_{\text{gap}}/r_0 = 0.31$) below which no plastic instability waves are likely to develop. The tubes will increase thickness uniformly instead of developing asymmetric compression beads. This mode of deformation (hereafter referred to as ‘mode 1’) is not appropriate for producing inclined tube attachments and always takes place when there is limited unsupported free length of the tube between the upper and lower dies.

On the contrary, when the slenderness ratio is large (say, $l_{\text{gap}}/r_0 = 1.56$) there is always the risk of getting multiple plastic instability waves that will collide with each other. This mode of deformation (hereafter referred to as ‘mode 3’) can be observed and understood from the computed evolution of the finite element mesh at the middle and end of stroke (refer to Fig. 7.5e, f). In fact, when the unsupported

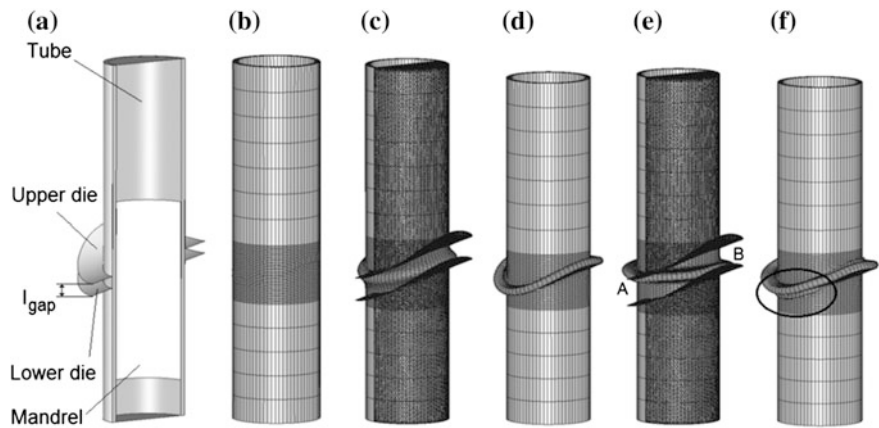


Fig. 7.5 Numerical modelling of the development and propagation of inclined, out-of-plane, instability waves in tubes subjected to axial compression with contoured dies ($\alpha = 15^\circ$). **a** Axial cross section showing a model of the tube and active tool parts. Finite element predicted geometry for **b** mode 1 ($l_{gap}/r_0 = 0.31$), **c** mode 2 ($l_{gap}/r_0 = 0.94$) at the middle of stroke, **d** mode 2 ($l_{gap}/r_0 = 0.94$) at the end of stroke, **e** mode 3 ($l_{gap}/r_0 = 1.56$) at the middle of stroke and **f** mode 3 ($l_{gap}/r_0 = 1.56$) at the end of stroke

Table 7.2 Modes of deformation as a function of the slenderness ratio l_{gap}/r_0 and the inclination angle α of the dies

Angle α (°)	Mode				
45°	1	1	2	3	3
30°	1	2	2	2	3
15°	1	2	2	2	3
0°	1	2	2	2	3
l_{gap}/r_0	0.31	0.63	0.94	1.25	1.56
l_{gap} (mm)	5	10	15	20	25

The enclosed pictures show experimental results associated with the light and dark grey cells of the table

free length of the tube l_{gap} is very large, local buckling starts by developing naturally into an axisymmetric instability wave until it comes into contact with the upper and lower contoured dies (refer to 'A' and 'B' in Fig. 7.5e). From this moment, the instability wave is forced to bend towards the inclined contoured dies and a second wave will plow into the previous (refer to the region surrounded by a circle in Fig. 7.5f).

The above-mentioned bending effect is much less pronounced in case of 'mode 2' (Fig. 7.5c, d), which is commonly associated with the development of sound inclined, out-of-plane, plastic instability waves.

The overall agreement between finite element predicted and experimentally observed modes of deformation is good and allowed identifying the process window of inclined connections of tubes. The results are summarized in Table 7.2 and the enclosed black dashed line separates the process operating conditions that give rise to sound inclined, out-of-plane, instability waves from those that originate non-existing (mode 1) or non-admissible (mode 3) instability waves.

The pictures included in Table 7.2 help uncoupling the combined influence of the slenderness ratio l_{gap}/r_0 and the inclination angle α of the contoured dies on the resulting modes of deformation. The light grey cells, for example, show the influence of the slenderness ratio l_{gap}/r_0 on plastic flow and the corresponding experimental results presented in the uppermost picture may be successfully compared with the finite element predictions of Fig. 7.5. The dark grey cells, disclose the influence of the inclination angle α of the contoured dies on the final geometry of the asymmetric compression beads. As seen in Table 7.2, the inclination angle α of the contoured dies also plays a significant influence on the resulting modes of deformation because the development of sound plastic instability waves is greatly reduced as α increases from $\alpha = 30^\circ$ to $\alpha = 45^\circ$.

Figure 7.6 shows applications of above-mentioned out-of-plane instability waves for producing innovative and flexible inclined connections of tubes (perpendicular connections are taken as a special case corresponding to an inclination angle $\alpha = 0^\circ$) that can be easily applied to a wide range of materials with custom sizes. Figure 7.6a shows a typical tee fitting that was produced at room temperature without resort to filling materials and heat-cooling cycles due to welding or brazing.

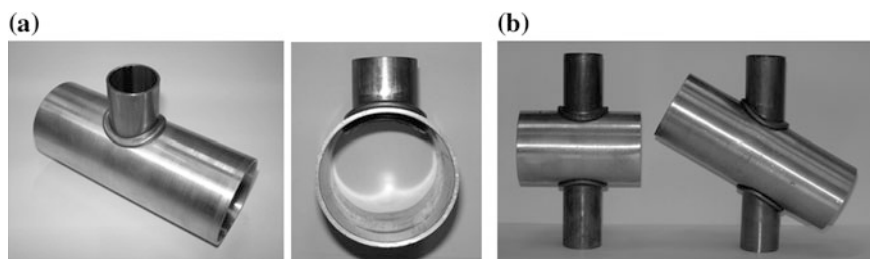


Fig. 7.6 Application of the new proposed joining technology for connecting tubes at different inclination angles

Figure 7.6b discloses the potential of the proposed joining technology to produce connection elements (nodes) of lightweight structures.

7.4.2 End-to-End Joining of Tubes

End-to-end joining of tubes is accomplished by a succession of different plastic deformation mechanisms (Fig. 7.7). First, the upper tube is forced against the lower tube in order to expand along the chamfered edge of the lower tube and match its counterfacing surface. Second, both tubes collapse simultaneously by local buckling and propagate, in-plane, instability waves after experiencing material flow restrictions at the side clearance of the upper and lower dies. Finally, a compression bead locks the tubes by their ends. The photograph included in Fig. 7.7 shows the cross section of a test specimen.

Figure 7.8 presents different experimental test samples and their corresponding finite element predicted geometries that were obtained by varying the slenderness ratio l_{gap}/r_0 . As seen, the leftmost test sample (corresponding to $l_{\text{gap}}/r_0 = 1.88$)

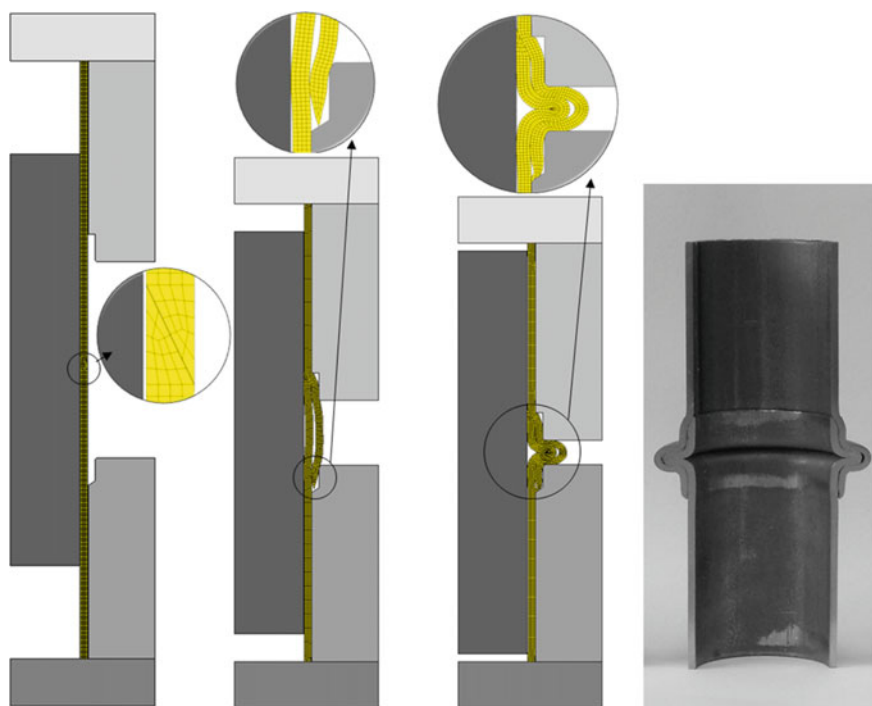


Fig. 7.7 Finite element predicted evolution of the initial, intermediate and final stages of the end-to-end joining of tubes with a photograph of a test sample



Fig. 7.8 Modes of deformation as a function of the slenderness ratio l_{gap}/r_0 when attempting to connect tubes by their ends with the new proposed technology. **a** Experimental results with cross-section details of the joints and **b** associated finite element predictions

does not ensure locking between the two tubes, whereas the rightmost test sample (corresponding to $l_{\text{gap}}/r_0 = 4.38$) presents a joint with two compressions beads instead of one.

In case of the leftmost test sample, the absence of connection is because the initial unsupported gap height l_{gap} is not big enough to allow compression beads to develop and lock with each other by plastic instability. In case of the rightmost test sample, the formation of two compression beads instead of one is due to the fact that high values of the initial unsupported gap height l_{gap} provide conditions for the development of multiple compression beads that will interfere and be placed on top of each other, as they are formed in-between the upper and lower dies.

Neither the operative conditions corresponding to the leftmost test sample nor those corresponding to the rightmost test sample are acceptable for connecting two tubes by their ends using lap joints produced by plastic deformation. The process window is therefore restricted to values of the slenderness ratio l_{gap}/r_0 in the range between 2.5 and 3.75.

7.4.3 Inclined Connections of Tubes to Sheets

Table 7.3 summarizes the modes of deformation and the process window associated with the development and propagation of inclined, in-plane, instability waves in thin-walled tubes subject to compression. As in case of out-of-plane instability waves that were discussed in Sect. 4.1 (refer also to Table 7.2), results allow uncoupling the combined influence of the slenderness ratio l_{gap}/r_0 and the inclination angle α of the dies on plastic flow.

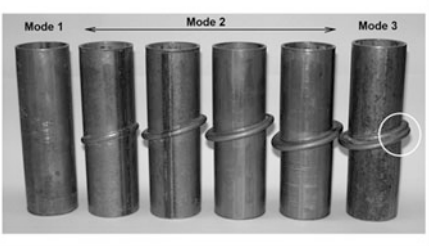
Considering, for example, the light grey cells associated with an inclination angle $\alpha = 15^\circ$ in Table 7.3, it is possible to conclude that low values of the slenderness ratio l_{gap}/r_0 will not promote collapse of the tube under local buckling. The corresponding mode of deformation (hereafter named ‘mode 1’) is not appropriate for joining sheets to tubes by plastic deformation because no compression beads can be found (refer to the leftmost specimen in the photograph included in Table 7.3). Moreover, the investigation showed that plastic flow in mode 1 gave rise to a wall thickness increase up to 16 % at the unsupported length l_{gap} of the tube and below 1 % elsewhere.

With increased values of l_{gap}/r_0 tubes gradually start developing sound inclined compression beads (‘mode 2’) that growth in diameter as the slenderness ratio increases (refer to the centre specimens in the photograph). This is the appropriate mode of deformation for producing inclined connections of tubes to sheets by plastic deformation. For larger values of l_{gap}/r_0 the development of inclined compression beads leads to the development of multiple instability waves interfering, destructively, with each other as they are formed in-between the upper and lower dies (‘mode 3’). This type of plastic flow corresponds to the rightmost specimen in the photograph (refer to the region surrounded by a circle in Table 7.3).

The role played by internal mandrels in the development and propagation of inclined, in-plane, instability waves in tubes subjected to axial compression is illustrated in Fig. 7.9. As seen, instability waves resulting from compression

Table 7.3 Modes of deformation as a function of the slenderness ratio l_{gap}/r_0 and the inclination angle α of the dies

Angle α (°)	Mode					
60°	1	3	3	3	3	3
45°	1	2	2	3	3	3
30°	1	2	2	2	3	3
15°	1	2	2	2	2	3
0°	1	2	2	2	3	3
l_{gap}/r_0	0.31	0.63	0.94	1.25	1.56	1.88
l_{gap} (mm)	5	10	15	20	25	30



The enclosed pictures show deformation modes 1, 2 and 3 in tubular specimens associated with the light grey cells of the table

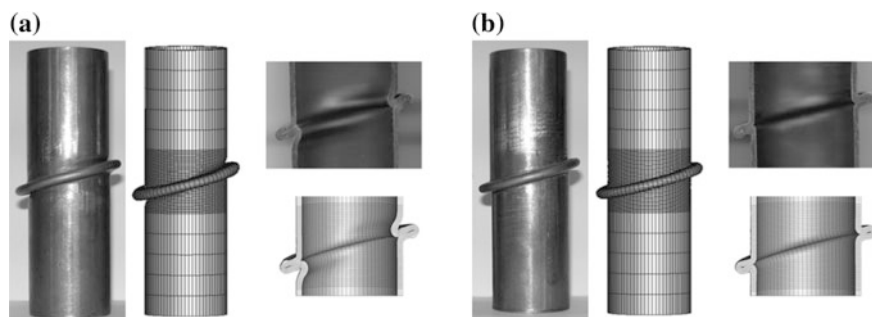


Fig. 7.9 Experimental and numerically predicted influence of the utilization of internal mandrels in the development and propagation of inclined, in-plane, instability waves in thin-walled tubes subjected to axial compression. **a** Specimen produced without internal mandrel and **b** specimen produced with internal mandrel

beading without a mandrel, exhibit both inward and outward plastic flow that lead to non-acceptable geometric unconformities along the inner and outer surfaces of the tube (refer to the leftmost axial cross section of the specimen and corresponding finite element mesh). The utilization of internal mandrels is, therefore, mandatory to ensure the overall quality and tolerances that are required for the inclined tube-sheet plastically deformed joints (refer to the rightmost results in Fig. 7.9).

In what concerns the evolution of the forming load with displacement, Fig. 7.10 shows that the forming load increases with the inclination angle α of the dies for a constant value of the slenderness ratio l_{gap}/r_0 . As seen in the figure, there is a steep increase of the load up to roughly 100 kN as the tube starts being axially compressed and the instability wave is triggered, followed by a load drop as a result of the propagation of the wave in order to match the contour of the dies. The final

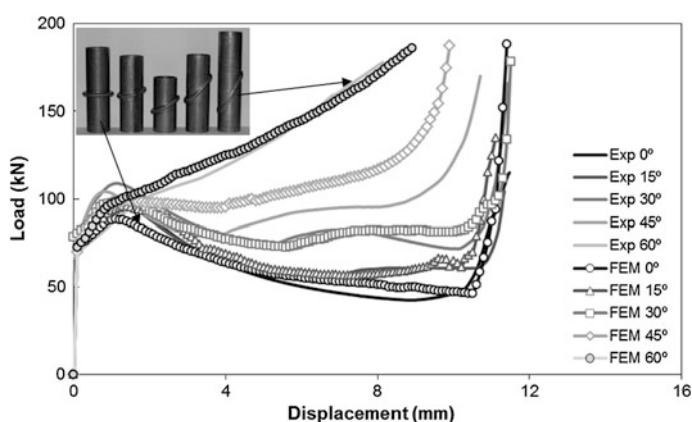


Fig. 7.10 Experimental and numerically predicted evolution of the load with displacement for the process operating conditions corresponding to the dark grey cells of Table 7.3

abrupt increase in load is caused by closure of the instability waves into a compression bead after contacting the upper and lower inclined dies. The monotonically increasing evolution of the load with displacement that is registered for the inclination angle $\alpha = 60^\circ$ is the result of difficulties in producing sound instability waves in such inclined angles.

In fact, for producing inclined, in-plane, instability waves at inclination angles $\alpha > 45^\circ$, it is necessary to employ an elastomer-assisted procedure made from a combination of tube bulging by elastomer forming and compression beading with inclined contoured dies. The process is schematically illustrated in Fig. 7.11 together with a photograph of a instability wave that was successfully produced at an inclination angle $\alpha = 60^\circ$.

To conclude, Fig. 7.12 shows applications of the above-mentioned in-plane instability for producing innovative and flexible inclined connections of tubes to sheets (perpendicular connections are taken as a special case corresponding to an inclination angle $\alpha = 0^\circ$) that can be easily applied to a wide range of materials with custom sizes.

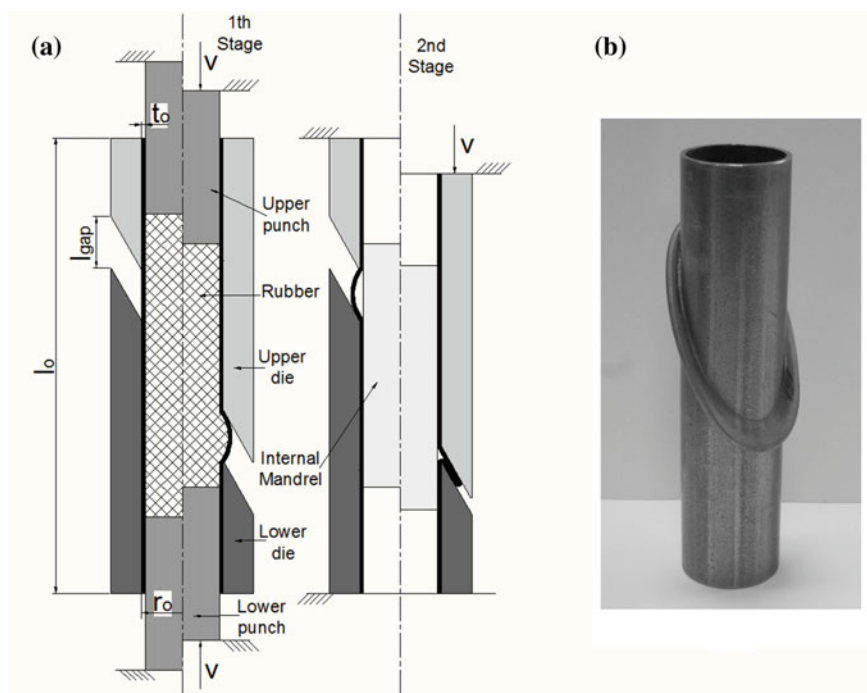


Fig. 7.11 **a** Sectional schematic view of the elastomer-assisted axial compression of tubes that is needed to produce extreme inclined, in-plane, instability waves in thin-walled tubes. **b** Photograph showing a compression bead with an inclination angle $\alpha = 60^\circ$

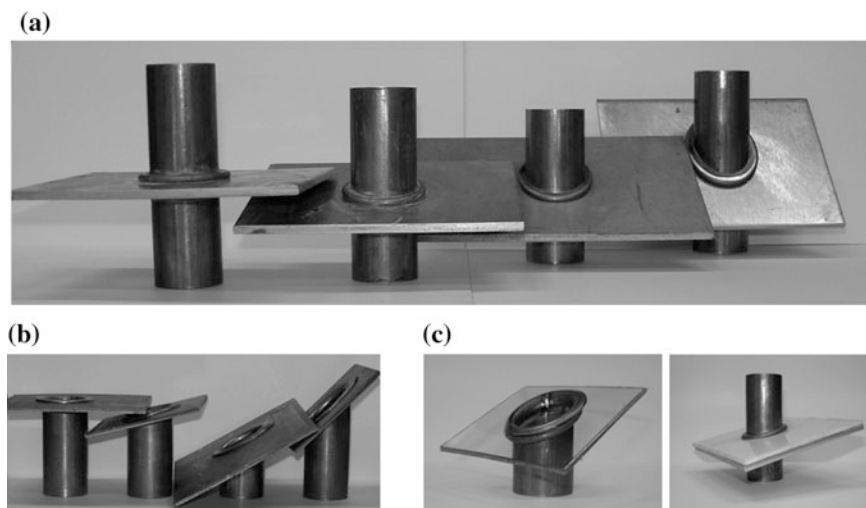


Fig. 7.12 Application of the new proposed joining technology for connecting tubes to **a**, **b** metal sheets and **c** polymer and sandwich sheets at different inclination angles

7.5 Conclusions

This chapter presented innovative and cost-effective joining technologies based on tube forming for connecting tubes and fixing tubes to sheets in situations where the axis of the branch tube or sheet is perpendicular or inclined to the axis of the main body tube. The technologies are aimed to successfully replace conventional solutions based on mechanical fixing with fasteners, welding and structural adhesive bonding, and cope with growing concerns on the demand, lifecycle and recycling of materials.

The technologies are based on the development and propagation of axisymmetric or asymmetric plastic instability waves in thin-walled tubes subjected to axial compression and may be successfully applied to connect dissimilar materials (e.g. polymers and metals). In case of extreme fixing conditions $\alpha > 45^\circ$, the elastomer-assisted joining technology made from a combination of tube bulging by elastomer forming and compression beading is required.

The chapter identifies the process operating conditions for each specific technology in terms of the slenderness ratio l_{gap}/r_0 between the initial gap opening and the outer radius of the tube, and of the inclination angle α of the contoured dies (if available). The utilization of internal mandrels was also found to be mandatory for preventing defects and ensuring good quality joints.

Results from finite element analysis help understanding the typical modes of deformation and conceptual applications included in the paper which illustrate the potential of the new proposed joining technologies to develop new industrial products.

Acknowledgments The authors would also like to acknowledge the support provided by MCG-Mind for Metal, Carregado, Portugal.

References

1. Mori KI, Bay N, Fratini L, Micari F, Tekkaya AE (2013) Joining by plastic deformation. *CIRP Ann Manuf Technol* 62:673–694
2. Groche P, Wohletz S, Brenneis M, Pabst C, Resch F (2014) Joining by forming: a review on joint mechanisms, applications and future trends. *J Mater Process Technol* 214:1972–1994
3. Gonçalves A, Alves LM, Martins PAF (2014) Tube joining by asymmetric plastic instability. *J Mater Process Technol* 214:132–140
4. Silva CMA, Nielsen CV, Alves LM, Martins PAF (2015) Environmentally friendly joining of tubes by their ends. *J Clean Prod* 87:777–786
5. Gonçalves A, Alves LM, Martins PAF (2014) Inclined tube-sheet plastically deformed joints. *Steel Res Int* 85:67–75
6. Alves LM, Martins PAF (2012) Tube branching by means of asymmetric compression beading. *J Mater Process Technol* 212:1200–1208
7. Alves ML, Rodrigues JMC, Martins PAF (2004) Three-dimensional modelling of forging processes by the finite element flow formulation. *J Eng Manuf* 218:1695–1707
8. Nielsen CV, Zhang W, Alves LM, Bay N, Martins PAF (2013) Modeling of thermo-electro-mechanical manufacturing processes with applications in metal forming and resistance welding. Springer, London

Chapter 8

Lean Manufacturing

Ali Hosseini, Hossam A. Kishawy and Hussein M. Hussein

Abstract Manufacturing of parts and products regardless of their shape, geometric features and materials involves a series of processes and operations. Nowadays, it is broadly recognized through the industrial sectors that many manufacturing techniques which are currently implemented in fabricating products lead to production of industrial waste. Lean manufacturing (LM) is a business template that has philosophies designed to eliminate waste in the manufacturing process. The Lean philosophies target activities that absorb resources but create no value and aim to eliminate them. This chapter describes the lean manufacturing as a fairly new concept in industry. The origin and historical background of lean manufacturing as well as the different sources of waste in manufacturing systems are thoroughly explained. In addition, different methods of preventing or eliminating wastes are also discussed. By reviewing a broad range of available academic resources, this chapter mainly aims to provide a strong and thorough understanding of lean manufacturing and its importance in the modern industry.

8.1 Introduction

Lean manufacturing is a fairly new concept in modern manufacturing that is gradually restructuring the way industries in the world view production. In the other word, it is a revolutionized manufacturing philosophy compared to the traditional

A. Hosseini (✉) · H.A. Kishawy
Machining Research Laboratory (MRL), Faculty of Engineering and Applied Science,
University of Ontario Institute of Technology (UOIT), Oshawa, ON L1H 7K4, Canada
e-mail: sayyedali.hosseini@uoit.ca

H.A. Kishawy
e-mail: hossam.kishawy@uoit.ca

H.M. Hussein
Advanced Manufacturing Institute, King Saud University, Riyadh, Saudi Arabia
e-mail: hhusein@ksu.edu.sa

© Springer International Publishing Switzerland 2015
J.P. Davim (ed.), *Modern Manufacturing Engineering*, Materials Forming,
Machining and Tribology, DOI 10.1007/978-3-319-20152-8_8

249

mass production standard that has been used for nearly a century. However, the concept of lean manufacturing is not new and the origins of this philosophy may be traced to Japan in the late 1940s [1], when a few top engineers at a then struggling Toyota Motor Company rethought the way manufacturing was being done out of necessity to survive in the marketplace [2].

Traditionally known as the Toyota Production System, and also being labelled as Just-In-Time (JIT) Manufacturing, Pull Manufacturing, and Total Quality Management (TQM) [3], lean manufacturing is primarily intended to eliminate waste, improve system capability, reduce flow time, decrease inventories, satisfy customers, eliminate bottlenecks, and finally enhance communications [3]. All of these features contribute to increasing a manufacturer's product quality while decreasing production costs [1]. To understand how the above-mentioned objectives can be accomplished, one must first comprehend how the necessity for such a system was realized. It is important to note that much of the history of production systems is based on automobile history. Since the inception of the automobile, most significant advances in production of all types has initiated in automotive industry before being adopted into other business sectors.

Industry first began to use machines in the 1860s for the purpose of weaving cloth [4]. Due to primitive designs and materials, these machines did not reduce the labour intensive nature of the textile industry and for almost 60 years the use of machines and the production environment was stuck in craft production [1]. A manufacturing operation that is performed mostly by hand with or without using any kind of machine or tool is usually called craft production. In the other word, craft production is a method of production in which highly skilled workers use their hands or implement simple but flexible tools and machines to create a product based on the customer desires [1]. Products are built one at a time, hence despite high possible variety, the production quantity is low and consequently the product cost is high. The first automobiles, built by Panhard and Levassor (P&L) in the 1880s and 1890s [1], were manufactured using this method of production. Using the craft production method, many of the components are manufactured outside of the assembling company. At that time, there was no standardized method of measurement; moreover, tools and machines capable of cutting and forming pre-hardened steel had not yet been created. As a result, each part made was different from its predecessor and successor regardless of being created from the same blueprint design [1].

In 1908, Henry Ford completed his design of the Ford Model T car [5]. The design of this vehicle was a combination of 5 years and 20 different renditions in which Ford worked to accomplish two goals [1]. Ford's first goal was to build an automobile that was easy to manufacture, and the second goal was building an automobile that was user-friendly [1]. Prior to the Model T, automobile owners were limited to the wealthy individuals as operation required the expertise of a chauffeur, repair required the expertise of a mechanic, and the general cost to own an automobile was extremely high. Ford's Model T was the first vehicle that could be driven and maintained by the common working man. It was from the basic design of the Ford Model T that mass production was born. The parts and

components of the Model T could be easily cut and stamped from pre-hardened steel using new age tools, as a result, Ford was able to first create the stationary assembly line in 1908, followed by the first moving assembly line in 1913. Ford is currently being acknowledged as the father of mass production due to his great influence to the development and growth of automotive industry as well as his valued lessons for mass production and product platforming [6], even though his contribution outspread well beyond these horizons.

Mass production is a method of production in which unskilled or semi-skilled workers assemble product that has been designed by narrowly skilled professionals with parts made by expensive and highly inflexible machinery [1, 7]. Ford's moving assembly line caught the attention of industries all around the world due to its greatly increased production volume and its ability to reduce production costs. Due to his advances in production, Ford was constantly able to reduce the price of the Model T, making it readily available to the common man.

In the early 1920s, Alfred Sloan became the President of General Motors and further perfected the art of mass production [1, 8]. By analysing the system from a market point of view, Sloan was able to effectively manage the total system of factories, engineering operations, and marketing systems in a way Ford had previously been unable. Although it is still widely used in the western civilization today, mass production reached its peak in 1955. It was at this time that the combination of Ford's and Sloan's techniques had been perfected, and as a result, more than 7 million vehicles were sold in one year for the first time in history [1]. At the same time, the methods for achieving successful mass production were well known throughout all industries around the world and as a result, competition from around the world began to increase, thus reducing the advantage western civilization had held for 30 years.

Although great for reducing production costs and increasing production volume, the mass production system had many areas of wasted energy and resources. The system created a divide in the labour force required to create a product; hence, there was little communication and little attention paid to improving the systems. The focus was on creating as much output, as fast as possible and consequently the quality of the resulting product was low. The weaknesses of mass production became a window of opportunity for a better designed manufacturing system that could meet the needs of the consumer by increasing quality, decreasing costs, and minimizing wastes. Targeting the above-mentioned goals led to introduction of lean manufacturing, a system that combines the advantages of craft production and mass production, while minimizing their disadvantages [9].

Struggling in the aftermath of the Second World War, manufacturers in Eastern countries, particularly Japan, were faced with a number of challenges that would prevent them from successfully achieving mass production as practiced in the western world. Toyota, formerly Toyoda, was a successful textile machinery company at the turn of the nineteenth century. When the war broke out in the 1930s [1], the government encouraged Toyoda to enter the motor vehicle industry and produce trucks for the military. Following the war, the Toyoda family led by Kiichiro and Eiji Toyoda were determined to enter the full-scale automobile

production industry [10]. Following a visit to the Rouge Ford Plant in the United States (at the time the largest and most efficient mass production facility) [1, 9], Eiji recognized that mass production as it was could never work in Japan, and also recognized the faults in the current westernized system. With the help of his associate production engineer Taiichi Ohno (further recognized as the father of Toyota Production System), a new system of manufacturing would evolve over a 20-year span that would prove more viable and efficient than the western mass production system.

The first problem Eiji Toyoda and Taiichi Ohno identified with the mass production system was related to the part production for the assembly lines. For automobiles, the standard method of creating steel body panels was to use hundreds of stamping lines. These lines would run upwards of 12 strokes per minute, 24 hours per day and 7 days per week to create millions of identical parts per year [1]. The stamping dies were extremely complex and difficult to change resulting in manufacturing time loss and increased costs as specialists were required to complete the transitions. Instead of trying to find improvements in the parts, and designs of the parts these stamping lines would produce, Ohno turned his attention to the stamping dies themselves. He devised an idea in which the changing of dies was simple and therefore could be completed quickly and easily, and potentially by the stamp operator as opposed to specialists [1, 11]. Ohno began to experiment with this idea in the late 1940s and within 10 years had reduced the 1-day operation of changing a die using a specialist to a 3-min operation that could be completed by the stamp operator. Through this advancement, Ohno and Toyoda unexpectedly discovered that making small batches of parts rather than large runs, as was the norm in mass production, was more cost-effective due to the eliminated need for inventory storage. Small batches also resulted in the ability to identify and correct any part issues earlier in the assembly process saving money in reworking costs.

Taiichi Ohno's improvement had created one problem not faced in the traditional mass production system. As specialists were hired to complete the difficult die replacements, the stamp operators could have no experience or skill set, and as a result workers were easy to find. Although a simplified process, by making the die transition the responsibility of the stamp operator, Ohno created the requirement for at least semi-skilled workers. Fortunately for Ohno, this problem would solve itself in the late 1940s when Toyota proposed to fire a quarter of its workforce [1, 9], resulting in a strike by the union and a resulting deal that would help to further shape the lean manufacturing methods. Following negotiations, Toyota was allowed to fire a quarter of the workforce, but on two conditions; first, the remaining employees were guaranteed employment with the company for life, and second, pay would become steeply graded based on seniority [1]. In addition, many other Japanese companies followed suit in basing pay on seniority with the company further encouraging the remaining employees to stay with Toyota [1]. Because of this deal, the workforce was no longer a variable cost to the manufacture as had previously been the case. Instead, the employee became an asset whom through proper training could earn a company greater return. An additional stipulation required the employee to be flexible in work assignments and be active in

promoting the interests of the company. Toyoda and Ohno now had the skilled and motivated workers they required for their system to continue to develop.

Through analysis of the western mass production system, Ohno was able to identify a number of aspects of 'muda', a Japanese word for waste [1, 12]. Ohno saw a main source of waste in the mass production system in the division of the labour force. He believed all of the jobs that had been separated, the assembly, the housekeeping, the problem-solving, and the supervising, could all be completed by the individuals completing the assembly process. Instead of a number of individuals with specific tasks, Ohno created teams and assigned a set of assembly steps to them. The teams were then told to work together to determine the best way to complete the assigned steps [1]. Instead of having a foreman who did nothing but observe, the teams had a team leader who was to be actively involved in completing the tasks and solving the problems that presented themselves [1]. Once the team was actively completing all roles that had been divided in the western system, Ohno had them set aside time to suggest ways to collectively improve the processes. This continuous style of improvement is known as Kaizen which is a Japanese word for "change for better" [13]. It is now often referred to as a quality circle in western processes.

Furthermore, Ohno banished the idea of pushing product with error down the line in the name of keeping production volumes up. Instead, he installed line stops at every assembly station and workers were encouraged to stop the line at the moment a problem was discovered [1]. The problem would then be rectified before the product was allowed to move down the line. Taking this one step further, Ohno insisted that any problem was not a random occurrence and instituted a process to help ensure the problem never occurred again. This process is called the 'five why' approach [1] in which the team traces every error in production back to its root cause by asking the question "Why?" as each layer of the problem is discovered. When the root cause is found, a solution is created to prevent the same problem from ever occurring again [1, 14]. The end result of these systems has continuously decreased rework at the end of the production process, and continuously increased quality levels.

In the 1950s, Toyota began to apply approaches similar to its production to its supply chain [1]. Ohno, Toyoda, and others within the company agreed that the process of selecting, making, or buying components and then acquiring these components from the manufacturer with the lowest price and defect rate was not ideal [1, 11]. The result of this process was short and unsteady relationships, lack of communication and product defects stemming from lack of information. As an alternative, Toyota divided their suppliers into tiers with the suppliers in each tier having different functions and responsibilities. Suppliers in the first tier were integral parts of the product development teams [1]. In product development, Toyota differed from the western ways again by providing the supplier with the specifications that were to be met by the new product rather than a set blueprint for how the product should be made. How the product actually functioned or was created was left up to the firm which allowed them the freedom to design the product based on expertise which they had and Toyota designers did not. Further,

because firms within a tier each specialized in a particular system and were not competitors, they were encouraged to communicate and share ideas [1]. Second-tier suppliers were the suppliers of the components for the systems designed by the first tier suppliers. Similarly, communication between all of the firms was encouraged by Toyota as it results in a better designed and manufactured product mutually benefitting all involved. Toyota further improved the processes by lending their team members to the supplier firms in any way they were required [1]. Instead of the suppliers simply working for the manufacturer, Toyota adjusted the system so the suppliers work together as one with the manufacturer to deliver the best possible components, for the lowest possible prices, with the least amount of muda.

To complete improvement of the supply chain system, Ohno developed the Kanban, or Just-in-Time (JIT) style of inventory management [1, 15]. In this system, essentially all inventory is eliminated. New parts are made for use in assembly when the previous batch of parts runs out. Because of this idea, the Kanban system is extremely difficult to implement as one delay in the supply process can bring the entire manufacturing system to a halt. At the same time, this is the beauty of this idea because it removes the safety nets created by excess inventory and forces suppliers to be proactive in identifying potential problems that would slow or halt the system [1]. The end result is increased quality and efficiency throughout the entire supply chain [15, 16].

The marketing aspect of any manufacturer is equally as important as the production of the product and Eiji Toyoda recognized this. If the manufacturer cannot come up with the means or strategy to sell the product to the consumer, the whole system will fail. Together with his marketing expert Shotaro Kamiya [1], Toyoda designed a system that was as efficient between the production line, dealer, and consumer as the systems Ohno had developed between the production line, supplier, and employee. The result is a system similar to that of Toyota's supply chain in which each dealer is tied into Toyota's way of thinking [1]. Communication is encouraged, and over time the dealer became a part of the production system when Toyota switched to a build-to-order style of manufacturing. By submitting the order for the required vehicle, the dealer acts as the first step in the Kanban system, thus creating the pull or JIT style of manufacturing.

By the early 1960s Toyota had fully worked out the principles of the lean manufacturing system [1]. As consumers began to become more diverse and aware regarding the products they used, Toyota's methodologies gave them a huge advantage over companies in the western world that were still employing the traditional mass production techniques. Today, all industries are moving towards lean manufacturing systems similar to the way industries in the early 1900s migrated to mass production as the benefits for the manufacturer are being demonstrated repeatedly. The results for the consumer are more adept producers who are better able to meet changing needs with lower cost, higher overall quality and reliability, and this is becoming the expectation [4]. The result for the manufacturer is the ability to compete with the established mass manufacturers, reduce waste in the production system, and save money that may be in turn used to reduce product costs or determine and create the next new technology. Although more practice and

training are required in the western world, it is becoming clear that the companies that will succeed in the future will be those who embrace lean manufacturing, while those who do not will fade into the background. Generally speaking, effective implementation of lean manufacturing without identifying the sources of waste is meaningless. As a result, potential sources of waste in manufacturing systems will be discussed in the following section.

8.2 Various Sources of Waste in Manufacturing Systems

It is a very clear and well acknowledged fact that manufacturing plays an integral role in today's society and it is the backbone of almost every industry in the world. Unfortunately, industrial waste from manufacturing is becoming a serious concern over the past decades. Waste in manufacturing systems can be described as something that adds no value or something that is not needed but consume resources in terms of time, money, workforce, space, etc. In general, waste is anything that provides no benefit to the company and can be eliminated without any adverse effect on the quality and profitability of final product.

For these reasons, waste elimination becomes more and more important over the time. Waste elimination, as one of the main objectives of lean manufacturing, can increase the production and profit of any business or company. To eliminate waste efficiently, it is important to understand what the waste is and where is it coming from. Companies typically classify manufacturing waste into eight different categories which include transportation, inventory, motion, waiting, over processing, over production, defects or rework and skills/poor utilization of human resources [17].

These types of wastes are seen everyday in factory settings and can be reduced or eliminated using specific lean manufacturing techniques such as implementing a lean six sigma or quality programme [14, 18, 19]. Some wastes can be easily yet effectively eliminated by changing the layout of a factory to minimize motion between work cells. Inventory wastes can be reduced by utilizing a certain production technique. Transportation of materials or goods can be reduced by improving production configuration and/or layout. Unnecessary waiting can be reduced by improving production operating and set-up time of material, order or machine input. Underutilized people can be completely neglected if all the right training and certification was completed to the person operating the machine/equipment. Waste from defected parts can be improved by meeting customer requirements. And finally, overprocessing can be eliminated by cutting all unnecessary production stages that add no value or meaning to the material or part being manufactured.

However, it is important for every manufacturer of some kind to fully understand the eight major sources of waste that may be encountered. Manufactures are responsible for reducing production waste as much as possible, otherwise it will lead into inefficient production. To avoid inefficient production, there are certain possible paths for improvement and elimination. It is crucial to understand the value

added to the product, identify the main value stream, develop product flow, and implement schedules [20]. These paths are lean six sigma's main goals in a business. Understanding these paths will help eliminate the root cause of the problems using statistical analysis, which is the major method used in six sigma [19].

Waste reduction is the most effective way to increase production efficiency and rate. Many different waste management techniques are being implemented into industrial settings to reduce or ideally eliminate waste. The main reason behind implementing these techniques is to improve manufacturing efficiency and reduce the environmental drawbacks caused by waste.

8.2.1 Transportation

Transportation or material handling system, both internally or externally, is a necessary part of each manufacturing system but is also considered as one of the major sources of waste.

Transportation is defined as moving the product or material from one place to another. The process of moving material does not add any value to the product itself; however, it may be still necessary to transfer the parts between several stations for processing. The movement of the material can also cause excessive damage to the material which eventually reduces the value of the product. Although the process of transportation is an inevitable part of each manufacturing system, but in order to reduce this waste, it must be controlled and optimized in terms of distance and time. The longer the product is in transport, the more prone it is to being damaged; moreover, the larger the distance being travelled, the longer no value is being added to the product. This is often seen in manufacturing companies that own several branches or facilities in different locations. Unnecessary transportation between branches can be a main source of waste to the company. This can be eliminated by implementing a more efficient grouping method of all parts and materials necessary in the same branch.

Depending on the nature of the raw material (weight, volume, volatility, sensitivity), transportation costs can be a large percentage of the product cost. Transportation costs and waste are directly related to one another. This is important because in every manufacturing process, whether it be a machining/forming process or an assembly process, the movement of materials/products occurs. As above mentioned, a manufacturing system cannot eliminate transportation of materials but it can optimize the process so that transportation is limited.

In order to fully eliminate or more optimistically minimize the transportation waste in a manufacturing system, there are a number of key factors that need to be taken into consideration. Poor machine layouts result in an increased distance that material needs to travel. Lengthy or complex material handling systems also add to the transportations costs. However, material handling systems usually increase worker efficiency if properly utilized. Large batch sizes also create waste by increasing the changeover time. If transportation equipment is limited inside a plant,

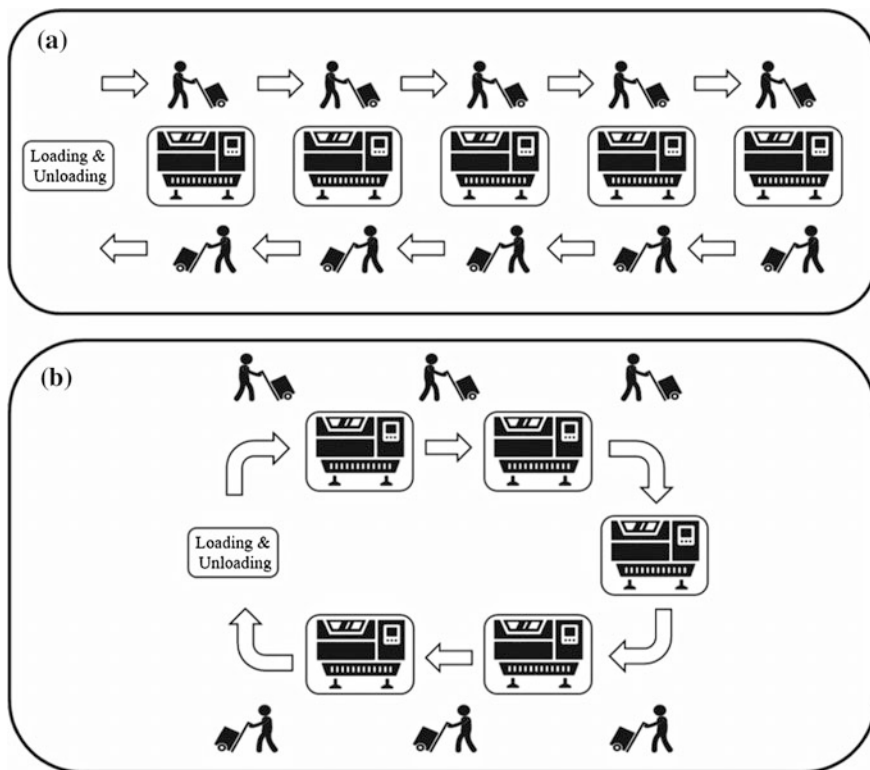


Fig. 8.1 Possible source of waste due to transportation/material handling in a simple manufacturing cell, **a** nonoptimal case with redundant movement, **b** optimal case with minimum required moves

the batch changeover could occur simultaneously and create wasted time in waiting. Working at a faster rate than the customer requires also creates waste as the finished parts need to be transferred to storage before it can be moved out of the door to the customer. This results in multiple storage locations which is also not ideal for a number of obvious reasons with the most important being that space in the factory is wasted [21]. Figure 8.1 schematically shows the possible source of waste due to transportation in a simple manufacturing cell and the way it can be improved.

8.2.2 Inventory

Acquiring an excess of inventory is considered wasteful and occurs when the manufacturing process produces products at a rate faster than that in which the customers require the products. Inventory is considered a waste because having a

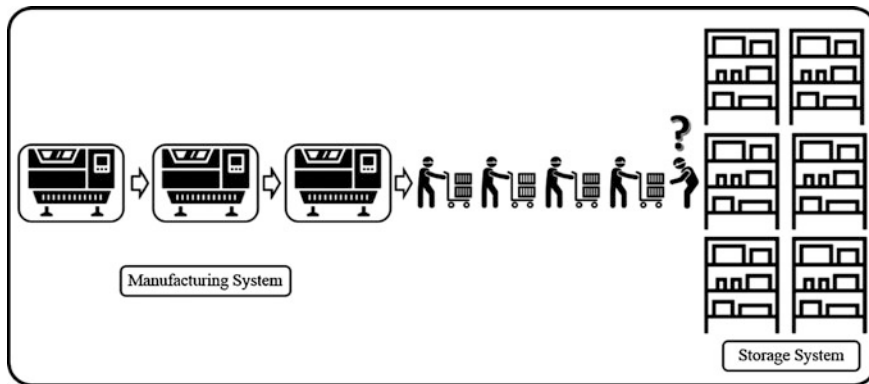


Fig. 8.2 Waste of resources due to excess inventory and storage

product stored adds no value and provides no profit to the company or business; however, that is not the whole story. Having too much inventory occupies useful floor space, increases lead time, constrains communication, and finally reduces efficiency as a portion of available resources must be dedicated to inventory control. It also creates numerous wastes in which they are often compounded by the other seven wastes of manufacturing.

Inventory is important as it directly affects different aspects of the manufacturing system. Each unit of inventory ties up the resources which could be profitable for the company and the company experiences that cost until it sells that product. Inventory has also to be stored somewhere which results in wasted space and it possibly has to be moved numerous times resulting in wasted time and money in transporting (see Fig. 8.2). Furthermore, inventory is also at risk of being damaged in storage or even becoming obsolete.

Inventory is a direct consequence of overproduction. Waste of inventory can be eliminated by using a certain production technique called Just-in-Time (JIT) production. JIT production simply means making only what is needed, when it is needed, and in the amount needed [22, 23]. According to Just-in-Time manufacturing, the company or system must produce just enough products to meet the customers' demands which eliminates the possibility of inventory accumulating [15, 22, 23]. Figure 8.3 schematically demonstrates the concept of Just-in-Time manufacturing.

Another way of managing the amount of inventory that accumulates is looking at the cell layout and balancing each production process. Each process does not have to run at full speed all the time but instead run just as quickly as required which gives the employees time to perform other value-adding tasks in between cycle times [24]. Inventory waste can also be eliminated by buying only the needed materials, reducing the breaks between the production processes, and having a smooth flow between the work centres.

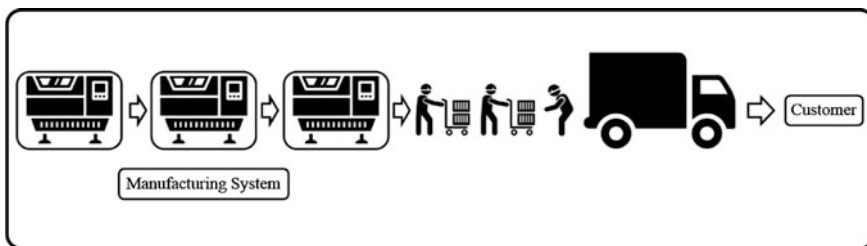


Fig. 8.3 Just-in-Time manufacturing

8.2.3 Motion

The waste of motion is similar to the waste generated by transportation but involves any specific movement that is not as short or as easy as possible. It is mainly related to the ergonomics of manufacturing, which consist of bending, lifting, stretching and walking. This is considered a waste because many jobs in the manufacturing industry make employees perform unnecessary movements throughout the day, which wastes time and energy. This includes aspects like employees bending over to pick up material or getting products from a higher shelf. These wasteful motions can cause the company money and also stress on the employees. This is extremely important because any added stress to the employees that results in the degradation of performance will generate waste and cost money. Figure 8.4 shows the schematic view of several possible moves from ergonomic point of view. The cost of training a new employee while a previous one is off on medical leave due to uncomfortable repetitive movements is a result of waste of motion. Unnecessary motion also increases cycle time between work stations and can wear out machines quicker.

In order to reduce the waste of motion, the job needs to be re-analysed and re-designed in order to reduce the amount of motion required and the distance travelled by the employee. Eliminating waste of motion is typically very simple. It can be eliminated by improving the cell layout for the operator to make sure any necessary tool or device is around. This reduces the unnecessary motion from one end of the plant to another by the operator. Moreover, instead of having an

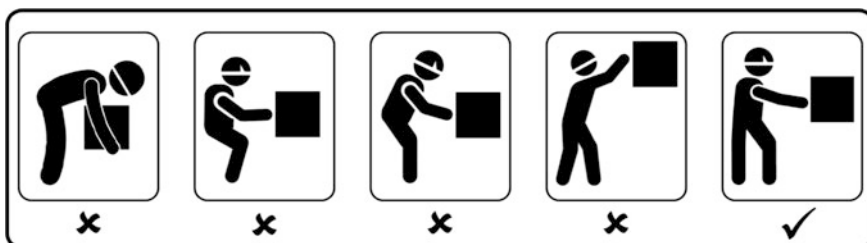


Fig. 8.4 Different moves from ergonomic point of view

employee pick up material from the floor, have the material fed at waste height on a conveyor. This will reduce the stress on the worker and increase the efficiency of material travel. Another big source of wasted motion is excessive motion by machining operations or robots. Excessive motion by a robot leads to a decreased life cycle of the robot and increased cycle time. An exception of excessive motion by a robot is considered when manufacturing a welded assembly. The welding sequence of the robot typically travels from one side of the part to the other in a Zig-Zag fashion. This is for the sole purpose of reducing the heat affected zones and warping that occur during a welding process. The motion seems excessive but lowers the geometric defects of the final product.

8.2.4 Waiting

Waste caused from waiting is generated anytime that a worker is stagnant and thus not adding value to the product. In the other word, waste caused by waiting occurs when products and materials are not moving or waiting to be processed. It has been shown that undesirably most of a material's life is spent waiting to be processed. This waste is usually caused by different scenarios such as long production runs, large distances between the work centres, and poor workflow which ultimately disrupts the flow of a manufacturing process. Waste due to waiting can be initiated by a machine that is down for repairs, waiting for raw material at a workstation, waiting for an answer from upper management or the lead design engineer, or even the changeover from one batch to another.

Waiting can be a vital source of waste as it is one of the most non-noticeable one among them. Time spent waiting for material, people or machine input is considered as a huge source of waste (see Fig. 8.5). In a typical manufacturing system, short waiting time for material input may not sound like much; however, when multiplied by the number of employees, machines, parts per day, per week, per month and per year, it will eventually accumulate to a large amount of unnecessary time wasted. Waiting is a problem that occurs quite frequently but is usually very easy to correct and manage.

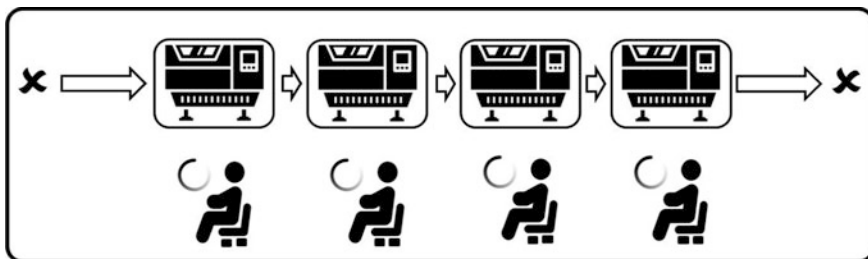


Fig. 8.5 Waste of time due to waiting

The elimination of stagnant employees in the workforce starts at the top with upper management. Poor management is typically the main cause of waste in the form of waiting [24]. If the management team can recognize the areas where people are waiting, then typically the solution is very simple. Instead of utilizing a batch production process where there is a wait period between batches, the line could switch to a continuous production process. Other causes of waiting come from long changeovers, unreliable manufacturing processes, rework, long machining cycles where the worker could be doing something in between cycles and machine coordination. All of these problems can be solved by a strong management team who can recognize the areas that need help and utilizing the workforce to eliminate waiting [25]. From downstream point of view, waste due to waiting can be eliminated by either optimizing the material handling system or by re-designing the flow of work for improving operator and machine time so that both parties coincide together nicely, without any time lost in between.

8.2.5 Overprocessing

Over processing occurs when processing exercises are more than what is needed for the desired functionality of the final product or adding value to the product that is not valued by the customer. Simply, investing extra effort and time into something that adds no value to the final product is considered as waste. This is a waste as the company spends money on excessive inspections, reworks, and rejects for overprocessing. Waste due to overprocessing typically resulting from defining specifications that are not clear, assigning tolerances that are too tight, utilizing equipment or machining techniques that are too advanced for the current application, grinding and polishing when not required, and painting unseen areas (exception for corrosion prevention). Figure 8.6 schematically shows the overprocessing as a waste of resources.

Being aware of over processing is important because there is a fine distinction between what is necessary and what is considered to be overkill. To reduce the waste due to overprocessing, it is necessary to compare the manufacturing specifications with the customer requirements and try to make the manufacturing process simpler.

In doing so, one must remove all processes that have no meaning throughout production. Meaningless processes are the ones in which the customer is not willing to pay for.

Eliminating overprocessing is most effectively achieved through communication between the customer, designer and manufacturer. Having a closed loop communication system allows the designer to understand the use and purpose of the product and allows for input from the manufacturer. This allows a product to be designed with the considerations of manufacturing processes and eliminates areas of overprocessing that arise from an unclear application of the product.

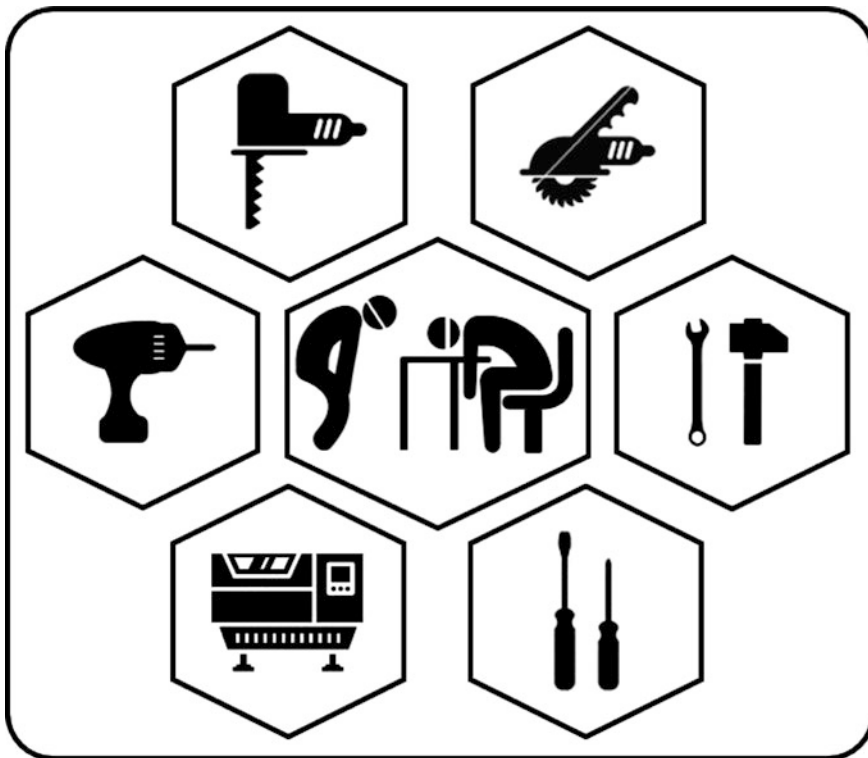


Fig. 8.6 Waste of resources due to overprocessing

8.2.6 Overproduction

Overproduction is considered by many the worst form of waste. It is the process of making too much of a product too early when there is not that much demand from the customer side (see Fig. 8.7). Overproduction is costly as it disrupts the smooth workflow and decreases the productivity and quality. This type of waste is usually caused by large batch sizes and poor communication with suppliers. A direct result of overproduction is a large amount of inventory.

Overproduction is a very important issue because it increases the storage costs, creates excessive lead times, and masks and obscures the defects. Consequently, it makes the potential points of improvement hard to detect. The philosophy that a company is meeting all of its orders on time leads to a false pretense in which improvement is halted. It also leads to unreliable processes, unstable scheduling, and unbalanced cell production.

The elimination of over production is most commonly solved by a Just-in-Time (JIT) production philosophy. This is outlined above in Sect. 8.2.2 (inventory) as the

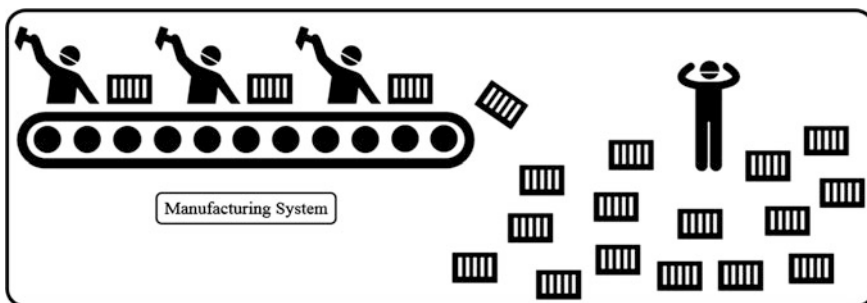


Fig. 8.7 Waste of resources due to overproduction

two of these wastes (inventory and overproduction) are directly related to one another. Simply balancing the supply to the demand when the product can be transported preferably immediately fixes the overproduction and eliminates waste.

8.2.7 Defects and Rework

One of the most visible wastes of resources is in the form of wasted material. A finished part that is out of tolerance and has to be thrown out or has to be reworked is considered waste (see Fig. 8.8). Waste of resources due to defective parts is also one of the most expensive wastes, as it is normally detected when the product is already produced or even after being utilized by the customer which may eventually lead to a lost in customers.

Quality errors in a manufacturing process that cause defects ultimately cost more than just the replacement of the component. This extra cost is originated because the additional efforts being put to rework or scrap defective parts add zero value to the final cost of the product. In addition, all the other wastes that are in the whole

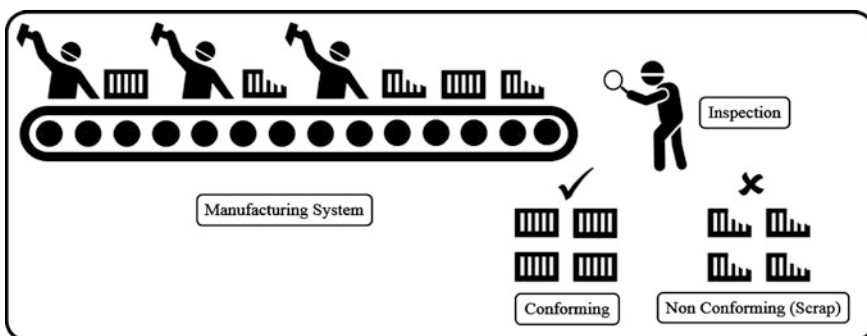


Fig. 8.8 Waste of resources due to producing defective parts

manufacturing process are then compounded twice for the completion of one part. It wastes time and in most cases results in paperwork and an inspection process from management to ensure that the quality of parts is fixed and maintained in the future.

To eliminate defective parts, customer requirements must be thoroughly understood at the start of production as the main reasons behind scrap parts is because they do not meet customer requirements. There are different ways that manufacturing processes can ensure the quality of the parts; however, it must be noted that the process to ensure the quality depends on the complexity of the part. Defects can also be avoided by designing processes that detect any malfunctions immediately, determining why the defects occur, and creating jobs that involve consistency so that defects are less likely to occur. In many cases there are test fixtures where a part is periodically pulled off the production line and certain measurement characteristics are checked. Typical systems include a GO/NOGO gauge or pokayokes to ensure geometrical accuracies are maintained. Visual inspection systems can be put into place to eliminate any user error that may occur if each part is checked by a human worker. Weight testing and scanning techniques also ensure the quality of a finished product [18].

8.2.8 Skills/Poor Utilization of Human Resources

Skills, talents, and level of expertise are important assets for the workers and they play an important role in success or failure of the production process. The skills and talents are normally wasted when companies fail to make use of the people involved in their organization in the appropriate positions where the maximum performance can be achieved. As a result, if the workers' skills are not efficiently used, it can be considered as a huge source of waste. Imagine a company with a workforce that has the potential to run numerous machines simultaneously. This allows for a manufacturing system with more flexibility and provide the opportunity for a system to run shorter cycle times on multiple production lines. Moreover, it increases the system flexibility to run more than one production machine/line at a time. In such case, if management team does not utilize the full talents and abilities of the workforce and if this worker is mistakenly assigned to operate one machine or supervise one system at a time, his/her skills and talents are being wasted due to poor utilization (see Fig. 8.9).

The elimination of wasted skills or poor utilization of human resources is not so much an elimination but a discovery. Identifying the employees that are capable of handling more responsibility and then providing them with the proper training and granting them with the additional responsibility is a positive way of utilizing the talent more effectively and consequently eliminating waste [26]. Improved level of communication between workers and management also reduce the waste of skills and talents due to better mutual understanding.

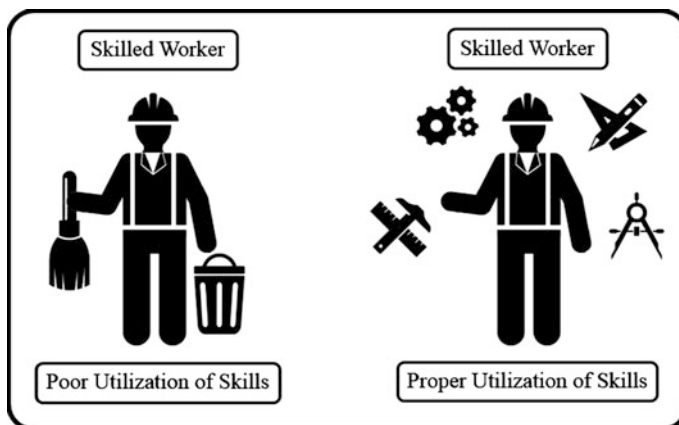


Fig. 8.9 Waste of resources due to skills or poor utilization of human resources

In conclusion, the waste definitions described above must be fully understood in order to eliminate and reduce waste. In order for a business or company to improve its overall performance and production efficiency, a strong foundation of lean manufacturing principles must be established. The development of a strong lean manufacturing system requires that the elimination of waste be paramount. The eight forms of waste listed above that are present in a manufacturing system are all in one way or another related and effected by each other. When developing a lean manufacturing system one must take into account aspects such as cell layout (cellular manufacturing), material handling, supply and demand, quality assurance, material storage, and transportation but most importantly have a strong management team in place that can identify certain problems and utilize the resources to solve them. In addition to above-mentioned items, communication between workers and management is also very important. With communication, management obtains the information required to allow the employees to be more efficient and ultimately produce less waste.

All these techniques strive for better performance with reduced waste outcome; therefore, implementing them will allow the companies to make value-adding processes with less waste. It must be noted that the wastes cannot be completely eliminated; however, they can be at least minimized.

8.3 Impact of Lean Manufacturing on System Performance

Lean manufacturing is a broad yet flexible concept that can be applied to almost every industry. This includes manufacturing companies, retail stores, fast food chains, airlines, and even government institutions such as hospitals. Interestingly, the service inventory accounts for 58 % of the world's GDP [27].

The impact of lean manufacturing on an organization varies depending on the type of organization. Several research studies on the effects of lean manufacturing on the organizational performance have proven that the proper implementation of lean concept has significantly reduced space and scrap, and increased productivity, stock turns and delivery. It has also been shown that lean production would allow waste reduction by 80 %, labour reduced by 50 % and inventory reduction by 80 % [28]. Other common areas of improvement from the implementation of lean are as follows:

- Smaller amount of defects and rework (improved quality performance)
- Higher efficiencies, higher production rate per labour hour
- Fewer machine and process breakdowns
- Lower inventory level
- Greater stock turnover level
- Improved delivery performance
- Less space required
- Faster development
- Greater customer satisfaction
- Improved supplier relations
- Improved employee morale and involvement
- Higher profits

Lean manufacturing will benefit a company or organization in all above-mentioned ways. Items such as improved employee morale and involvement as well as improved supplier relations will help an organization to continue its success in the long term, while higher profits allow for business expansion.

Lean Manufacturing focuses on the customer or consumer by nature of its principles. Processes are made more efficient with LM which ultimately creates shorter delay times on customer orders. Regardless of the type and nature of the product, e.g. food product or an automotive part, the process has been altered by LM to get the high-quality goods into the hands of the consumer faster and cheaper. For instance, lean production has shown to provide a 50 % reduction in manufacturing cycle time [27] which undoubtedly benefits the customer.

Lean manufacturing has proven itself to provide many benefits in terms of profit, quality of goods, customer service, company perception and many other factors. As a result LM participants have been able to thrive. Organizations such as companies have been able to edge out the competition, selling for less and expanding more aggressively. Furthermore, lean manufacturing has accelerated the economic timeline of competing companies. Corporations have been able to rise and fall faster with a tool such as LM in the hands of thriving companies. As a result, today we see a competition of LM itself. Companies compete in marketing, quality, customer service and now lean manufacturing.

Another change LM has brought on is a better quality of life. Goods produced by LM principles are of higher quality and cost less. The same amount of money goes

further in the hands of any global consumer. In addition, LM is adopted by non-competitive institutions that are often government funded or non-profit organizations. Lean Principles have helped these organizations to allow their budgets to take them further, ultimately providing more service (or better service) for their users. The simplest example of this is reduced waiting time at a hospital [27]. These benefits are not always financial. On the topic of health care, LM has also been proven to reduce infections and contamination in hospitals [27].

Generally speaking, lean manufacturing is helpful to every industry it is applied to. Most of the time, LM provides financial gain for complex manufacturing procedures. The main principles of LM correlate to simplifying and organizing the workspace and cutting down on wasted time. These universal principles accelerate the economic battle between competitive companies as well as contribute financial and social benefits to non-competitive organizations.

8.4 Conclusion

There is always room for improvement in manufacturing engineering, as customers will always demand a better quality and a consistent process, with reasonable prices. That is the reason why lean manufacturing exist. However, accomplishing a job with high quality and in a reasonable time is highly preferred overdoing the job wrong in a shorter period of time.

Companies in the twenty-first century are focusing on the concept of “Lean Manufacturing” as a solution for the constant problem of manufacturing products that had less efficiency and high cost. Lean manufacturing is a multidimensional approach to problems that could happen in the work field. It mainly aims to completely eliminate or partially reduce the eight major sources of waste. The automobile industry was the first to address this problem and it was soon implied in the developing industries.

Lean manufacturing must be always implemented from the top of the company to the bottom, due to the fact that the managers or CEOs are authorities that the whole company looks up to. Moreover, LM can be effectively performed if implemented at the early stages of any development process when all the problems that factory may face and the possible solutions can be thoroughly investigated. For this reason, lean manufacturing could be applied more effectively to new plants rather than the older ones, because newer plants are more advanced in many ways and they are way easier to make changes at.

In conclusion, lean manufacturing can be implemented in any type of industry but it is important to keep in mind that when a company is considering adopting the lean concept, the decision will have great results. It must be also noted that adopting LM requires dedication and a continuous reminder that time is the answer to achieve the end goal of becoming lean [29].

References

1. Womack JP, Jones DT, Roos D (2008) The machine that changed the world. Simon and Schuster
2. Moore R (2011) Selecting the right manufacturing improvement tools: what tool? when?. Butterworth-Heinemann
3. Plenert G (2010) Reinventing lean: introducing lean management into the supply chain. Butterworth-Heinemann
4. Hobbs DP (2004) Lean manufacturing implementation: a complete execution manual for any size manufacturer. J. Ross Pub
5. Sward K (1948) The legend of henry ford. Rinehart
6. Alizon F, Shooter SB, Simpson TW (2009) Henry ford and the model T: lessons for product platforming and mass customization. Des Stud 30(5):588–605
7. Sabel C, Zeitlin J (1985) Historical alternatives to mass production: politics, markets and technology in nineteenth-century industrialization. Past Present. p 133–176
8. Sloan AP (1964) My years with general motors. Broadway Business
9. Zhang W (2010) Intelligent energy field manufacturing: interdisciplinary process innovations. CRC Press
10. History of Toyota (2015). Available from: http://www.toyota-global.com/company/history_of_toyota/1867-1939.html
11. Womack JP, Jones DT (2010) Lean thinking: banish waste and create wealth in your corporation. Simon and Schuster
12. Melton T (2005) The benefits of lean manufacturing: what lean thinking has to offer the process industries. Chem Eng Res Des 83(6):662–673
13. Imai M (1986) The key to Japan's competitive success. McGraw-Hill/Irwin
14. Mi Dahlgaard-Park S, Dahlgaard JJ, Mi Dahlgaard-Park S (2006) Lean production, six sigma quality, TQM and company culture. The TQM mag 18(3):263–281
15. Sugimori Y et al (1977) Toyota production system and kanban system materialization of just-in-time and respect-for-human system. Int J Prod Res 15(6):553–564
16. Krajewski LJ et al (1987) Kanban, MRP, and shaping the manufacturing environment. Manage Sci 33(1):39–57
17. Gaspersz V, Fontana A (2007) Lean six sigma for manufacturing and service industries. PT Gramedia Pustaka Utama, Jakarta
18. Byrne G, Lubowe D, Blitz A (2007) Using a lean six sigma approach to drive innovation. Strategy Leadersh 35(2):5–10
19. Raisinghani MS et al (2005) Six sigma: concepts, tools, and applications. Ind Manage Data Syst 105(4):491–505
20. García-Alcaraz JL, Maldonado-Macías AA, Cortes-Robles G (2014) Lean manufacturing in the developing world
21. Dorota Rymaszewska A (2014) The challenges of lean manufacturing implementation in SMEs. Benchmarking: Int J 21(6):987–1002
22. Cheng T, Podolsky S (1996) Just-in-time manufacturing: an introduction. Springer Science and Business Media
23. Monden Y (2011) Toyota production system: an integrated approach to just-in-time. CRC Press
24. MS Campos L (2013) Lean manufacturing and Six Sigma based on Brazilian model PNQ An integrated management tool. Int J Lean Six Sigma 4(4):355–369
25. McCullen P, Towill D (2001) Achieving lean supply through agile manufacturing. Int Manuf Syst 12(7):524–533
26. Cassell C, Worley J, Doolen T (2006) The role of communication and management support in a lean manufacturing implementation. Manag Decis 44(2):228–245
27. Leite HR, Vieira GE (2015) Lean philosophy and its applications in the service industry: a review of the current knowledge. Production, (AHEAD): p 00–00

28. Keitany P, Riwo-Abudho M (2014) Effects of lean production on organizational performance: a case study of flour producing company in kenya. *Eur J Logistics Purchasing Supply Chain Mgmt* 2(2):1–14
29. Soriano-Meier H, Forrester PL (2002) A model for evaluating the degree of leanness of manufacturing firms. *Integr Manuf Syst* 13(2):104–109

Chapter 9

Object-Based Final-Year Project: Designing and Manufacturing a Quick Stop Device

A. Pramanik, Hem Sanghvi and A.K. Basak

Abstract This chapter focuses on teaching and learning of a final-year project in undergraduate mechanical engineering degree in the field of manufacturing. The final-year project allows students to apply the knowledge they learned through undergraduate course work. In addition, it provides the opportunity to get practical involvement in design, project management, manufacturing, creativity, practical applications, etc. However, most final-year projects, nowadays, are either a portion of a big project or performing tests to understand the trends of certain parameters. As a result, such projects only allow the opportunity for partial knowledge to the students. Thus, an object-based project in the final year has been explored in this chapter. A quick stop device (QSD), which is used to investigate chip formation mechanism during machining, was proposed as an object to design, manufacture, and apply in the current investigation. It was found that this project allow students the opportunity of applying their course work knowledge in project works, taking complete responsibility, being innovative, free thinking, being creative, learning new things, and performing research.

Keywords Object • Project • Teaching and learning • Undergraduate degree • Quick stop device

9.1 Introduction

It is possible to enhance teaching and learning by incorporating different approaches including technological tools [1]. Technological tools, such as information and communication technologies, online games, online learning, portable devices (smart phones and tablets), and others affect the teaching/learning process through learning

A. Pramanik (✉) • H. Sanghvi

Department of Mechanical Engineering, Curtin University, Bentley, WA, Australia
e-mail: alokesh.pramanik@curtin.edu.au

A.K. Basak

Adelaide Microscopy, The University of Adelaide, Adelaide, SA, Australia

© Springer International Publishing Switzerland 2015

J.P. Davim (ed.), *Modern Manufacturing Engineering*, Materials Forming,
Machining and Tribology, DOI 10.1007/978-3-319-20152-8_9

271

management systems, personal response systems, discussion boards, blogs, wikis, social networking, podcasts, and a variety of web-based applications. On the other hand, different approaches in teaching—such as critical incident analysis, identifying attributes of workplace problems, module-based teaching, emphasis on strategic engineering education, and the like—ease the process of student learning. All of these educational tools have been tested for different teaching units in different areas and have improved students' learning [2]. With the advancement of technology, the increase of learning materials, and the interdisciplinary nature of courses, it is the time to rethink the way that engineering subjects are taught. A number of engineering courses are frustrating as the course itself is difficult and boring due to lack of proper teaching methods. Students choose to drop out of these courses or fail in exams. It is believed that the dropout rates for these courses or the high failure rate on exams is due to insufficient talent and attention of students. However, the brighter students often leave because of disinterest [3–5]. This can be avoided through a cooperative learning approach which supports students in terms of intrinsic motivation, higher-level reasoning, academic and social support, social development, self-esteem, etc. The best learning is achieved when (i) students build on and relate to past experiences, (ii) the content is relevant to them, (iii) there is a chance for a direct 'hands-on' experience, and (iv) students can construct their own knowledge in collaboration with other students and faculty to communicate effectively [6, 7]. The modern engineering profession deals constantly with uncertainty, with incomplete data and competing (often conflicting) demands from clients, governments, environmental groups, and the general public. It requires skills in human relations as well as technical competence. While trying to incorporate more 'human' skills into their knowledge base and professional practice, today's engineers must also cope with continual technological and organizational change in the workplace. In addition, they must cope with commercial realities of industrial practice in the modern world, as well as the legal consequences of every professional decision they make [8]. The final-year project reinforces the above 'human' as well as technical skills. In final year projects, most students cannot have an object-based project due to shortage of time. Instead they work on a part of big projects or experiment-based projects to test behaviors of some practical trend. In these cases, students do not get the taste of total responsibility, creativity, and excitement of successful completion of a project. Therefore, an object-based final-year project has been considered in this investigation to address the above-mentioned issues.

Objective-based projects (OBP) organize learning around an object that needs to design, manufacture, and utilize. It is based on challenging questions or problems that involve students in design, problem-solving, decision-making, and investigative activities. This approach allows students the opportunity to work relatively autonomously over extended periods of time and culminate in realistic products or presentations [9, 10]. Effective investigation in 'design thinking' consists of (i) 'convergent component' which generate deep reasoning questions by systematically asking lower-level, 'convergent questions' and (ii) 'divergent component' creates the concepts on which the 'convergent component' can act [11]. The learning of higher-level cognitive skills via OBP is associated with increased capability on the part of students for applying those learning in problem-solving contexts [12].

9.2 Object: ‘Quick Stop’ Devices

The object which was designed and manufactured in this project was a ‘quick stop’ device (QSD). It is an effective tool to gain an in-depth knowledge into fundamental study of chip formation during machining process. The device is used to seize the machining operation by disengaging the tool and the workpiece so rapidly that the static situation resulting due to the halt will precisely portray the dynamic situation allowing ‘chip-root’ to achieve. Figure 9.1 shows the chip root region being analyzed in this project.

9.3 Background Information

During machining process the material is removed by the tool at a certain force which leads to plastic deformation to occur at the surface resulting in a varying strength along the machined surface. QSD these days are designed not only to understand the frozen chip design for traditional machining processes but also for complex machining processes like twist drilling and spiral point twist drills [13]. Most QSD devices are based on shear pin designs in which the tool has a shear pin passing through it, which can bear the cutting forces but is notched at the center. On a sudden impact, it forces the tool away from the workpiece, thus freezing the chip root to the workpiece providing a good sample to examine. This design is fairly simple to construct and deploy. However, engineers should refrain from excessive use of material, which will be wasted on each testing session. The result obtained by employing this design does not necessarily produce uniform results at each go [14]. Further researches took the help of external power source such as explosives to accelerate the tool away from the workpiece. The rate of acceleration varies in every try in this case. When it is initiated, the bolt is accelerated to the notched

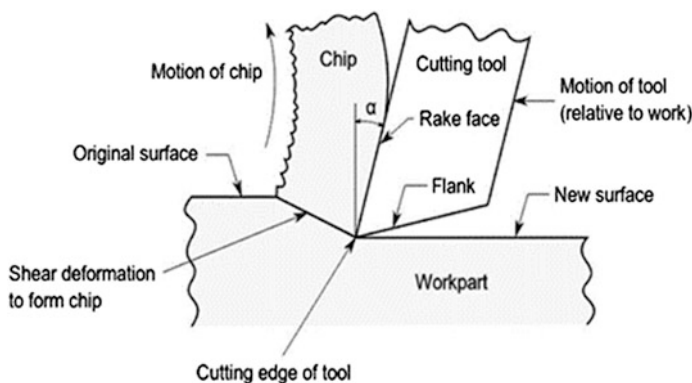


Fig. 9.1 Schematic of tool–chip interface

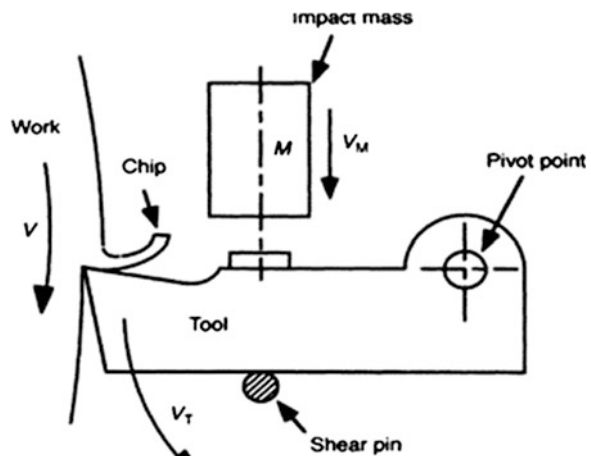
shear pin to break it. The root diameter for the pin is selected to resist the cutting tangential forces, but not the total sum of cutting force and the bolt force. Some of the recent devices apply mechanical shock or impact of mass which are actuated by an explosion in order to break the tool and escalate it out of the cut [15, 16].

9.4 Design Consideration

The shear pin technique explained earlier will be utilized as a source of inspiration for this project. In order to understand chip formation the foremost reason behind the invention of QSD was to follow the dynamic variations of chip flow. This could be achieved using transparent tools like diamond and sapphire, but the region to focus is the point of deformation, which is relatively small compared to the cutting velocities. Researchers are ready to give up on the dynamic data for the microscopic details revealed by ‘freezing’ the cut. The QSD actually carries out the function mentioned above. The machining process would be required to stop by separating the tool and workpiece at a speed greater than the cutting speed, preferably to achieve the appropriate results. As a result, chips stuck to the workpiece and sometimes even fragments of the cutting edge can be found attached to it. For the current scenario of turning, the setup shown in Fig. 9.2 is a good example to learn the basic requirement from a quick stop device that will be designed and manufactured for this project.

As shown in Fig. 9.2, the tool is supported at a pivot point and a shear pin; mass M is being struck on the tool holder with a velocity of V_m . It is ensured that the force with which the mass strikes is much greater than that required for breaking the shear pin. This would cause the toolholder to swing away from the workpiece. The velocity of the tool V_t does not reach the cutting velocity V instantaneously due to its own inertia. Therefore, in order to increase the accuracy of the test V_m and M

Fig. 9.2 Mechanism of a QSD



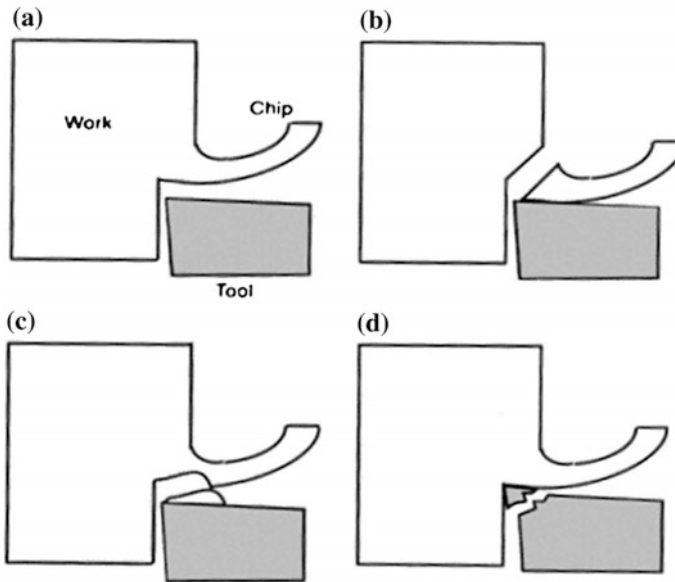


Fig. 9.3 Various ways of cutting tool disengagement during chip formation

should be made large and the inertia of the toolholder should be reduced. In order to get more accurate results, firing it using a gun repeatedly increases the value of V_m . For lower turning speeds, a hammer is used to strike the tool away. Using the slaughter gun with captive bolts a tool displacement of 2.5 mm in 1.2×10^{-4} s was achieved. It is assumed that, in order to achieve a successful quick stop, V_t must reach V in a very short time.

Successful ‘quick stop’ becomes more difficult with increasing operating speed, as the acceleration required of the tool increases with the square of the cutting velocity. This can also be done in milling operation. It is tough to guide the workpiece away from the cutting tool as the work and its holder would have higher inertia compared to the tool, which requires the ‘quick stop’ device to be completely synchronized with the cyclic cutting action. Therefore, the ‘quick stop’ device should be used in milling only when the difficulties to go through with the process are worthwhile. Figure 9.3 shows the various chip formation that can be achieved using the quick stop device, usually depending on the tool coating.

The design of QSD needs to follow certain design rules and parameters so that it does the function intended and does not become a hazard to human safety. The QSD for this project would not employ any explosives or breaking pins; instead it will employ a mechanism that will be developed in the second design. The initial design proposed for the QSD will only be used to observe the working of the tool and is hoped to shine some light on any downfalls of the idea implemented. So the objective of the second design is to improve those downfalls and provide a QSD that actually operates for a broader range of manufacturing condition. This can also

shed some light on how this process could be refined so that a better result can be foreseen. The design proposed for this project had been made keeping in mind the design constraints. Two designs have been proposed and will be followed by a final design that will be based on a mechanism as shown in reference [14]. In order to replicate such a mechanism, two other designs with increasing complexity will be designed to understand the function of QSD. The finding through these designs will then be refined toward the third design. The project will only focus on QSD from the point of view of designing and manufacturing to perform its task efficiently; no further study of the frozen chip root would be done in this project.

The interrupted cut was developed on a very basic principle to abruptly separate the tool from the workpiece. Hence the deformation process has been frozen and can be isolated by metallographic preparation and examined under microscope. Although the interruption is sudden, it is slowed down from the initial cutting speed at high deceleration. Thus, frozen deformation does not represent an accurate account of the incident that takes place during the machining process. The cutting process is not frozen at operating cutting speed, but at a period that is unsteady and gradually slowing down, yet the results are accepted widely as they do not differ much from the actual value. This method should be actively avoided on machining highly time-dependent processes, like a thermally dominated process.

The cutting speed at the chip formation process will determine the design of the tool. The tool will be required to work with minimum time interval t_0 with increasing cutting speed. Figure 9.4 illustrates a simplified speed ratio required for the interrupted cut method. The constant acceleration, a , for the calculation purpose is considered negative, i.e., decelerating therefore

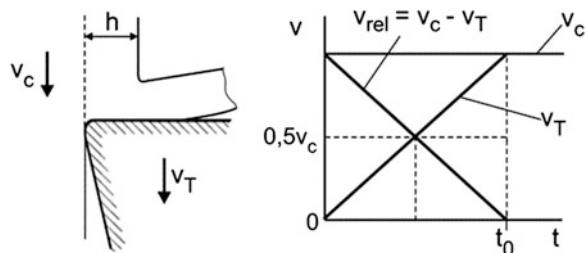
$$v_{\text{rel}} = v_c - a_T \cdot t \quad (9.1)$$

With $v_{\text{rel}} = 0$ m/min after t_0 , the required braking distance Δx is

$$\Delta x = \frac{1}{2} v_c t_0 \quad (9.2)$$

Equations 9.1 and 9.2 can be used to compute the necessary deceleration (a) and the corresponding braking distance.

Fig. 9.4 Speed ratio calculation [17]



$$a_T = \frac{v_c^2}{2\Delta x} \quad (9.3)$$

According to Eq. 9.3, there is a clear indication pointing toward a high value of deceleration even if the cutting speeds are low and a maximum permitted braking distance of 10 % of the undeformed chip thickness should be maintained. It is important to keep the decelerated mass to a minimum so as to keep the deceleration forces within limits.

There are different ways to interrupt the cut as shown in Fig. 9.5. The two major ways to do so is either the tool or the workpiece is accelerated or decelerated. Figure 9.5a depicts the principle of interrupting the cut by accelerating the tool. It is usually carried out by accelerating the complete tool unit by means of the tool-holder. The potential energy is stored in the tool springs, compressed air, and explosive material. This stored energy is then converted into kinetic energy within milliseconds. In some cases a mechanical cutoff is also utilized, by including a barrier that would initially revolve with the tool and it is within a revolution that it would accelerate the tool away from the workpiece [17].

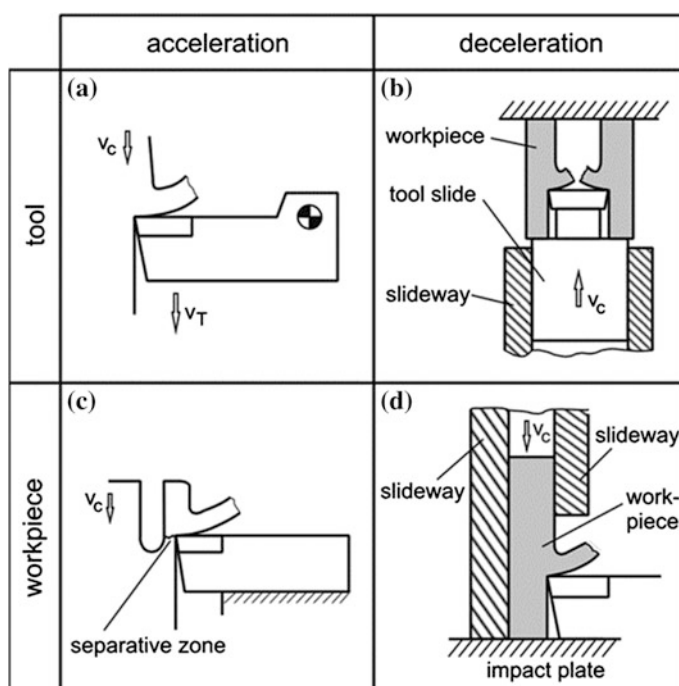


Fig. 9.5 Different methods for interrupted cut [17]

9.5 Design 1: Orthogonal Movement 1 (X-Y Axis)

Design 1 had the following assumptions and objectives to satisfy: (a) the design needs to be sturdy with minimum movement during machining, (b) the cutting tool required for this design can include any type of cutting insert as long as it can handle machining above 500 rpm spindle speed, (c) the tool will be housed in a body that will be kept as minimum as possible, while being rigid, as it will be under pressure due to the screws of the toolholder clamping it during machining, and (d) the tool and the tool housing weight will be kept to a minimum in order to support swift movement of the tool away from the point of cut.

9.5.1 Design Components

The design for the primary tool would have an orthogonal movement along x-y axis as its quick stop mechanism. The tool was designed under the guidance of the tool manufacturer, as they would be able to shine some light on what sort of tool would suit the task at hand efficiently. The design would utilize springs to propel the tool after releasing the clamp. Therefore, all the major components have been shown in Fig. 9.6, explaining their involvement in making the design complete its objectives.

9.5.1.1 Tool Housing Body

The design was created keeping in mind the required slot for the spring that has maximum mean coil diameter. The height of the tool housing can accommodate safely without comprising its body integrity.

The design for the body at the front end is angled at the right outer side at 125° from the horizontal as shown in Fig. 9.7 to provide the tool clearance to move orthogonally without any obstruction in its path to reduce its acceleration rate or to damage the tool.

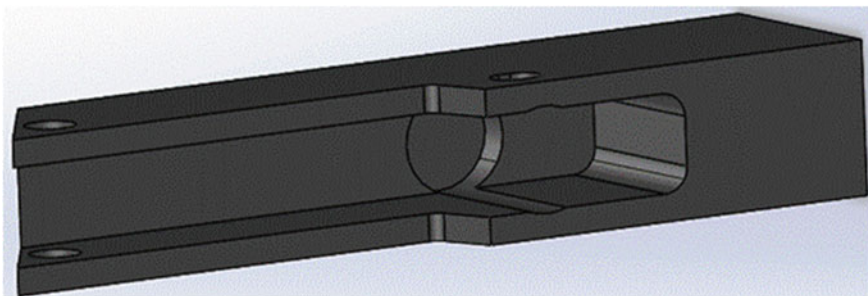


Fig. 9.6 Solid view of the tool housing



Fig. 9.7 Top view of the cutting tool

9.5.1.2 Cutting Tool

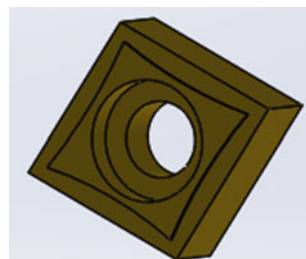
As this tool was the first of the four designs to be made, a general tool was designed with the back end of the tool being removed to provide more space for a lengthy spring which could increase the force exerted on release. The tool insert used was already available as spare even though it consists of a chip breaker on it. As the principle behind the quick stop tool was to separate the tool from the cutting action in the smallest time interval possible, therefore, the author did not use another tool insert. A C-type insert was used for the first design and is secured using a hexagonal headed screw as shown in Fig. 9.8.

9.5.1.3 Clamp and Spring

The tool after being secured by a bolt in the front part of the housing is clamped at the very end. The spring is also located at the end of the tool, hence it would help in increasing the force due to moment at the cutting edge. The clamp design was to be welded onto the top surface of the tool housing as shown in Fig. 9.9. The clamping style adopted was very primitive, hence it is easy to use for multiple attempts.

The spring used in this design has a wire diameter of about 1.72 mm and the outside diameter is about 17 mm, which was required to provide the required force to swing the tool away from the cutting site quickly. Figure 9.9 shows the position and the manner in which the locking mechanism and the spring will appear when the Quick stop tool is set up during machining.

Fig. 9.8 Carbide insert



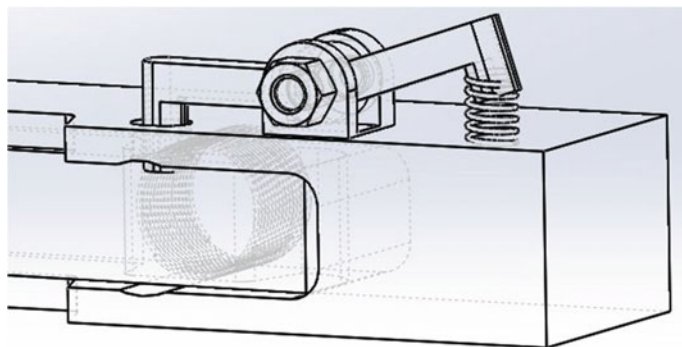


Fig. 9.9 Locking mechanism and spring arrangement

9.5.2 Manufacturing and Assembly

The proposed design required the tool to be made very precise and therefore most of the tool components were shaped on CNC milling center. CNC has been proved to be very effective in producing identical, precise, and repeated machine parts on demand at a very good production rate. The tool as well as the tool housing body was majorly shaped on the CNC milling unit. The images shown in Fig. 9.10 were taken during the manufacturing phase. As EN 31 is a hard material and requires constant flooding of lubricant to prevent cutting tool and surface damage to the machined object, hence the images taken cannot be very clean surface. After the tool components were manufactured, the components underwent nitriding which would help to increase surface toughness.

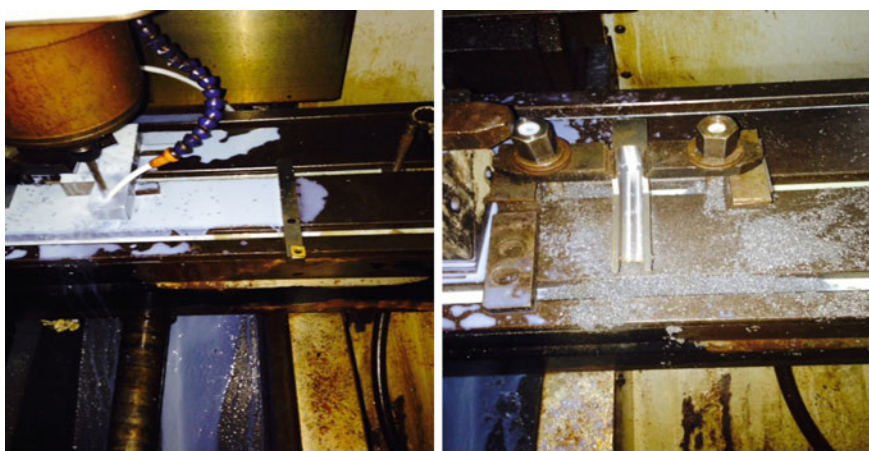


Fig. 9.10 Image during manufacturing the tool housing on CNC

ITEM NO.	PART NUMBER	DESCRIPTION	QTY.
1	MED2-0010	Tool Body	1
2	MED2-0012	Clamping Mechanism	1
3	B18.3.4M - 5 x 0.8 x 16 SBHCS --N		2
4	MED2-0011	Cutting Tool	1
5	MED2-013 - Copy	clamp stand	1
6	SPRING_D2	Spring	1
7	B18.3.4M - 8 x 1.25 x 30 SBHCS --N	Screw to secure Cutting tool	1
8	B18.2.4.1M - Hex nut, Style 1, M8 x 1.25 --D-N	Hexnut For the screw to secure the cutting tool	1
9	SPRING_D2.A	Spring For clamping Mechanism	1
10	B18.2.4.1M - Hex nut, Style 1, M5 x 0.8 --D-N	Hexnut for clamping Mechanism	1
11	TOOL BID	Carbide tool Insert	1

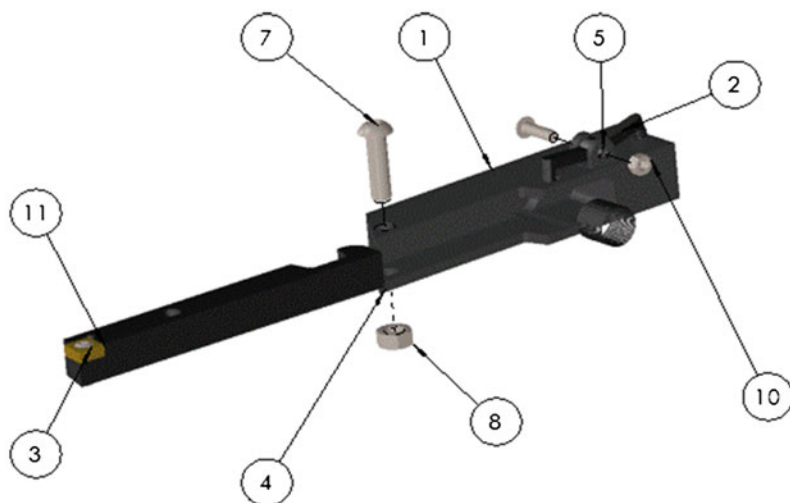


Fig. 9.11 Assembly of Design 1

The assembly of the entire unit is shown in Fig. 9.11. All the parts were designed for easy assembling to facilitate the ease of use of the tool. As shown in the assembly figure (Fig. 9.11) the following steps are required to be followed to assemble and operate the quick stop tool: (a) The spring needs to be inserted into the slot provided, (b) the cutting tool needs to be aligned with the holes provided in the front of the tool housing and then be secured by the bolt and made parallel to the tool housing by pushing it inside the house and by pressing on the clamp welded on the top surface of the housing.

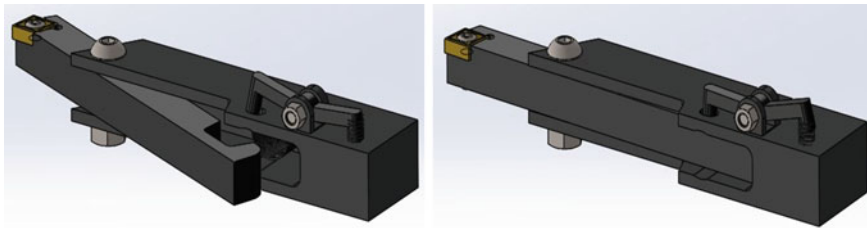


Fig. 9.12 Images showing the tool before and after QSD activation

For operating the quick stop tool, it requires the clamp to be pressed so that it lifts up and releases the stopping force exerted on it to hinder its orthogonal motion. The cutting tool will then swing in the direction opposite to the feed direction of the tool. The images shown in Fig. 9.12 represent the quick stop tool: (a) when it is loaded and (b) when the quick stop tool is activated.

9.5.3 Testing the Quick Stop Tool

The quick stop tool was tested on a circular piece of aluminum 6262 bar. The spindle speed for frozen chip root tests are 200, 250, 310, and 500 rpm and feeds 0.1, 0.13, 0.16, 0.19 mm/rev. The test conditions mentioned above would remain consistent throughout the designs that will be tested further. On using the quick stop tool using the above-mentioned cutting conditions, the rotation of the spindle at the lowest speed, i.e., 200 rpm had proven to be faster than the acceleration of the tool away from the point of cut after the quick stop had been activated. On closer observation, after the testing was completed, it was found the tool on being released scratched the workpiece surface; thereby it would produce vibration within the work material that would break any chances of the chip root being intact.

9.5.4 Outcome

It was then noted that the acceleration of the quick stop tool needs to be increased and the primary cutting tool needs to be changed. As the current carbide insert had a chip breaker on it, which initially was believed not to be an issue. If the acceleration of the tool away from the point of cut was fast enough.

9.6 Design 2: Orthogonal Movement 2 (X - Y Axis)

Learning from the previous design, the following assumptions and design consideration were made for Design 2: (a) the proposed design requires being sturdy enough to perform as primary cutting tool, (b) effort needs to be concentrated on reducing the weight of the cutting tool so its acceleration can be increased, (c) the outside diameter as well as the wire diameter of the spring needs to be increased to the maximum as permitted by the restricted height of the tool body due the toolholder's fixed height of 25 mm, (d) the main cutting tool also requires to be changed to a standard V cutting tool, (e) a new approach to restricting the motion of the tool during machining to be adopted.

9.6.1 Design Components

The second design was created to try and improve the tool acceleration when triggered. Also, tool change was required as the previous tool was not suitable for the task. The new proposed design has the same x - y axis orthogonal movement as its tool movement away from the point of cut. Hence the following parts have been designed to suit the design consideration.

9.6.1.1 Tool Body Housing

The tool body housing for this design was created using tool steel but did not undergo nitriding as the stock material possessed the required toughness to withstand the constant pressure due to the four screws on the toolholder. As the tool was not surface treated the spring diameter was reduced to 11 mm from 17 mm in the Design 1, whereas the length was increased from 26.50 mm in the first design to 35 mm in the second design. The tool housing is shown in Fig. 9.13 to indicate the changes in the spring slot and locking mechanism placement in the new design .

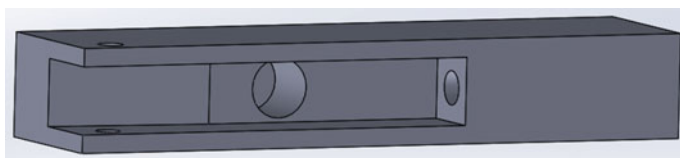


Fig. 9.13 Tool housing (Design 2)

9.6.1.2 Cutting Tool

For this design, a standard V tool with minor changes to its length and body to fit perfectly in the tool housing was used. As this tool has no chip breaking feature, it will help gain an advantage as the chip being formed by the machining and will not be forced to break if the tool accelerates fast enough to overcome the spindle speed. Hence, the images shown in Fig. 9.14 will indicate the changes made to the tool to make it adjust to the current scenario. The front hole is to secure the part to the tool housing and to restrict its motion around that axis. The hole at the end of the tool is for stopper mechanism to avoid any motion during machining.

9.6.1.3 Stopper Mechanism

For this design the stopper mechanism has been applied as the complete tool housing will lie inside the toolholding equipment and therefore the stopping mechanism needs to be in line with the tool (Fig. 9.15).

9.6.2 Manufacturing and Assembly

The manufacturing process was similar to that of Design 1; a CNC milling machine was used to machine the tool housing body using AISI M2. This material possesses good toughness and work hardening properties (interalloy M2). The cutting V tool was bought standard from the shop and the necessary holes were drilled according to the design requirements. The Assembly for this tool setup does not differ much



Fig. 9.14 Solid view of the V cutting tool (Design 2)

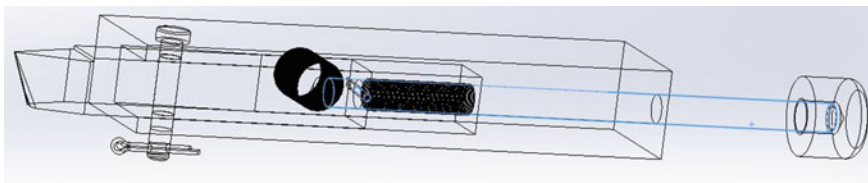


Fig. 9.15 Stopper mechanism in wireframe view (Design 2)

from Design 1 previously mentioned: (a) the spring needs to be slid into the slot provided, (b) the V tool then needs to be aligned with the hole provided and secured using a bolt and Circlip and then pushed into the tool housing, (c) align the tool with the stopper rod, and insert the rod in the hole at the back of the tool as shown in Fig. 9.15.

The quick stop tool is ready to be operated. In order to operate the quick stop tool the stopper needs to be pulled with force as it is spring loaded. This will release the rod, removing the restriction for the V tool to sway orthogonally away from the point of cut. The images in Fig. 9.14 represent the quick stop tool before and after activation.

9.6.3 Testing the Quick Stop Tool

The testing for this tool will be done at the same spindle and feed rate as mentioned before in the first design section. Uniformity is provided so that the changes made while developing each design are aimed at improving its performance for the known parameters. During testing the tool was found to still scratch the surface on its way after being activated. It would naturally happen as the V tool is secured at the point and the movement of the tool away from the cut will follow a circular path pivoted at the point it is secured to the tool housing. The acceleration of the tool away from the point of cut has increased due to reduction in weight, but the orthogonal movement direction needs to be reevaluated to take into account the above-mentioned factors (Figs. 9.16 and 9.17).

9.6.4 Outcome

This design operates faster than design 1, but still further weight reduction and higher stiffness spring might to be able to increase the acceleration rates further. The orthogonal direction also needs to be changed by shifting the plane of movement by 90° anticlockwise. Hence Design 3 will be developed to improve on the shortcomings of this design.

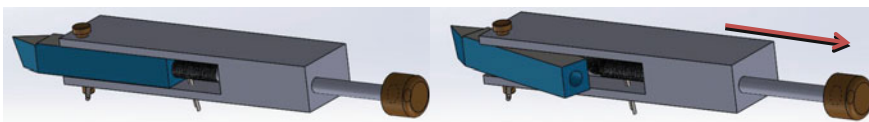


Fig. 9.16 QSD before and after activation (Design 2)

ITEM NO.	PART NUMBER	DESCRIPTION	QTY.
1	HOUSING	Tool Housing	1
2	MED1-0011	Cutting Tool	1
3	MED1-0012	Pin to secure the tool to the Housing	1
4	MED1-0013	Locking Mechanism Pin	1
5	MED1-0014	Knob for Locking Pin	1
6	SPRING_1	Spring	1
7	SPRING_2	Spring to push the Locking Pin	1
8	GB CONNECTING PIECE_PIN_AP 2.5X18	Circlips	2

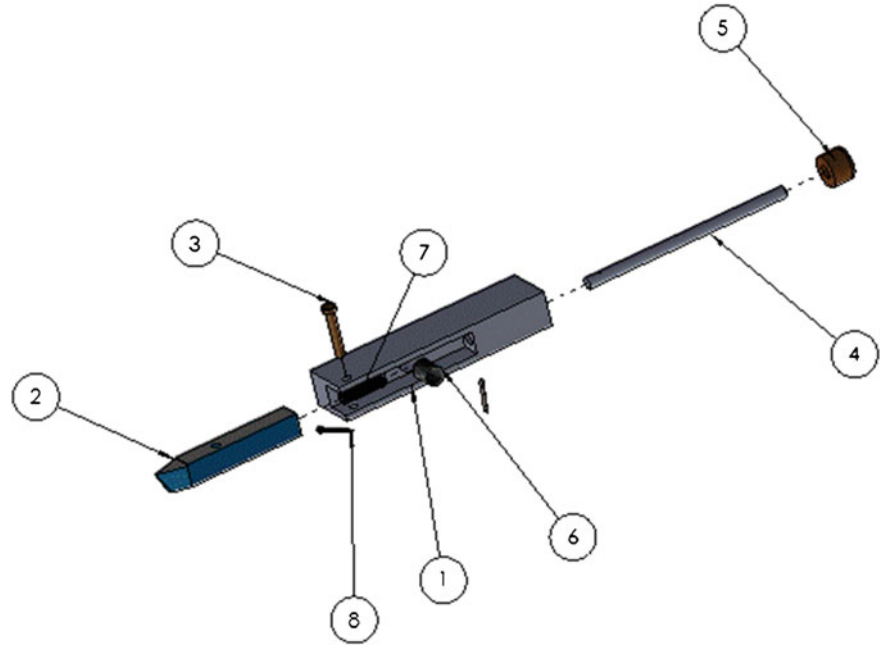


Fig. 9.17 Design 2-Assembly Drawing

9.7 Design 3: Orthogonal Movement (Y-Z Axis)

After two attempts at designing and manufacturing the quick stop tool, a considerable amount of knowledge has been gained by previous attempts. Using that data as input the following design considerations and assumptions were made for Design 3: (a) the previous assumption of the tool design being sturdy to perform its task as a stand-alone cutting tool still applies, (b) the weight reduction of the cutting tool only will be focused on this design, as this tool is a part of the research cost of manufacturing the tool is not a major issue to address, (c) the movement of the tool

on activation will be changed to up-down movement from the left to right movement applied in the first two designs, (d) spring will be used to generate the necessary force to push the cutting tool away from the cut, (e) the position of the spring will be kept in such a manner to maximize the force due to moment, (f) the front end of the tool housing will need to have an inclination to allow space for the tool to rotate downwards on releasing the stopper.

9.7.1 Component Designs

Keeping in mind the design considerations and assumptions made prior to the designing the following components have been produced:

9.7.1.1 Tool Body Housing

The housing for this attempt will need to be different as the movement of the tool is in $Y-Z$ plane. Hence the tool housing needs to be L-Shaped body. As the one end will be inside the toolholder the other half will house the other components of the design. The proposed tool housing has been shown in a wireframe image in Fig. 9.18 so that the changes made in the layout of the tool housing can be noticed.

The inclination at the start of the housing body is 55° below the horizontal. This angle is sufficient enough to allow the tool to move away from the point of cut without any chances of bouncing back onto the workpiece.

9.7.1.2 The Cutting Tool

V tool has been chosen to be the type of turning tool that would be used for this attempt. The weight has been further reduced from the previous design, but still keeping the tool standard. As the tool was required to function perfectly for the task,

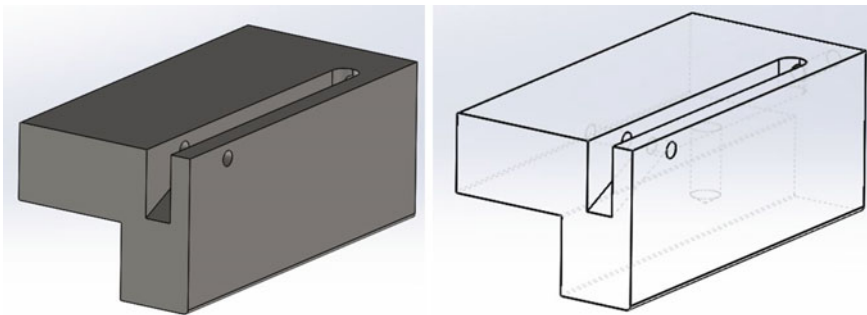


Fig. 9.18 Solid and wireframe view of the tool housing (Design 3)



Fig. 9.19 V tool (Design 3)

attempt can be made to perfect the cutting tool to maximize the output. The cutting tool is shown in Fig. 9.19 with its feature displayed.

The position of the axis of the hole on the front of the tool has been shifted by 90° , so the axis of rotation. The overall size has been reduced from the previous design; the length has been reduced to 90 mm from 105 mm, whereas the width of the tool has been reduced to 9 mm from 16 mm in the previous design.

9.7.1.3 Stopper Mechanism

The mechanism has not changed from the previous design, but has just been scaled down to accommodate for the smaller cutting tool. The image shown in Figs. 9.20, 9.21 and 9.22 will help in understanding how the stopper on being released will cause the cutting to fall downwards with addition to the force coming from the vertically loaded spring.

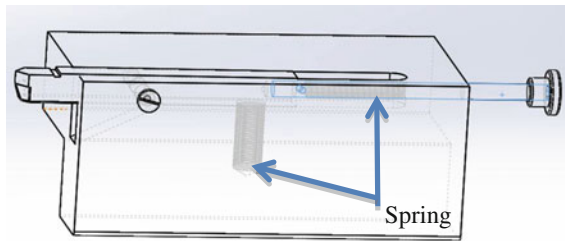


Fig. 9.20 Stopper mechanism explained (Design 3)

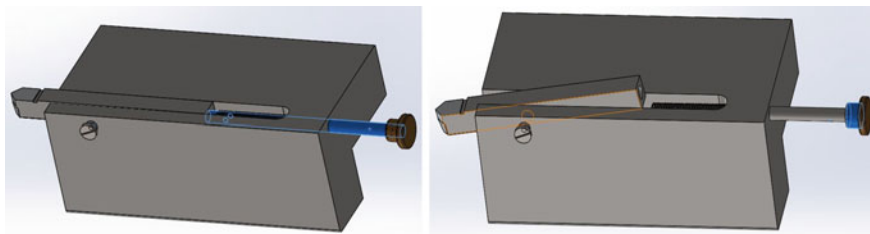


Fig. 9.21 QSD before and after activation (Design 3)

ITEM NO.	PART NUMBER	DESCRIPTION	QTY.
1	MED-0010	Tool Housing Body	1
2	MED-0015	Cutting Tool	1
3	MED-0011	Stopper Mechanism Rod	1
4	MED-0012	Stopper Mechanism Grip Point	1
5	MED-0013	Short Pin to lock the spring	1
6	MED-0014	Pin to secure the tool to the body	1
7	GB_SLOTTED_TYPE5 M2X6-S	screw to help move the pin	1
8	Spring Large	Spring to force the tool away from Cut	1
9	Spring Small	Spring for the stopper Mechanism	1

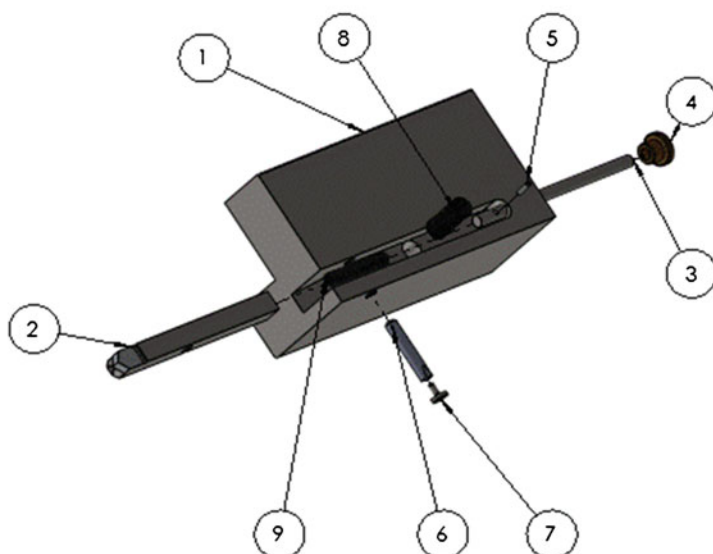


Fig. 9.22 Design 3-assembly Drawing

9.7.2 Assembly and Manufacturing

All the components except tool housing have been sourced through vendors to fit the job and machined to fit the arrangement, whereas tool housing has been machined from the block of AISI M2 on a CNC milling machine. In order to assemble the quick stop tool the following steps need to be followed in order: (a) prepare the stopper mechanism by inserting the rod through the hole provided at the back of the body, then screw the grip cap, insert the spring from the other end, and

insert the pin to lock the spring from sliding outwards, (b) insert the other spring (bigger one) into the vertical slot provided in the tool housing body, (c) the cutting tool can be rested on the inclination and aligned with the hole provided on the front end of tool housing. The pin can be inserted to lock its movement; the cutting tool can then be pressed and locked using the stopper mechanism provided. Hence, the quick stop tool will be ready to perform its task. In order to activate the quick stop tool the stopper at the back end needs to be pulled to remove the restriction on the cutting tool to rotate; the spring will unload after the lever has been pulled thereby increasing its initial acceleration away from the cutting point.

9.7.3 Testing the Quick Stop Tool (Design 3)

The test will be done at a round bar of aluminum 6060 at the same spindle speed and feed as mentioned in design 1. This design is still not able to freeze the chip root during machining. While the testing was being done it was noticed that even though the chip was thicker than the actual width of cut, it is a normal occurrence during machining. The chip even though at this thickness does not possess the strength to stay attached after the tool has been released to rotate downwards. The device was not able to perform at speeds higher than 200 rpm.

9.7.4 Outcome

After the test conducted on the 6060 aluminum alloy using the quick stop tool design 3 it was noted that the acceleration of the cutting tool on activation of the quick stop mechanism as well as the chip thickness play a vital role to help freeze the chip root. The chips require the necessary strength to stay attached to the workpiece even after the tool has been moved away at the maximum acceleration possible through the design, as the rotating spindle will cause to break off if it is not thick enough to stay attached at that spindle speed. In order to increase the chip thickness the tool needs to change to a cutoff tool, as its width of cut is significantly larger to the V tool. Hence it will help in producing the necessary chips with sufficient thickness.

9.8 Design 4: Retracting Action (X-Axis)

Utilizing the outcomes from the previous designs, the following objectives and assumption were made to aid in a successful design that would be able to help in obtaining the frozen chip root during turning machining operation: (a) the design that will be proposed in this section will be sturdy enough to perform as a cutting

tool itself as the quick stop tool is a research tool that requires to mimic the performance of a standard tool in action which has an additional capability to freeze the chip root during machining, (b) retraction of the cutting tool will be the movement away from the cutting point when the quick stop tool is activated, (c) the cutting tool for this tool will remain the V tool as used before, this design is being created to analyze the effectiveness of different types of cutting tool movement away from the point of cut. If time will permit a cutoff tool will be designed for this model, (d) the V tool used will be of the same magnitude as used in Design 3 and will be modified from that point to fit this model, (e) springs will be used to force the back from the point of cut.

9.8.1 Component Design

9.8.1.1 Tool Body Housing

For this design as retraction is the movement of the tool, two springs were used in parallel to help develop the force to pull the V tool back. To do so the interior of the tool body housing required space for this layout. Hence the following design (Fig. 9.23) was proposed for this purpose the wireframe view (Fig. 9.23) is also provided on right to show the interior of the housing.

9.8.1.2 Push and Locking Mechanism

The locking mechanism from the previous design has been used as push tool here, as the cutting tool has two springs attached parallel to them as shown in the image. It needs to be pushed forward and then locked to perform its machining task. The images shown in Fig. 9.24 will be able to shed some light on how this combination of push and lock mechanism will work during machining. The lock mechanism for this design will just restrict the backward motion being forced due to the loaded springs.

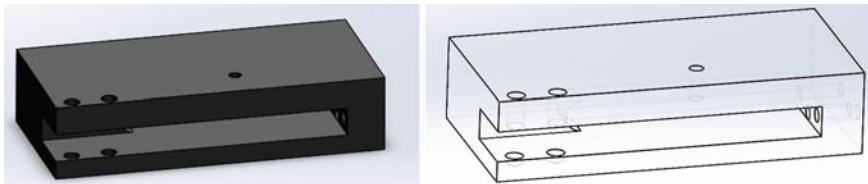


Fig. 9.23 Solid and wireframe view for tool housing (Design 4)

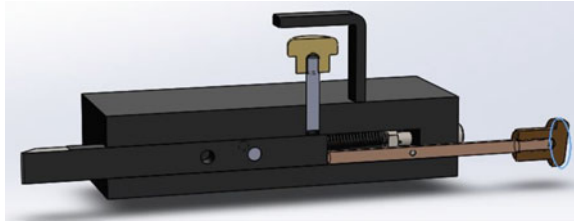


Fig. 9.24 Working of stopper mechanism (Design 4)

9.8.1.3 V Cutting Tool

The cutting tool used is the same as Design 3 despite the outcome that suggests trying a cutoff tool; the same tool is used in this design so that the tool can be ruled out as a viable option. The cutoff tool has been designed for the previous design. Two holes have been provided on the cutting tool to adjust the retraction force by manipulating the extended spring length to get the most out of it. The assembled tool spring system is shown in Fig. 9.25 to help in understanding the concept used for this design.

9.8.2 Manufacturing and Assembly

As in all the previous designs all the components except the tool body housing are sourced from vendors and are standard parts machined to fit the design. The tool housing has been machined from a block of EN 31 on CNC milling Centre. The assembly of the design has been included later in the drawing section. The following steps explained below need to be followed to complete the assembly of the Quick stop tool: (a) the push mechanism needs to be inserted into the hole provided at the back of the housing, (b) the spring and tool needs to be assembled and screwed into the back wall of the housing into the proper slots provided for them, (c) the front block then needs to be screwed onto its place so that the path for the tool to slide along has been restricted to X-axis. Following the steps mentioned above

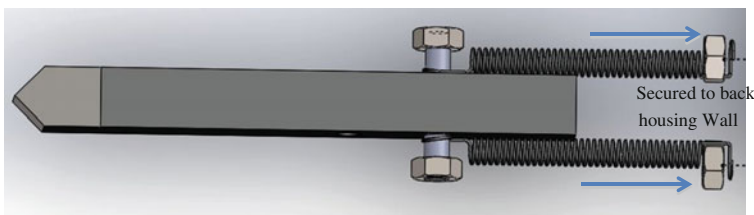


Fig. 9.25 Tool and spring assembly (Design 4)

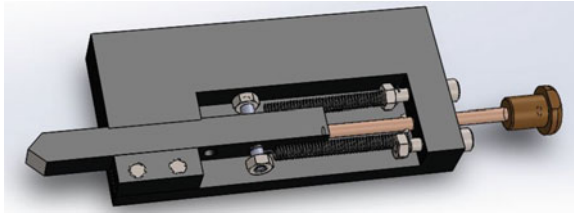


Fig. 9.26 Sectional image of the tool (Design 4)

along with referring to the official drawing for this design will help in its assembly as the spring and tool setup needs to go into a tight space and hence requires considerable amount of time and patience and the right tool to get the job done.

The quick stop tool requires to be pushed forward using the push rod till the locking mechanism falls into place and for activation of the quick stop stopper at the top requires to be pulled up for the cutting tool slide back. The images in Fig. 9.26 are of the quick stop tool before activation and Fig. 9.27 after activation.

9.8.3 Testing of the Quick Stop Tool (Design 4)

The quick stop like all other designs will be tested at the same spindle speeds and feeds mentioned in Design 1. On testing this design on the lowest speeds it was discovered that the design did not function properly as the sliding action of the tool on activation was on a greased surface. Also, the chips did not possess the required strength to stay on the workpiece when the tool is retracted away from it.

9.8.4 Outcome

Hence the outcome that was deduced from the testing done for Design 3 was accurate and the tool needs to be changed at this rate of acceleration of the tool away from the point of cut. This design can be re analyzed to find the flaws encountered and use these findings to redesign to make sure it does its task efficiently.

9.9 Cutoff tool design

As this tool will be made to order, the following design requirements would be required and certain assumptions will be made while designing the tool: (a) the cutoff tool will need to have a minimum width of cut of 4 mm or higher to produce

ITEM NO.	PART NUMBER	QTY.
1	Tool Body Housing	1
2	stopper pin assembly	1
3	L bracket	1
4	Housing Block	1
5	B18.3.1M - 5 x 0.8 x 20 Hex SHCS-- 20NHX	2
6	B18.3.1M - 4 x 0.7 x 20 Hex SHCS-- 20NHX	2
7	Push pin	1
8	Tool Assembly	1
9	B18.2.4.1M - Hex nut, Style 1, M4 x 0.7 --D-N	2
10	release spring	2

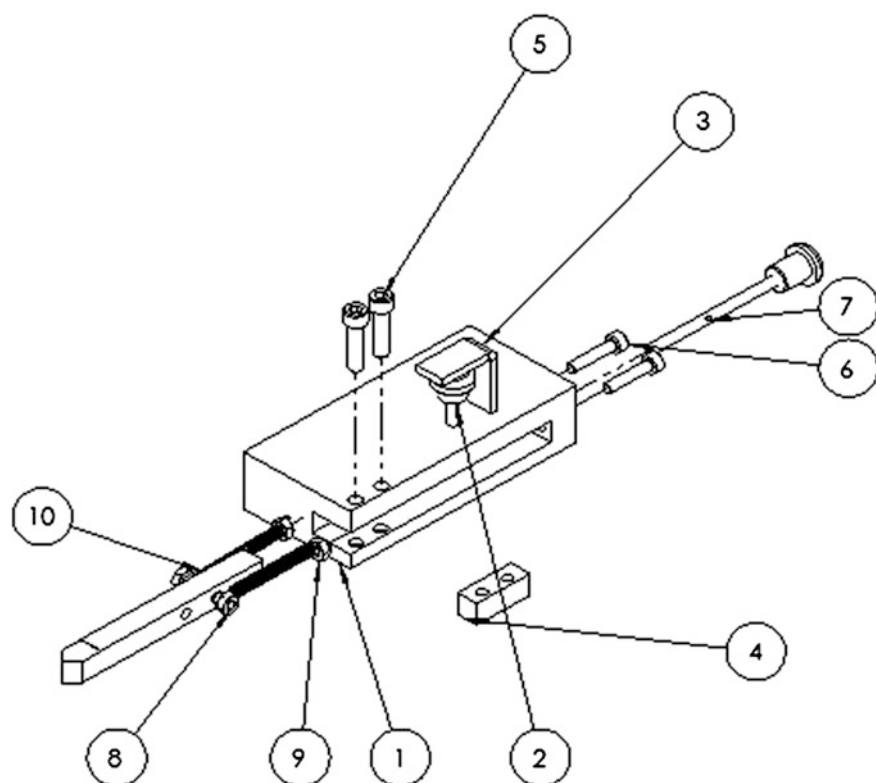


Fig. 9.27 Design 4-assembly drawing



Fig. 9.28 Solid and wireframe image of cutoff tool (Design 3)

chip that would possess the strength to stay on the workpiece after the quick stop tool has been activated (Design 3), (b) the clearance angle required to make sure only cutting edge is in contact with the workpiece to be within 5° – 8° , (c) the other feature to be machined on the tool needs to replicate the V tool used in Design 3 as the tool being designed needs to be able to fit in that housing perfectly, (d) the tool is required to undergo the same testing criteria as the previous designs, the direction of feed will change and the initial setup of testing will require some change to accommodate for the new tool type, (e) high-speed steel will be used to manufacture the designed cutoff tool. Utilizing the design consideration and assumption the following design (Fig. 9.28) for the cutoff tool has been proposed to serve for Design 3.

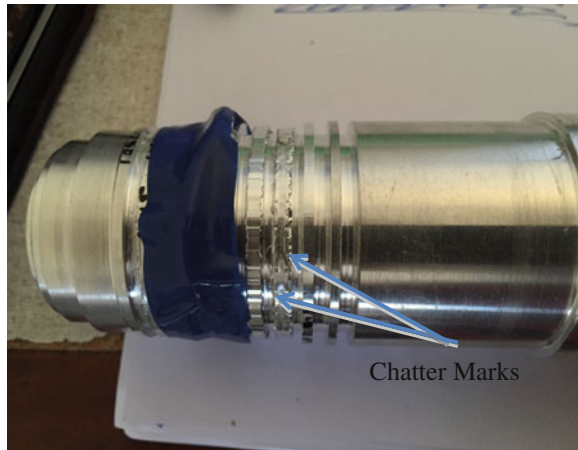
9.9.1 Testing the Quick Stop with Cutoff Tool (Design 3)

On testing the quick stop device developed during the 3rd design at 200 rpm spindle speed and feed of 0.10 mm/rev the quick stop tool was found to be successful in producing a chip root. But at higher speeds this arrangement was found to lack the speed to move away faster than the spindle rotation. The images of the successful quick stop tool performance have been included in the discussion section and will be used to explain the reason for the different decisions made during the entire project.

9.9.2 Outcome

It can be safely assumed that cutoff tool is the right tool to obtain a chip root sample. These designs that have been manufactured to obtain the chip root can be modified to use the cutoff tool. It was noticed during higher spindle speeds and feeds, i.e., 315 rpm and 0.165 mm/rev the tool was producing chatter as the tool is considerably harder than the stopper used to restrain it. This leads to the rod being bent and tool being imbalanced experiences chatter. The chatter mark (Fig. 9.29) on the actual test aluminum 6060 sample is clearly visible for 315 rpm and 0.165 mm/rev feed. Hence the validity of the outcome is proved.

Fig. 9.29 Problems occurred during (Design 3)



9.10 Discussions

For this project, a quick stop tool needed to be designed and manufactured that would be successful in obtaining a chip root sample. Chip root is an important region that requires to be monitored during machining. As chip formation takes place, when shear stress exceeds shear strain plastic deformation occurs and shear is the main cause for failure during machining. Shear stress is known when the force that causes deformation on due to material slippage along the plane or planes parallel to that stress. If we are causing deformation by force due to machining the various materials, it would help to know the effect of different machining conditions and their corresponding final surface conditions obtained. Crack, which is the usual starting point of failure, can be avoided with very accurate predictions of the surface integrity obtained after machining. This knowledge can help avoid disasters by providing a precise life of the machined material if substantial study of the chip root of that material has been done for various speeds and feeds to help determine the surface integrity that will be produced at various speeds and feeds.

Hence, for this project certain assumptions and objectives were decided upon before commencing the task of designing to make sure that the process goes through an orderly fashion leaving very little margin for error to occur. The design for the quick stop would employ spring force to propel the tool away from the point of cut. No explosives or any type of destructive method will be used in any of the designs. It was initially decided that only one design will be attempted, but soon it was discovered that a single method employed to force the tool away would not be the right way to get a successful tool developed. Hence three main types of tool movement away from the cutting point were decided upon and are listed as follows:

- X-Y axis orthogonal motion,
- Y-Z axis orthogonal motion, and finally
- X-axis retraction motion

The tool initially used for this project was the carbide insert (c type), on a custom-made insert holder.

The primary objective while designing the quick stop device was to make sure that the motion of the tool on activation of the quick stop feature should be relatively faster than the rotation of the spindle on which the workpiece is mounted. Also, the tool is required to be sturdy enough to perform as a stand-alone tool for machining; if this quick stop device is to be used in the industry it should not lead to decrease in the productivity of the workforce. The quick stop device would first be tested on machineable material, for example, aluminum (6060 for this project). As aluminum is a good example of ductile material it produces continuous chips at relatively high cutting speeds and feeds. The quick stop device was design initially to perform the task successfully, then further work would be done on the existing design to help it cover a wide range of cutting conditions [18].

The first two designs on testing were found not to perform even at lower speeds and feeds. The reason behind the failure was the motion as well as the tool used for the first three designs. The carbide inserts as well as the V cutting tool were not appropriate choices for the method chosen to force the tool away on quick stop activation. As the point of cut for the tools mentioned are very small, hence the chip produced does not hold sufficient strength to stay connected to the workpiece after the quick stop has been engaged as the chip will hit the top surface of the tool while the tool is moving away from the point of cut due limited amount of force that can be generated using springs. An alternative method using powerful electromagnets can help get the exit time interval down to the order of nanoseconds from the millisecond range a spring is capable to generate in the designs. The budget as well as the time restriction for this project denied the use of such tool to enhance the quick stop's performance.

It was later the third design when the outcomes were confirmed on the *Y-Z* axis rotation of the tool. It was observed that this motion was the most effective, as the tool moving downwards reduces the possibility for the chip to hit the rack face of the tool. But at this point it was confirmed that a tool is required whose feed is into the work material rather the across the surface of the material. This led to a change in the main cutting tool being a cutoff tool (Fig. 9.30). For this tool to be a successful replacement for the current ones the workpiece needs to be divided into small grooves whose number depends on the number of tests that need to be carried out. The distance

Fig. 9.30 Required grooves for testing using cutoff tool (Design 3)





Fig. 9.31 Test attempts using cutoff (Design 3)

between each groove should be kept smaller than the width. This routine needs to be followed to negate the effect of the radius of curvature of the workpiece, which can be calculated as a ratio of the radius of the workpiece to the feed per revolution to about 150:1. Also, the ratio of feed per revolution to the width of cut is less than 0.1, which indicates the plane strain condition was constant. Hence, this tool should be theoretically successful during orthogonal machining [14].

On testing the designed cutoff tool, it performed perfectly on 200 rpm and 0.10 mm/rev. But as the speeds increased the tool started showing signs of chatter as seen in the image in Fig. 9.31. Although the quick stop tool on activation at speeds till 315 rpm produces a chip root, the chatter during machining could indicate the results yielded would not be accurate as it showed signs of surface damage. The tool had been designed at the end to fit the third quick stop design model, as a cutoff tool requires support in the front end of the tool. Machining causes an upward force at the end of the tool where the stopper is inserted to restrict upward motion; as the stopper material was general steel it would bend under the force and cause imbalance leading to chatter. The image in Fig. 9.31 shows the chip root of the workpiece.

9.11 Conclusions

The undergraduate final year project gives opportunities to students to apply their engineering knowledge in the practical field, taste the practical engineering environment, and gain research experience in a specific field. In addition, the students feel confident, appreciate the creation, think to further improve the creation, and apply wide range of knowledge of a specific field when the final-year project is based on producing a practical object. In this study, the student designed and manufactured a quick stop device. While doing this the student had to define

objectives, understand the underlying mechanisms, study the background, create own design, manufacture the product, redesign to improve the performance, and finally develop the successful product. When compared with other students doing other projects, this student showed huge enthusiasm, creative attitude, and sharp attention, and was in a relaxed mode most of the time. This investigation and the above points strongly support that an object-based final-year project enhances the quality, quantity, and speed of learning.

References

1. Pramanik A, Islam M (2014a) Introduction of a new software package in teaching design methodology for material selection. *Int J Inf Educ Technol* 4(4)
2. Pramanik AI (2013) Technology tools and approaches to improve undergraduate education. *Int J Res Educ Methodol* 4(1):390–400
3. Carter CS, Brickhouse NW (1989) What makes chemistry difficult? Alternate perceptions. *J Chem Educ* 66(3):223
4. Seymour E (1995) Revisiting the “problem iceberg”: science, mathematics, and engineering students still chilled out. *J College Sci Teach* 24:392
5. Tobias S (1992) Revitalizing undergraduate science: why some things work and most don't. An occasional paper on neglected problems in science education. ERIC
6. Anthony SMH, Spencer B, Gutwill J, Kegley S, Molinaro M (1998) The ChemLinks and ModularCHEM consortia: using active and context-based learning to teach students how chemistry is actually done. *J Chem Educ* 75(3):322
7. Pramanik A, Islam MN (2014b) Module-based teaching of mechanical design. Using technology tools to innovate assessment, reporting, and teaching practices in engineering education, p 60
8. Mills JE, Treagust DF (2003) Engineering education—is problem-based or project-based learning the answer? *Austral J Eng Educ* 3(2)
9. Jones BF, Rasmussen CM, Moffitt MC (1997) Real-life problem solving: a collaborative approach to interdisciplinary learning. American Psychological Association, Washington, DC
10. Thomas JW (1999) Project based learning: a handbook for middle and high school teachers. Buck Institute for Education, Novato
11. Dym CL et al (2005) Engineering design thinking, teaching, and learning. *J Eng Educ* 94 (1):103–120
12. Thomas JW (2000) A review of research on project-based learning
13. Griffiths B (1986) The development of a quick-stop device for use in metal cutting hole manufacturing processes. *Int J Mach Tool Des Res* 26(2):191–203
14. Chern G-L (2005) Development of a new and simple quick-stop device for the study on chip formation. *Int J Mach Tools Manuf* 45(7):789–794
15. Black J, James C (1981) The hammer QSD-quick stop device for high speed machining and rubbing. *J Manuf Sci Eng* 103(1):13–21
16. Ozturk S, Altan E (2012) Design of a computer aided quick-stop device for study of dead metal zone formation. *J Braz Soc Mech Sci Eng* 34(4):501–505
17. Toenshoff HK, Denkena B (2013) Basics of cutting and abrasive processes. Springer, Berlin
18. Armarego E, Brown RF (1969) The machining of metals. Prentice-Hall Inc., Englewood Cliffs, p 437

Chapter 10

Quantifying Quality of Learning During Teaching an Undergraduate Unit: Manufacturing Processes

A. Pramanik and M.N. Islam

Abstract Multiple-choice questions have been introduced in the Manufacturing Processes 233 unit at Curtin University recently to assess students' learning in this core subject. The questions were set based on the learning outcomes proposed in the unit outline. There are three learning outcomes of this unit. This paper investigates students' learning capability and approach of answering questions based on the learning outcomes. The analysis was performed by interpreting the students' answers in the midterm and final examinations. It was found that students' overall learning in this unit was reasonably good. However, students performed better in the area where knowledge can be applied directly to the workplace. On the other hand, students are marginally weaker in understanding theoretical and analytical facts of the subject matter.

10.1 Introduction

Multiple-choice Questions (MCQs) are referred to as “objective questions” which have a correct answer (usually only one) in addition to several wrong answers. The term “objective” means that there is complete objectivity in marking the test where the construction, specification and writing of the individual questions (items) are influenced by the judgements of examiners as much as in any other test [1]. This tests mainly knowledge of factual material and the understanding of concepts. MCQ tests can be useful for developmental assessment and to excite students' lively and self-managed learning. These expand students' learning enactment and their insights into the quality of learning skill [2]. MCQs have become progressively widespread in modern education because automatic processing encourages its application in educational testing in a wide range of circumstances, such as secondary and tertiary level education talent testing, proper examinations, and also as

A. Pramanik (✉) · M.N. Islam

Department of Mechanical Engineering, Curtin University, Bentley WA 6102, Australia
e-mail: alokesh.pramanik@curtin.edu.au

© Springer International Publishing Switzerland 2015
J.P. Davim (ed.), *Modern Manufacturing Engineering*, Materials Forming,
Machining and Tribology, DOI 10.1007/978-3-319-20152-8_10

301

part of surveys and attitudinal measures. Computers with optical character recognition (OCR) are used in evaluating the answer sheet, and integral parts in modern educational practice. The ability to test large numbers of students using computer-based marking systems has helped ease the marking burden of teachers involved in large courses, a problem common to many early undergraduate science and engineering programs [3].

Substantial attention in quality of education has begun to emerge mainly in higher educational institutions [4–6] though the argument about quality is continuing [7] as the perception of quality when applied to higher education has been inconclusive [8–10]. It can be said that the quality in education is a multiple perception with varying conceptualizations and this poses problems in formulating a single and complete definition [11]. Engineering students should have the quality to solve workplace problems. Students must develop sufficient analytical and theoretical backgrounds, and apply them in solving complex problems [12]. These kind of problems have (i) vaguely defined or undecided goals and unspecified constraints, (ii) several solutions and solution paths or no consensual agreement on the proper solution, (iii) multiple criteria for assessing solutions, (iv) no explicit meaning to determine suitable relationships among concepts, rules and principles and (v) the requirement for engineers to make judgments about the problem and defend them [13]. If engineering education programs are to meet these challenges, they must comprehend the nature of workplace problem-solving in order to better prepare their graduates for the workplace [12]. This paper proposes multiple-choice questions to understand and investigate students' learning and ability in Manufacturing Processes 233, based on the answers of examination questions. This helps to identify the overall weakness and strength of the students in different areas of learning outcomes and put more effort in those areas to improve learning ability.

Manufacturing Processes 233 is a core unit in undergraduate Mechanical Engineering course at Curtin University. This unit is taught in the second year when students are relatively fresh to grab the knowledge in the field of manufacturing easily. Students need to learn and apply analytical skill in addition to memorizing huge amount of information related to manufacturing processes in this unit. The syllabus of this unit is as follows: Introduction to Manufacturing Processes and Safety, Standards and Specifications, Traditional Shaping and Machining Processes, Production Planning, Computer Numerical Control (CNC) Machining, Primary Forming Processes, Secondary Forming Processes, Joining Processes. There are ten lectures and five laboratory activities in teaching this unit. The lectures were delivered to cover the syllabus under different titles such as (a) Measurement, Inspection and Testing, (b) Machining Processes, (c) Introduction to CNC Machining, (d) Production Planning and Interchangeable Manufacture, (e) Casting Processes, (f) Joining Processes, (g) Forming Processes, (h) Bulk Deformation Processes 1, (i) Bulk Deformation Processes 2, (j) Sheet metalworking. The laboratory activities were on (a) Measurement, (b) CNC Programming, (c) Casting, (d) Welding and (e) Machining Project.

10.2 Learning outcomes

There were three learning outcomes of this unit. On successful completion of this unit students can (a) Explain and apply the manufacturing processes of engineering materials and components, (b) Apply the principles of primary and secondary forming processes, and specialized fabrication techniques and (c) Analyse and select the appropriate manufacturing methods for specific types of components. Outcomes (a) and (b) involve correlations of different theories and analytical understanding. On the other hand, learning outcome (c) is related to apply ready-made knowledge on the practical field. These learning outcomes addressed four graduate attributes. These are (i) apply discipline knowledge, (ii) communication skills, (iii) use analytical skill to solve problems and (iv) confidence to investigate new ideas. The first learning outcome addressed the first and second graduate attributes, the second learning outcome addressed the first graduate attribute and the last learning outcome addressed the third and fourth graduate attributes.

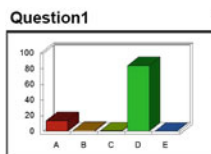
10.3 Learning Outcomes, examination questions and Student Response

To assess the students' learning there were short answers as well as multiple-choice questions in the midterm and final examinations. All the questions were based on the learning outcomes. Student responses on multiple-choice questions are easy to quantify, present and analyse. Thus, only multiple-choice questions have been considered in the paper to analyse students' learning ability. The questions and responses of students under different learning outcomes are discussed below.

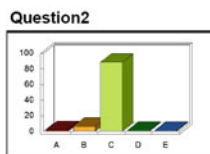
10.3.1 Explain and Apply the Manufacturing Processes of Engineering Materials and Components

Question 1. "Stick" welding is a term sometimes applied when referring to which one of the following processes?

Possible answers: A. Flux Cored Arc Welding (FCAW), B. Gas Metal Arc Welding (GMAW), C. Gas Tungsten Arc Welding (GTAW), D. Shielded Metal Arc Welding (SMAW), E. None of the above.



Response	Percent
A	13.67
B	1.44
C	0.72
D	84.17
E	0.00

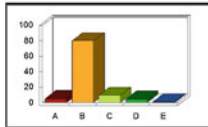


Response	Percent
A	2.16
B	6.47
C	88.49
D	1.44
E	1.44

Question 2. Which one of the following arc-welding processes uses a nonconsumable electrode?

Possible answers: A. Flux Cored Arc Welding (FCAW), B. Gas Metal Arc Welding (GMAW), C. Gas Tungsten Arc Welding (GTAW), D. Shielded Metal Arc Welding (SMAW), E. None of the above.

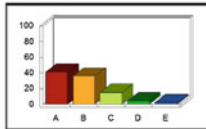
Question3



Correct: B

Response	Percent
A	5.04
B	79.86
C	9.35
D	4.32
E	0.72

Question11



Correct: C

Response	Percent
A	41.01
B	35.97
C	15.11
D	4.32
E	2.16

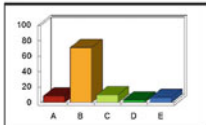
Question 3. MIG welding is a term sometimes applied when referring to which one of the following processes:

Possible answers: A. Flux Cored Arc Welding (FCAW), B. Gas Metal Arc Welding (GMAW), C. Gas Tungsten Arc Welding (GTAW), D. Shielded Metal Arc Welding (SMAW), E. None of the above

Question 11. Which one of the following surface roughness parameters is the most frequently used and internationally accepted?

Possible answers: A. Peak-to-valley height, B. Root means squared, C. Arithmetic average, D. Ten-point-average, E. skewness

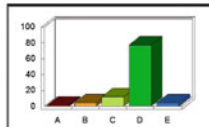
Question12



Correct: B

Response	Percent
A	8.63
B	71.22
C	10.07
D	3.60
E	6.47

Question13



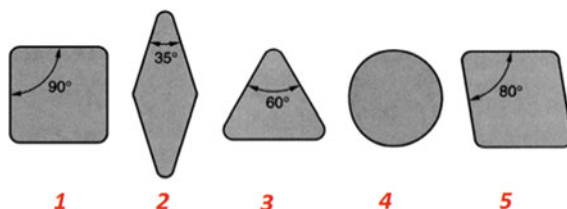
Correct: D

Response	Percent
A	1.44
B	4.32
C	12.23
D	77.70
E	4.32

Question 12. A broaching operation is best described by which one of the following?

Possible answers: A. A rotating tool moves past a stationary workpiece, B. A tool with multiple teeth moves linearly past a stationary workpiece, C. A workpiece is fed past a rotating cutting tool, D. A workpiece moves linearly past a stationary single-point tool, E. None of the above.

Question 13. Which one of the following is a characteristic of the *orthogonal cutting model*? Possible answers: A. A circular cutting edge is used, B. A single-point tool is used, C. The cutting edge is parallel to the direction of cut, D. The cutting edge is perpendicular to the direction of cut, E. None of the above



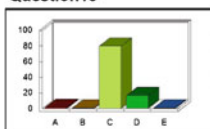
Question 18. What size of a feature is checked by a GO gauge?

Possible answers: A. Nominal size, B. Basic size, C. Maximum material size, D. Least material size, E. None of the above

Question 20. Which one of the common insert shapes shown below has the most accessibility?

Possible answers: A. 1, B. 2, C. 3, D. 4, E. 5

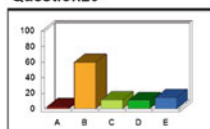
Question18



Correct: C

Response	Percent
A	1.44
B	0.72
C	79.86
D	16.55
E	0.72

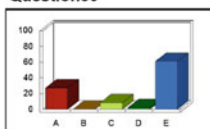
Question20



Correct: B

Response	Percent
A	2.88
B	59.71
C	11.51
D	10.79
E	14.39

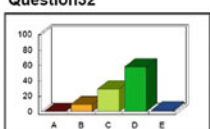
Question30



Correct: A

Response	Percent
A	27.34
B	0.00
C	8.63
D	2.16
E	61.15

Question32



Correct: D

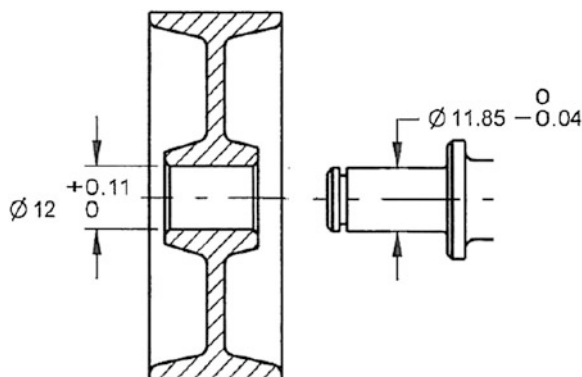
Response	Percent
A	0.00
B	9.35
C	29.50
D	58.27
E	2.16

Question 30. Machine loading refers most closely to which one of the following:

Possible answers: A. Assigning jobs to a work centre, B. Floor foundation in the factory, C. Managing work-in-progress in the factory, D. Releasing orders to the shops, E. Sequencing jobs through a machine

Question 32. For manufacturing the shaft shown in question 31 which one of the following raw materials you would you recommend?

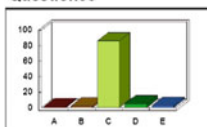
Possible answers: A. 28 × 56 mm billet, B. 30 × 56 mm billet, C. φ30 mm rod, D. φ 34 mm rod, E. None of the above



Question 33. Figure below shows two mating parts. For the hole-based fit between the hole and the mating shaft, what is the *minimum clearance* between the hole and the shaft?

Possible answers: A. 0.04 mm, B. 0.11 mm, C. 0.15 mm, D. 0.30 mm, E. None of the above

Question33

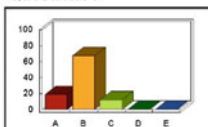


Correct: C

Response

Percent

Question34



Correct: C

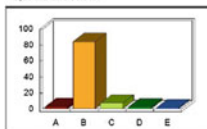
Response

Percent

Question 34. In the previous question what is the *nominal size* of the shaft?

Possible answers: A. 11.81 mm, B. 11.85 mm, C. 12 mm, D. 12.11 mm, E. None of the above

Question35

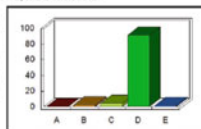


Correct: B

Response

Percent

Question36



Correct: D

Response

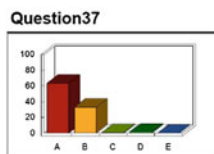
Percent

Question 35. In the same question (Question 33) what is the *tolerance size* on the hole?

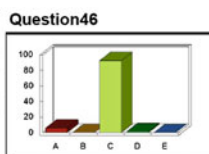
Possible answers: A. 0.04 mm, B. 0.11 mm, C. 0.15 mm, D. 0.30 mm, E. None of the above

Question 36. In the same question (Question 33) what is the *maximum material size* of the shaft?

Possible answers: A. 11.00 mm, B. 11.45 mm, C. 12.00 mm, D. 11.85 mm, E. None of the above



Correct: B

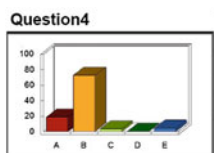


Correct: C

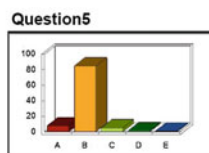
Question 37. In the same question (Question 33) what is *the least material size* of the hole? Possible answers: A. 12.00 mm, B. 12.11 mm, C. 12.45 mm, D. 12.85 mm, E. None of the above

Question 46. A tolerance is which one of the following?

Possible answers: A. Clearance between a shaft and a mating hole, B. Measurement error, C. Total permissible variation from a specified dimension, D. Variation in manufacturing, E. None of the above



Correct: B



Correct: B

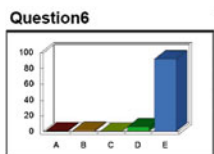
10.3.2 Apply the Principles of Primary and Secondary Forming Processes, and Specialized Fabrication Techniques

Question 4. Springback in a sheet-metal-bending operation is the result of which one of the following?

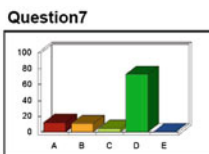
Possible answers: A. Elastic modulus of the metal, B. Elastic recovery of the metal, C. Overbending, D. Overstraining, E. Yield strength of the metal.

Question 5. The upper half of a sand-casting mould is called which of the following?

Possible answers: A. Flask, B. Cope, C. Drag, D. Core, E. Runner



Correct: E



Correct: D

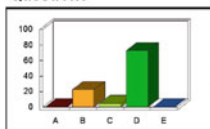
Question 6. Investment casting is also known by which one of the following names?

Possible answers: A. Fast-payback moulding, B. Full-mould process, C. Lost-foam process, D. Lost-pattern process, E. Lost-wax process

Question 7. The starting workpiece in steel hot rolling of plate and sheet stock is which of the following?

Possible answers: A. Bar stock, B. Billet, C. Bloom, D. Slab, E. Wire stock

Question8

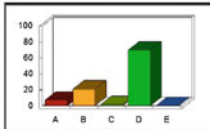


Correct: D

Response

Percent

Question9



Correct: D

Response

Percent

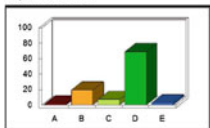
Question 8. Which one of the following casting processes is the most widely used?

Possible answers: A. Centrifugal casting, B. Die casting, C. Investment casting, D. Sand casting, E. Shell casting

Question 9. In cold drawing of fence wire what are the two most important mechanical properties of stock material?

Possible answers: A. Hardness and tensile strength, B. Toughness and ductility, C. Hardness and toughness, D. Yield strength and ductility, E. None of the above

Question14

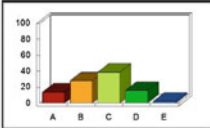


Correct: D

Response

Percent

Question15



Correct: C

Response

Percent

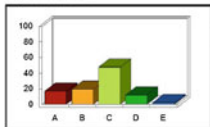
Question 14. Which one of the following manufacturing processes will likely to result in the worst surface finish?

Possible answers: A. Turning, B. Grinding, C. Drilling, D. Sand casting, E. Milling

Question 15. Which method of casting would be suitable for the production of a gas turbine blade?

Possible answers: A. Sand casting, B. Die casting, C. Investment casting, D. Centrifugal casting, E. None of the above.

Question17

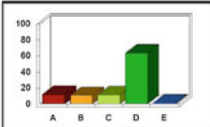


Correct: C

Response

Percent

Question27



Correct: D

Response

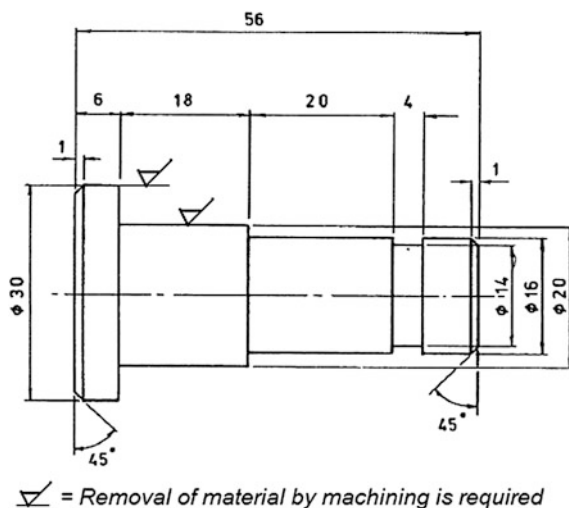
Percent

Question 17. Based on the number of pieces produced, which of the following forging operations is the most widely used?

Possible answers: A. Open-die forging, B. Impression-die forging, C. Upsetting, D. Roll forging, E. Swaging

Question 27. It is found that after 1 h a shaft of 40.00 mm diameter deviated from the set size due to tool wear. If the tool wear is 100 micron, what is the measured size of the shaft?

Possible answers: A. 39.80 mm, B. 39.90 mm, C. 40.10 mm, D. 40.20 mm, E. None of the above



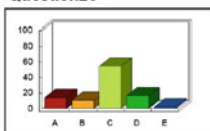
Question 28. Which method of manufacturing would be suitable for the production of aluminium window frames—ongoing production?

Possible answers: A. Casting, B. Forging, C. Extrusion, D. Rolling, E. None of the above

Question 31. For making 45° bevelled feature on the left side of the shaft as shown in the figure below, which one the turning operation would you recommend?

Possible answers: A. Facing, B. Cut off, C. Chamfering, D. Boring, E. None of the above

Question28

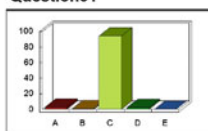


Correct: C

Response

Percent

Question31



Correct: C

Response

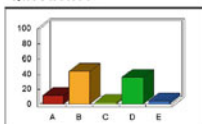
Percent



Question 39. Which one of the following manufacturing processes is commonly used for making kitchen sinks?

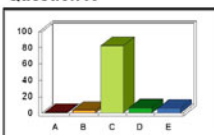
Possible answers: A. Extrusion, B. Forming, C. Milling, D. Drawing, E. None of the above

Question39



Correct: D

Question45

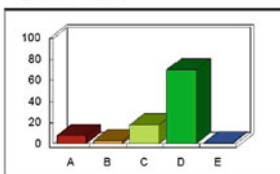


Correct: C

Question 45. A riser in casting can be described by which one of the following:

Possible answers: A. An insert in the casting that inhibits bounciness of the core, B. Gating system in which the sprue feeds directly into the cavity, C. Source of molten metal to feed the casting and compensate for shrinkage during solidification, D. Vertical channel into which metal is poured into the mould, E. None of the above

Question49

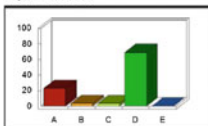


Correct: D

Question 49. Which one of the following processes is classified as precision forging? A. Upset forging, B. Open-die drop forging, C. Impression-die drop forging, D. Flashless forging

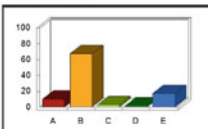
E. None of the above

Question16



Correct: D

Question19



Correct: B

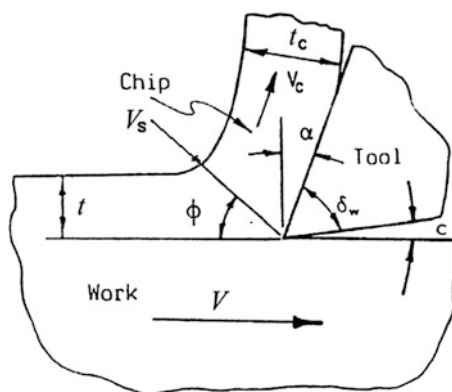
10.3.3 Analyse and Select the Appropriate Manufacturing Methods for Specific Types of Components

Question 16. If the current position of a milling cutter is $x = 0$ and $y = -50.00$; what will be the position of the same cutter after executing the codes? G90 and G02 X -35.35 Y -35.35 I0 J50.00 F 250?

Possible answers: A. $x = -35.35$ and $y = -85.35$, B. $x = -35.35$ and $y = -50.00$, C. $x = 0$ and $y = -50.00$, D. $x = -35.35$ and $y = -35.35$, E. None of the above

Question 19. Which one of the following assembly strategies is preferred by most modern manufacturers?

Possible answers: A. Unit assembly, B. Interchangeable assembly, C. Selective assembly, D. Adjust at assembly, E. Manufacture to fit



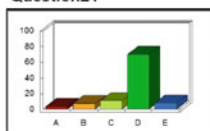
Question 21. Identify which one of the following applications is point-to-point and not continuous path operation?

Possible answers: A. Strait turning, B. End milling, C. Arc welding, D. Drilling, E. None of the above

Question 22

Figure below illustrates the Basic Metal Cutting Model, in which angle α is known as _____,

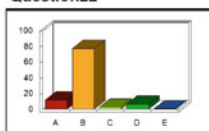
Question21



Correct: D

Response	Percent
A	3.60
B	7.19
C	10.79
D	69.78
E	7.91

Question22



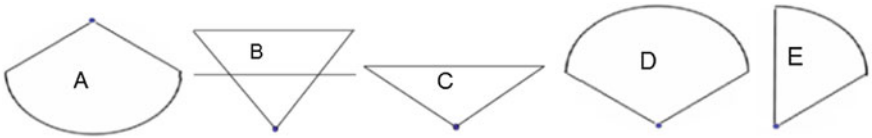
Correct: B

Response	Percent
A	12.23
B	77.70
C	2.88
D	6.47
E	0.72

Possible answers: A. Shear angle, B. Tool rake angle, C. Tool clearance angle, D. Wedge angle, E. None of the above

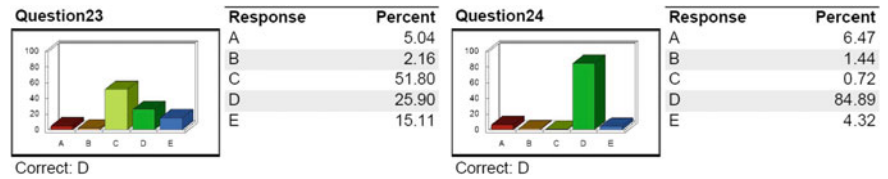


Question 23. Which one of the following manufacturing processes would you recommend for making this part?



Possible answers: A. Extrusion, B. Rolling, C. Die casting, D. Forming, E. None of the above

Question 24
The following CNC program will produce which of the *in-cut tool paths* below?
G91; M03; G00 X 0 Y 0 Z-24.00; G01 X 0 Y 0 Z-6.00 F 50; G01 X 20.00 Y 20.00 F 250
G03 X-20.00 Y 20.00 I-20.00 J0 F 250; G03 X-20.00 Y-20.00 I0 J-20.00 F 250;
G01 X 20.00 Y-20.00 F250; G00 X 0 Y 0 Z 30.00; M05; M30
Possible answers:



Question 26 Compressor frame shown below weighs about 700 kg, which one of the following casting processes would you recommend for making this part?

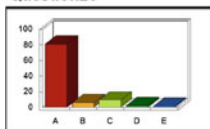


Possible answers: A. Sand casting, B. Investment casting, C. Die casting, D. Centrifugal casting, E. None of the above

Question 29. Most externally threaded fasteners are produced by which one of the following processes?

Possible answers: A. Cutting the threads, B. Milling the threads, C. Tapping, D. Thread rolling, E. Turning the threads

Question26

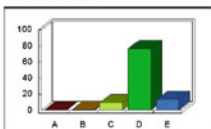


Correct: A

Response

Percent

Question29



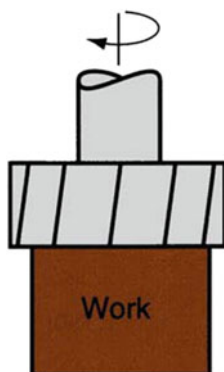
Correct: D

Response

Percent

Question 40. What type of milling operation is depicted in the figure below?

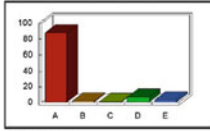
Possible answers: A. Face milling, B. Contour milling, C. Pocket milling, D. Side milling, E. None of the above



Question 41. For the milling operation depicted in the previous question what type of milling cutter is used?

Possible answers: A. Side cutter, B. Face cutter, C. Slitting saw, D. End mill, E. None of the above.

Question40



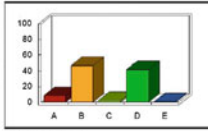
Correct: A

Response

Percent

A	87.77
B	1.44
C	0.72
D	6.47
E	2.88

Question41



Correct: B

Response

Percent

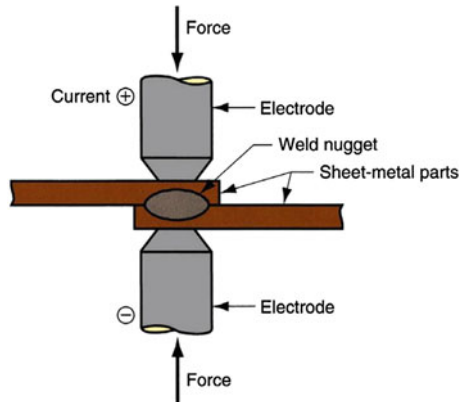
A	8.63
B	46.76
C	2.16
D	41.73
E	0.72

Question 42. A fillet weld has a cross-sectional shape that is approximately which one of the following:

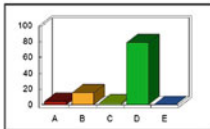
Possible answers: A. Rectangular, B. Round, C. Square, D. Triangular, E. None of the above

Question 43. Identify the welding process depicted below.

Possible answers: A. Oxy fuel gas welding, B. Arc gas welding, C. Solid state welding, D. Resistance welding, E. None of the above



Question42



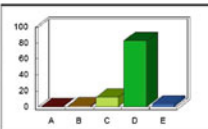
Correct: D

Response

Percent

A	4.32
B	15.11
C	2.16
D	78.42
E	0.00

Question43



Correct: D

Response

Percent

A	0.00
B	1.44
C	12.23
D	82.73
E	3.60

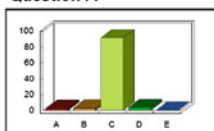
Question 44. In the previous question identify the type of weld being produced.

Possible answers: A. Butt weld, B. Fillet weld, C. Spot weld, D. Groove weld, E. None of the above

Question 47. Which one of the following processes is commonly used for making Olympic medals?

Possible answers: A. Hubbing, B. Coining, C. Roll forming, D. Notching, E. None of the above

Question44

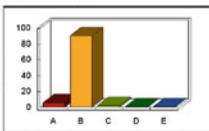


Correct: C

Response

Percent

Question47



Correct: B

Response

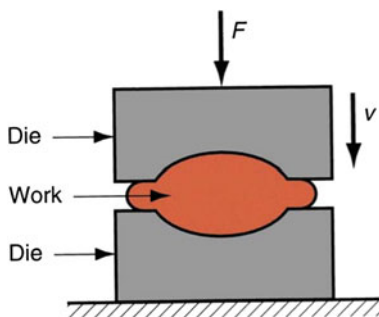
Percent

Question 48. Which statement is not true as related to a wire cold drawing process?

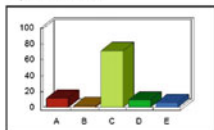
Possible answers: A. During the process, wire material ductility is decreased, B. During the process, strain hardening takes place, C. During the process, unlimited area reduction r can be achieved, D. During the process, wire material strength is increased, E. Before cold drawing annealing is sometimes conducted.

Question 50. Identify the manufacturing process depicted below:

Possible answers: A. Die casting, B. Extrusion, C. Drawing, D. Forging, E. None of the above



Question48

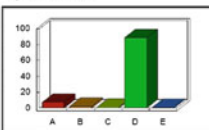


Correct: C

Response

Percent

Question50



Correct: D

Response

Percent

10.4 Students' Learning

The above section shows the questions under different learning outcomes as well as responses of the students in the corresponding graph. The graphs show the percentages of students' choice of the respective possible answers. In this study, it is assumed that the higher the percentage of students choosing the right answers the more the students achieve the designed learning outcomes. The percentage of students who choose the right answers based on the learning outcomes are given in the table below. There were 16, 15, and 16 questions under learning outcomes (LO) 1, 2, and 3 respectively. The highest and lowest percentages of students choosing the right answers under learning outcome 1 were 92.81 and 15.11 respectively. Similarly, they were 94.25 and 35.97 for learning outcome 2 and, 91.37 and 25.09 for learning outcome 3 respectively. These highest and lowest limits of percentages clearly indicate that learning outcome 2 was more successful compared to that of learning outcomes 2 and 3.

Question numbers			Percentage of students who chose right answers		
Learning outcomes			Learning outcomes (LO)		
LO 1	LO 2	LO 3	1	2	3
1	4	16	84.7	72.66	69.06
2	5	19	88.49	84.89	67.63
3	6	21	79.86	92.09	69.78
11	7	22	15.11	72.66	77.70
12	8	23	71.22	72.66	25.09
13	9	24	77.70	69.78	84.89
18	14	26	79.86	69.06	81.29
20	15	29	59.71	38.85	76.26
30	17	40	27.34	47.48	87.77
32	27	41	58.27	63.31	46.76
33	28	42	86.33	54.68	78.42
34	31	43	12.23	94.24	82.73
35	39	44	84.17	35.97	91.37
36	45	47	91.37	82.73	90.65
37	49	48	33.09	69.78	71.22
46		50	92.81		88.49
Average			65.14	68.06	74.32

10.5 Conclusions

It takes considerable time and requires scrupulous care in the design, review and validation stages of an effective MCQ test. It is necessary to ensure each of its individual items is well aligned with the course learning objectives. Multiple-choice questions are a good means to assess students' learning. Though the overall learning of students for Manufacturing Processes 233 was reasonably good the students performed better in the area where knowledge can be applied directly to the workplace. Students are marginally weaker in understanding theoretical and analytical facts of the subject matter.

References

1. Trigwell KR (ed) (1992) Information for UTS staff on assessment. University of Technology, Sydney: UTS Working Party on Assessment. <http://www.iml.uts.edu.au/assessment/types/mcq/>
2. Velan GM, Jones P, McNeil HP, Kumar RK (2008) Integrated online formative assessments in the biomedical sciences for medical students: benefits for learning. *BMC Med Educ* 8(1):52
3. Dalziel J, Gazzard S (2012) The future of multiple choice questions in learning: formative assessment, interactive teaching modules and student-created questions within WebMCQ. In: Proceedings of the Australian conference on science and mathematics education (formerly UniServe Science Conference)
4. Coate LE (1990) TQM on campus: implementing total quality management in a university setting. *Bus Officer* 24(5):26–35
5. Cope R, Sherr L (1991) Total quality management for organizations: concepts and tools, a handbook for tertiary education, technical and further education. National Centre for Research and Development Ltd, Leabrook
6. Cornesky R, McCool S, Byrnes L, Weber R (1991) Implementing total quality management in higher education. Magna Publications, Madison
7. Goodlad S (1995) The quest for quality – sixteen forms of heresy in higher education. SRHE and Open University Press, Buckingham
8. Cheng YC, Tam WM (1997) Multi-models of quality in education. *Qual Assur Educ* 5 (1):22–31
9. Pounder J (1999) Institutional performance in higher education: is quality a relevant concept. *Qual Assur Educ* 7(3):14–22
10. Vroeijenstijn T (1992) External quality assessment, servant of two masters?, the netherlands university perspective. Falmer Press, London
11. Sahney S, Banwet DK, Karunes S (2004) Conceptualizing total quality management in higher education. *TQM Mag* 16(2):145–159
12. Jonassen D, Strobel J, Lee CB (2006) Everyday problem solving in engineering: Lessons for engineering educators. *J Eng Educ* 95(2):139–151
13. Jonassen DH (1997) Instructional design model for well structured and ill-structured problem-solving learning outcomes. *Educ Technol: Res Dev* 45 (1):65–95

Index

A

Abrasive water jet machining (AWJM), 117
Anisotropy, 45, 54, 55, 57, 59, 61
Automated framework, 167
3-axis milling, 148
5-axis milling, 149

B

Body centered, 54
Boundary conditions, 69, 78, 211–213, 216, 220
Boundary element method, 123, 127, 128

C

Chip separation, 70, 72, 77, 79, 88
CNC programming, 145, 147, 148, 150, 168, 173, 174
Computational methods, 208, 209
Computer Aided Design (CAD), 144, 146, 148, 149, 153, 167
Constraints, 150, 151, 158, 160, 162, 168
Conventional machining processes, 100
Cross rolling, 41–46, 53–58, 60–62
Crystallographic texture, 45, 46, 49, 51
Cutting, 8, 16, 18, 23–29, 31–37
Cutting tools, 146, 151, 158

D

Deep drawing, 201, 204–207
Defects, 181, 182, 186–189, 192, 196, 253, 255, 260, 262, 263, 266
Deformation mode, 1, 15–22, 26, 28–30, 32
Design, 272, 273, 275, 278–280, 282–285, 287, 288, 290, 291, 293, 295–299
Designing, 287, 293, 296
Drilling, 100, 109, 111–115, 117

E

Electric discharge machining (EDM), 116
Electrochemical machining (ECM), 119
End-to-end joining, 242
Equal-Channel Angular Pressing (ECAP), 1–11, 13–15, 19, 22, 26, 27, 29–35
Euler angle, 48, 49, 51, 52, 57
Examination questions, 302, 303
Extrusion, 2–4, 8, 10, 13, 15, 22–27, 29–32

F

Face centered cubic, 54
FEM formulation, 220
Final year project, 272, 298
Finite element method (FEM), 66, 67, 69, 76, 85, 86
Finite element modelling, 233, 237
Formability, 187, 200, 201, 204–207
Forming, 200, 201, 203–206, 221
Friction, 67, 69, 78–84, 86, 87, 89, 90
Friction model, 219
Friction stir welding (FSW), 180

G

Genetic algorithm, 160, 164–169, 171–174
Geometric modelling, 125, 216
Grain refinement, 1, 2, 4, 8, 22, 32
Grinding, 113, 114, 124

H

Heat-treatment, 205
Hexagonal close packed, 54, 56
High-precision cutting, 168
Honing, 100, 113, 114
Human resources, 255, 264
Hybrid turning processes, 108
Hydroforming, 205

I

Inclined connections, 241, 244, 246
 Incremental forming, 206
 Intelligent CNC, 144, 145, 147, 151
 Inventory, 252, 254, 255, 257, 258, 262, 265

J

Johnson–Cook model, 71, 72, 74, 79
 Joining technologies, 231, 233, 236, 238, 247

L

Large strain extrusion machining (LSEM), 1, 31–37
 Laser beam machining (LBM), 118
 Lean manufacturing (LM), 249, 250, 252, 254, 255, 265–267
 Learning, 301, 302, 317
 Learning outcomes, 302, 303, 316
 Loads, 100–104, 122, 129

M

Machinability, 104, 105, 117, 118, 120, 121
 Machining, 100–105, 108, 109, 111, 113, 115–124, 126, 127, 130–132, 144–155, 157–163, 167, 168, 170, 171, 173
 Machining processes, 66, 82, 83, 86–88
 Macro scale, 124
 Manufacturing, 144, 146, 148–150, 152, 153, 164, 167, 168, 276, 280, 284, 286
 Manufacturing assembly, 280, 284, 292
 Manufacturing processes, 302, 310, 312, 317
 Manufacturing systems, 254, 255
 Material, 66–74, 77, 78, 80, 82, 85–87, 89, 90
 Material flow, 184, 186–188, 197, 209, 210, 213–215, 221
 Material models, 127
 Materials, 1–4, 8, 9, 15, 19, 20, 22, 27, 29, 31, 32
 Mechanical characterization, 234, 236
 Meshing, 67, 70, 76, 77
 Metal forming, 41, 55
 Metal matrix composites (MMCs), 100, 115, 123, 130
 Micromachining, 87–90, 100, 115
 Micro scale, 123, 124, 128
 Milling, 100, 109–111
 Modeling techniques, 212
 Modelling, 100, 120, 123–127, 129, 131, 132
 Molecular dynamics (MD), 124, 127, 128
 Motion, 255, 259
 Multi-pass, 1, 2, 8, 11, 22, 31, 32, 188, 189

N

Nanostruturing, 22, 29

NC verification, 151

Non-conventional machining processes, 100

Normalization, 161

Numerical analysis, 210

Numerical models, 120

O

Optimization, 145, 155, 156, 160, 162–164, 167, 168, 170, 171, 174

Orientation distribution function (ODF), 45, 49, 51, 54

Over processing, 255, 261

Over production, 255, 262

P

Plastic anisotropy, 45, 56, 61

Plastic deformation, 2, 3, 11, 15, 26, 30, 36

Pole figure, 45, 49–51

Preferred orientation, 47, 53, 55

Pure shear, 15–22

Q

Quick stop device, 274, 275, 295, 297, 298

R

Reference system, 48–50

Re-meshing, 76, 77

Residual stress, 45, 46

Rework, 253, 255, 263, 266

Rolling, 41, 42, 44–47, 52, 54–60

S

Sawing, 100, 114, 115

Scallop height control, 158

Sculptured surface machining (SSM), 145, 150, 152, 168, 174

Severe plastic deformation (SPD), 1–4, 11, 22, 30, 31

Shear strain, 6, 15, 17, 18, 20, 22, 23, 25, 26, 28, 30, 37

Sheets, 231–233, 236, 237, 244, 247

Simple shear, 1, 4, 5, 15, 16–19, 21, 22, 28–30, 32

Soft computing models, 130

Strain distribution, 208, 220, 221

Strength, 41, 55, 56, 59

Structure development, 18

Student's learning, 302, 303, 317

Surface quality, 104, 106–108, 110, 112, 118, 119

System performance, 265

T

Tapping, 100, 113

- Teaching, 302
Temperature distribution, 210, 214, 219, 221
Tensile test, 46, 59–61
Texture, 41–43, 45, 47, 49–58, 62
Thermal model, 219
Tool, 66–71, 76, 78–82, 85, 86, 88–90
Tool design, 290, 293
Tool modelling, 67, 71, 76
Tool path, 144–153, 155, 157, 158, 160, 162, 164, 167–169, 171, 173
Tool path planning, 144, 148, 150
Tools, 189, 190, 208
Tool selection, 107, 108, 110, 112
Tool wear, 101–104, 106–113, 115, 121, 122, 127
Transportation, 255, 256, 259, 265
Tube forming, 239, 247
Tubes, 231–236, 239–241, 243, 244, 246
Turning, 100, 105–111, 120
Twin-tool, 190, 192
U
Ultrasonic assisted FSW, 192, 196
Ultrasonic machining (USM), 100, 120, 194
Ultrasonic welding, 195, 196
Undergraduate unit, 302
V
Virus operators, 165, 169
Virus-evolutionary, 164, 167, 169–172, 174
W
Waiting, 255, 257, 260, 267
Waste, 250, 253–258, 261, 263, 265, 267
Z
Zerilli–Armstrong model, 74